Technische Universität München
TUM School of Engineering and Design

Design, Modelling and Control of a Highly Modular Power Electronics System for Novel Renewable Energy Sources

Simon Klaus Krüner, M.Sc.

Vollständiger Abdruck der von der TUM School of Engineering and Design der Technischen Universität München zur Erlangung eines

Doktors der Ingenieurwissenschaften (Dr.-Ing.)

genehmigten Dissertation.

Vorsitz: Prof. Dr. sc. ETH Zürich Marcelo Lobo Heldwein

Prüfende der Dissertation:

1. Prof. Dr.-Ing. habil. Christoph M. Hackl
2. Prof. Dr. rer. nat. Thomas Hamacher

Die Dissertation wurde am 13.11.2024 bei der Technischen Universität München eingereicht und durch die TUM School of Engineering and Design am 13.06.2025 angenommen.

This document is typeset with LaTeX/TeX.

Danksagung

An dieser Stelle möchte ich Prof. Dr.-Ing. habil. Christoph M. Hackl meinen aufrichtigen Dank aussprechen. Du hattest immer ein offenes Ohr für mich und unsere Gespräche haben mich jedes Mal neu inspiriert, motiviert und mit frischem Elan erfüllt. Besonders schätze ich, wie Du mir geholfen hast, ein tiefes Verständnis für elektrotechnische Sachverhalte durch eine präzise mathematische Herangehensweise zu entwickeln. Dank dieses Fundaments fällt es mir deutlich leichter, komplexe Zusammenhänge ganzheitlich zu verstehen und darauf aufbauend weitere Entwicklungen schneller voranzutreiben. Diese Herangehensweise wird mir in meiner zukünftigen Laufbahn sehr hilfreich sein. Zudem hast Du mich herzlich in Deine Forschungsgruppe aufgenommen, was mir einen wertvollen Austausch mit anderen Doktorandinnen und Doktoranden ermöglicht hat. Ohne Deine fantastische Unterstützung wäre diese Arbeit nicht zustande gekommen. Vielen herzlichen Dank dafür.

Ein weiterer Dank gilt Prof. Dr. rer. nat. Thomas Hamacher für die Übernahme des Zweitgutachtens. Bei Prof. Dr. sc. ETH Zürich Marcelo Lobo Heldwein bedanke ich mich für die Übernahme des Prüfungsvorsitzes. Außerdem danke ich meinem Mentor, Dr.-Ing. Simon Feuersänger, der mir mit seiner Erfahrung und seinem Fachwissen immer Unterstützung und wertvolle Hilfe bieten konnte.

Ich möchte meinen Kolleginnen und Kollegen aus der Doktorandengruppe meinen aufrichtigen Dank aussprechen, die mich von Anfang an offen und freundlich integriert haben – Korbinian Schechner, Christian Dirscherl, Hisham Eldeeb, Julian Kullick, Athina Birda, Katharina Bär, Markus Landerer, Oliver Kalmbach, Andre Thommessen und Niklas Monzen. Ein besonderer Dank gilt Zhao Song, mit der ich gemeinsam an einem Forschungsthema arbeiten durfte und mit der ich stets einen konstruktiven fachlichen Austausch pflegen konnte.

Ebenfalls möchte ich mich bei allen Kolleginnen und Kollegen von SINN Power für die gemeinsame Zeit innerhalb und außerhalb der Arbeit bedanken, aus der wertvolle und langlebige Freundschaften entstanden sind. Gemeinsam haben wir ein großartiges Projekt vorangebracht und uns dabei fachlich wie persönlich weiterentwickelt. Mein Dank gilt auch den Studierenden, die ich während ihrer Abschlussarbeiten betreuen durfte. Der Austausch mit ihnen war stets bereichernd und führte zu einem wechselseitigen Lernprozess.

Besonders möchte ich mich bei meinen Eltern, Lydia und Klaus, und meiner Schwester, Isabella, bedanken. Ihr habt mich während meiner gesamten Ausbildung immer unterstützt und mir vollstes Vertrauen geschenkt, ohne irgendwelche Erwartungen an mich zu stellen.

Mein allerherzlichster Dank geht an Dich, liebe Kerstin, für Deinen Rückhalt und Deine Unterstützung, dafür, dass Du mir die Zeit gegeben hast, die ich brauchte, und dass Du meine Launen ertragen hast. Du, liebe Talea, hast mir seit Deiner Geburt immer die größte Freude bereitet. Du zauberst mir immer ein Lächeln ins Gesicht und erinnerst mich immer daran, was im Leben wirklich wichtig ist. Ich freue mich auf all die Jahre, die wir als Familie gemeinsam verbringen werden.

München, November 2024 Simon Krüner

Contents

Contents **8**

Abstract **9**

List of Publications **11**

Nomenclature **13**

1 Introduction **1**
1.1 The Contribution of Wave Energy 2
1.1.1 Wave Energy – Origin and Potential 3
1.1.2 Wave Energy Converters 5
1.1.3 Development Problems 7
1.2 The Novel Wave Energy Converter 9
1.2.1 Functional Principle 10
1.2.2 Patented Power Take-Off System 11
1.2.3 Control of a Point Absorber Wave Energy Converter 12
1.3 Specification and Contribution 14

2 Highly Modular Power Electronics System **19**
2.1 Topology of the Power Electronics 19
2.1.1 Switching Elements and Half-Bridges 21
2.1.2 Dimensioning of the DC link Capacitor and Voltage Balancing 23
2.1.3 Electromagnetic Compatibility Filter 26
2.2 Modulation 28
2.2.1 Pulse With Modulation 28
2.2.2 Space Vector Modulation 31
2.2.3 Extended Space Vector Modulation 36
2.2.4 High-Frequency Current Measurement 37
2.3 DC/DC Converter 39
2.3.1 Modelling 41
2.3.2 Voltage Control 43
2.3.3 Current Control 46
2.3.4 Maximum Power Point Tracking for Photovoltaic Systems 49
2.4 Generator Unit 54
2.4.1 Model of the Permanent Magnet Synchronous Machine 55
2.4.2 Current Control 58
2.4.3 Optimal Feedforward Torque Control 60
2.5 Grid Inverter 67

2.5.1 Filter of the Grid Inverter . . . 69
2.5.2 Connection of the Filter Star-Point . . . 73
2.5.3 Modelling . . . 78
2.5.4 Proportional-Integral State Feedback Control . . . 80
2.5.5 Observer Design . . . 82
2.5.6 Implementation . . . 84
2.5.7 Experimental Results . . . 85
2.5.8 Full Parallel Connection of Multiple Grid Inverters . . . 90

3 Control of the Modular DC Grid **95**
3.1 Droop Control . . . 97
3.1.1 Droop Control in AC Grids and the Low-Inertia Problem . . . 99
3.1.2 Droop Control in DC grids . . . 103
3.1.3 Implemented Droop Control with Characteristic Curve . . . 105
3.2 Modelling and Stability Analysis of the DC Link Dynamics . . . 109
3.2.1 Nonlinear Grid-Side DC Link Dynamics of a Single Grid Inverter . . . 110
3.2.2 Nonlinear Grid-Side DC Link Dynamics with Multiple Grid Inverters . . . 114
3.2.3 DC Link Dynamics on the Side of the Renewable Energy Sources . . . 115
3.2.4 Linearisation in the State-Space Representation . . . 119
3.2.5 Stability Analysis of the DC Link Dynamics . . . 124
3.3 Power Smoothing . . . 133
3.3.1 Short-Term Energy Storage . . . 133
3.3.2 Control of the Electrical System of a Wave Energy Converter . . . 137
3.3.3 Power Smoothing with a Controllable Short-Term Energy Storage Unit . . . 149

4 Conclusion and Outlook **161**

Bibliography **181**

List of Figures **188**

A Formulary and Calculations **189**
A.1 Clarke Transformation . . . 189
A.2 Park Transformation . . . 190
A.3 Transformation of the Grid Inverter Dynamics . . . 191
A.4 Calculation of the Transfer Function from the State Space . . . 192
A.5 Root Locus . . . 194
A.6 First-Order Low-Pass Filter . . . 195
A.7 Coupling of AC and DC Droop Control Methods . . . 198

Abstract

Wave energy converters (WECs) use the energy from ocean waves to generate electricity. Although these have been under development for a long time, none have yet been able to establish themselves on the market. In order to advance this development, this thesis addresses the realisation of the electrical system and the grid connection of a novel modular WEC. The power electronics components developed include a DC/DC converter, a motor drive and a grid inverter. Dynamic models in the state space are derived for all devices and controllers are designed, implemented and tested. The devices are connected on the DC side, resulting in a highly modular DC grid. To maximise the efficiency of the WEC's power take-off system, a generic identification method is developed to determine the optimum current vector for the electrical machine. To ensure that the grid connection corresponds to the modularity of the WEC, a new grid inverter topology is presented that enables a full parallel connection on both the AC and DC sides simultaneously. The DC grid voltage is controlled by a droop controller, which also considers the load sharing between the inverters. A dynamic model for the DC grid is derived and analysed for stability. Due to the natural wave movement, the generated power must be smoothed before it can be fed into the grid. Power smoothing is realised with supercapacitors connected to the DC/DC converter. A newly developed droop control makes it possible to connect several DC/DC converters to the DC grid in parallel for power smoothing.

Kurzzusammenfassung

Wellenkraftwerke nutzen die Energie aus Meereswellen zur Stromerzeugung. Obwohl an diesen seit langem entwickelt wird, konnte sich bisher keines auf dem Markt durchsetzen. Um diese Entwicklung voranzutreiben, befasst sich diese Arbeit mit der Realisierung des elektrischen Systems sowie der Netzanbindung eines neuartigen modularen Wellenkraftwerks. Die entwickelten Leistungselektronikkomponenten umfassen einen DC/DC-Wandler, einen elektrischen Antrieb und einen Wechselrichter. Für alle Geräte werden dynamische Modelle im Zustandsraum hergeleitet und Regler entworfen, implementiert und getestet. Die Geräte sind auf der DC-Seite verbunden, wodurch ein hochmodulares DC-Netz entsteht. Zur Maximierung des Wirkungsgrades des Abtriebssystems des Wellenkraftwerks wird eine generische Identifikationsmethode entwickelt, um den optimalen Stromvektor für die elektrische Maschine zu bestimmen. Damit die Netzanbindung der Modularität des Wellenkraftwerks entspricht, wird eine neue Wechselrichtertopologie vorgestellt, die eine vollständige Parallelisierung sowohl auf der AC- als auch auf der DC-Seite ermöglicht. Die Regelung der DC-Netzspannung erfolgt durch eine Statikregelung, die auch die Lastverteilung zwischen den Wechselrichtern berücksichtigt. Ein dynamisches Modell für das DC-Netz wird hergeleitet und auf Stabilität untersucht. Aufgrund der natürlichen Wellenbewegung muss der erzeugte Strom geglättet werden, bevor er ins Netz eingespeist werden kann. Die Leistungsglättung wird mit Superkondensatoren realisiert, die an den DC/DC-Wandler angeschlossen sind. Eine neu entwickelte Statikregelung ermöglicht es, mehrere DC/DC-Wandler parallel zur Leistungsglättung an das DC-Netz anzuschließen.

List of Publications

The following publications were written during my employment at SINN Power GmbH and membership at the Graduate Center of the Munich School of Engineering (MSE) at the Technical University of Munich (TUM) in cooperation with the research group “Control of Renewable Energy Systems (CRES)”, followed by a change of membership to the Graduate Center of Engineering and Design (GC-ED) at the TUM from October 2021.

- S. Krüner and C. M. Hackl, “Experimental Identification of the Optimal Current Vectors for a Permanent-Magnet Synchronous Machine in Wave Energy Converters,” *Energies*, vol. 12, no. 5, 2019, [1].
- S. Krüner, Z. Song, and C. M. Hackl, “3D-Modulation and PI State-Feedback Control of Voltage Source Inverters with Split DC-Link,” in *2021 IEEE 30th International Symposium on Industrial Electronics (ISIE)*, pp. 1–7, 2021, [2].
- S. Krüner and C. M. Hackl, “Nonlinear Modelling and Control of a Power Smoothing System for a Novel Wave Energy Converter Prototype,” *Sustainability*, vol. 14, no. 21, 2022, [3].
- Z. Song, S. Krüner, and C. M. Hackl, “Modeling and Proportional-Integral State Feedback Control of Fully Parallel Grid-Connected Inverters,” *IEEE Open Journal of the Industrial Electronics Society*, vol. 6, pp. 618–636, 2025, [4].

Nomenclature

This chapter provides an overview of the mathematical symbols and notations. In addition to the common symbols for physical quantities, the symbol font, superscripts, and subscripts are used to identify specific properties such as the dimension or the reference frame.

General Notation

The following mathematical symbols and functions are used.

$\mathbb{N}, \mathbb{R}, \mathbb{C}$	Sets of natural, real and complex numbers
$x \in \mathbb{R}$	Real scalar variable
$\Re\{z\}, \Im\{z\}$	Real and imaginary part of the complex number $z \in \mathbb{C}$
$x \coloneqq y$	x is defined as y
$x \stackrel{!}{=} y$	x must be equal to y
$\boldsymbol{x} \coloneqq (x_1, \dots, x_n)^\top \in \mathbb{R}^n$	Column vector of dimension n, and $n \in \mathbb{N}$ ($\square^\top$ means transposed)
$\lVert\boldsymbol{x}\rVert \coloneqq \sqrt{\boldsymbol{x}^\top \boldsymbol{x}} = \sqrt{\sum_{i=1}^{n} x_i^2}$	Eucilidean norm of $\boldsymbol{x}$
$\boldsymbol{X} \in \mathbb{R}^{n \times m}$	Real matrix with n rows and m columns, with $n,m \in \mathbb{N}$
$\boldsymbol{O}_{n \times m} \in \mathbb{R}^{n \times m}$	Zero matrix
$\mathrm{diag}(\boldsymbol{x}) \in \mathbb{R}^{n \times n}$	Diagonal matrix of dimension $n \times n$, with vector $\boldsymbol{x} \in \mathbb{R}^n$ on its main diagonal
$\mathbf{1}_n \coloneqq (1, \dots 1)^\top \in \mathbb{R}^n$	Unity (column) vector of dimension n
$\boldsymbol{I}_n \coloneqq \mathrm{diag}(\mathbf{1}_n) \in \mathbb{R}^{n \times n}$	Identity matrix
$x^\star, \boldsymbol{x}^\star$	Operating point
$\hat{x}, \hat{\boldsymbol{x}}$	Estimated value
$\overline{x}$	Average value
$\mathrm{sign}(x) \coloneqq \frac{x}{\lVert x\rVert}$	Sign function
$n = \lfloor x \rfloor$, $n = \lceil x \rceil$	Floor and ceiling functions that round a real number $x \in \mathbb{R}$ to the next lower or greater integer $n \in \mathbb{N}$, respectively
$\left.\frac{\partial f}{\partial x}\right\vert_{x^\star}, \left.\frac{\partial \boldsymbol{f}}{\partial \boldsymbol{x}}\right\vert_{\boldsymbol{x}^\star}$	The partial derivative of the function f with respect to x is evaluated at the operating point $x^\star$

Indices

A quantity that has a certain meaning or is related to a unit or location is indicated by a subscript ($x_\square, \boldsymbol{x}_\square$).

nom	Nominal or rated value
max	Maximum value
min	Minimum value
d	Discrete quantities
ref	Reference (setpoint) value or vector
el	Electrical
m	Mechanical
ac	Alternating current
dc	Direct current
σ, sw	Switching
f	Filter
l	Inductance
c	Capacitance
d	Droop
esr	Equivalent series resistance
w	Ocean wave
b	Bouy or bouyancy
ec	Energy conversion systems
wc	Wave energy converter
wt	Wind turbine
pv	Photovoltaic
ps	Power smoothing
es	Energy storage System
dd	DC/DC converter
g	Grid
pcc	Point of common coupling
l	DC link transmission line

Other indices may occur, which are explained in the text.

Reference frame

A superscript ($x^{\square}, \boldsymbol{x}^{\square}$) is used to indicated the location or the assigned reference frame of a quantity. The superscript is not to be confused with exponentiation.

x^{dc}	One dimensional signal assigned to the DC link or DC grid
$\boldsymbol{x}^{abc} := \left(x^{a}, x^{b}, x^{c}\right)^{\top}$	Three-phase signal assigned to the (a,b,c)-reference frame
$\boldsymbol{x}^{a\text{-}b\text{-}c} := \left(x^{a\text{-}b}, x^{b\text{-}c}, x^{c\text{-}a}\right)^{\top}$	Three-phase line-to-line signal assigned to the (a-b-c)-reference frame
$\boldsymbol{x}^{\alpha\beta} := \left(x^{\alpha}, x^{\beta}\right)^{\top}$	Two-phase signal assigned to the stationary and orthogonal (α,β)-reference frame
$\boldsymbol{x}^{\alpha\beta\gamma} := \left(x^{\alpha}, x^{\beta}, x^{\gamma}\right)^{\top}$	Three-phase signal assigned to the stationary and orthogonal (α,β,γ)-reference frame
$\boldsymbol{x}^{dq} := \left(x^{d}, x^{q}\right)^{\top}$	Two-phase signal assigned to the rotating and orthogonal (d,q)-reference frame
$\boldsymbol{x}^{dq\gamma} := \left(x^{d}, x^{q}, x^{\gamma}\right)^{\top}$	Three-phase signal assigned to the rotating and orthogonal (d,q,γ)-reference frame

Chapter 1

Introduction

On 25 September 2015, the United Nations, with 193 member states, adopted the 2030 Agenda with the title "Transforming our world: the 2030 Agenda for Sustainable Development" [5]. Never before have so many world leaders committed to such a comprehensive and universal policy agenda. They announced 17 goals to tackle the major problems of humanity. It is a plan of action to reduce poverty, improve the lives of people everywhere and preserve the world for future generations. The Global Goals, also called Sustainable Development Goals (SDGs), are shown in Fig. 1.1.

Since 2015, progress has been made, but there is still work to be done. It is obvious that such ambitious goals cannot be fully achieved in the desired time. Still, it is sometimes necessary to strive for the impossible to achieve the possible. These ambitions can only be realised in a global partnership, and the United Nations is the only global intergovernmental organisation available. The 17 goals are intended to inspire and motivate everyone – politicians, companies, and each individual – to fundamentally improve the lives of all and change our world for the better.

Ocean energy, especially wave energy, as the largest unused renewable energy source, can contribute to these goals. With around 40 % of the global population living within 100 kilometres of the coastline [6, 7], wave energy can provide an excellent complement to existing renewable energy sources. Harvesting wave energy contributes directly to achieving SDGs 7 and 13 by providing affordable and clean energy and reducing carbon emissions. Furthermore, it indirectly contributes to other goals. If wave energy can be used in developing countries, thereby creating decent work and economic growth (SDG 8) as well as enabling industry, innovation, and infrastructure (SDG 9), poverty and hunger would decrease in these regions (SDGs 1 and 2).

The power plants that convert the energy stored in ocean waves into electrical energy are called wave energy converters (WECs). Ocean waves naturally fluctuate on a second-by-second basis. There are many different WEC technologies, but all absorb these fluctuating waves and convert them into electrical energy. Like solar or wind energy, wave energy also fluctuates in larger time scales, ranging from hourly to seasonal. However, wave energy has very high continuity compared to solar and wind energy, can be well predicted, and is considered a reliable energy source [7–9]. Due to these remarkable properties and synergies with other renewable energy sources, it has the potential to become an important part of tomorrow's energy generation.

Section 1.1 starts with the origin and potential of ocean waves, followed by an illustration of the different techniques of WECs. The section concludes by discussing why wave energy is not yet used on a large scale. Section 1.2 explains the approach of the novel wave energy converter developed by SINN Power. Section 1.3 highlights the contribution of this work and how it can enhance the development of WECs.

Figure 1.1: The Global Goals or Sustainable Development Goals from the 2030 Agenda adopted by the United Nations in 2015, taken from [10].

1.1 The Contribution of Wave Energy

Wave energy is only one of several renewable energy sources the ocean provides. The different forms of ocean energy are often confused, especially tidal and wave energy, which is why they will be briefly discussed below [11, Sec. 3.7].

Tidal energy has by far the largest share of installed ocean energy. Wave energy is often mixed up or associated with tidal energy, although they are very different phenomena, and the conversion of energy works differently. Tides are caused by the combined gravitational force of the sun and the moon on Earth. The resulting centrifugal and gravitational forces acting on the Earth cause an accumulation of water masses on two opposite sides of the Earth. Due to the Earth's rotation, all points on its surface move through these two tidal peaks, resulting in two ebb and two flood tides per day, at least in theory. Land masses, Coriolis forces and natural oscillations in ocean bays lead to strongly varying local characteristics. However, it is very predictable for every location, which is an advantage compared to other renewable technologies. There are two types of technology for harnessing tidal energy. The most common, with 98 % and approximately 520 MW worldwide installed capacity, is tidal barrage technology [7]. The potential energy between a tidal basin and the open water, separated by a dam, is used to generate electricity as the water flows through turbines. In contrast, tidal stream technology uses the incoming and outgoing flow in open water, like wind turbines underwater. Currently, the tidal barrage is the dominating technology, but it is expected that the installed capacity of the tidal stream will exceed that of the tidal barrage in the future. This is because tidal barrage has limited site availability, high capital investment and environmental impacts.

Salinity gradient energy can be converted to electrical energy utilising the salt concentration difference, resulting in osmotic pressure. They are very efficient if used where fresh and saltwater come together. In theory, they can run continuously, providing a base load. However, the overall potential is relatively small due to geographical limitations.

Ocean thermal energy conversion uses the temperature difference between the warmer surface and the nearly constant 4 °C in deep water.

Ocean current energy works similarly to tidal stream technology, but the movement of the water is caused by other effects like the Gulf Stream.

1.1.1 Wave Energy – Origin and Potential

Ocean waves are produced by wind blowing over large water surfaces, building up wave crests. Continuous wind action on the ocean transfers more and more energy into the waves. Wave energy could, therefore, be described as a concentrated form of wind energy. Since the density of water is about 830 times higher than air, waves can achieve very high energy densities that exceed those of wind and sun by far [12], [13, Sec. 2.2], [14, Sec. 5.1].

In deep water, where waves are not affected by bottom effects like bottom friction and wave breaking, waves can travel over great distances with no significant loss of energy, even if the wind responsible for their generation is no longer present [12]. These waves are called swell waves or gravity waves and have a typical period from about 1 s up to 30 s [13, Sec. 3.1.1].

The wave energy flux Φ_w is the average power per metre along the wave crest for a specific sea state. For irregular waves, as they occur on the ocean, it can be obtained from the wave spectral parameters with

$$\Phi_\mathrm{w} = \frac{\rho_\mathrm{w}\, g^2}{64\,\pi}\, T_\mathrm{e}\, H_\mathrm{s}^2 \quad \left(\text{in } \frac{\mathrm{W}}{\mathrm{m}}\right) , \tag{1.1}$$

where ρ_w is the ocean water density, g is the gravity acceleration, T_e the energy period and H_s the significant wave height [15–17]. A sea state is characterised by the statistical wave parameters T_w and H_s in the frequency domain. The mean wave period T_w is defined as the period where the spectrum has its peak at the significant wave height H_s. The wave spectrum describes the distribution over the frequency. The two most commonly used wave spectra are the Pierson-Moskowitz (PM) spectrum and the JONSWAP (Joint North Sea Wave Project) spectrum.

The energy period T_e in (1.1) can be estimated from the spectral shape by

$$T_\mathrm{e} = \alpha_\mathrm{w}\, T_\mathrm{w} \,. \tag{1.2}$$

The coefficient α_w is not exactly defined and is not always consistent in the literature. It varies from $\alpha_\mathrm{w} = 0.538$ in [15] up to $\alpha_\mathrm{w} = 0.90$ in [16]. This introduces some uncertainty into the wave power estimation. However, this necessary assumption is accepted since the wave energy flux Φ_w is proportional to the square of the significant wave height H_s, meaning errors in the period are less significant than errors in wave height [15].

Many publications address the assessment of global wave energy resources. For this purpose, wave data is used to estimate the available wave energy near coasts. Wave climates were analysed before for navigation purposes and harbour, coastal and offshore engineering. In these scientific fields, however, wave energy is interpreted as a disturbance [12]. Wave data is derived using numerical models of the oceans from wind and ice datasets. The results are iteratively improved by calibration with satellite data and validated with buoy data [15]. Typically, linear wave theory is applied, which is valid if the motion of water particles is not affected by the seabed. This is the case whenever the water depth is greater than half of the wavelength. As waves propagate into the shore, nonlinear wave theory must be applied in coastal areas as well as for storms and breaking waves [13, Sec. 3.2.2]. However, as this is very complex and must be adapted to a specific location, wave energy and its absorption is mainly analysed with linear wave theory [12].

There are debates about the estimated wave energy available worldwide. This is mainly due to the diversity in the data regarding the recording period and sources. Moreover, it depends on how the coastline is segmented and whether the direction of the waves is considered. In [15], the global wave power is estimated to be 32 000 TWh/a. Thereby, a data set with over 60 years is covered, and regions are excluded, which are potentially covered with ice or have an energy flux below 5 kW/m. It is further reduced to 16 000 TWh/a if the direction of wave energy flux is considered. This means that a WEC that works independently of the direction can generate up to twice as much energy as a WEC that has to be aligned with the direction of the waves. Similar results were obtained in [18] and [8]. For comparison, in 2023, global electricity consumption was about 29 500 TWh/a, and primary energy consumption was about 183 200 TWh/a [19]. The potential in Germany for photovoltaic energy integrated into buildings is estimated to be 742 TWh/a, of which around 504 TWh/a is accounted for by roof systems and 238 TWh/a by facade systems [20].

It could be stated that wave energy can satisfy a large part of the electricity demand. However, this is unrealistic because WECs can only be installed in some coastal areas. Nevertheless, wave energy is the largest unused renewable energy source and can become an excellent complement to other renewable energies. Sea states are steadier than wind fields, so integrating WEC farms into offshore wind energy farms offers strong synergies. Combined wave and wind energy farms could reduce downtime and contribute to a more stable grid [21]. Moreover, both technologies can share the grid connection infrastructure as well as operation and maintenance costs [9, 22].

It is essential to state the global wave energy resources to highlight their potential. For a more detailed site analysis, more than the mean sea states are required. Seasonal variations must be included for a financial and technical assessment. In addition, WECs should be optimised for certain sea states, which are typical for the planned location [15].

Fig. 1.2 shows the results from [23], with a map of the globe, where the coastlines are classified into six classes. In this case, they clustered the groups by considering the energy density with the square of significant wave height H_s^2 and the variation of the waves. To quantify the variation of the sea states, a normalised non-dimensional ratio of the standard deviation is typically used [15, 23].

Class 1 represents the lowest and class 6 the highest energy density. On the right side of Fig. 1.2 are the mean H_s-T_w joint occurrence matrices associated with class 3 to class 6. They show the occurrence o_w of sea states, defined by the significant wave height H_s and the wave period T_w. Classes 1 and 2 are found in enclosed areas, resulting in low power. Thus, they are not very relevant for the installation of a WEC. The range of the period T_w in which waves occur that are relevant for energy absorption is between 3 s and 20 s. The peak occurrence for each class is between 5 s and 15 s.

Classes 3 and 4 represent moderate wave energy. Areas with an annual average wave energy flux between 20 and 70 kW/m are considered good sites [12], which are represented by classes 5 and 6. The Northern Hemisphere is dominated by class 5 due to seasonal variations, which are also considered in this classification. Seasonal variations are generally more extensive in the northern than in the Southern Hemisphere. Class 6 marks the most stable resources, which are located near the coasts of South America, Africa, and Australia. Off these coasts are vast ocean areas where waves can accumulate wind energy over long distances, becoming very energy dense and continuous. These locations are desirable for wave energy. However, WECs located at these sites are exposed to stronger storms and, therefore, need to be more robust [12, 15, 23].

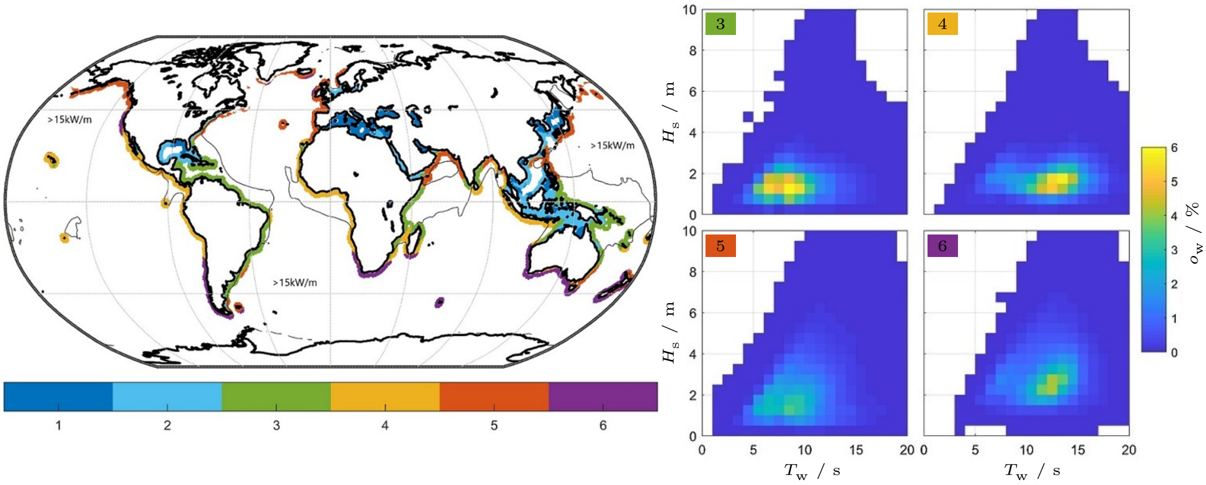

Figure 1.2: Classification of the global coastlines into six groups of wave energy potential, from low (class 1) to high energy (class 6), with corresponding mean H_s-T_w joint occurrence matrices. The figure is taken from [23] and slightly adapted.

1.1.2 Wave Energy Converters

The idea of harvesting wave energy is not new. In 1799, the first patent for a wave energy converter was filed by a father and his son named Girard. Their WEC was designed to drive heavy machinery using direct mechanical action [12]. In 1974, wave energy got much attention due to the oil crisis the year before and the resulting energy shortage. An article in the journal Nature by Prof. Stephen Salter about a new method for using the power of ocean waves drew more attention to wave energy [24]. His WEC became known as Salter's duck. In practical implementation, however, WECs had difficulties with the power take-off (PTO) system and the natural fluctuation of the waves in several time scales. The fluctuation of ocean waves ranges from a second-by-second basis (from wave to wave) to hourly, daily, and seasonal fluctuations [15, 23]. In addition, the new nuclear energy led to a decline in interest in wave energy. Since the start of the new millennium, though, wave energy has experienced a revival. New WECs have been built or are under construction in several countries, led by Scotland and Portugal [13, Sec. 2.3.1].

Unlike other renewable energy sources, wave energy converters are still immature. Since there are many ways to absorb the energy of the waves, there is also a large variety of technologies. These WEC technologies can be classified according to their functional principle. The most common classification was proposed in [12] and suggested three main categories, which are illustrated in Fig. 1.3. For a more detailed consideration, these categories are usually subdivided into floating and fixed structures. The subdivision is omitted here, and only an overview is given.

The **oscillating water column** (OWC) is a semi-submerged chamber with an opening underwater. Above the water is another opening with a turbine connected to a generator. With the fluctuation of the waves, the air pressure in the chamber changes, causing an airflow through the turbine. Since the airflow is bidirectional, a self-rectifying turbine is used, meaning the rotation direction remains unchanged regardless of the direction of the airflow [25].

The functioning of **oscillating bodies** is based on the direct wave motion, i.e., the circular motion of the water particles. A subdivision must be made between the oscillating wave surge converter (OWSC) and heaving devices or point absorbers. The OWSC can be described as a pendulum, which is set into motion by the horizontal movement of the water particles. In the

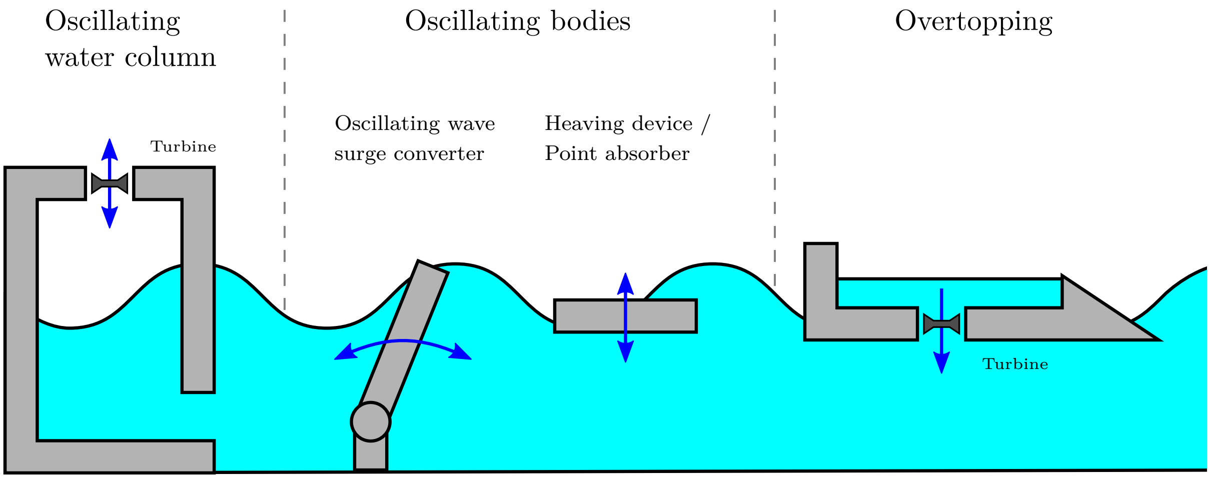

Figure 1.3: Illustrations of the functioning principle of WECs for the three main categories.

joint, the surge or pitch motion of the pendulum is converted into electricity, either directly or via a hydraulic system. Point absorbers use a buoyancy body to absorb the vertical movement of the waves.

Overtopping converters consist of a basin or reservoir which is higher than the nominal water level. When waves wash over the structure, the reservoir fills up. The potential energy of the water is converted into electricity by flowing back into the sea through an opening and driving a turbine.

Here, the focus is on oscillating bodies. Their energy absorption of waves can be compared to a sound wave that is cancelled out by an active noise control system, as those used in earphones. In theoretical analysis, the WEC is considered to produce its own wave, which cancels or reduces the incoming wave. The interference of both waves results in energy absorption by the WEC [12, 26] [13, Sec. 6.1.1].

Like the Betz limit, which states that no more than 59.3 % of the wind power can be extracted and converted to turbine power [27], capture width c_w is introduced for WECs. It is defined as

$$c_\mathrm{w} = \frac{p_\mathrm{w}}{\Phi_\mathrm{w}} \quad \text{(in m)} \ , \tag{1.3}$$

where the average absorbed power p_w from the WEC is divided by the wave energy flux Φ_w, resulting in a number with the unit metre. It can be interpreted as the width of the wave crest that the WEC completely absorbs.

For oscillating bodies, where linear wave theory can be applied, it can be shown that there is a theoretical maximum capture width, assuming an axisymmetrical body and optimal control. The optimal WEC control is discussed in Sec. 1.2.3. For heaving devices like point absorbers, the maximum capture width is

$$c_\mathrm{w,max} = \frac{\lambda_\mathrm{w}}{2\pi} \ , \tag{1.4}$$

which only depends on the wavelength λ_w. The maximum capture width for OWSC with a surge and pitch motion is twice as high ($c_\mathrm{w,max} = \frac{\lambda_\mathrm{w}}{\pi}$) [12, 26, 28, 29]. This illustrates why the subdivision between these two technologies is necessary for oscillating bodies.

The capture width cannot be used to compare different WEC technologies, as their size and, thus, their hydrodynamic efficiency is not included. Therefore, the capture width ratio is introduced

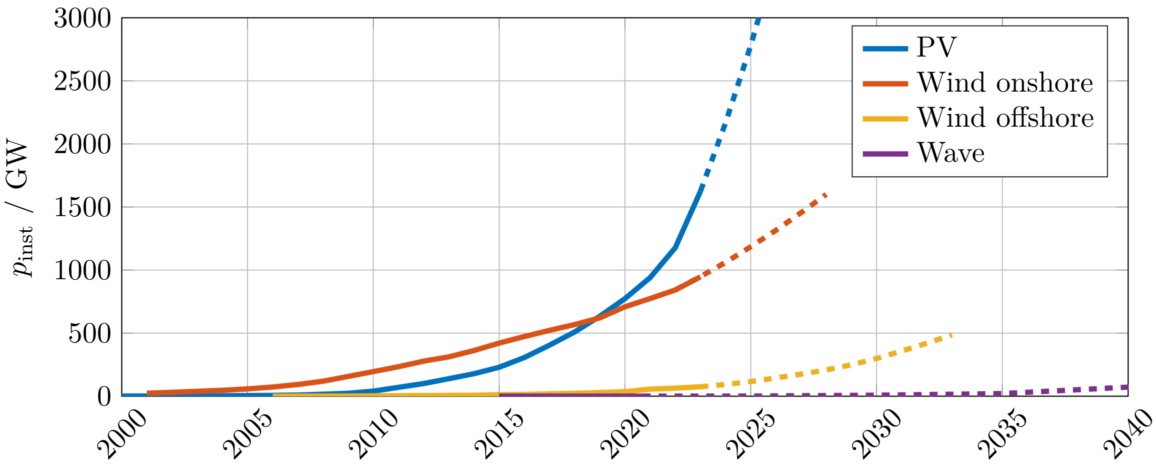

Figure 1.4: Globally installed capacity of PV [—] [31], onshore wind [—] [32], offshore wind [—] [32, 33] and wave [—] [7, 34–36] and the expected outlook in dashed lines.

with

$$\eta_{\mathrm{w}} = \frac{p_{\mathrm{w}}}{\Phi_{\mathrm{w}}\, w_{\mathrm{w}}}\,, \tag{1.5}$$

which is the capture width c_{w} divided by the characteristic dimension w_{w} of the WEC.
The authors in [30] collected about 100 measurements and compared different WEC technologies based on the capture width ratio. The highest mean capture width ratio of 37 % was achieved by surging devices (OWSCs), followed by oscillating water columns with 29 %. Heaving and overtopping WECs have around the same capture width ratio, with 16 % and 17 %, respectively. However, these quantities should be interpreted cautiously, as most analysed WECs are still prototypes that are not yet fully developed, which is also reflected in the standard deviation of the statistical analysis in [30]. Nevertheless, they show a tendency and the potential of the different technologies.

1.1.3 Development Problems

Wave energy converter technology is far from fully developed. There are still major challenges that must be overcome before WECs can be established in the market. The aforementioned second-by-second natural fluctuation in the wave energy flux needs to be smoothed to a continuous power output before it can be fed into the grid. This places high requirements on the power take-off (PTO) system, which needs to deal with this fluctuation. The PTO system is typically a hydraulic system, an air turbine, an electric generator, or a combination of these systems. Furthermore, it must withstand the harsh environment of the sea and, therefore, be designed to be very robust, like all the other components of the WEC. Robust technology usually correlates with high costs. [12]
However, the most frequently cited reason for the lag in the development of WECs is the diversity of technologies. There is no convergence in WEC design like with wind turbines, where a three-blade wind turbine is the current standard. This diversity leads to a spread of investments, which would have to be concentrated on one or a few technologies to drive progress [23].
Fig. 1.4 shows the globally installed capacity p_{inst} of photovoltaic (PV), on- and offshore wind turbines compared to wave energy, as well as the expected outlook in dashed lines, respectively. Although hydropower and biomass currently account for a large share of renewables, they are omitted, as these technologies have been mature for some time and would make the compari-

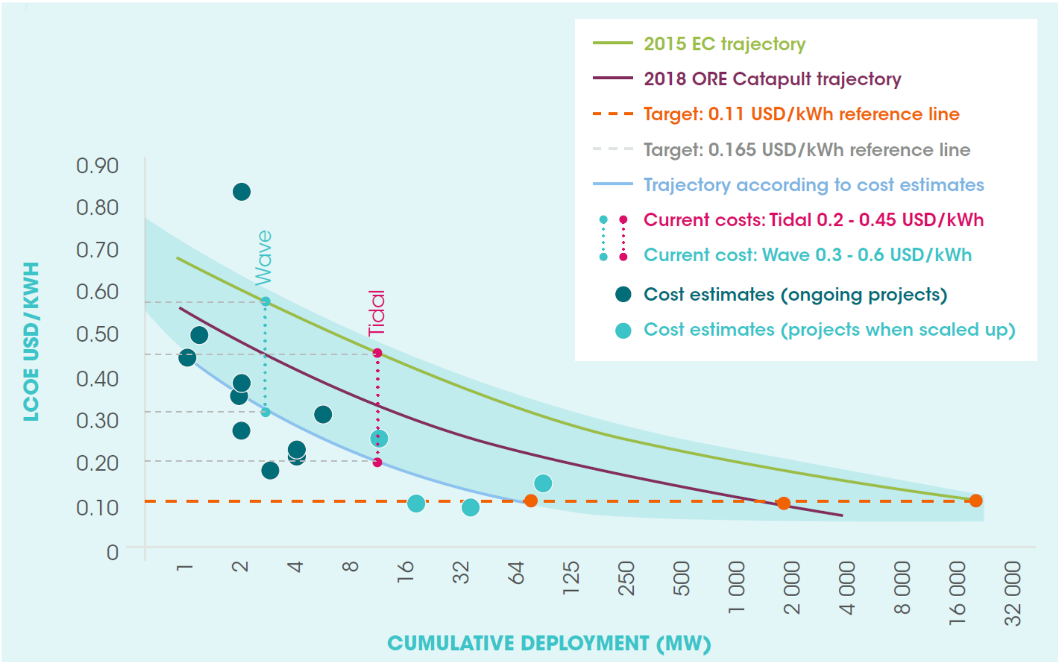

Figure 1.5: Current LCOE and estimated LCOE reduction over the installed capacity (Figure is taken from [7]).

son less clear. The installed capacity of onshore wind turbines has been growing steadily since around 2000. The solid exponential growth in PV systems is remarkable. Around March 2022, the total installed PV capacity reached 1 TW [37], and in 2024, the 2 TW mark will be exceeded [31]. These two technologies show how quickly a new renewable energy technology can develop once the first challenges are overcome. Offshore wind is also on the verge of overcoming those challenges, but not as quickly as PV and onshore wind. The harsh environment inhibits progress due to high investment and maintenance costs. It is noticeable that the installation of wave energy converters is lagging. The forecast is hard to assess, as the numbers are very different from report to report, and the estimates are vague. Still, the figure should give an idea of what to expect if the diffuse investments do not converge.
Fig. 1.5, taken from [7], shows the estimated levellised cost of electricity (LCOE) over the overall installed capacity. The LCOE (in €/kWh or $/kWh) is the sum of all costs of an electricity generating plant, consisting of investment, operation, and maintenance costs, divided by the sum of the electrical energy produced over the entire lifetime. The figure shows that the costs are expected to decrease with the cumulative installed capacity. At the beginning of the development, the costs of prototypes are very high, as many parts have to be custom-made. Once the functionality is given, the performance can be increased, resulting in greater energy output, reducing the LCOE, even at the same cost. After the first projects, cost reductions can be made through a more efficient planning and installation phase. As more projects are implemented, more economies of scale occur, and costs are further reduced due to mass production, standardisation, established supply chains and shared licensing and maintenance facility costs.
This price development can also be observed for PV and wind turbines, as shown in Fig. 1.6. It shows the globally weighted average LCOE over the installed capacity. The price of PV systems is the clearest indicator of this correlation. Although the installed capacity of PV systems has exceeded that of wind turbines, onshore wind turbines still have a lower LCOE on average. A similar, if not steeper, price trend than for PV can be observed for offshore wind turbines. However, this price development is also related to the expansion of onshore wind turbines, as

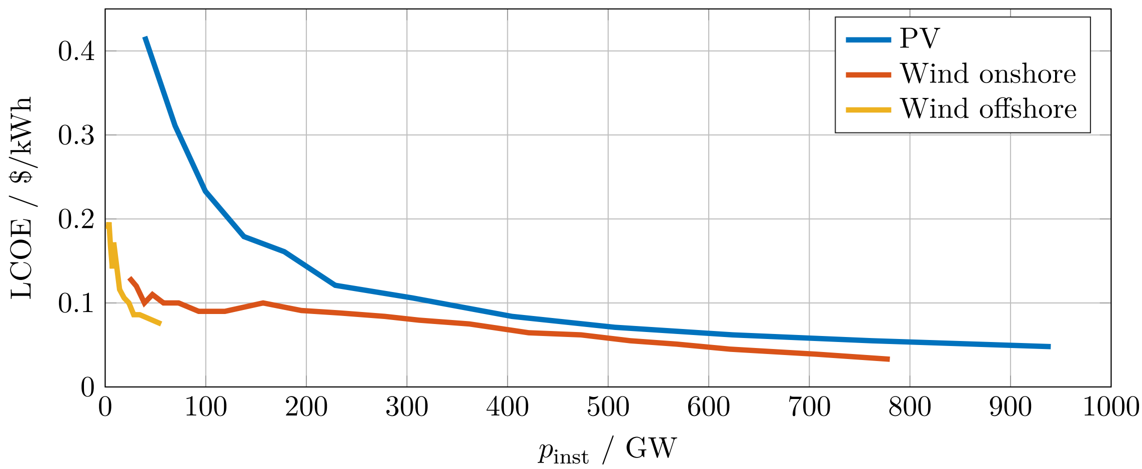

Figure 1.6: Globally weighted average LCOE of PV [—] [38], onshore wind [—] [38, 39] and offshore wind [—] [38].

many parts can be used for both types.
Again, this shows how technologies can complement and support each other, as WEC and offshore wind turbines could do. The power performance and optimisation of the capture width ratio of WECs is not the only important aspect. During development, it is also vital to consider the economic performance, LCOE-wise, including production, installation, and operation sosts. It is important to know which type of WEC technology is more energy efficient regarding the capture width ratio. Still, ultimately, the technology will be measured against its cost and, more importantly, by its return on investment for investors. If an energy-efficient WEC is very cost-intense, it cannot compete with a more LCOE-efficient WEC.
On the other hand, the LCOE is an indicator of the development and progress necessary for the technology to become competitive in the energy market. The lack of design convergence is one of the main drawbacks of wave energy development so far, which needs to be solved to concentrate investments on the most promising technologies. Once investments are made on a larger scale, it is expected to grow like the other renewable technologies. [30, 40]
To attract these investments, wave energy converters must prove that they can reliably generate electricity to gain the confidence of investors and manufacturers and, thus, achieve economies of scale. Wave energy is the largest unused renewable energy source. All available renewable energy source should be used if the aim is to create a carbon-free energy system and ensure access to clean and affordable electricity for future generations. This will allow technologies to benefit from potential synergies and create a more stable electrical grid.

1.2 The Novel Wave Energy Converter

To overcome the challenges that WECs face, SINN Power has developed a new approach. Their novel WEC uses a modular system of interconnected point absorber units to harvest wave energy. A grid-shaped structure interconnects the point absorber units in a rectangular form. Economies of scale should occur more quickly due to repetitive components within one system. In addition, broken parts can be replaced more easily, which reduces maintenance costs, and the structure can be adapted to local conditions and typical sea states. [41]
In addition to the WEC functionality, other, more mature renewable energy technologies can optionally be added to reduce the LCOE. On the top of the structure, the available area can be equipped with PV modules, and wind turbines can be mounted on extended lifting rods. The

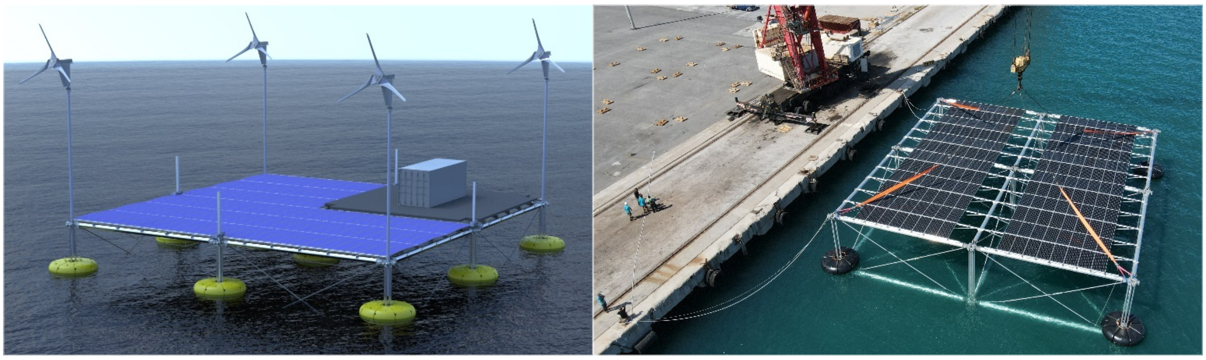

Figure 1.7: Rendering of the hybrid platform, equipped with wave energy converter, wind turbines and PV modules on the left and a picture of the prototype on the right.

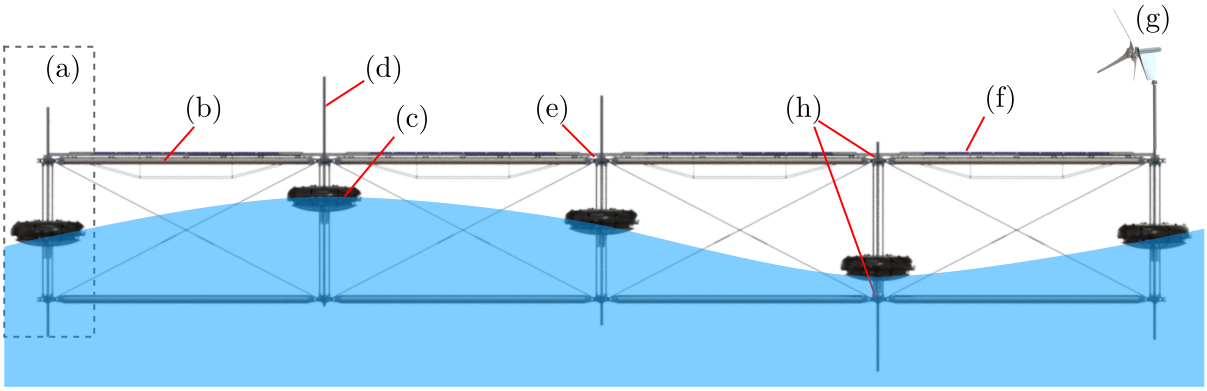

Figure 1.8: Illustration of the functioning principle of the floating WEC.

lifting rods with wind turbines are no longer movable, and the floating buoy is only used for the buoyancy of the platform, which is also helpful for WEC operation. Fig. 1.7 shows a rendering of the smallest configuration of this hybrid platform on the left and a picture of the prototype on the right. The prototype was installed in 2020 and is only equipped with PV modules to test the mechanical structure.

1.2.1 Functional Principle

Fig. 1.8 shows the functional principle of the WEC, as seen from the side. The WEC consists of multiple point absorber units (a), connected to the WEC structure (b) made from aluminium tubes. The lower tubes of the WEC structure are hermetically sealed, which creates additional buoyancy. The number of point absorbers in a row is modularly expandable, and the row itself can be multiplied as often as desired orthogonally in the direction of wave propagation. A point absorber unit, in turn, consists of a floating buoy (c), a square lifting rod (d) and generator units (e). The platform can optionally be equipped with PV modules (f) and wind turbines (g). The distance between the point absorbers is 12 m, and the height from the lower to the upper tube is 6 m. The diameter of the floating buoy is about 3.2 m.
The lifting rod is attached to the buoy and bearing mounted (h) at the top and bottom of the WEC structure. The floating buoy of the WEC floats on the water and moves in a vertical direction with each wave. The generators slow down the upward movement by applying torque, thus generating electricity. This also creates a force that pushes the structure upwards. The

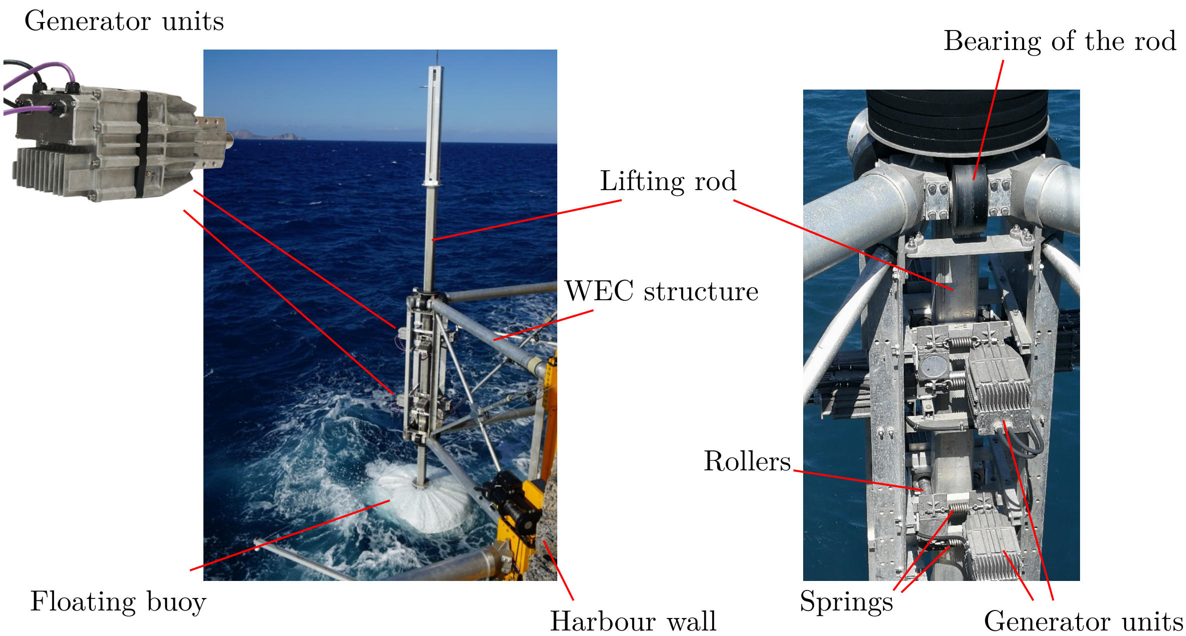

Figure 1.9: Picture of the point absorber prototype in Crete on the left and a detailed picture of the PTO system on the right.

WEC control system provides a reference torque to the generator units. It is responsible for keeping the structure horizontal and stable while optimising the energy output by maximising the lifting movement of the point absorber.

1.2.2 Patented Power Take-Off System

The power take-off (PTO) system comprises the parts required to convert the mechanical power of the WEC into electrical power. Hydraulic PTO systems are often used, where the motion of the waves is first converted into hydraulic pressure via pumps. A generator then produces the electrical power. Hydraulic components are a mature technology, and some power smoothing can already be integrated into the system by varying the hydraulic pressure [9, 25, 42]. Power smoothing is a common challenge for wave energy converters. The electrical power generated fluctuates with the natural movement of the waves with a period of a few seconds. It must be smoothed before the power can be used and fed into the grid. Power smoothing will be further discussed in Section 3.3.

However, implementing a hydraulic system is expensive, complex and requires high maintenance, which is why a mechanical direct drive system is used here. In Fig. 1.9, the full-sized prototype of the point absorber is shown, which is mounted on the harbour wall of Heraklion on the Greek island of Crete. At the time of installation, it was not yet planned to have the lower part of the structure underwater. The generator units constitute the patented PTO system to generate electricity out of the linear movement of the point absorber.

Several generator units are mounted on a point absorber, whereby the rollers of the generators bear on the lifting rod. Two generators are constantly pressed against the lifting rod by springs between the generator pairs. This frictional connection between the rollers and the lifting rod allows for converting the vertical movement of the rod into a rotary motion. The rod's up-and-down movement causes the electrical machines of the generator units to rotate back and forth. Due to the wave movement and the diameter of the rollers, rotational speeds of up to 1000 rpm

can be reached.
Since the mechanical power transmission from the rollers to the lifting rod is limited due to the frictional connection, it is necessary to use several generators to generate the required braking force for the point absorber. Empirical tests on the prototype have shown that a torque of about 60 Nm can be transmitted. If the torque is higher, the static friction changes to sliding friction and the rollers slip. This must be prevented, not only because energy is lost but mainly because mechanical damage to the rollers can occur otherwise. In addition, the point absorber would move almost freely and drive unbraked into the mechanical limit. The energy would have to be absorbed by the WEC structure alone, which cannot withstand it in the long term. For these reasons, the torque of the generator units is limited to 50 Nm by the power electronics.
The main components of the generator unit are the rollers connected to a permanent-magnet synchronous machine (PMSM) and a voltage source inverter (VSI). The VSI controls the current through the PMSM and, thus, the torque of the generator rollers. The control system of the generator unit will be discussed in Sec. 2.4.

1.2.3 Control of a Point Absorber Wave Energy Converter

The interaction of bodies with ocean waves is already known from ship hydrodynamics and offshore engineering. This theory can be applied in the same way to WECs. The motion of a point absorber is typically considered with a single degree of freedom, where the body is only oscillating in heave. By assuming a small excursion z_b of the body from its equilibrium position and linear wave theory, the dynamics can be governed by the superposition of all hydrodynamic forces, which yields [43, Sec. 5.9], [12, 44]

$$m_\mathrm{b}\,\ddot{z}_\mathrm{b} = F_\mathrm{e} + F_\mathrm{b} + F_\mathrm{r} + F_\mathrm{v} + F_\mathrm{f} + F_\mathrm{c}\,. \tag{1.6}$$

The excitation force F_e and the buoyancy force F_b represent the total wave force. The forces F_v and F_f represent viscous and friction effects, respectively. The PTO system applies the force F_c and can be controlled to influence the point absorber's movement and convert wave energy into electrical energy. In this case, the torque of the generator units is transmitted to the lifting rod via the generator rollers. With negligible rolling friction, the force results in

$$F_\mathrm{c} = \frac{1}{r_\mathrm{r}} \sum_{i=1}^{N_\mathrm{m}} m_{\mathrm{s},i}\,, \tag{1.7}$$

where r_r is the radius of the generator rollers, N_m is the number of generator units per point absorber and $m_{\mathrm{s},i}$ the torque of the generator unit i at its shaft.
The buoyancy force F_b can be assumed to be proportional to the excursion z_b with

$$F_\mathrm{b} = -k_\mathrm{b}\,z_\mathrm{b}\,, \tag{1.8}$$

where k_b is the buoyancy stiffness. The radiation force F_r occurs if the floating buoy oscillates. It describes the hydrodynamic damping that results from the fact that the floating buoy also generates waves during its movement. The radiation force can be modelled based on Cummins equation, introduced in [45], which leads to

$$(m_\mathrm{b} + m_\mathrm{a})\,\ddot{z}_\mathrm{b} + \int_0^t D_\mathrm{b}(t-\tau)\dot{z}_\mathrm{b}\,\mathrm{d}\tau + k_\mathrm{b} z_\mathrm{b} = F_\mathrm{e} + F_\mathrm{c}\,. \tag{1.9}$$

The mass m_a accounts for the additional mass resulting from the inertia of the water surrounding the floating buoy, which must be moved along. The convolution term introduces a dependency on the past motion of the body, where D_b is the impulse response function that describes the dynamic behaviour of the damping. It is strongly dependent on the shape of the floating buoy. This function and the hydrodynamic parameters m_a and k_b can be computed numerically by solvers like Orcaflex, WAMIT [46] or NEMOH [47]. Furthermore, a relation between the excitation force F_e and the wave elevation can be provided, which results from the pressure distribution on the surface of the floating buoy caused by the incoming wave. The implementation is usually done in the time domain to account for nonlinearities in the hydrodynamic parameters. Therefore, the convolution can be approximated by a state-space system [48–50].

The optimal control of WECs is a popular topic of research work. A review of different control strategies can be found in [51–54]. Due to the analogy, WECs are considered damped harmonic oscillators in the literature. By setting the control force to

$$F_\mathrm{c} = d_\mathrm{c}\dot{z}_\mathrm{b} + k_\mathrm{c}z_\mathrm{b}\,, \tag{1.10}$$

the overall damping and stiffness can be affected, and the point absorber can be put in resonance with the incoming wave, which results in maximum energy absorption [48, 55].

If the body is in resonance, its velocity $\dot{z}_\mathrm{b}$ is in phase with the excitation force F_e. When this condition is achieved by acting on the PTO force F_c appropriately, the control strategy is called phase control [12, 55]. This control strategy is sometimes called reactive control because the energy flow is reversed during a part of the wave cycle [12]. This means that the WEC temporarily absorbs power within a wave cycle. On average, however, the power output is significantly higher. With direct drive PTO systems, like the one presented here, the coefficients in (1.10) can be chosen arbitrarily. Therefore, the control stiffness k_c can be set to negative values to change the resonance frequency of the point absorber. With hydraulic PTO systems, this might be more restricted.

The optimal parameters to set the point absorber into resonance can only be concretely determined for regular waves, where the wave is considered sinusoidal. Natural irregular waves are described by a frequency spectrum and are, therefore, a superposition of many different regular waves with different frequencies, amplitudes, and phases. Thus, the control parameters can only be determined stochastically for varying sea states. In [44], an artificial neural network is used to adapt the coefficients according to the actual sea state, and in [56, 57] model predictive control is applied.

An alternative and practical approach is latching control. With this method, the floating buoy is fixed at the lower position when its velocity becomes zero. It is released after a certain period within the wave cycle. The challenge here is to determine the appropriate duration for which the movement of the point absorber must be locked, especially for natural irregular waves, where each wave differs from the other. Although it does not correspond to theoretically optimal phase control, it has been shown that approximately the same energy extraction can be achieved. A frequently stated advantage over phase control is that the power flow does not reverse. This is particularly significant for hydraulic PTO systems. For the direct drive PTO system described here, it is irrelevant since the generator unit work bi-directionally. More detailed theory about latching control can be found in [49, 55, 58].

Besides the control strategy, the efficiency and performance of the PTO system are also very crucial. In [59], it is shown that slow PTO response leads to a severe reduction in efficiency and can even cancel out the benefits of optimal control. A response time of less than 50 ms should be aimed for. This is no issue for modern drive systems with electrical machines controlled by power electronics. The implementation of the current controller is presented in Sec. 2.4.2. It is shown that the reference torque is reached within a few milliseconds if implemented correctly.

Not only is the response time critical, but the efficiency of the PTO also has a significant impact on the overall efficiency of the point absorber. In [60], the effect of non-ideal PTO systems on the performance of reactive control for point absorbers is investigated. With low-efficiency PTO systems of less than 80 %, the absorbed energy is only one-tenth of the energy of the ideal case. Even with an efficiency of 90 %, only 70 % can be achieved compared to ideal PTO systems. This shows that a significant improvement can be achieved with every increase in drive efficiency, even in the upper-efficiency range. Therefore, in Sec. 2.4.3, optimal feedforward torque control is presented, which leads to the maximal efficiency of the generator unit.
The PTO system with the modular generator unit presented here offers a very flexible and bidirectional direct drive PTO system for point absorbers. This makes it possible to implement all known control strategies for WECs. An optimal control strategy is essential for the success of WECs. The increase in efficiency of such control strategies improves the overall efficiency by a multiple compared to a passive control system [49, 60, 61]. The optimal control for the full-size WEC prototype mounted on a fixed wall can be applied directly. For the floating WEC with an array of many point absorbers, the additional control objective of keeping the structure floating must also be satisfied, which has a higher priority than optimal control. In the following, the control of the WEC is no longer considered. It is assumed that an overall control unit gives the optimal reference torque for the generator units.

1.3 Specification and Contribution

This work focuses on the realisation of the electrical system for the modular wave energy converter, including the optional renewable energy sources. The mechanical system and the hydrodynamic description of the WEC will not be discussed further. Especially the hydrodynamic modelling of WECs is already extensively addressed in the literature. Likewise, the control of WECs is a very popular topic in research. The brief discussion on the control of a point absorber is intended to provide an understanding of the intersection between the WEC and the electrical system and to clarify the requirements of the electrical system.
The control of wind turbines is also not considered here. Generally, the torque of the electrical machine must be set proportional to the square of the rotational speed of the wind turbine. A detailed theory can be found in [27].
The connection of a wave energy converter to the electrical grid has not yet been fully explained in detail in the literature. This thesis attempts to fill this gap and introduces a modular power electronics system suitable for the scalable approach of the novel WEC. Fig. 1.10 provides an overview of the complete electrical system with references to the corresponding sections in this thesis.
Since the idea of the WEC came first, the electrical system was designed starting with the generator units. It is desirable to connect all generator units of a point absorber in parallel to save cables and assembly time. This is possible due to the voltage source inverter (VSI), which is integrated into the generator unit and controls the electrical machine. The output of the VSI can be considered as a direct current (DC) source, which allows for connecting them in parallel. Therefore, the proposed electrical system is based on a low voltage direct current (LVDC) grid. Besides the VSI for the generator units, two more power electronic devices are necessary, namely a grid inverter and a DC/DC converter. The grid inverter connects the DC grid to the grid with alternating current (AC). The DC/DC converter is used to integrate PV systems and storage solutions. The focus regarding storage solutions is on short-time storage with supercapacitors, as these are mandatory for power smoothing. Long-time energy storage units with lithium iron phosphate (LiFePO4) batteries have also been developed. However, since its integration is not very relevant to the operation of the WEC, it is omitted.

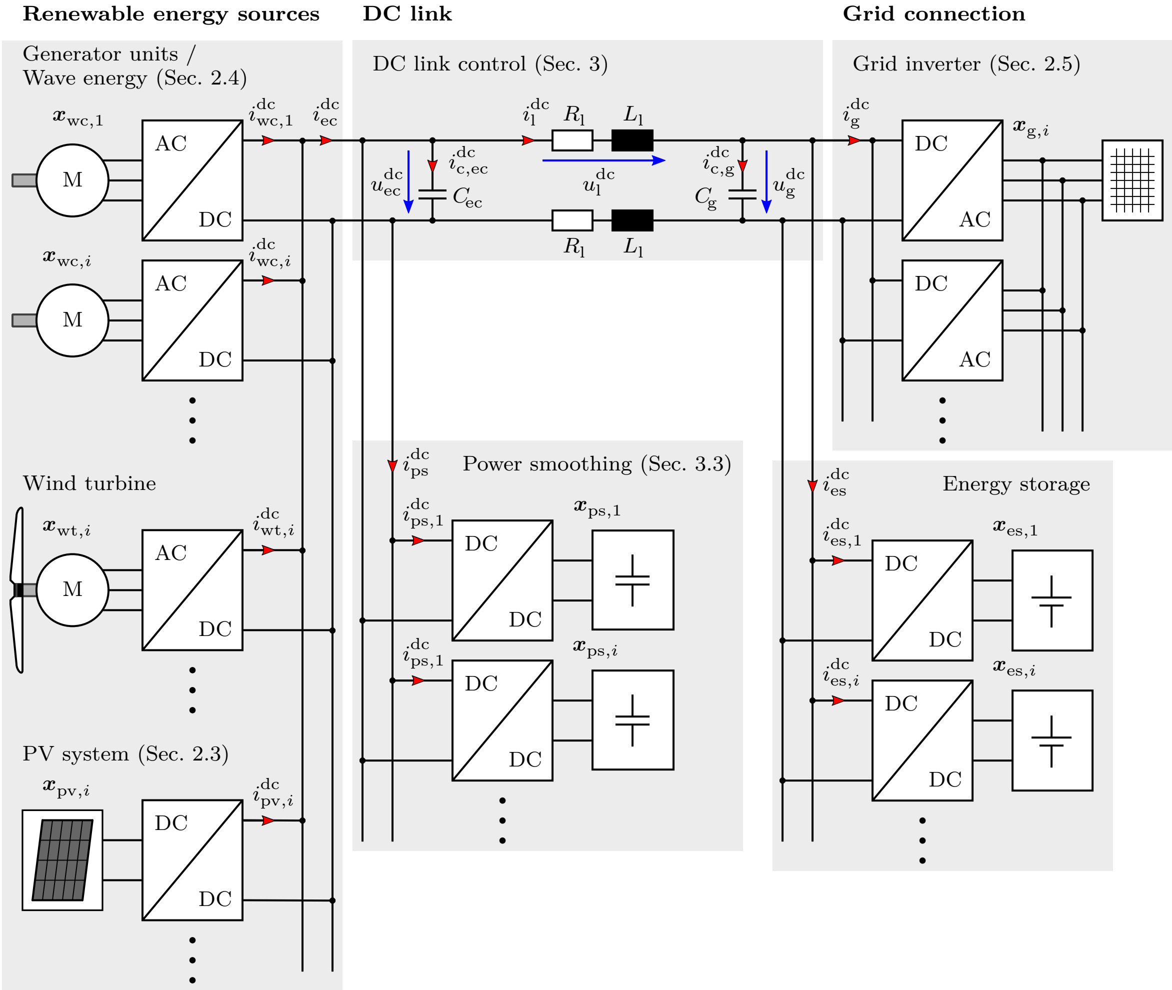

Figure 1.10: Overview of the modular power electronics system with all possible components and references to the corresponding section in this thesis.

Like with the mechanical design of the WEC, great emphasis was placed on modularity and the use of repetitive components to promote economies of scale. The topology of the basic power electronics of the VSI can be used for both other devices as well, which reduces the number of components in the system dramatically. Chapter 2 starts with introducing the basic power electronics components and continues with a discussion of each of the three power electronic devices by introducing a model of the dynamics and the design of a suitable controller.

In Chapter 3, the connection of all devices to a DC grid is considered. In the beginning, the control strategy of the system is explained. The objective of the control is a safe and stable operation whereby the current is to be shared between the devices. The challenge is to prevent a circulating or oscillating currents that could result from the parallel connection of the many devices and storage units. After the general functioning of the system is explained, a stability analysis is carried out to prove stable operation. Furthermore, a parameter analysis is performed with regard to DC link stability in order to determine optimisation potential.

The power smoothing will be discussed in Section 3.3. The proposed control system was tested on the prototype in Crete under harsh sea conditions. However, when the prototype had to be installed, the DC/DC converter was not yet fully developed and was not ready to be installed.

Therefore, the supercapacitors were integrated directly into the DC link. The experiment could not be repeated later with the DC/DC converter, as there were problems with the supply of semiconductors due to the pandemic. Unfortunately, the project was cancelled afterwards. Hence, power smoothing with the integration of supercapacitors via the DC/DC converter is only presented based on simulations. Nevertheless, the previously implemented control system and the corresponding simulation were validated with real measurement results. Furthermore, the simulation of each power electronic device is also compared with real measurement results and thus validated. This confirms the accuracy of the simulation, and it can be assumed that the results of the simulation are very close to those of the real implementation.
The following specifications were defined during the development of the electrical system. These specifications serve as essential design criteria for the development and the methodical approach throughout this thesis. In the following sections, references are made to the corresponding specifications to clarify the decisions made.

(S1) The components must be waterproof and robust for the harsh marine environment.

(S2) Use of repetitive components to promote economies of scale.

(S3) The implementation must be based on industrial components using low-cost but also robust and high-quality parts to enable scaling effects.

(S4) It must be possible to integrate any energy storage system with full controllability.

(S5) Integrating other renewable energy sources, particularly PV and wind, must be possible.

(S6) Enabling full controllability of the WEC with a bidirectional direct drive PTO system.

(S7) The system should be designed to ensure maximum modularity so that it can be expanded as required.

(S8) The PTO system must ensure a high-performance and optimised conversion of mechanical energy into electrical energy.

(S9) Direct grid integration while maintaining modularity must be guaranteed.

(S10) The system will be designed to be ready for off-grid applications and future grid support needs.

(S11) The overall system must be capable of power smoothing to smooth the fluctuating power of a WEC.

The key contributions of this work can be summarised as follows.

(i) Proposal of a highly modular power electronics system for the grid integration of a novel wave energy converter.

(ii) Presentation of a very flexible PTO system for point absorbers, which allows for the implementation of all known control strategies for WECs.

(iii) Proposal of a generic experimental identification method to obtain the optimal current vectors for any electrical machine leading to minimal losses and maximum efficiency, including iron and inverter losses.

(iv) Proposal of a novel grid inverter topology for a full parallel connection, simultaneously on the DC and AC sides.

(v) Detailed modelling of a complete modular power electronics system, forming a DC grid, for the grid connection of a novel wave energy converter.

(vi) Detailed modelling and controller design for all power electronic devices required for the integration of all types of renewable energy sources.

(vii) Hardware-based implementation and realisation of the developed theories on an industrial microcontroller with an implementation-oriented explanation.

(viii) Proposal for a new droop control strategy that combines two methods, which ensures ideal energy balancing among distributed energy storage systems.

(ix) Presentation of a power smoothing control system for the developed electrical system to optimally smooth the fluctuating power of the WEC and, thus, enable the grid connection.

Chapter 2

Highly Modular Power Electronics System

The proposed highly modular power electronics system consists of three devices. They can be combined into a smart DC grid to integrate many types of renewable energy sources, particularly wave energy converters (WECs). The three power electronic devices are a motor drive for the generator unit, a DC/DC converter, and a grid inverter. Each device is housed in a patented aluminium extruded profile and sealed to make it waterproof and robust for the harsh marine environment, as required by Specification (S1) for the installation on a WEC. An electrical machine was also developed for the generator unit, which is integrated into the same aluminium extruded profile to connect it directly to the motor drive.
The individual modules can be connected to form a string of several modules by simply plugging them together. For example, one of the most straightforward possible implementations would be to connect a motor drive to an inverter to create a frequency converter, also called a back-to-back converter, for drive applications. Several devices of one type can also be connected to a string to expand the power. The DC/DC converter allows to integrate storage units easily. Two storage units, one with supercapacitors and one with battery modules, are designed to be mounted in the same housing so that they can be connected directly to the DC/DC converter. The individual strings can then be connected via DC cables to form the whole DC grid. This flexibility makes it very easy to meet the requirements of different projects, especially when installing WECs.
In Sec. 2.1, the general topology of the power electronics will be explained. The following section discusses the modulation, which is the interface between the implemented control algorithm in software and the switching elements on the hardware. It is required for each of the three devices. However, they all have slightly different requirements, which are discussed in more detail in the respective sections. After considering these generally applicable elements, a mathematical model of the dynamics is derived, and an appropriate controller is proposed for each of the three devices. It starts with the DC/DC converter in Sec. 2.3, followed by the motor drive in Sec. 2.4, and finally, the grid inverter in Sec. 2.5. This order is chosen due to increasing complexity from device to device.

2.1 Topology of the Power Electronics

The system was developed, starting with the generator unit. A three-phase voltage source inverter (VSI) is necessary for the motor drive to control the electrical machine in the generator unit. This VSI is the basic electronic component, which is also used for both other devices, the

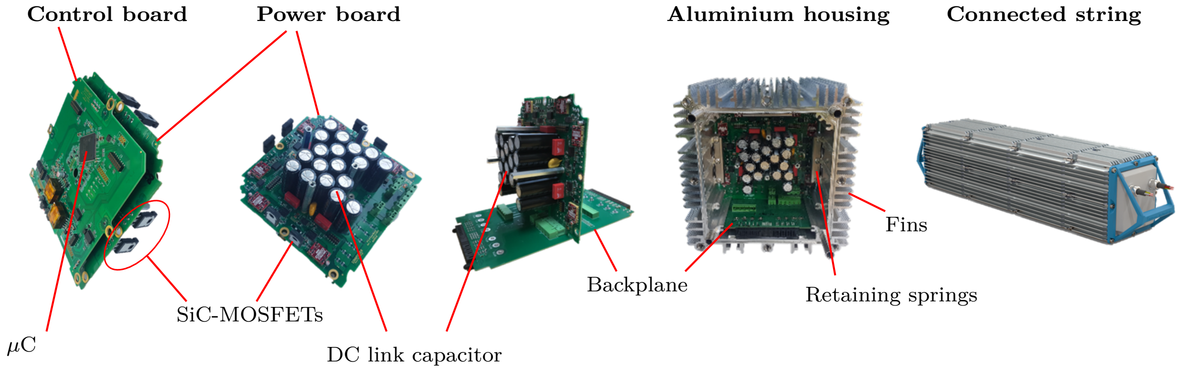

Figure 2.1: Photo of the basic power electronics components and the modular housing.

grid inverter and the DC/DC converter. This is an excellent benefit as repetitive components can be used throughout the system, contributing significantly to Specification (S2). A photo of the basic power electronics components is shown in Fig. 2.1. On the left is a photo of the two printed circuit boards (PCBs) for the control and power circuits, which are called control and power board. On the control board are the microcontroller (μC), analogue circuits for the signal processing of the measured quantities, and auxiliary supplies for the different voltage levels required. With the use of surface-mount devices (SMD), low-cost and industrial components can be used, which is especially crucial for the microcontroller. To fulfil Specification (S3), all control algorithms presented here must be implemented in the C programming language on this microcontroller. The power board contains the six silicon carbide metal–oxide–semiconductor field-effect transistors (SiC-MOSFETs), including the gate drivers, the DC link capacitor bank, and the measuring circuits for voltages and currents. Both boards are stacked on top of each other and connected to transmit the measurement and control signals.

The two boards are mounted on the backplane, which is used for the signal and power connection to the other devices. For example, the DC link is passed through all backplanes so that any device can connect to it. Each unit has its backplane on which the device-specific internal connections are made. The whole assembly is built into the system's housing, an aluminium extruded profile with fins on the outside. The MOSFETs are pressed on the inside of the housing by patented retaining springs for transistors. This is very important because the dissipated power of the MOSFETs must be transmitted to the outside of the sealed housing to avoid overheating.

An additional filter board is required for the DC/DC converter and the grid inverter. On the filter board is an LC filter with the inductance L_f and the capacitance C_f, one filter for each of the three phases. The three capacitors are connected in star. To keep the similarity between the devices and reduce component diversity (Specification (S2)), the DC/DC converter and the grid inverter use the same inductor. Since the requirements for the grid inverter are stricter, the inductor is designed for this device. The dimensioning of the filter will be described in Sec. 2.5.1. In the case of the DC/DC converter, the star-point is connected to the lower DC link potential DC−. The star-point is connected to the midpoint M of the split DC link capacitors for the grid inverter. The reason for this is explained in Sec. 2.5.2. These individual connections are made on the respective backplane. Fig. 2.2 shows a block diagram of the three devices with the different variations of the star-point connection.

The power rating of the generator units are given by the WEC design. With a maximum torque of 50 Nm and a rotational speed of up to 1000 rpm, the resulting power is about 5.2 kW. Since the same power electronics are used, the nominal power of the grid inverter is also in this range.

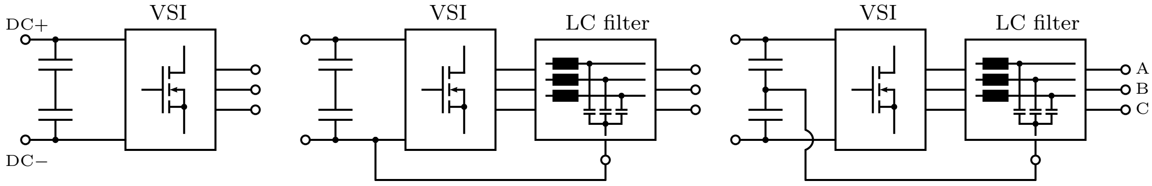

(a) Motor drive. (b) DC/DC converter. (c) Grid inverter.

Figure 2.2: Block diagram of the three devices with the different variations of the star-point connection.

With the DC/DC converter, significantly higher power can be achieved because a DC voltage and no sinusoidal AC voltage are connected at its phases. For the functionality of the inverter, the DC link voltage must be higher than twice the peak value of the grid voltage. The grid voltage's root mean square (RMS) value is 230 V in Europe. Hence, the chosen DC link voltage range is between 750 V and 875 V.

The chosen topology that can be used equally for all three devices is a three-phase two-level VSI. The circuit of the basic power electronics is shown in Fig. 2.3. The connections and signals on the backplane are illustrated at the bottom. All communication signals and power connections that must be passed to the neighbouring devices are connected to the backplane. RS-485 and the controller area network (CAN) are used for communication between the devices. Various logical signals on the backplane are controlled via the serial peripheral interface (SPI). Not all connections are always required. For instance, the quadrature encoder pulse (QEP) signals are used only in the case of the motor drive for the position encoder of the electrical machine.

In the centre is the microcontroller that measures the various signals and controls the MOSFETs. The current sensors for the three phases are mandatory for the current control. They are located on the converter side, mainly because they must be placed on the power board to keep it common for all units. A helpful feature is that they can also be used at this position to protect the power electronics and prevent overcurrents.

The LC filter for the DC/DC converter and the grid inverter has two connections for the star-point. Depending on the device, the necessary connection is made on the backplane. For those two devices, a voltage measurement on the filter output is required. Since the filter is placed on a different board and the transmission path is longer, the transmission must be more robust, which is guaranteed by the $\Delta\Sigma$-modulated measurement.

2.1.1 Switching Elements and Half-Bridges

The six SiC-MOSFETs are forming three half-bridges, one for each phase. With a half-bridge, the desired voltage can be applied to one phase. SiC-MOSFETs were chosen because they exhibit lower losses than conventional silicon (Si) MOSFETs at this voltage rating. Specifically, their drain-source on resistance $R_{\mathrm{ds,on}}$ is lower than for Si-MOSFETs. Moreover, they have an internal body diode with a much lower reverse recovery current, which further reduces losses [62]. An alternative would be an insulated-gate bipolar transistor (IGBT). Still, they cannot achieve such high switching frequencies as desired here. With IGBTs, switching frequencies up to about 30 kHz can be achieved. SiC-MOSFETs have a lower gate charge, which enables higher switching frequencies and, thus, smaller filter components [63, Sec. 4.4.2]. It is shown that an efficiency increase of about 1 % can be achieved by simply replacing the IGBT with SiC-MOSFETs in an existing device [64, Sec. 2.7]. In general, it is to be expected that SiC-MOSFETs will increasingly

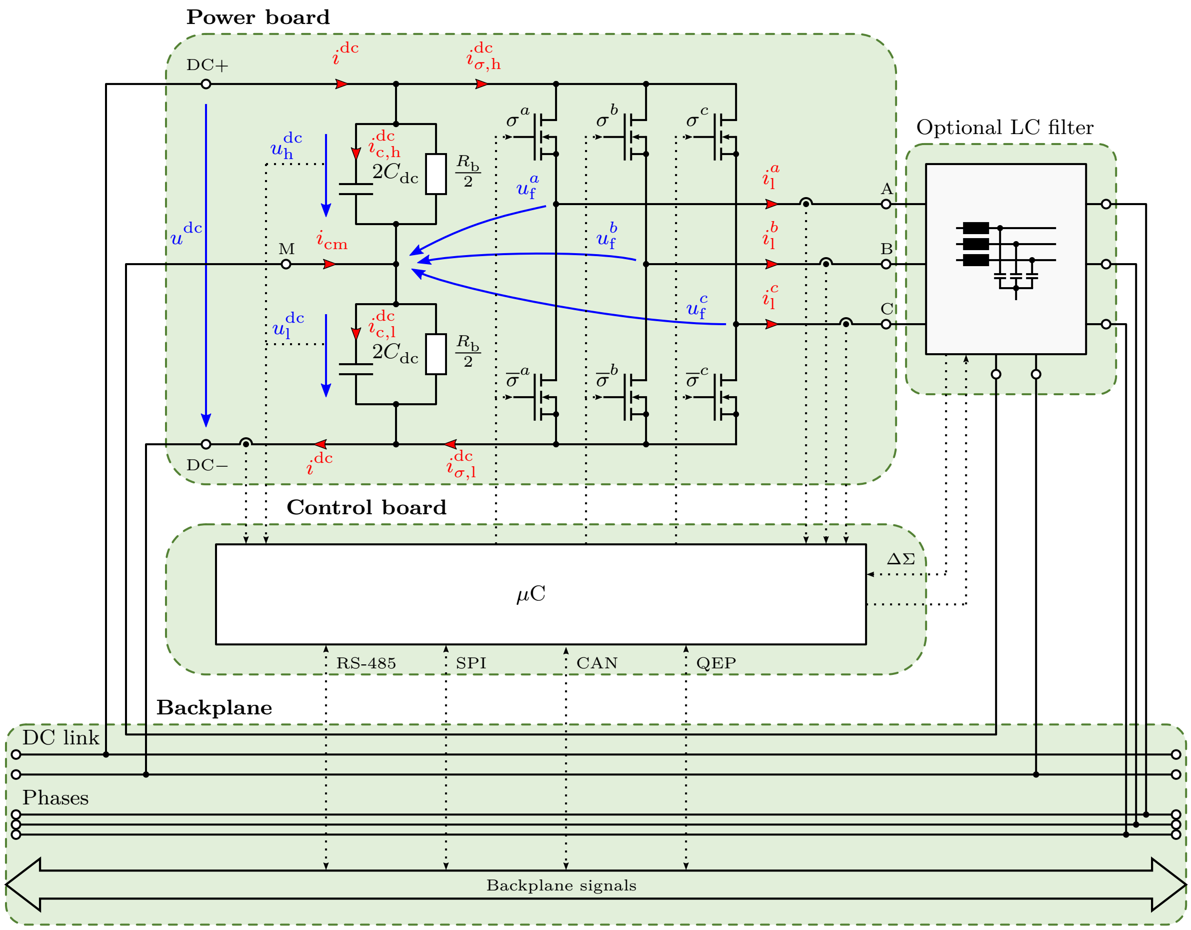

Figure 2.3: Electrical circuit of the basic power electronics with the split DC link capacitors and the six SiC-MOSFETs.

replace IGBTs. It was already demonstrated that SiC-MOSFETs with a rated voltage over 10 kV are possible, which can enable high-power devices [65, 66].

The switching frequency is chosen as high as possible to keep the inductance small and, at the same time, not to let the switching losses become too large. For the DC/DC converter and the grid inverter, the switching frequency is 70 kHz. For the motor drive, the switching frequency does not have to be as large as for the other two devices, as the inductance of the electrical machine is significantly greater than the filter inductance L_f. Therefore, it is set at 20 kHz. The advantage of selecting a frequency above approximately 16 kHz is that the human ear can no longer perceive that noise caused by the switching processes.

Fig. 2.4 shows the derivation of the model for the half-bridge. Fig. 2.4(a) shows a half-bridge with two MOSFETs and the filter inductor with its inductance L_f and its equivalent series resistance R_fl. The bridge works in complementary mode, meaning that if the upper MOSFET is on ($\sigma = 1$), the lower one has to be off ($\overline{\sigma} = 0$) and vice versa. A so-called dead time must be added to avoid a short circuit that can occur if both MOSFETs are turned on simultaneously. The dead time is a short period during which both switches are off. It is inserted after one switch is turned off and before the other is turned on. During this time, the current is flowing through a body diode. In Fig. 2.4(b), the MOSFETs are replaced by their equivalent circuit, which consists of ideal switches, the drain-source on resistance $R_\mathrm{ds,on}$ and the body diodes.

Since SiC-MOSFETs switch very fast, the dead time can be very short. Compared to the

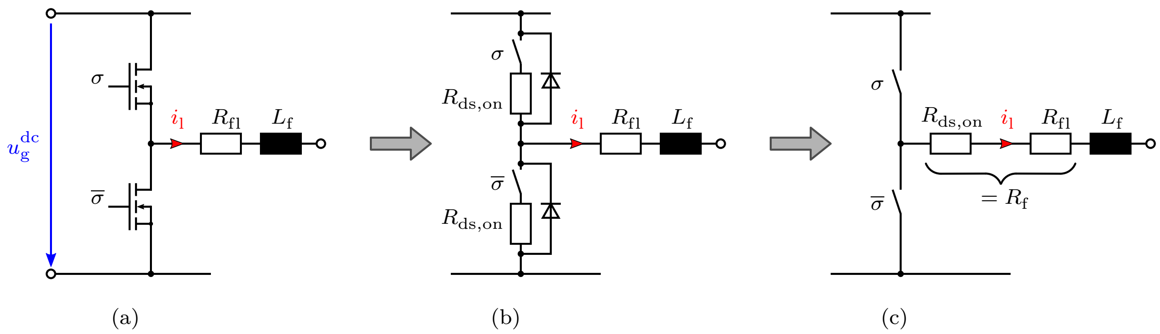

Figure 2.4: One half-bridge of the VSI with (a) the two MOSFETs, (b) the equivalent circuit of the MOSFETs and (c) the simplification of the half-bridge.

switching period, the dead time and the associated influence of the body diodes and the switching behavior can be neglected. Neglecting this may only sometimes be possible and should be evaluated for each case [67, 68]. Fig. 2.4(c) represents the simplification of the half-bridge. Because the current i_l flows either through the upper or the lower switch, the resistance $R_{ds,on}$ can also be considered to be in series with the inductor [1]. In the following, both resistances will be combined to the resistance R_f with

$$R_f = R_{ds,on} + R_{fl}\,. \tag{2.1}$$

With the electrical machine, where no additional filter inductance is required, the drain-source on resistance $R_{ds,on}$ can be combined similarly with the copper resistance R_s of the electrical machine. Thus, the conduction losses of the MOSFETs are modelled and included, which allows for a better controller design and loss calculation.

2.1.2 Dimensioning of the DC link Capacitor and Voltage Balancing

Multiple aspects must be considered when dimensioning the DC link capacitor. One of the first considerations is sufficient voltage strength. The rated voltage of the DC link capacitor must be higher than the maximum expected DC link voltage, which is 875 V in this case. Single capacitors with such a high-rated voltage are film capacitors. Typical electrolytic capacitors for this application have a voltage strength of around 450 V. Therefore, two capacitors must be connected in series to achieve the required voltage strength. However, the capacitance of electrolytic capacitors compared to film capacitors is higher for a given space, which contributes to the stability of the overall system (see Sec. 3.2.5). On the other hand, the parasitic equivalent series resistance (ESR) of film capacitors is much lower, which makes them more efficient. A compromise must therefore be found between installation space, stability, efficiency, and costs. This compromise determines the lifetime of the capacitors. According to [69], capacitors usually have the most significant impact on the lifetime of power electronic devices. A capacitor can break when a notable external anomaly occurs, such as an overvoltage. During regular operation, this can be avoided with safety measures in the software. However, capacitors also age over time. The ESR also plays an essential role in lifetime calculation. The life of a capacitor ends when its parameters exceed the specified values, which are affected by operating conditions. For example, the typical end of life is reached when the capacitance has dropped by 20 %. If the typical tolerance of 20 % of the capacitance is also considered, the capacitance at the end of life is only 64 % of the stated nominal value [70–72]. It is essential to take this into account when considering the stability of the system.

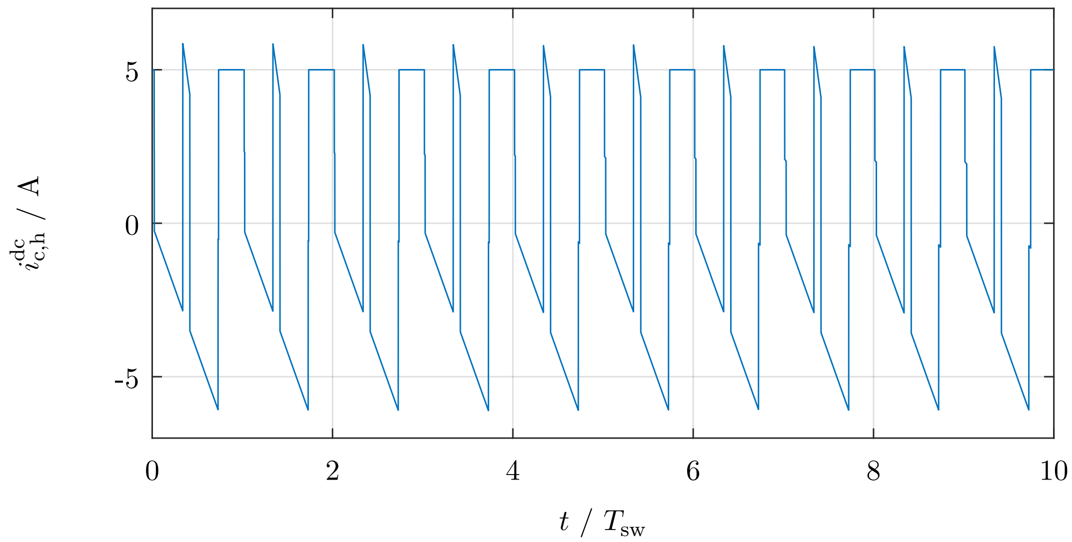

Figure 2.5: Exemplary current $i_{\mathrm{c,h}}^{\mathrm{dc}}$ through the capacitor of the grid inverter with a constant input DC current $i^{\mathrm{dc}} = 5$ A during ten switching periods T_{sw}.

The factor that has the most effect on the lifetime is temperature [72]. The law of Arrhenius can be applied to all kinds of electrochemical storages to estimate the influence of temperature on lifetime. From this, it can be deduced that an increase in temperature of 10 K halves the lifetime of the storage [73, 74]. The highly pulsating current flowing through the capacitor causes power loss on the ESR and induces self-heating of the capacitor. Therefore, the maximum root-mean-square (RMS) value of the alternating current is typically limited in the datasheets of the manufacturers.

Fig. 2.5 shows a simulation of the current through the capacitor of the grid inverter with a constant input DC current i^{dc}, which is reasonable for a short period. The DC link capacitor must provide the switched current, resulting in a rapidly changing current that causes high thermal stress. The current $i_{\mathrm{c,h}}^{\mathrm{dc}}$ through the high-side capacitor (indicated by the subscript h) is defined by

$$i_{\mathrm{c,h}}^{\mathrm{dc}} = i^{\mathrm{dc}} - \frac{u_{\mathrm{h}}^{\mathrm{dc}}}{\frac{R_{\mathrm{b}}}{2}} - \underbrace{\left(\boldsymbol{\sigma}^{abc}\right)^{\top} \boldsymbol{i}_{\mathrm{l}}^{abc}}_{=:i_{\sigma,\mathrm{h}}^{\mathrm{dc}}}, \tag{2.2}$$

where $u_{\mathrm{h}}^{\mathrm{dc}}$ is the high-side DC link voltage, R_{b} is the balancing resistance, $\boldsymbol{\sigma}^{abc} := (\sigma^a, \sigma^b, \sigma^c)^{\top}$ are the switching states, and $i_{\sigma,\mathrm{h}}^{\mathrm{dc}}$ is the sum of the switched phase currents $\boldsymbol{i}_{\mathrm{l}}^{abc} := (i_{\mathrm{l}}^a, i_{\mathrm{l}}^b, i_{\mathrm{l}}^c)^{\top}$ through the high-side MOSFETs. To limit this so-called ripple current through one capacitor, more can be connected in parallel to share the current and thermal stress, thereby increasing the overall capacitance. Since a high capacitance makes the system more stable, the DC link capacitance was designed to be as large as possible, which is why aluminium electrolytic capacitors are used here. Section 3.2.5 discusses the effect of the capacitance on the system's stability in more detail.

A side effect of the aluminium oxide layer inside the capacitors is that a small current, the so-called leakage current, continuously flows through it. This current depends on the applied voltage, the temperature, the time, and the parameter dispersion between the individual capacitors. If these capacitors are connected in series, this unavoidable dispersion can lead to a voltage unbalance, which needs to be compensated for to avoid overvoltage [75]. The manufacturers recommend a simple resistive voltage divider connected in parallel to the capacitors.

The formula to calculate the resistance differs between the manufacturers. However, the main statement is the same, namely that the balancing current must dominate the leakage current. Therefore, the resulting resistance values are always about the same as well [72, 75].

For the used parallel-series connection, where nine capacitors are connected in parallel to one capacitor bank and two banks are connected in series, one balancing resistor R_b for each bank is provided and considered in the model. Applying Kirchhoff's law on the current node of the midpoint M gives

$$i_\mathrm{c,h}^\mathrm{dc} + \frac{u_\mathrm{h}^\mathrm{dc}}{\frac{R_\mathrm{b}}{2}} + i_\mathrm{cm} = i_\mathrm{c,l}^\mathrm{dc} + \frac{u_\mathrm{l}^\mathrm{dc}}{\frac{R_\mathrm{b}}{2}} \,. \tag{2.3}$$

Since the midpoint M is only connected in the case of the grid inverter, the current i_cm can be influenced externally. However, the current i_cm can also be interpreted as a leakage current of the capacitors. In both cases, it introduces an unbalance, and can lead to a voltage difference

$$\Delta u^\mathrm{dc} \coloneqq u_\mathrm{h}^\mathrm{dc} - u_\mathrm{l}^\mathrm{dc} \tag{2.4}$$

between the high- and low-side DC link voltages u_h^dc and u_l^dc, respectively, leading to

$$\begin{aligned} \Delta u^\mathrm{dc} &= \frac{R_\mathrm{b}}{2}\left(i_\mathrm{c,l}^\mathrm{dc} - i_\mathrm{c,h}^\mathrm{dc} - i_\mathrm{cm}\right) \\ &= \frac{R_\mathrm{b}}{2}\, 2\, C_\mathrm{dc}\, \frac{\mathrm{d}}{\mathrm{d}t}\left(u_\mathrm{l}^\mathrm{dc} - u_\mathrm{h}^\mathrm{dc}\right) - \frac{R_\mathrm{b}}{2}\, i_\mathrm{cm} \\ &= -R_\mathrm{b}\, C_\mathrm{dc}\, \frac{\mathrm{d}}{\mathrm{d}t}\Delta u^\mathrm{dc} - \frac{R_\mathrm{b}}{2}\, i_\mathrm{cm} \,. \end{aligned} \tag{2.5}$$

Rearranged, the dynamics of the voltage difference Δu^dc are given by

$$\frac{\mathrm{d}}{\mathrm{d}t}\Delta u^\mathrm{dc} = -\frac{1}{R_\mathrm{b}\, C_\mathrm{dc}}\Delta u^\mathrm{dc} - \frac{1}{2\, C_\mathrm{dc}} i_\mathrm{cm} \,. \tag{2.6}$$

The dynamics of the voltage difference Δu^dc depends on itself but with a negative sign, which indicates a decaying behaviour that is introduced by the balancing resistors. Furthermore, for steady-state conditions, the voltage difference is given by

$$\Delta u^\mathrm{dc} = -\frac{R_\mathrm{b}}{2}\, i_\mathrm{cm} \,. \tag{2.7}$$

The smaller the balancing resistance R_b, the smaller the voltage unbalance. However, this reduces the efficiency.

For the motor drive and the DC/DC converter, the midpoint M of the split DC link capacitance is not connected and remains floating, meaning only the leakage current causes an unbalance. Equation (2.6) shows that the balancing resistors R_b reduces the voltage difference, and since the leakage current is very small, the voltage difference is also minimal and can therefore be neglected. Thus, the assumption

$$u_\mathrm{h}^\mathrm{dc} = u_\mathrm{l}^\mathrm{dc} = \frac{u^\mathrm{dc}}{2} \tag{2.8}$$

can be made, and the DC link capacitance can be combined into one single capacitance C_dc for the devices without a midpoint connection. In the case of the grid inverter, the current i_cm must be kept at zero by the controller to avoid an unbalanced DC link.

2.1.3 Electromagnetic Compatibility Filter

Every electrical device on the market must meet the requirements for electromagnetic compatibility (EMC). It must be proven that the device does not disturb other devices and cannot be disturbed. The emitted electromagnetic energy can affect the functioning of other devices. This effect is called electromagnetic interference (EMI).
To verify the EMC, measurements must be made to prove that the disturbances remain below the limits defined by standards. The standards differentiate between conductive and radiative coupling. Radiative coupling is EMI caused by electromagnetic waves. Since the aluminium housing of this electrical system is earthed, meaning the metal is connected to the protective earth (PE), the electromagnetic waves are very well shielded. For the conductive coupling, current harmonics and voltage disturbance on the cables are measured. In Europa, the current harmonics are measured up to the 40th harmonic, meaning 2 kHz [76]. These current limits are mainly relevant for uncontrolled diode rectifier. With a VSI, these limits do not pose any difficulties, especially if the switching frequency is much higher than 2 kHz.
On the other hand, with a high switching frequency, it is more challenging to comply with the voltage limits in the higher frequency range. These interferences are measured from 150 kHz to 30 MHz [77]. Unlike the current harmonics, this interference frequency is higher than the switching frequency, and they cannot be affected by the current controller due to the Nyquist-Shannon sampling theorem [78, Sec. 10.2]. Therefore, passive filter components are used to attenuate the disturbance signals. The lower frequency limit of 150 kHz is also a reason why 70 kHz is chosen as the switching frequency. If the switching frequency is below 75 kHz, the second harmonic does not fall within the measurement range, making the design of the EMI filter somewhat easier.
Many sources in the electrical device can cause the disturbance. They can be caused by auxiliary components like power supplies, communication signals, or oscillators, but the primary source is usually the switching of the power MOSFETs. The switching process and the associated steep voltage transient on the phases of the VSI generate interference signals with a high-frequency range. The problem is that real components do not have ideal behaviour over the whole frequency range. For example, the adjacent wires of the inductor of the LC filter form a capacitance that causes the inductor to behave capacitively in the high-frequency range [79, Sec. 5.6]. This capacitance does not block the high-frequency signals so that they can propagate through the circuit and into the grid. This unwanted capacitance is called parasitic capacitance. Additional and well-designed EMI filters are required to attenuate the disturbing signals.
The EMC theory distinguishes between differential- and common-mode interference [79, Sec. 6.1]. The interference just described is a differential-mode interference as they flow into the grid via one phase and back via another. Common-mode interference occurs when it flows out of one phase and back over peripheral conductors like the PE and housing. They can be caused by current paths that run parallel to earthed parts and, thus, also form parasitic capacitances. The MOSFET itself makes one of the most important contributions to this. The back of the TO-247 housing, in which the MOSFET is built, is connected to the drain terminal, as shown in Fig. 2.6(a). This results in better thermal behaviour, as the MOSFET can be better thermally coupled to the heat sink. As the heat sink is usually earthed, a special insulating foil must be inserted between them, which insulates electrically but conducts well thermally. The downside is that this builds a parasitic capacitance $C_{\mathrm{par,m}}$ from the drain terminal of the MOSFET to the earthed heat sink, as shown in Fig. 2.6(b).
A simplified single-phase circuit illustrates the sources of differential- and common-mode interference in Fig. 2.6(c). The parasitic capacitance $C_{\mathrm{par,m}}$ is only added to the low-side MOSFETs, since the drain potential of these MOSFETs, in contrast to the high-side MOSFETs, changes permanently with the switching process. To model the non-ideal behaviour of the filter induc-

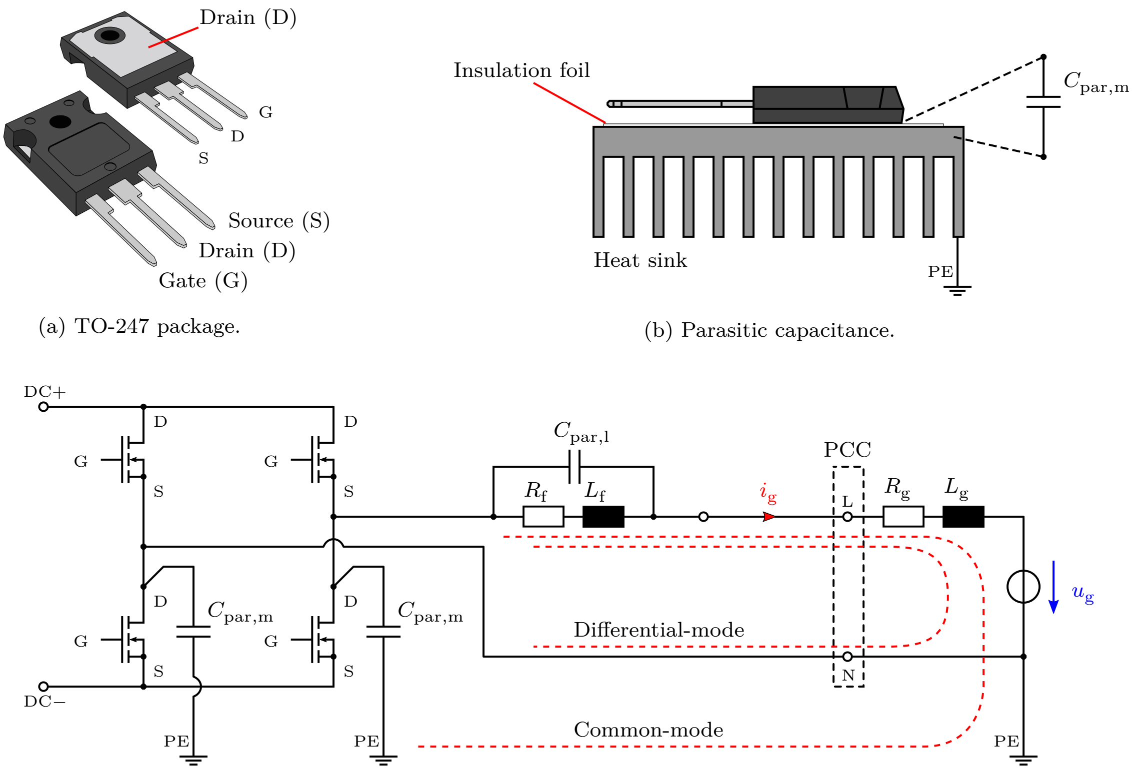

(a) TO-247 package.

(b) Parasitic capacitance.

(c) Electrical circuit.

Figure 2.6: Illustration of the (a) TO-247 package of the MOSFET, (b) creation of the parasitic capacitance, and (c) the simplified single-phase circuit with the differential- and common-mode interference.

tor, a parasitic capacitance $C_{\mathrm{par,l}}$ can be added in parallel to the inductance L_{f} and the filter resistance R_{f}. Caused by the switching of the MOSFET, high-frequency interference current will flow into the grid, resulting in an interference voltage that can be measured at the terminals of the device. In the case of the common-mode, the current is flowing back via the earth connection.

In addition to EMI filter components designed to block the flow of these currents, current paths can also be provided to allow the current to flow back to the source of interference already within the device. For this reason, special-rated capacitors are connected from the PE potential to paths of the main circuit. Where these connections must be made is strongly dependent on the layout of the circuit. Usually, those capacitors are installed between PE and the DC link potentials and from PE to the EMI filter at the terminals of the device.

The required EMI filter also consist of a combination of inductors and capacitors. However, since the components must act mainly at high frequencies, the component values are small compared to the LC filter for current filtering. They are several orders of magnitude smaller and can therefore be neglected for the controller design. Moreover, since the fundamental frequency of the interference is the switching frequency, the high-frequency interference signals can only be damped by passive filter elements and not by the control algorithm. Therefore, the EMI filter components are neglected for the modelling of the dynamics and not further considered in the following.

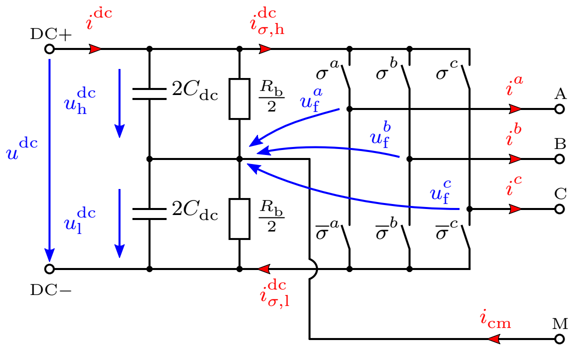

Figure 2.7: Circuit of the examined three-phase two-level inverter topology with the six switching elements.

2.2 Modulation

The modulation is the interface between the implemented control algorithm in software and the hardware with the switching elements, for example, MOSFETs. It takes the desired reference voltages, which should be applied, and generates the switching signals $\boldsymbol{\sigma}^{abc} := (\sigma^a, \sigma^b, \sigma^c)^\top$. Three-phase two-level VSI, like the one examined here, shown in Fig. 2.7, have six switching elements, where two are connected in series to a half-bridge, controlling one phase voltage. Each of the three half-bridges is connected in parallel to the DC link. To avoid current shoot-through faults, the half-bridges work in complementary mode, meaning that if the upper switch is closed ($\sigma = 1$), the lower one must be open ($\overline{\sigma} = 0$), and vice versa. The voltages $\boldsymbol{u}_{\mathrm{f}}^{abc} := (u_{\mathrm{f}}^a, u_{\mathrm{f}}^b, u_{\mathrm{f}}^c)^\top$, applied to the phases, are related to the switching states with

$$\boldsymbol{u}_{\mathrm{f}}^{abc} = u_{\mathrm{h}}^{\mathrm{dc}}\,\boldsymbol{\sigma}^{abc} - u_{\mathrm{l}}^{\mathrm{dc}}\left(1 - \boldsymbol{\sigma}^{abc}\right) . \tag{2.9}$$

The indices of the quantities are omitted here and not explicitly specified because they are intended for the end application. Here, a general consideration should be made.
The objective of the modulation process is to find switching states $\boldsymbol{\sigma}^{abc}$, so that the average voltage applied during a switching period T_{sw} matches the required reference voltages $\boldsymbol{u}_{\mathrm{f,ref}}^{abc} := (u_{\mathrm{f,ref}}^a, u_{\mathrm{f,ref}}^b, u_{\mathrm{f,ref}}^c)^\top$. This yields the condition

$$\boldsymbol{u}_{\mathrm{f,ref}}^{abc}[k] = \frac{1}{T_{\mathrm{sw}}} \int\limits_{k\,T_{\mathrm{sw}}}^{(k+1)T_{\mathrm{sw}}} \left(u_{\mathrm{h}}^{\mathrm{dc}}\,\boldsymbol{\sigma}^{abc} - u_{\mathrm{l}}^{\mathrm{dc}}\left(1 - \boldsymbol{\sigma}^{abc}\right)\right) \mathrm{d}\tau\,, \tag{2.10}$$

where $k \in \mathbb{N}$ is the number of the sampling period and $\boldsymbol{u}_{\mathrm{f,ref}}^{abc}[k]$ are the computed reference voltages at the period k.
There are many different modulation techniques discussed in literature, see [80, Sec. 5.3] and [81, Sec. 8.4]. However, only the two most widely used methods in the industry, pulse width modulation (PWM) and space vector modulation (SVM), are briefly discussed here.

2.2.1 Pulse With Modulation

For PWM, the reference voltage is compared to a so-called carrier signal or modulation signal, which is usually a sawtooth or a triangular signal. The intersection points of the signals determine the switching times of the MOSFETs.

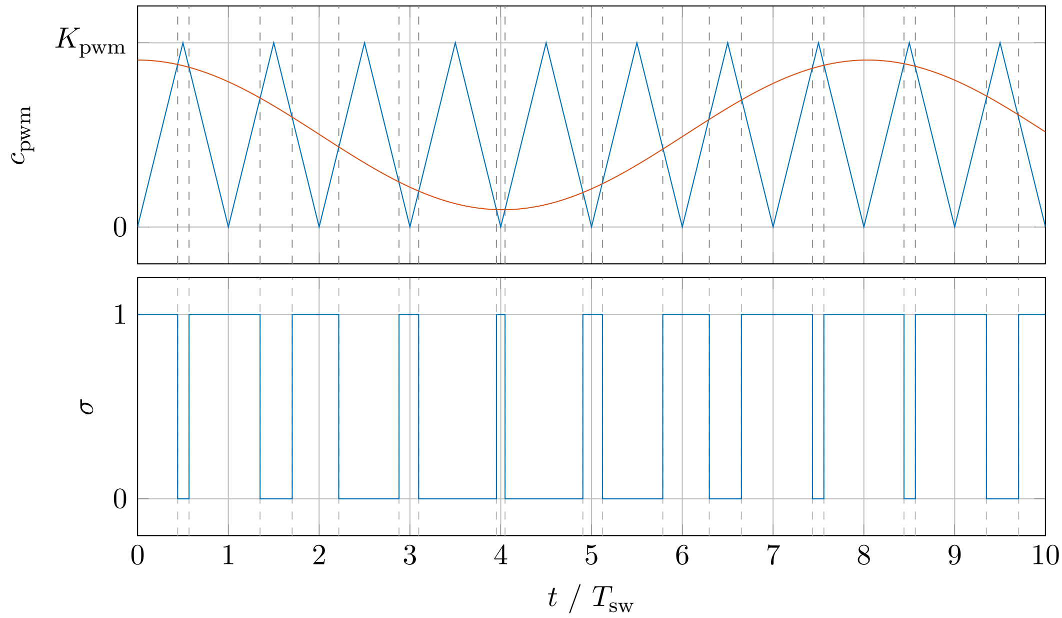

Figure 2.8: Example of a PWM for one half-bridge, where the switching state σ in the lower subplot is generated by comparison of the scaled reference voltage [—] with the carrier sawtooth signal [—].

Microcontrollers for power electronics applications have an integrated PWM module that only needs to be configured and can be used immediately. It takes a scaled reference voltage and generates the switching states. The significant advantage is that this process works on a hardware level of the microcontroller, where many additional features, such as reactions to specific events, for example, tripping events for overcurrent protection, are also implemented. Additionally, the mandatory dead-time, sometimes called dead-band, can easily be added, which is a short time between toggling the semiconductor where both switches are off to prevent a short circuit. This necessary dead-time leads to a nonlinear deviation of the applied output voltage from the reference voltage, which needs to be compensated for if the effects are no longer negligible [82].

The hardware implementation of the PWM module by the manufacturer makes the modulation fail-safe, fast and frees up the processor for other tasks. The modules of a microcontroller are also interconnected to each other, which allows to configure a desired schedule. In many applications, it is necessary to sample the current at a specific instance during the PWM period. Therefore, the PWM module can trigger the analogue to digital converter (ADC). Once the ADC has finished converting the analogue signals into digital signals, it can trigger an interrupt where the control algorithm can be computed. The result of the control algorithm is a new PWM reference value for the following period.

With all these advantages, it is only reasonable to utilise the existing PWM module of the microcontroller. Figure 2.8 shows example modulation signals for one haft-bridge. The carrier signal c_{pwm} is selected as sawtooth for symmetrical modulation. If the scaled reference voltage is greater than the carrier signal, the upper switch is turned on. Otherwise, the lower one is turned on. The carrier signal c_{pwm} is an integer up/down counter, clocked with the carrier frequency $f_{\text{c,pwm}}$ defined by the PWM module and derived from the system frequency of the microcontroller. The PWM frequency $f_{\text{c,pwm}}$ and the maximum counter value K_{pwm} define the switching frequency

$$f_{\text{sw}} = \frac{1}{T_{\text{sw}}} = \frac{f_{\text{c,pwm}}}{2\,K_{\text{pwm}}}\,. \tag{2.11}$$

The interface between the controller and the PWM module is the compare values $\boldsymbol{c}^{abc}_{\mathrm{ref}}$ defining the switching instances. These integers must be between 0 and the maximum value K_{pwm} of the carrier signal. The calculation of this can be derived very easily from Figure 2.8. It will be assumed that the upper and lower DC link voltages are equal, i.e.

$$u^{\mathrm{dc}}_{\mathrm{h}} = u^{\mathrm{dc}}_{\mathrm{l}} = \frac{u^{\mathrm{dc}}}{2} \,. \tag{2.12}$$

Furthermore, switching is assumed to be ideal, and the DC link voltages do not change considerably during one switching period. Thus, (2.10) becomes

$$\boldsymbol{u}^{abc}_{\mathrm{f,ref}} = \frac{u^{\mathrm{dc}}}{2} \left(2\, \boldsymbol{d}^{abc}_{\mathrm{ref}} - 1\right) \,, \tag{2.13}$$

where $\boldsymbol{d}^{abc}_{\mathrm{ref}} := (d^{a}_{\mathrm{ref}}, d^{b}_{\mathrm{ref}}, d^{c}_{\mathrm{ref}})^{\top}$ are the duty cycles, defined as the ratio of the on-time $\boldsymbol{t}^{abc}_{\sigma,\mathrm{on}}$ of the upper switches to the switching period T_{sw} with

$$\boldsymbol{d}^{abc}_{\mathrm{ref}} = \frac{1}{T_{\mathrm{sw}}} \int_{nT_{\mathrm{sw}}}^{(n+1)T_{\mathrm{sw}}} \boldsymbol{\sigma}^{abc}\, \mathrm{d}t \;=\; \frac{\boldsymbol{t}^{abc}_{\sigma,\mathrm{on}}}{T_{\mathrm{sw}}} \,. \tag{2.14}$$

Since the on-time can be at most the switching period, the duty cycle is limited to

$$0 \leq \left\{d^{a}_{\mathrm{ref}}, d^{b}_{\mathrm{ref}}, d^{c}_{\mathrm{ref}}\right\} \leq 1 \,. \tag{2.15}$$

It can be set with the corresponding values $\boldsymbol{c}^{abc}_{\mathrm{ref}}$ of the PWM module with

$$\boldsymbol{d}^{abc}_{\mathrm{ref}} = \frac{\boldsymbol{c}^{abc}_{\mathrm{ref}}}{K_{\mathrm{pwm}}} \,. \tag{2.16}$$

Rearranging (2.13) and inserting (2.16), the compare values $\boldsymbol{c}^{abc}_{\mathrm{ref}}$ can be derived from the reference voltages $\boldsymbol{u}^{abc}_{\mathrm{f,ref}}$ for each phase with

$$\boldsymbol{c}^{abc}_{\mathrm{ref}} = \left(\frac{\boldsymbol{u}^{abc}_{\mathrm{f,ref}}}{u^{\mathrm{dc}}} + \frac{1}{2}\right) K_{\mathrm{pwm}} \,. \tag{2.17}$$

The maximum feasible output voltage can be derived from the inverse function of (2.17), given by

$$\boldsymbol{u}^{abc}_{\mathrm{f,ref}} = u^{\mathrm{dc}} \left(\frac{\boldsymbol{c}^{abc}_{\mathrm{ref}}}{K_{\mathrm{pwm}}} - \frac{1}{2}\right) \,. \tag{2.18}$$

As the compare value is limited to 0 and K_{pwm}, the absolute value of the maximum feasible output voltage is limited to $\frac{u^{\mathrm{dc}}}{2}$, which is also shown in [81, Sec. 8.4.5] and [83, Sec. 2.2.5]. This must be guaranteed by limiting the reference voltage by the controller with

$$-\frac{u^{\mathrm{dc}}}{2} \leq \left\{u^{a}_{\mathrm{f,ref}}, u^{b}_{\mathrm{f,ref}}, u^{c}_{\mathrm{f,ref}}\right\} \leq \frac{u^{\mathrm{dc}}}{2} \,, \tag{2.19}$$

or

$$\left\|\boldsymbol{u}^{\alpha\beta}_{\mathrm{ref}}\right\| = \sqrt{\left(u^{\alpha}_{\mathrm{ref}}\right)^2 + \left(u^{\beta}_{\mathrm{ref}}\right)^2} \leq \frac{u^{\mathrm{dc}}}{2} \tag{2.20}$$

if considered in the (α,β)-plane, which is introduced in the following section.
As indicated in (2.10) and (2.16), the reference voltage is only fully reached on average at the end of the switching period. Additionally, the calculated duty cycle is typically updated in the subsequent switching period to avoid intermediate switching. Both lead to time delay τ_{avg} between the update of the reference voltages $\boldsymbol{u}_{\mathrm{f,ref}}^{abc}$ until the average voltages $\overline{\boldsymbol{u}}_{\mathrm{f}}^{abc}$ are fully applied, which depends on the implementation and varies within the interval

$$\tau_{\mathrm{avg}} \in \left[\tfrac{1}{2},\, 2\right] T_{\mathrm{sw}}\,. \tag{2.21}$$

In the frequency domain, this delay can be approximated with a first-order transfer function by building a Taylor series and truncating it after the first term, which is valid for a small delay $\tau_{\mathrm{avg}} \ll 1$. This yields the transfer function [84, Sec. 14.3.1.3]

$$\frac{\overline{\boldsymbol{u}}_{\mathrm{f}}^{abc}(s)}{\boldsymbol{u}_{\mathrm{f,ref}}^{abc}(s)} = e^{-s\,\tau_{\mathrm{avg}}} = \frac{1}{1+\frac{s\,\tau_{\mathrm{avg}}}{1!}+\frac{(s\,\tau_{\mathrm{avg}})^2}{2!}+\dots} \approx \frac{1}{1+s\,\tau_{\mathrm{avg}}}\,, \tag{2.22}$$

which is used to model the modulation process and account for it in the controller design.

2.2.2 Space Vector Modulation

For PWM, each phase is considered individually. When used with electrical machines or the grid, which is also generated by electrical machines, the three phases are not completely independent. The three windings a, b and c of an electrical machine are spatially shifted by $120^\circ = \frac{2}{3}\pi$ to each other. In classical space vector theory, the three-phase system is considered on a plane, and the three phases span a reference frame with three axes. When the three phases of the VSI are connected to this three-phase system, the applied voltages act in the respective direction of the connected phase. Since there are two switching states per phase, two voltage vectors can be applied either in the direction of the respective axis or the opposite direction. These six vectors are called switching vectors or sometimes active or basic vectors.
The fundamental idea behind space vector modulation (SVM) is to obtain the reference voltage vector $\boldsymbol{u}_{\mathrm{f,ref}}^{abc}$ by the geometrical combination of the two adjacent switching vectors during one switching period. Since the reference frame is overdetermined in the plane with three vectors shifted by 120°, it is transformed into the orthogonal (α,β)-reference frame. For this purpose, the switching vectors are transformed by applying the Clarke transformation matrices [84, Sec. 14.2.4], [85]

$$\boldsymbol{T}_{\mathrm{c}} := \kappa \begin{bmatrix} 1 & -\frac{1}{2} & -\frac{1}{2} \\ 0 & \frac{\sqrt{3}}{2} & -\frac{\sqrt{3}}{2} \\ \frac{1}{\sqrt{2}} & \frac{1}{\sqrt{2}} & \frac{1}{\sqrt{2}} \end{bmatrix} \quad \text{and} \quad \boldsymbol{T}_{\mathrm{c}}^{-1} := \frac{1}{\kappa} \begin{bmatrix} \frac{2}{3} & 0 & \frac{\sqrt{2}}{3} \\ -\frac{1}{3} & \frac{1}{\sqrt{3}} & \frac{\sqrt{2}}{3} \\ -\frac{1}{3} & -\frac{1}{\sqrt{3}} & \frac{\sqrt{2}}{3} \end{bmatrix}. \tag{2.23}$$

Here, the full Clarke transformation matrices are given, which lead to an orthogonal (α,β,γ)-reference frame. The coefficient $\kappa = \frac{2}{3}$ is chosen, which yields an amplitude-correct transformation. This means

$$x^a = x^\alpha\,, \tag{2.24}$$

which only holds for symmetrical systems with $x^a + x^b + x^c = 0$ (see Appendix A.1). The electrical power is given by

$$p_{\mathrm{el}} = (\boldsymbol{u}^{abc})^\top \boldsymbol{i}^{abc} = \tfrac{3}{2}(\boldsymbol{u}^{\alpha\beta\gamma})^\top \boldsymbol{i}^{\alpha\beta\gamma}\,. \tag{2.25}$$

Table 2.1: All eight possible switching state combinations for σ^a, σ^b and σ^c for each phase and the respective vector notation $\boldsymbol{\sigma}^{abc} := (\sigma^a, \sigma^b, \sigma^c)^\top$ with the corresponding active voltage vector $\boldsymbol{u}^{\alpha\beta\gamma}$.

σ^a	σ^b	σ^c	$\boldsymbol{\sigma}^{abc}$	$\boldsymbol{u}^{\alpha\beta\gamma}$
0	0	0	$\boldsymbol{\sigma}^{abc}_{000} = \boldsymbol{\sigma}^{abc}_{0}$	$\boldsymbol{u}^{\alpha\beta\gamma}_{000}$
1	0	0	$\boldsymbol{\sigma}^{abc}_{100} = \boldsymbol{\sigma}^{abc}_{1}$	$\boldsymbol{u}^{\alpha\beta\gamma}_{100}$
1	1	0	$\boldsymbol{\sigma}^{abc}_{110} = \boldsymbol{\sigma}^{abc}_{2}$	$\boldsymbol{u}^{\alpha\beta\gamma}_{110}$
0	1	0	$\boldsymbol{\sigma}^{abc}_{010} = \boldsymbol{\sigma}^{abc}_{3}$	$\boldsymbol{u}^{\alpha\beta\gamma}_{010}$
0	1	1	$\boldsymbol{\sigma}^{abc}_{011} = \boldsymbol{\sigma}^{abc}_{4}$	$\boldsymbol{u}^{\alpha\beta\gamma}_{011}$
0	0	1	$\boldsymbol{\sigma}^{abc}_{001} = \boldsymbol{\sigma}^{abc}_{5}$	$\boldsymbol{u}^{\alpha\beta\gamma}_{001}$
1	0	1	$\boldsymbol{\sigma}^{abc}_{101} = \boldsymbol{\sigma}^{abc}_{6}$	$\boldsymbol{u}^{\alpha\beta\gamma}_{101}$
1	1	1	$\boldsymbol{\sigma}^{abc}_{111} = \boldsymbol{\sigma}^{abc}_{7}$	$\boldsymbol{u}^{\alpha\beta\gamma}_{111}$

For a three-phase two-level VSI there exist $2^3 = 8$ possible switching states, listed in Table 2.1. The switching vectors $\boldsymbol{u}^{\alpha\beta\gamma}$ results by applying the Clarke transformation to (2.9) with

$$\boldsymbol{u}^{\alpha\beta\gamma} = \boldsymbol{T}_\mathrm{c}\, \boldsymbol{u}^{abc}\,. \tag{2.26}$$

In Fig. 2.9, the switching vectors are shown in the (α,β)-plane, which span the familiar voltage hexagon with the six sectors. The order of the switching states in Tab. 2.1 corresponds to the counter-clockwise order of the vectors in this figure. The numbering is also adapted to this order and does not correspond to a binary interpretation of the switching states. The two vectors $\boldsymbol{u}^{\alpha\beta\gamma}_{000}$ and $\boldsymbol{u}^{\alpha\beta\gamma}_{111}$ in the centre are called zero vectors because they do not contribute any α- or β-component. The desired reference voltage vector $\boldsymbol{u}^{abc}_{\mathrm{f,ref}}$ can be composed of the adjacent voltage vectors, which define a sector. The sector can be determined by the angle

$$\theta_\mathrm{ref} = \begin{cases} 0 & , u^\beta_\mathrm{f,ref} = 0\ \mathrm{V},\ u^\alpha_\mathrm{f,ref} > 0\ \mathrm{V} \\ \arctan \frac{u^\alpha_\mathrm{f,ref}}{u^\beta_\mathrm{f,ref}} & , u^\beta_\mathrm{f,ref} > 0\ \mathrm{V} \\ \pi & , u^\beta_\mathrm{f,ref} = 0\ \mathrm{V},\ u^\alpha_\mathrm{f,ref} < 0\ \mathrm{V} \\ \arctan \frac{u^\alpha_\mathrm{f,ref}}{u^\beta_\mathrm{f,ref}} + 2\pi & , u^\beta_\mathrm{f,ref} < 0\ \mathrm{V} \end{cases} \tag{2.27}$$

of the reference voltage vector. The searched sector k_s is given by the floor function

$$k_\mathrm{s} = \left\lfloor 6\, \frac{\theta_\mathrm{ref}}{2\pi} \right\rfloor\,. \tag{2.28}$$

The duty cycles d_r and d_l can then be calculated for the right and left adjacent switching vectors with

$$\left.\begin{aligned} d_\mathrm{r} &= \frac{t_\mathrm{r}}{T_\mathrm{sw}} = \sqrt{3}\, \frac{\left\| \boldsymbol{u}^{\alpha\beta\gamma}_\mathrm{f,ref} \right\|}{u^\mathrm{dc}} \sin\left(\frac{\pi}{3} - \left(\theta_\mathrm{ref} - k_\mathrm{s}\frac{\pi}{3}\right)\right) \qquad \text{and} \\ d_\mathrm{l} &= \frac{t_\mathrm{l}}{T_\mathrm{sw}} = \sqrt{3}\, \frac{\left\| \boldsymbol{u}^{\alpha\beta\gamma}_\mathrm{f,ref} \right\|}{u^\mathrm{dc}} \sin\left(\theta_\mathrm{ref} - k_\mathrm{s}\frac{\pi}{3}\right), \end{aligned}\right\} \tag{2.29}$$

respectively [80, Sec. 5.4.1]. For the remaining time of the switching period, the zero vectors

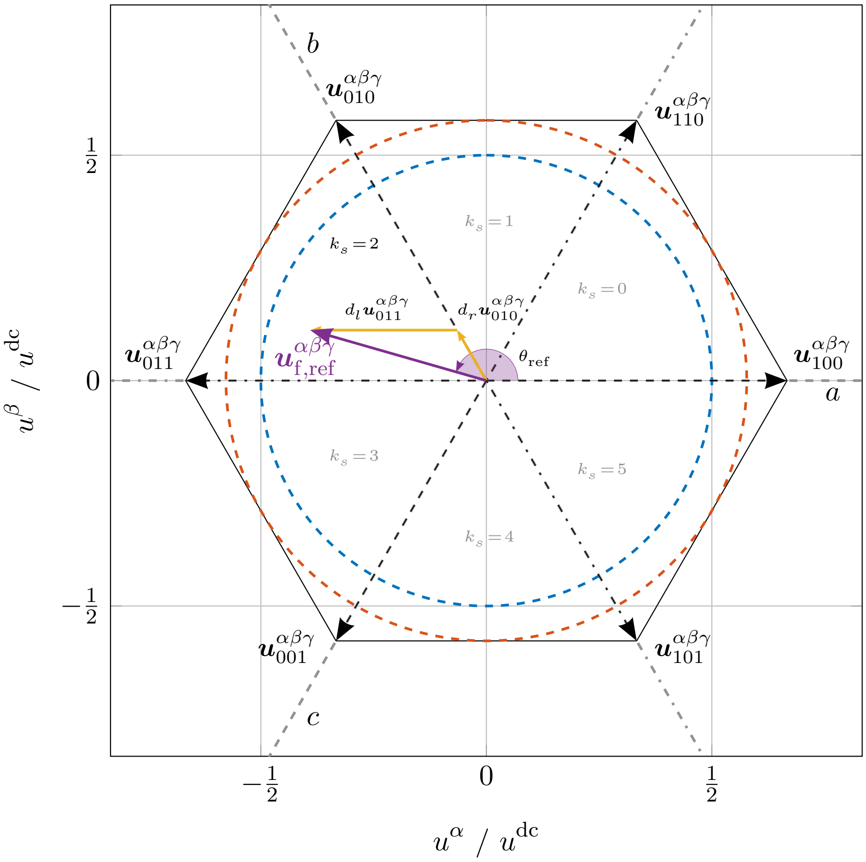

Figure 2.9: Voltage hexagon spanned by the six active voltage vectors in the (α,β)-plane, the reference voltages $\boldsymbol{u}_{\mathrm{f,ref}}^{abc}$ [—] in the sector $k_{\mathrm{s}} = 2$ composed by the adjacent switching vectors [—] and the voltage limits for PWM [- - -] and SVM [- - -].

with the duty cycles d_0 and d_7 are used such that

$$d_0 + d_7 + d_{\mathrm{r}} + d_{\mathrm{l}} = 1 \tag{2.30}$$

is satisfied. Since both zero vectors do not contribute to the reference vector, the duty cycles d_0 and d_7 can be divided arbitrarily. There are different approaches with different purposes [86]. The straightforward one is to split the remaining duty cycle equally between d_0 and d_7. Another approach is a so-called hardware-determined switching pattern, where the remaining time is assigned to only one zero vector. This has the advantage that one switching state does not change during the period, which reduces switching losses. But it also leads to asymmetry and results in small harmonics due to the unevenly used dead-time among the three half-bridges [87].

The resulting duty cycles can now be assigned to the duty cycles $\boldsymbol{d}_{\mathrm{ref}}^{abc}$ with

$$\boldsymbol{d}_{\mathrm{ref}}^{abc} = \begin{cases} \begin{bmatrix} \boldsymbol{\sigma}_{k_{\mathrm{s}}+1}^{abc} & \boldsymbol{\sigma}_{k_{\mathrm{s}}+2}^{abc} & \boldsymbol{\sigma}_{7}^{abc} \end{bmatrix} \begin{pmatrix} d_{\mathrm{r}} \\ d_{\mathrm{l}} \\ d_7 \end{pmatrix} & , 0 \leq k_{\mathrm{s}} \leq 4 \\ \begin{bmatrix} \boldsymbol{\sigma}_{6}^{abc} & \boldsymbol{\sigma}_{1}^{abc} & \boldsymbol{\sigma}_{7}^{abc} \end{bmatrix} \begin{pmatrix} d_{\mathrm{r}} \\ d_{\mathrm{l}} \\ d_7 \end{pmatrix} & , k_{\mathrm{s}} = 5\,. \end{cases} \tag{2.31}$$

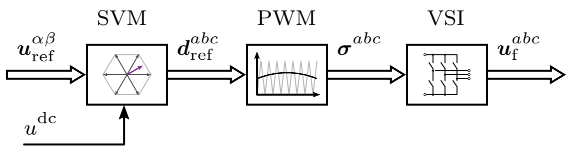

Figure 2.10: Block diagram of the space vector pulse width modulation (SVPWM).

Using (2.16), the compare values $\boldsymbol{c}_{\text{ref}}^{abc}$ can be computed from the duty cycles, which can be passed directly to the integrated PWM module, as shown in Fig. 2.10. The advantages of the PWM module can be used again, and the desired switching patterns are generated by hardware. Therefore, it is still reasonable to utilise the existing PWM module of the microcontroller. The SVM can be seen as an additional module between the controller output and PWM Module. This combination is sometimes referred to as space vector pulse width modulation (SVPWM).

The maximum feasible output voltage is limited to

$$\left\| \boldsymbol{u}_{\text{f,ref}}^{\alpha\beta} \right\| = \sqrt{\frac{2}{3}} \left\| \boldsymbol{u}_{\text{f,ref}}^{abc} \right\| \leq \frac{u^{\text{dc}}}{\sqrt{3}} \,, \tag{2.32}$$

which is defined by the circle that touches the edges of the hexagon. In Fig. 2.9, both limitations for PWM and SVM are shown with their respective circle.

The reason why the SVM has an extended range lies in the utilisation of the γ-component. This becomes clear when looking at the result of the modulation in Fig. 2.11. It shows the fundamental frequency of the output voltage from PWM and SVM. The switching frequency and its harmonics are removed by forward-backward filtering, where the signal is first filtered forward and then backward to remove phase distortion [88]. The reference voltages for both cases are the same sinusoidal, symmetrical three-phase voltages, indicated by the black dashed line. PWM follows the reference signal very well, as seen in the first subplot. A small delay between the reference and the filtered voltage can be noticed, which is half the switching period T_{sw}. This is caused by the fact that the voltage can only be reproduced on average during one switching period. The transfer function (2.22) takes this delay into account.

The plot in the middle shows the result of SVM, where both zero vectors are equally applied. The difference in the results from PWM arises from the utilised γ-component. The sum of all three voltages is shown by the violet dashed line, which lies on top of the diagonals. Note that this is not exactly the γ-voltage u^{γ}, since

$$u^{\gamma} = \frac{\sqrt{2}}{3} \left(u^{a} + u^{b} + u^{c} \right) \,. \tag{2.33}$$

However, the fundamental of the line-to-line voltages $\boldsymbol{u}^{a\text{-}b\text{-}c}$ with

$$\boldsymbol{u}^{a\text{-}b\text{-}c} = \begin{bmatrix} 1 & -1 & 0 \\ 0 & 1 & -1 \\ -1 & 0 & 1 \end{bmatrix} \boldsymbol{u}^{abc} \tag{2.34}$$

are not affected by this γ-component, shown in the third subplot. Both PWM and SVM result in the exact same line-to-line voltages. From the point of view of a connected electrical machine, there is no difference in the applied voltage. The additional γ-component only changes the fundamental frequency of the potential between the star-point of the machine and ground according to the violet curve in Fig 2.11. The desired current remains unaffected by this.

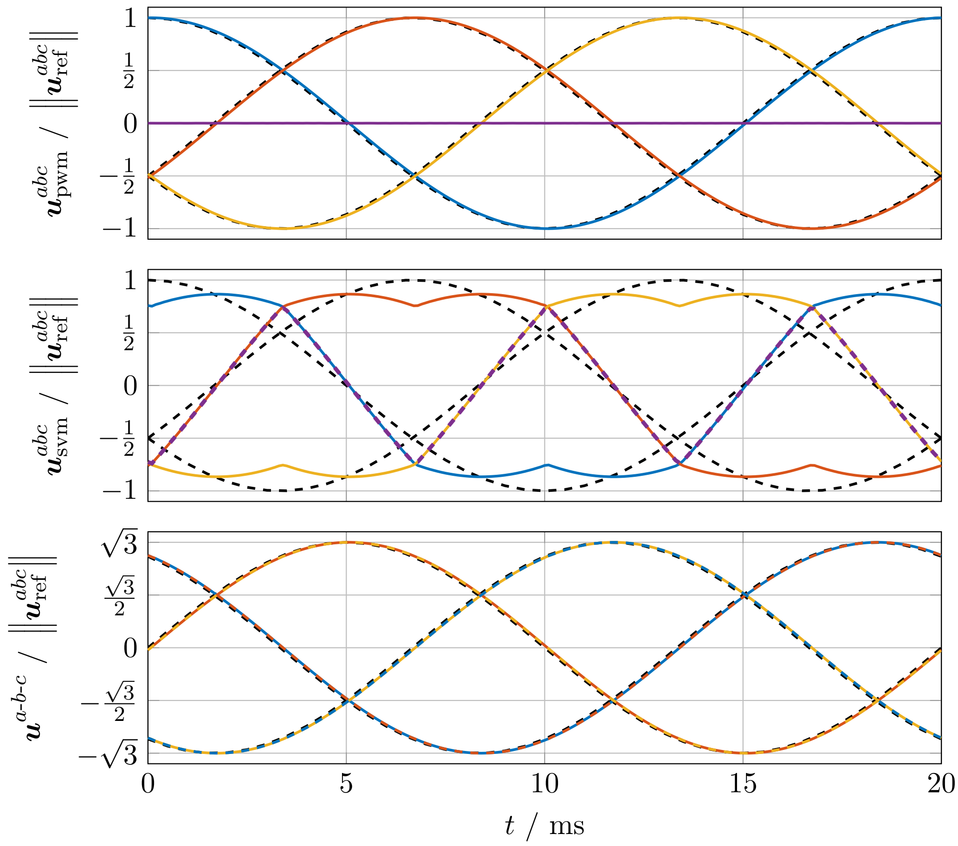

Figure 2.11: Comparison of the filtered results of PWM in the upper subplot and SVM in the second subplot with the sum of all three voltages [——] and the same reference voltages [- - -], which results in the same line-to-line voltages $\boldsymbol{u}^{a\text{-}b\text{-}c}$, shown in the lower subplot.

The reason for the behaviour of SVM is that each of the six active vectors also has a γ-voltage with an amplitude of $\frac{\sqrt{2}}{6}u^{\mathrm{dc}}$. This can be seen in Fig. 2.12, where the three-dimensional voltage space is shown in an orthogonal projection onto the (α, β)-, (α, γ)- and (γ, β)-plane. Notice that the (γ, β)-subplot at the top right has a reversed horizontal axis so that the plots fit together accordingly. The first subplot shows the same hexagon as the previous figure on the (α, β)-plane. The view on the (α, γ)-plane, shown in the lower subplot, reveals the γ-component of the switching vectors. From this point of view, the vector $\boldsymbol{u}^{\alpha\beta\gamma}_{101}$ is lying over $\boldsymbol{u}^{\alpha\beta\gamma}_{110}$, and $\boldsymbol{u}^{\alpha\beta\gamma}_{001}$ over $\boldsymbol{u}^{\alpha\beta\gamma}_{010}$. The space spanned by all switching vectors forms a cube and not a more complex polyhedron, as it might be assumed. The four switching vectors $\boldsymbol{u}^{\alpha\beta\gamma}_{101}$, $\boldsymbol{u}^{\alpha\beta\gamma}_{110}$, $\boldsymbol{u}^{\alpha\beta\gamma}_{001}$ and $\boldsymbol{u}^{\alpha\beta\gamma}_{010}$ point at the centre of the edges of the cube from the (α, γ)-perspective [2].

The two yellow arrows indicate how the reference voltage vector is composed of the adjacent switching vectors. The contribution of the two zero vectors is not shown since they are of equal length and cancel each other out. In the (α, β)-plane, the two yellow vectors match with the reference voltage vector as desired. However, in the other planes, it becomes evident that the γ-component of the switching vectors leads to a deviation.

The γ-component is essential for the proper operation of the grid inverter and must, therefore, be considered in the modulation. If the γ-voltage does not lead to an undesired γ-current in the system, e.g., in motor drive applications, SVM can be used to increase the maximum feasible output voltage by $\frac{2}{\sqrt{3}} = 1.155$ compared to PWM. Similar results can be achieved by injecting harmonics in the reference voltages before passing it to the PWM module [83, Sec. 3.3], [86].

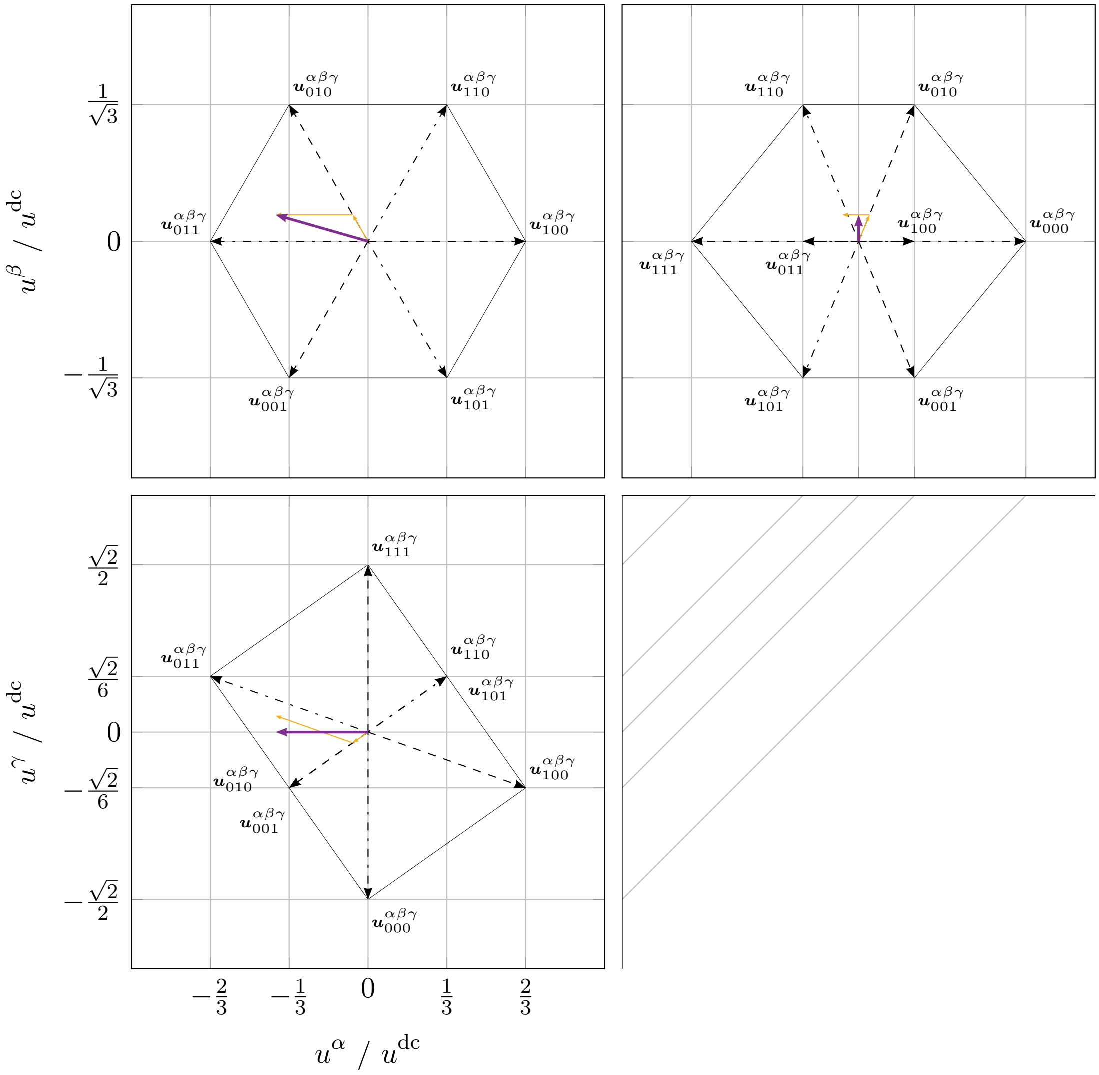

Figure 2.12: Three-dimensional voltage space represented in an orthogonal projection onto the (α, β)-, (α, γ)- and (γ, β)-plane with the reference voltage vector $\boldsymbol{u}_{\mathrm{ref}}^{abc}$ [—] in the sector $k_{\mathrm{s}} = 2$ composed by the adjacent switching vectors [—].

2.2.3 Extended Space Vector Modulation

If a specific γ-voltage also needs to be applied by the VSI, it can be included in the modulation process. Therefore, the zero vectors $\boldsymbol{\sigma}_0^{abc}$ and $\boldsymbol{\sigma}_7^{abc}$ are utilised as they are pure γ-vectors. The modulation objective from (2.10) can also be represented as

$$\boldsymbol{u}_{\mathrm{f,ref}}^{\alpha\beta\gamma} = \boldsymbol{T}_{\mathrm{c}}\, \boldsymbol{u}_{\mathrm{f,ref}}^{abc} = \frac{u^{\mathrm{dc}}}{2}\, \boldsymbol{T}_{\mathrm{c}}\, \boldsymbol{T}_{\sigma,k_{\mathrm{s}}+1} \begin{pmatrix} d_{\mathrm{r}} \\ d_{\mathrm{l}} \\ d_{\mathrm{z}} \end{pmatrix}, \tag{2.35}$$

by means of (2.16), whereby the assumption (2.12) still holds.

The (3×3)-matrix $\boldsymbol{T}_{\sigma,k_{\mathrm{s}}+1}$ is defined by the adjacent switching states $\boldsymbol{\sigma}_{ks+1}^{abc}$ and $\boldsymbol{\sigma}_{ks+2}^{abc}$ of the corresponding sector k_s with

$$\boldsymbol{T}_{\sigma,k_\mathrm{s}+1} = \begin{cases} \left[(2\,\boldsymbol{\sigma}^{abc}_{k_\mathrm{s}+1} - 1) \quad (2\,\boldsymbol{\sigma}^{abc}_{k_\mathrm{s}+2} - 1) \quad (2\,\boldsymbol{\sigma}^{abc}_{7} - 1)\right] & , 0 \leq k_\mathrm{s} \leq 4 \\ \left[(2\,\boldsymbol{\sigma}^{abc}_{6} - 1) \quad (2\,\boldsymbol{\sigma}^{abc}_{1} - 1) \quad (2\,\boldsymbol{\sigma}^{abc}_{7} - 1)\right] & , k_\mathrm{s} = 5\,. \end{cases} \tag{2.36}$$

Since the three active voltage vectors used in the matrix $\boldsymbol{T}_{\sigma,k_\mathrm{s}+1}$ are linearly independent, as all three vectors point in different directions, the matrix is invertible. Hence, the duty cycles can be calculated with

$$\begin{pmatrix} d_\mathrm{r} \\ d_\mathrm{l} \\ d_\mathrm{z} \end{pmatrix} = \boldsymbol{T}^{-1}_{\sigma,k_\mathrm{s}+1}\,\frac{2\,\boldsymbol{u}^{abc}_\mathrm{f,ref}}{u^\mathrm{dc}} = \boldsymbol{T}^{-1}_{\sigma,k_\mathrm{s}+1}\,\boldsymbol{T}_\mathrm{c}^{-1}\,\frac{2\,\boldsymbol{u}^{\alpha\beta\gamma}_\mathrm{f,ref}}{u^\mathrm{dc}}\,. \tag{2.37}$$

The duty cycle d_z represents the relative on-time of the zero vector $\boldsymbol{\sigma}^{abc}_{7} = \boldsymbol{\sigma}^{abc}_{111}$. As the γ-voltage can become negative, d_z will also be negative. This mean means that the zero vector $\boldsymbol{\sigma}^{abc}_{0} = \boldsymbol{\sigma}^{abc}_{000}$ needs to be more active than $\boldsymbol{\sigma}^{abc}_{7}$. Furthermore, the constraint (2.30) still must be satisfied, which means that the remaining time of the switching period has to be split equally between the two γ-vectors, leading to

$$d_7 = \frac{1}{2}\,(1 - d_\mathrm{r} - d_\mathrm{l} + d_\mathrm{z})\,. \tag{2.38}$$

Inserting the resulting duty cycles into (2.31) and (2.16) leads again to the compare values $\boldsymbol{c}^{abc}_\mathrm{ref}$, which can be passed to the PWM module. The inverse matrices $\boldsymbol{T}^{-1}_{\sigma,k_\mathrm{s}+1}$ can be computed offline for each sector to save computing time. The DC link voltage u^dc should not be included in the offline computation, as it changes and must be adapted during operation.
Applying the same reference voltages from the example in Fig. 2.11 to this extended SVM leads to the same results as PWM. Since this technique also determines the γ-voltage according to the desired reference voltages, no more degree of freedom is left to optimise the modulation. The three-phase VSI has three degrees of freedom to apply a voltage vector, and each of them needs to be used to apply the α, β, and γ-components of the reference voltages. Thus, the maximum feasible output voltage is limited to $\frac{u^\mathrm{dc}}{2}$ like with PWM, which eliminates the significant advantage of SVM in this case.
Furthermore, the saturation of the voltage vector is more complex in the three-dimensional space [2]. It has the advantage that it can be decided which voltage component is to be saturated so that, for example, the direction of the voltage vector is maintained but shortened. However, if this is not desired, the computing time can be saved using PWM with a simple limitation of the compare values, where the γ-voltage is adequately considered.

2.2.4 High-Frequency Current Measurement

Safety standards require double isolation between the high-voltage circuits and low-voltage signals that can be touched, like communication lines. For this reason, the signals of the current and voltage measurements need to be electrically isolated from the microcontroller. The industry provides many integrated circuits for this purpose. Here, the isolated amplifier AMC1302 from Texas Instruments is chosen for the current measurement [89].
The phase current i_l is measured indirectly by the voltage over a shunt resistor R_meas. This voltage is then connected to the isolated amplifier, as shown in Fig. 2.13. The amplifier needs two galvanically separated power supplies, each for the input and the output, which are not shown here. The amplified and isolated output voltage then goes to the ADC unit of the microcontroller.

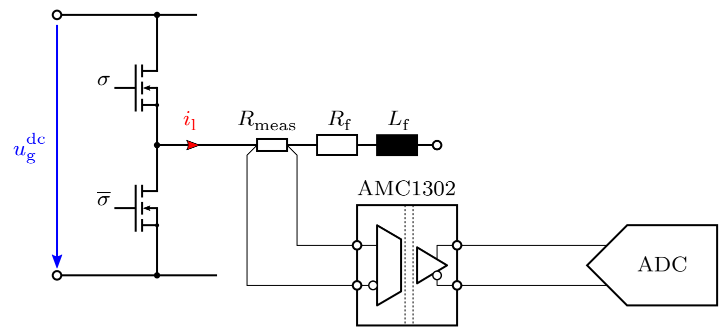

Figure 2.13: The electrical circuit of the current measurement with the reinforced isolated amplifier AMC1302.

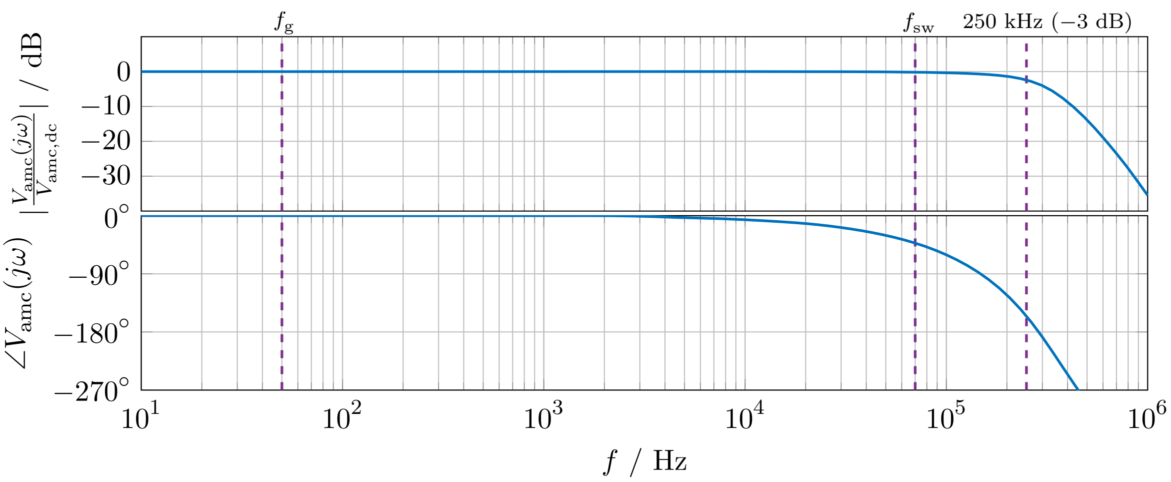

Figure 2.14: Frequency response of the gain V_{amc} of the amplifier AMC1302 [89] with the discussed frequencies written on top corresponding to the dashed lines.

Typically, the PWM module triggers the current measurement when the PWM counter becomes zero. At this instance, the upper MOSFET is open for half its off-time, regardless of the duty cycle. This is when the current is equal to the average current value over one switching period. Is the current sampled at this moment, the superimposed current ripple is ignored as desired, and only the lower frequency components are measured. However, the measured current is falsified if a propagation delay distorts the signal. The signal propagation time must be very low if the current ripple has high frequencies, whose fundamental is the switching frequency.

The amplifier AMC1302 has a stated bandwidth of 250 kHz, which seems sufficient. However, as the frequency response in Fig. 2.14 shows, the bandwidth is defined where the normalised gain reaches −3 dB. At the relevant switching frequency f_{sw}, the gain is about 0 dB, but the phase is around -45°, which results in a phase shift so that the usual trigger point leads to a falsified current measurement.

Fig. 2.15 shows an exemplary current curve and the trigger points. On the top subplot, the PWM carrier signal c_{pwm} with a constant compare value c_{ref} is shown. In the second plot, the actual current and the output of the amplifier are shown. The amplifier output is rescaled to a current to compare the signals. If the compare value exceeds the carrier signal, the upper MOSFET is on, and the current rises. Otherwise, the current falls. The dashed violet line marks the typical trigger point in both subplots. If there is no phase shift in the measured signal, the

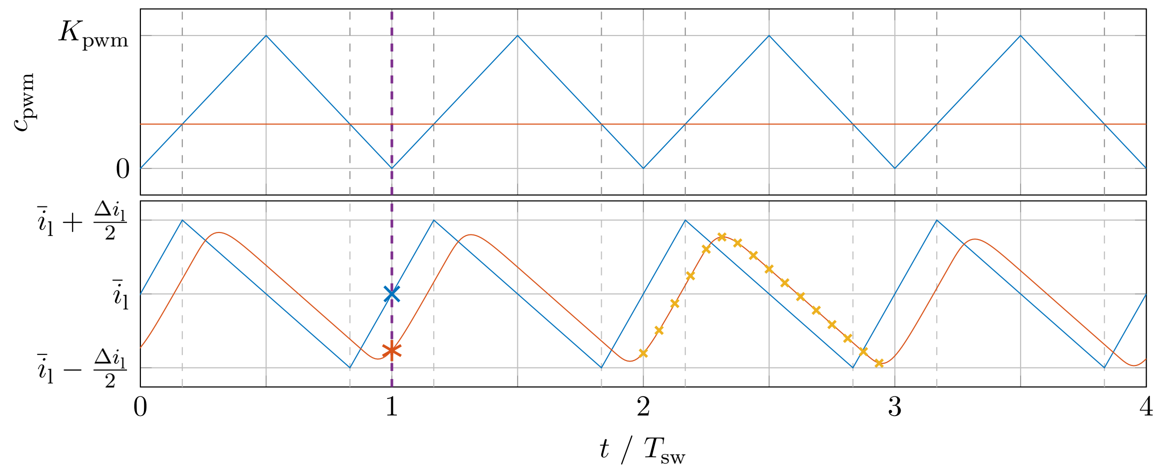

Figure 2.15: The top subplot shows the PWM carrier signal c_{pwm} [—] with a constant compare value c_{ref} [—] and the lower subplot shows an exemplary current i_l [—] and the amplifiers scaled output [—] as well as the typical trigger point [- - -] and the multiple sample points [×].

average current, marked by the blue cross, could be measured. With a phase shift, the sampled point corresponds not with the average current $\bar{i}_l$, marked with a red asterisk, and a duty cycle dependent error occurs.

To deal with this problem, a multi-sample method is introduced. Therefore, the ADC is triggered multiple times during one period with equidistant sample points, as shown in the following period in Fig. 2.15. The results of the ADC for each sample are transferred by the direct memory access (DMA) unit of the microcontroller to an allocated space in memory. In the subsequent period, the average value of all samples can be computed before the control algorithm. The average of all samples gives the same result as the ideal sample point at $c_{pwm} = 0$. In addition, the accuracy of the measured current is increased as the measurement noise is filtered by averaging. The downside of this method is that the control algorithm can only be calculated in every second period. Thus, the sampling period T_s is doubled, and, respectively, the sampling frequency f_s is halved with

$$T_s = \frac{1}{f_s} = \frac{2}{f_{sw}} \,. \tag{2.39}$$

However, this disadvantage can be tolerated since the switching frequency with 70 kHz is very high.

2.3 DC/DC Converter

The DC/DC converter is needed to integrate energy storage systems (Specification (S4)) and renewable energy sources (Specification (S5)) that provide DC voltage, such as photovoltaic (PV) systems. A photo of the hardware is shown in Fig. 2.16. Besides the basic power electronics unit, consisting of the power and control board, a filter board and a DC/DC board are required. On the filter board are the three LC filters placed. The inductors are loose in the picture, as they are screwed onto the housing during assembly. On the DC/DC board, the device-specific voltage measurement and the PV switch are located. The PV switch is required to meet the standards for PV systems.

The basic power electronics unit is used here, as shown in Fig. 2.17. The star-point of the filter is connected to the lower DC link potential DC−. This topology is a so-called bidirectional synchronous buck converter [90, Sec. 5.1.11]. Each of the three phases can be used independently,

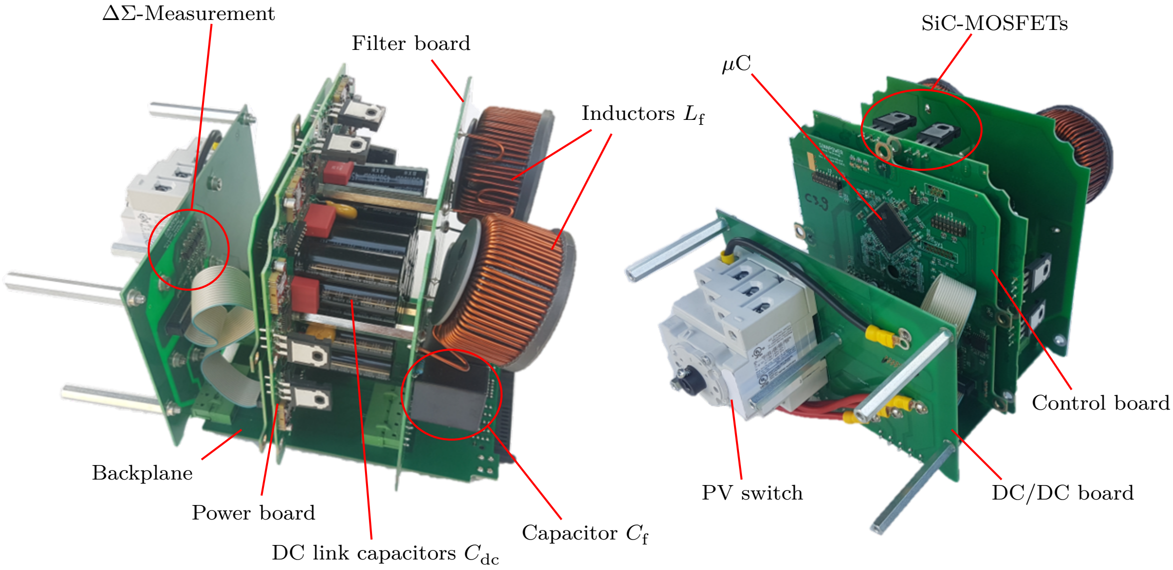

Figure 2.16: Photo of the DC/DC converter without the housing.

for example, each for one PV string, where more PV modules are connected in series. For the connection to a storage, the three phases are connected to get a multiphase buck converter and, thus, increase the output current. Therefore, each phase needs a separate current control loop.

At first, the model in state-space representation of the topology is introduced. It is followed by the design of a voltage and a current controller in Sec. 2.3.2 and 2.3.3, respectively. It is shown that this DC/DC converter can only be operated in current-mode. In Sec. 2.3.4, the implemented controller with a robust and fast converging maximum power point tracker (MPPT) is tested with a PV system under typical conditions. This also shows that Specification (S5) is fulfilled for the most frequently used renewable energy source.

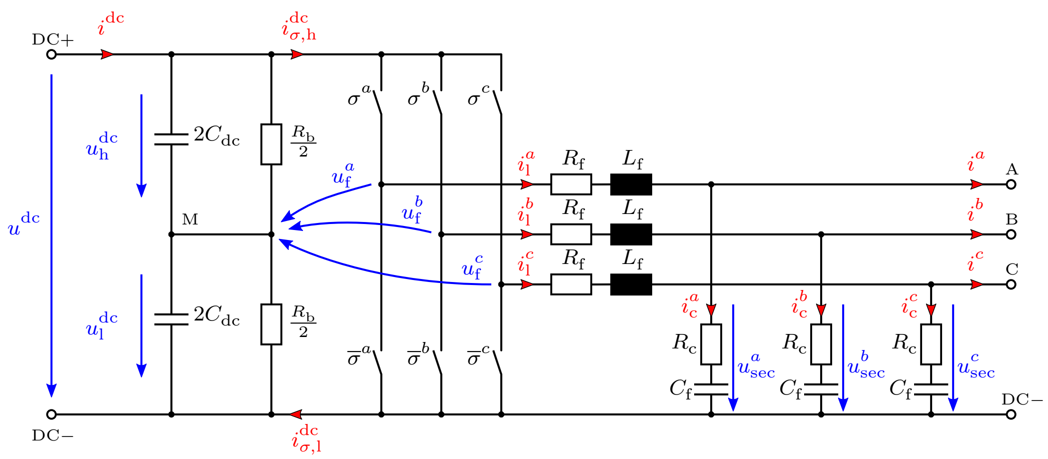

Figure 2.17: The electrical circuit of the three-phase bidirectional synchronous buck converter.

2.3.1 Modelling

Since the three phases are identical and independent, the modelling is done for only one phase and the superscripts a, b and c for the three phases are omitted. This bidirectional synchronous buck converter topology requires that the secondary side voltage u_{sec} is always lower than the DC link voltage u^{dc}, meaning the condition

$$u^{\mathrm{dc}} > u_{\mathrm{sec}} \tag{2.40}$$

must be fulfilled during normal operations. If this is not the case, the body diode of the upper MOSFET becomes conductive and an uncontrolled current flows into the DC link. However, this can be useful to perform a black start if the current of the connected energy source is limited, like for PV systems.
An advantage of the synchronous buck converter is that the inductor current i_{l} can also become negative. In a classical buck converter, the lower MOSFET is not present, and a diode is used instead, resulting in the fact that the inductor current can only be positive, as (2.40) must hold for a controlled operation. In case of low load, a classical buck converter enters the discontinuous conduction mode (DCM), where the inductor current becomes zero during the switching cycle. If this is not the case, the converter operates in continuous conduction mode (CCM). The implemented synchronous buck converter here always works in CCM [90, Sec. 1.5.2].

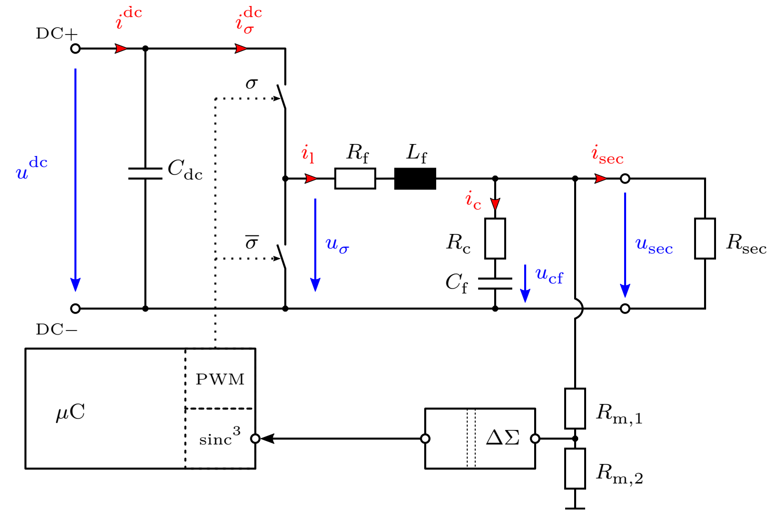

Figure 2.18: The electrical circuit of one phase of the bidirectional synchronous buck converter with the illustration of the voltage measurement and a connected load resistance R_{sec}.

The midpoint M of the split DC link capacitance remains floating. In Section 2.1.2 it is shown that the assumption

$$u_{\mathrm{h}}^{\mathrm{dc}} = u_{\mathrm{l}}^{\mathrm{dc}} = \frac{u^{\mathrm{dc}}}{2} \tag{2.41}$$

can be made, and the DC link capacitance can be combined to one single capacitance C_{dc}, and the balancing resistors are neglected. The topology of the DC/DC converter is shown in Fig. 2.18. Its dynamics are governed by the differential equations

$$\left.\begin{aligned} \frac{\mathrm{d}}{\mathrm{d}t} i_{\mathrm{l}} &= \frac{1}{L_{\mathrm{f}}} \left(\sigma\, u^{\mathrm{dc}} - (R_{\mathrm{f}} + R_{\mathrm{c}})\, i_{\mathrm{l}} - u_{\mathrm{cf}} + R_{\mathrm{c}}\, i_{\mathrm{sec}} \right) \\ \frac{\mathrm{d}}{\mathrm{d}t} u_{\mathrm{cf}} &= \frac{1}{C_{\mathrm{f}}} \left(i_{\mathrm{l}} - i_{\mathrm{sec}} \right) , \end{aligned}\right\} \tag{2.42}$$

where i_l is the current through the filter inductance L_f, and u_cf denotes the voltage across the filter capacitance C_f. Since the inductor current i_l or the secondary side voltage u_sec should be controlled, it is reasonable to define them as output. The output voltage depends highly on the output current i_sec. In order to derive an expression for the secondary voltage u_sec, a load resistance R_sec is added, yielding

$$i_\mathrm{sec} = \frac{u_\mathrm{sec}}{R_\mathrm{sec}} = \frac{1}{R_\mathrm{c} + R_\mathrm{sec}} \left(u_\mathrm{cf} + R_\mathrm{c}\, i_\mathrm{l}\right) . \tag{2.43}$$

This assumption is nearly always valid, especially for a small-signal analysis around a specified operation point. This allows to derive the state-space representation given by

$$\left.\begin{aligned}
\frac{\mathrm{d}}{\mathrm{d}t} \underbrace{\begin{pmatrix} i_\mathrm{l} \\ u_\mathrm{cf} \end{pmatrix}}_{=:\,\boldsymbol{x}_\mathrm{dd}} &= \underbrace{\begin{bmatrix} -\dfrac{R_\mathrm{f}\, R_\mathrm{c} + R_\mathrm{f}\, R_\mathrm{sec} + R_\mathrm{c}\, R_\mathrm{sec}}{L_\mathrm{f}\,(R_\mathrm{c} + R_\mathrm{sec})} & -\dfrac{R_\mathrm{sec}}{L_\mathrm{f}\,(R_\mathrm{c} + R_\mathrm{sec})} \\ \dfrac{R_\mathrm{sec}}{C_\mathrm{f}\,(R_\mathrm{c} + R_\mathrm{sec})} & -\dfrac{1}{C_\mathrm{f}\,(R_\mathrm{c} + R_\mathrm{sec})} \end{bmatrix}}_{=:\,\boldsymbol{A}_\mathrm{dd}} \begin{pmatrix} i_\mathrm{l} \\ u_\mathrm{cf} \end{pmatrix} + \underbrace{\begin{pmatrix} \dfrac{\sigma}{L_\mathrm{f}} \\ 0 \end{pmatrix}}_{=:\,\boldsymbol{B}_\mathrm{dd}} u^\mathrm{dc} \\
\underbrace{\begin{pmatrix} i_\mathrm{l} \\ u_\mathrm{sec} \end{pmatrix}}_{=:\,\boldsymbol{y}_\mathrm{dd}} &= \underbrace{\begin{bmatrix} 1 & 0 \\ \dfrac{R_\mathrm{c}\, R_\mathrm{sec}}{R_\mathrm{c} + R_\mathrm{sec}} & \dfrac{R_\mathrm{sec}}{R_\mathrm{c} + R_\mathrm{sec}} \end{bmatrix}}_{=:\,\boldsymbol{C}_\mathrm{dd}} \begin{pmatrix} i_\mathrm{l} \\ u_\mathrm{cf} \end{pmatrix} ,
\end{aligned}\right\} \tag{2.44}$$

where, $\boldsymbol{x}_\mathrm{dd} \in \mathbb{R}^2$ is the state vector, $\boldsymbol{A}_\mathrm{dd} \in \mathbb{R}^{2\times2}$ the state matrix, $\boldsymbol{B}_\mathrm{dd} \in \mathbb{R}^{2\times1}$ the input matrix and $\boldsymbol{C}_\mathrm{dd} \in \mathbb{R}^{2\times2}$ the output matrix. The index dd denotes quantities of the DC/DC converter.

As the switching state σ appears in the equations, this model is a discontinuous representation of the system, which does not allow to make classical stability analysis like Bode or Nyquist plots and the design of a suitable controller. A common way to handle this is to derive an averaged model where no switching states occur. The averaged model is a continuous representation and a mathematical abstraction and simplification of the system. This model enables stability analysis and speeds up simulations for long transient effects. The drawback is that detailed evaluations, such as switching losses, can no longer be made. There are several methods for model averaging [90, Sec. 2.7]. The state-space averaging method allows to derive the continuous model directly from the state-space representation, where the average of the state matrices is taken [90, Sec. 2.1], [91].

Here, only the input matrix $\boldsymbol{B}_\mathrm{dd}$ includes the switching state. The average is taken over one switching period T_sw, which results in

$$\overline{\boldsymbol{B}}^{\star}_\mathrm{dd} = \frac{1}{T_\mathrm{sw}} \int_0^{T_\mathrm{sw}} \boldsymbol{B}_\mathrm{dd}\, \mathrm{d}t = d_\mathrm{ref}\, \boldsymbol{B}_\mathrm{dd,on} + (1 - d_\mathrm{ref})\, \boldsymbol{B}_\mathrm{dd,off} = d_\mathrm{ref}\, \boldsymbol{B}_\mathrm{dd,on} , \tag{2.45}$$

where d_ref is the duty cycle and

$$\boldsymbol{B}_\mathrm{dd,on} = \begin{pmatrix} \dfrac{1}{L_\mathrm{f}} \\ 0 \end{pmatrix} \quad \text{and} \quad \boldsymbol{B}_\mathrm{dd,off} = \begin{pmatrix} 0 \\ 0 \end{pmatrix} \tag{2.46}$$

are the input vectors in case the upper switch is on ($\sigma = 1$) or off ($\sigma = 0$), respectively. The duty cycle is defined as the ratio of the on-time of the upper switch to the switching period, as introduced in Sec. 2.2. The duty cycle results from the controller output $u_{\sigma,\mathrm{ref}}$. The modulation is responsible for matching the reference voltage on average during one switching period, as defined in (2.10). Assuming that the voltage u_σ can be applied continuously, the model can alternatively be derived very quickly by considering $u_\sigma = d_{\mathrm{ref}}\, u^{\mathrm{dc}}$ as the input variable. The averaged input matrix $\overline{\boldsymbol{B}}_{\mathrm{dd}}$ is then given by

$$\overline{\boldsymbol{B}}_{\mathrm{dd}} = \begin{pmatrix} \frac{1}{L_\mathrm{f}} \\ 0 \end{pmatrix} . \tag{2.47}$$

Notice that this is not necessarily the case in general. For example, DC/DC converter with only one switch and one diode may have more than two discrete states, where the applied voltage no longer depends on the switching state. In this case, a different averaging method needs to be used.

The transfer function can be derived from the state-space representation with (see Appendix A.4)

$$\frac{\boldsymbol{y}_{\mathrm{dd}}(s)}{\boldsymbol{u}_{\mathrm{dd}}(s)} = \boldsymbol{C}_{\mathrm{dd}}\, (s\boldsymbol{I}_2 - \boldsymbol{A}_{\mathrm{dd}})\, \overline{\boldsymbol{B}}_{\mathrm{dd}} \,, \tag{2.48}$$

yielding

$$\frac{\boldsymbol{y}_{\mathrm{dd}}(s)}{u_\sigma(s)} = \begin{pmatrix} G_{\mathrm{dd,u}}(s) \\ G_{\mathrm{dd,i}}(s) \end{pmatrix} = \begin{pmatrix} \dfrac{1 + s\, R_\mathrm{c} C_\mathrm{f}}{1 + \frac{R_\mathrm{f}}{R_{\mathrm{sec}}} + s\left[R_\mathrm{c} C_\mathrm{f} + R_\mathrm{f} C_\mathrm{f}\left(1 + \frac{R_\mathrm{c}}{R_{\mathrm{sec}}}\right) + \frac{L_\mathrm{f}}{R_{\mathrm{sec}}}\right] + s^2\left[L_\mathrm{f} C_\mathrm{f}\left(1 + \frac{R_\mathrm{c}}{R_{\mathrm{sec}}}\right)\right]} \\[2ex] \dfrac{\frac{1}{R_{\mathrm{sec}}} + s\, C_\mathrm{f}\left(1 + \frac{R_\mathrm{c}}{R_{\mathrm{sec}}}\right)}{1 + \frac{R_\mathrm{f}}{R_{\mathrm{sec}}} + s\left[R_\mathrm{c} C_\mathrm{f} + R_\mathrm{f} C_\mathrm{f}\left(1 + \frac{R_\mathrm{c}}{R_{\mathrm{sec}}}\right) + \frac{L_\mathrm{f}}{R_{\mathrm{sec}}}\right] + s^2\left[L_\mathrm{f} C_\mathrm{f}\left(1 + \frac{R_\mathrm{c}}{R_{\mathrm{sec}}}\right)\right]} \end{pmatrix} . \tag{2.49}$$

2.3.2 Voltage Control

If a constant output voltage of a DC/DC converter is required, the converter can be operated in the so-called voltage-mode. This mode is the most common method of controlling a power supply because it is easy to implement and requires no current measurement. Typically, only the output voltage is used as feedback. However, stabilising such a system is more complicated. Voltage-mode can also be used to integrate PV systems. Since a PV cell behaves like a current source [92], a constant output voltage can be applied to operate the system at its maximum power point. Therefore, voltage-mode will be briefly discussed here.

The frequency response of the transfer function $G_{\mathrm{dd,u}}(s)$ from (2.49) with three different values for the load resistance R_{sec} is shown in Fig. 2.19. Due to the double pole of the LC filter with the resonant frequency

$$f_{\mathrm{lc}} = \frac{1}{2\pi\, \sqrt{L_\mathrm{f}\, C_\mathrm{f}}} \approx 2.56 \text{ kHz} \,, \tag{2.50}$$

the phase of the power stage can reach -180°, which is typical for voltage-mode buck converters in CCM. According to the Nyquist stability criterion, a control loop is stable if the magnitude of the open-loop transfer function

$$F_{\mathrm{o,u}}(s) = G_{\mathrm{r,u}}(s)\, G_{\mathrm{dd,u}}(s) \tag{2.51}$$

is below 0 dB when the phase intersects a critical phase of -180° [93, Sec. 6.3.4], [94, Sec. 3.13]. Note that the phase can cross this critical phase several times since it starts again at 0° after a complete turn.

The implemented controller should be designed to maintain a minimum phase margin to make

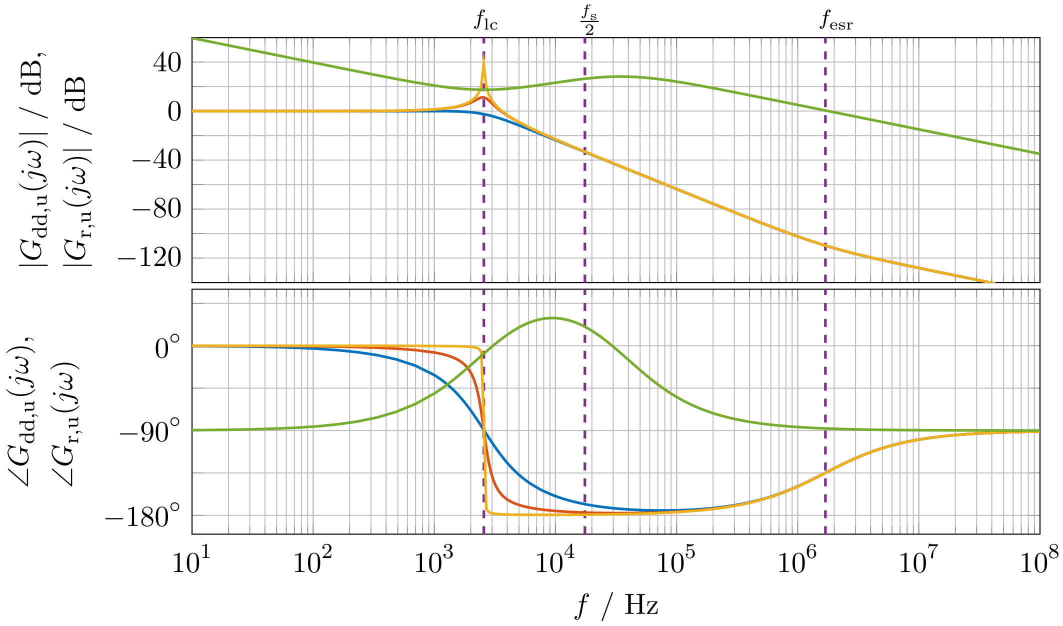

Figure 2.19: Frequency responses of the controller $G_{\mathrm{r,u}}(s)$ [—] and the transfer function $G_{\mathrm{dd,u}}(s)$ from (2.49) with $R_{\mathrm{sec}} = 10\ \Omega$ [—], $R_{\mathrm{sec}} = 50\ \Omega$ [—] and $R_{\mathrm{sec}} \to \infty\ \Omega$ [—]. The discussed frequencies are written on top corresponding to the dashed lines.

a control loop robust against parameter variations and reduce the overshoot after a transient response. The phase margin is the distance between the actual phase of the open-loop transfer function to -180° at the crossover frequency f_{x}, where the magnitude crosses 0 dB. For a good design, the phase margin should be between 30° and 60°, whereby 30° should be the absolute minimum [90, Sec. 3.3], [95, Sec. 8.5.5]. For digital control systems, a phase margin of about 75° should be aimed for.

A suggested controller for power electronics, where the phase of the power stage can reach -180°, is the so-called type 3 controller with the transfer function [90, Sec. 3.5.8]

$$G_{\mathrm{r,u}}(s) = \frac{\omega_{\mathrm{p,0}}}{s} \frac{\left(1 + \frac{s}{\omega_{\mathrm{z,1}}}\right)\left(1 + \frac{s}{\omega_{\mathrm{z,2}}}\right)}{\left(1 + \frac{s}{\omega_{\mathrm{p,1}}}\right)\left(1 + \frac{s}{\omega_{\mathrm{p,2}}}\right)}. \tag{2.52}$$

This controller can be compared to a real PID controller with an additional first-order low-pass filter. It has an integral term $\frac{\omega_{\mathrm{p,0}}}{s}$ with a pole at the origin to achieve zero steady-state error. The proportional gain, corresponding to the angular frequency $\omega_{\mathrm{p,0}} = 2\pi\, f_{\mathrm{p,0}}$, which defines the intersection with the 0 dB line for a pure integrator.

Since the integral term induces a 90° phase lag, two zeros are necessary to boost the phase back above the critical -180°. Hence, the two zeros $\omega_{\mathrm{z,1}}$ and $\omega_{\mathrm{z,2}}$ are placed around the resonance frequency f_{lc}. The placement of the two poles $\omega_{\mathrm{p,1}}$ and $\omega_{\mathrm{p,2}}$ depends on the zero of the plant, caused by the capacitor's ESR R_{c}, which is at the frequency

$$f_{\mathrm{esr}} = \frac{1}{2\pi\, R_{\mathrm{c}}\, C_{\mathrm{f}}} \approx 1.69\ \mathrm{MHz}. \tag{2.53}$$

If this frequency is within the control bandwidth, for example, near the resonance frequency, it needs to be compensated for with one pole of the controller to prevent the magnitude of the open-loop from flattening. A steep magnitude at higher frequencies is necessary to guarantee

stability if the phase crosses -180° and to attenuate high-frequency disturbances to a large degree. The second pole is placed at one-half of the sampling frequency f_s. If the frequency f_esr is higher than $\frac{f_\mathrm{s}}{2}$, as is the case here, both poles are placed there.
Finally, the proportional gain $\omega_{\mathrm{p},0}$ determines the crossover frequency f_x of the open-loop $F_{\mathrm{o,u}}(s)$. This determines the dynamics or bandwidth of the controller. The greater the crossover frequency can be selected, the faster the controller is and the faster it compensates for load steps. It should be at least five times higher than the resonance frequency f_lc to dampen the second-order filter effect. Otherwise, oscillations would appear during a transient response [90, Sec. 3.6.4]. Typically, one-twentieth of the sampling frequency in the case of digital design can be a target.

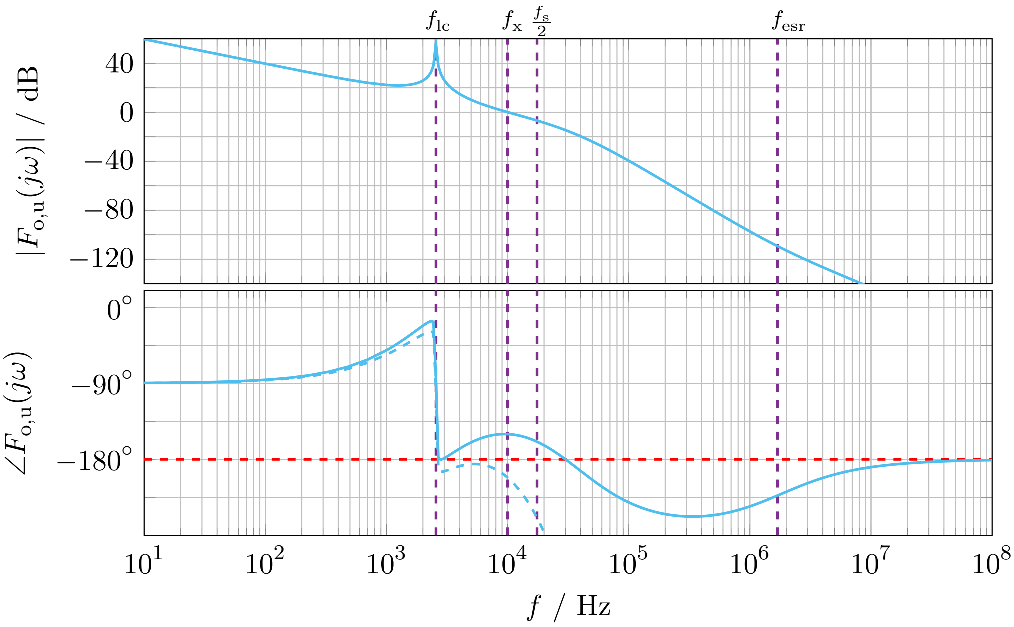

Figure 2.20: Frequency responses of the resulting open-loop $F_{\mathrm{o,u}}(s)$, with no load resistance R_sec [——]. The influence of the delay on the phase is shown by the dashed line [- - -]. The discussed frequencies are written on top corresponding to the dashed lines.

The frequency response of the proposed controller $G_{\mathrm{r,u}}(s)$ is also shown in Fig. 2.19. In Fig. 2.20, the resulting open-loop frequency response of $F_{\mathrm{o,u}}(s)$ is shown, where the worst case from $G_{\mathrm{dd,u}}(s)$ with no load resistance ($R_\mathrm{sec} \rightarrow \infty\ \Omega$) is used. The crossover frequency f_x is set to the smallest recommended value, which is five times the resonance frequency f_lc. There, the phase margin has a local maxima as desired. However, for digital control, the crossover frequency should be at least ten times lower than the sampling frequency f_s [90, Sec. 3.4], which is not given here. This necessity becomes clear when the phase lag

$$\angle e^{-s\,\tau_\mathrm{avg}} = -2\pi\, f\, \tau_\mathrm{avg} \tag{2.54}$$

is added, which is caused by digitalisation, see (2.22). The delay is caused by the reference voltage that must be applied by the VSI and by sampling the analogue signals and their discrete processing. The consequence is shown by the dashed turquoise line in Fig. 2.20. Since the phase lag is proportional to the frequency, it causes the phase to fall below the critical phase before the crossover frequency, clearly stating that this control loop is unstable.
One option would be to set the crossover frequency so low that the resonance frequency is already sufficiently damped, but that would slow down the system's dynamics so drastically that it is not practical. This problem can also not be solved by adding another zero to the

controller. Even though the switching frequency is chosen relatively high, it is still too low for this application. Typical power supplies in voltage-mode work with higher switching frequencies of several hundred kHz to achieve the desired dynamics. Another option would be to increase the output capacitance and reduce the resonance frequency. However, the crossover frequency is limited by the sampling frequency and the resulting delay, which is why it cannot be chosen much larger even with this measure.

The Nyquist stability analysis is a very practical stability criterion where a delay can be directly considered, which is why it was used here. Due to this delay and the design parameters, the plant is already unstable, and it is impossible or impractical to operate this DC/DC converter in voltage-mode. Usually, a constant voltage is required for PV systems. The following sections show how the operation with a PV system can still be achieved without voltage-mode.

2.3.3 Current Control

The previous section showed that voltage control is not possible with classical control theory for this configuration. This section introduces the current controller for the DC/DC converter, where a cascaded voltage control loop can be implemented, which is sufficient for this application.

A common approach to control the current of a DC/DC converter, especially for power supply applications, is to implement a peak current controller. This approach is not limited to the topology of the buck converter, and it works for almost any other DC/DC topology. In peak current control, the current through the inductance is measured and compared with a reference value. When the switch is closed, the current increases depending on the applied voltage and the inductance value. If the current exceeds the reference value, the switch is opened, and a complementary switch is closed if available. The switch is turned on again at regular intervals, which defines the switching period.

The comparison is usually made with a hardware comparator, making the switching fast and straightforward and enables very high switching frequencies. Moreover, extreme current overshoots are prevented as well. A drawback is that with duty cycles greater than 50 %, subharmonic oscillations occur, which can cause noise and induce output ripple. Injecting a so-called slope compensation eliminates this oscillation. This compensation signal increases over one switching period. When switching occurs, the ramp is reset. It is either added to the measured current signal or subtracted from the reference signal. Usually, the slope compensation is also realised in hardware since a software implementation is too slow for high switching frequencies. [90, Sec. 2.3]

Since it is impossible to integrate this slope compensation into the existing hardware, a classic proportional-integral (PI) controller is to be designed and implemented. The frequency response of the transfer function $G_{\mathrm{dd,i}}(s)$ from (2.49) with three different values for the load resistance R_{sec} is shown in Fig. 2.21. The double pole of the LC filter with the resonant frequency f_{lc} (see (2.50)) introduces a phase lag of -180°. However, since the zero also depends on the load resistance R_{sec}, unlike the voltage transfer function, the zero has a lower frequency and gives a phase boost of 90°. Thus, the power stage does not reach -180°, for which a PI controller is very suitable. The integral action of the controller is required to achieve zero steady-state error.

To design the PI controller, the secondary voltage u_{sec} is considered a disturbance. This allows the capacitance to be omitted so that only the inductance needs to be considered. Furthermore, it has the advantage that the controller will remain stable regardless of the connected load. This assumption is very reasonable if the DC/DC converter is connected to a battery or supercapacitors, as these stabilise the voltage. Therefore, it can be assumed to be constant in the range of several switching periods. Moreover, a voltage feedforward is used to support the controller.

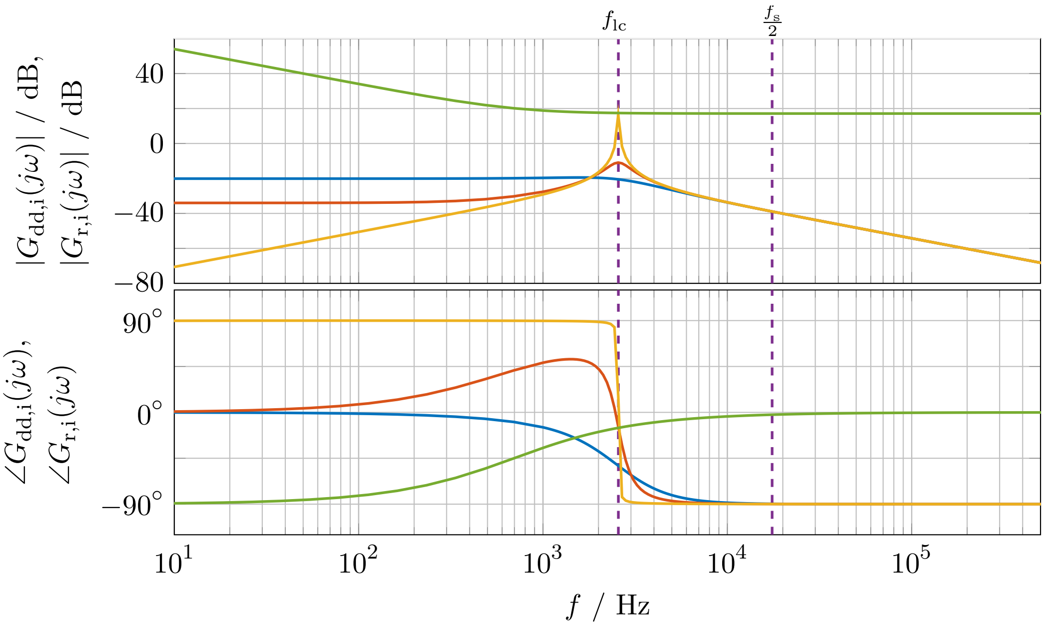

Figure 2.21: Frequency responses of the controller $G_{r,u}(s)$ [—] and the transfer function $G_{dd,i}(s)$ from (2.49) with $R_{sec} = 10\ \Omega$ [—], $R_{sec} = 50\ \Omega$ [—] and $R_{sec} \to \infty\ \Omega$ [—]. The discussed frequencies are written on top corresponding to the dashed lines.

According to this assumption, the transfer function can be simplified to

$$G^{\star}_{dd,i}(s) = \frac{i_l(s)}{u_{\sigma,ref}(s)} = \frac{\frac{1}{R_f}}{(1 + s\,\tau_{avg})\,(1 + s\,\tau_f)}\,, \tag{2.55}$$

where τ_{avg} is the time constant of the modulation, as defined in (2.22). The time constant of the filter is defined by

$$\tau_f = \frac{L_f}{R_f}\,. \tag{2.56}$$

The PI current controller is defined by the transfer function

$$G_{r,i}(s) = \frac{u_{\sigma,ref}(s)}{i_{l,ref}(s) - i_l(s)} = V_r\,\frac{1 + s\,\tau_r}{s\,\tau_r} = k_p + k_i\,\frac{1}{s}\,. \tag{2.57}$$

It is tuned according to the symmetrical optimum (SO) to achieve a maximum phase margin and a good disturbance rejection [84, Sec. 7], which yields

$$V_r = k_p = \frac{L_f}{2\,\tau_{avg}} \quad \text{and} \quad \tau_r = \frac{V_r}{k_i} = 4\,\tau_{avg}\,. \tag{2.58}$$

Even without the necessity of good disturbance rejection, tuning the controller according to the SO results in better performance because τ_f is much greater than τ_{avg}. It is recommended to use the SO if $\tau_f \geq 4\,\tau_{avg}$. In this case, the time constant τ_f of the filter is at least one hundred times greater than the time constant τ_{avg} due to the high switching frequency.

To implement the PI controller with anti-windup, the controller must be discretised. The PI controller is implemented in a parallel structure. There, the proportional gain remains the same, and only the integral part of the controller needs to be discretised. Here, the integrator is implemented by means of the rectangular rule, which yields the discrete PI controller

$$\left.\begin{aligned} e_\mathrm{l}[k] &= i_\mathrm{l,ref}[k] - i_\mathrm{l}[k] \\ u_{\sigma,\mathrm{p}}[k] &= k_\mathrm{p,d}\, e_\mathrm{l}[k] \\ u_{\sigma,\mathrm{i}}[k] &= u_{\sigma,\mathrm{i}}[k-1] + f_\mathrm{aw}\left(0, u_{\sigma,\mathrm{ref}}[k-1], u^\mathrm{dc}\right) k_\mathrm{i,d}\, e_\mathrm{l}[k] \\ u_{\sigma,\mathrm{ref}}[k] &= u_{\sigma,\mathrm{p}}[k] + u_{\sigma,\mathrm{i}}[k] + u_{\sigma,\mathrm{ff}}[k]\,, \end{aligned}\right\} \tag{2.59}$$

where $x[k] := x(kT_\mathrm{s})$ denotes the quantities at the discrete instants of time with the sampling period T_s and $k \in \mathbb{N}$. The feedforward voltage $u_{\sigma,\mathrm{ff}}$ is set to the filtered voltage u_sec and added to the controller output. The anti-windup function is defined by [84, Sec. 10.4.1], [96]

$$f_\mathrm{aw}(u_\mathrm{min}, u, u_\mathrm{max}) = \begin{cases} 1 & , u_\mathrm{min} \leq u_{\sigma,\mathrm{ref}} \leq u_\mathrm{max} \\ 0 & , \text{otherwise}\,. \end{cases} \tag{2.60}$$

The discrete controller parameter are given by

$$\left.\begin{aligned} k_\mathrm{p,d} &= k_\mathrm{p} = V_\mathrm{r} = \frac{L_\mathrm{f}}{2\,\tau_\mathrm{avg}} \\ k_\mathrm{i,d} &= k_\mathrm{i}\, T_\mathrm{s} = \frac{V_\mathrm{r}}{\tau_\mathrm{r}}\, T_\mathrm{s} = \frac{L_\mathrm{f}\, T_\mathrm{s}}{8\,\tau_\mathrm{avg}^2}\,. \end{aligned}\right\} \tag{2.61}$$

Fig. 2.22 shows the block diagram of the control loop with the discrete PI controller including anti-windup and voltage feedforward.

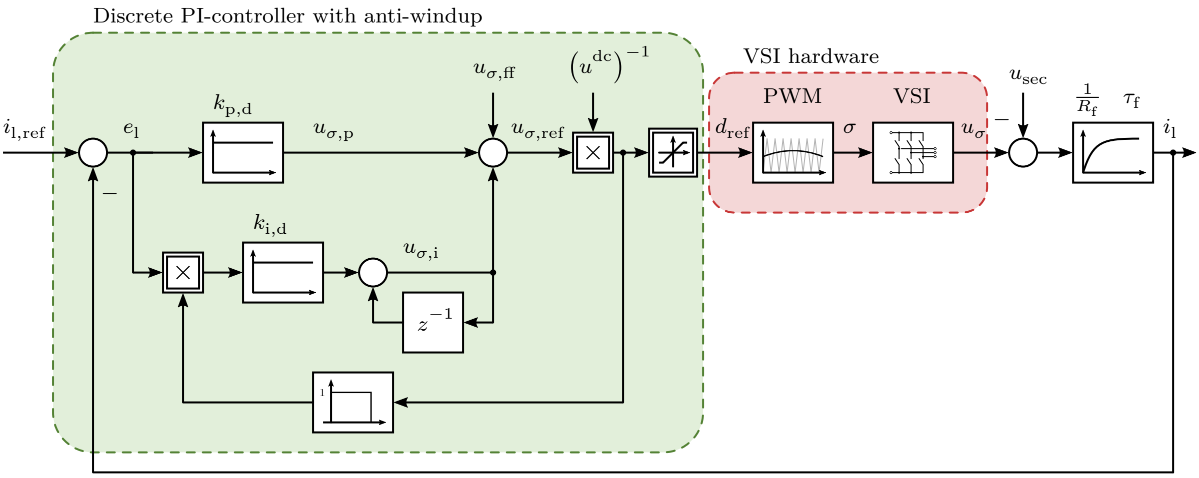

Figure 2.22: Block diagram of the implemented discrete current controller for one phase.

Since the time constant τ_avg is still uncertain, this value must be determined. For this purpose, an experiment was carried out in which the output of the DC/DC converter was connected to another half-bridge. By setting the duty cycle of the other half-bridge with open-loop control, the voltage u_sec at the output of the DC/DC converter can be changed, simulating a disturbance. In Fig. 2.23, the results of the experiment with $\tau_\mathrm{avg} = \frac{3}{2}\,T_\mathrm{s}$ and $\tau_\mathrm{avg} = 2\,T_\mathrm{s}$ are shown. The top subplot shows the secondary voltage, and the lower subplot shows the current. First, a voltage of 400 V was set and a current step response at about 0.5 ms to a final value of −5 A was

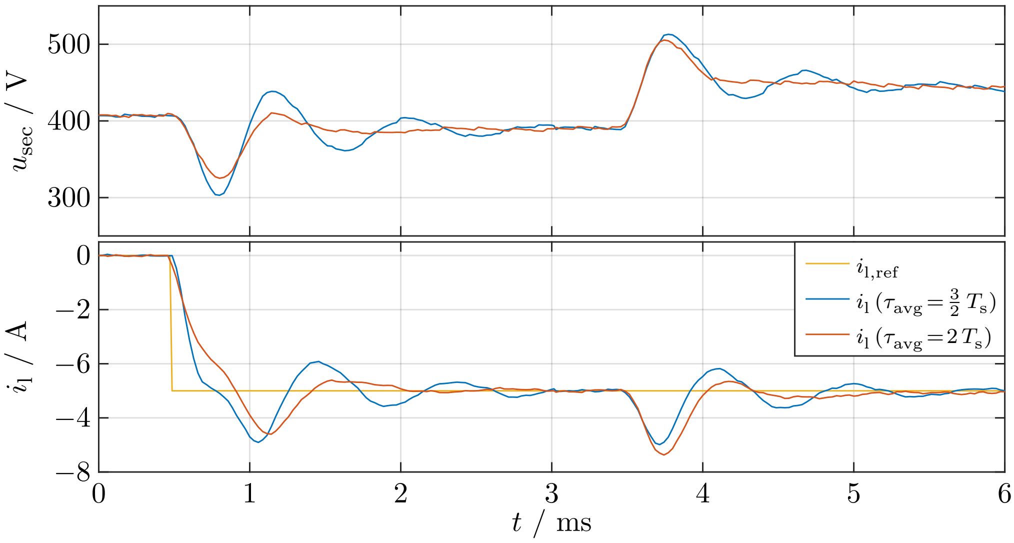

Figure 2.23: Measured result of the step response with $\tau_{\text{avg}} = \frac{3}{2}\,T_s$ [—] and $\tau_{\text{avg}} = 2\,T_s$ [—].

generated. Since the voltage u_{sec} is open-loop controlled and not adjusted by a control loop, it changes strongly with the current. Both configurations show stable behaviour, and the current reaches the final value. However, the controller with $\tau_{\text{avg}} = \frac{3}{2}\,T_s$ is showing some oscillations. At about 3.5 ms, a disturbance was generated by setting the voltage to about 450 V. Here, too, the oscillations can be seen. With $\tau_{\text{avg}} = 2\,T_s$, there are no oscillations, which is why this value was finally chosen.

In Fig. 2.24, the resulting open-loop frequency response of $F_{\text{o,i}}(s)$ is shown for stability analysis, where the same three values for the load resistance R_{sec} are applied as before. For any value of R_{sec}, the system is stable. As in the previous section, the phase lag of digitalisation must be added to prove stability. The phase lag is added to the phase of the continuous system, which results in the dashed lines in Fig. 2.24. The current controller remains stable even when the phase shift is added, which caused the voltage-mode control to become unstable. In all three cases, the phase crosses the critical value of -180° at about half the switching frequency f_{sw}. The magnitude is below -20 dB at this frequency, which is a sufficient gain margin. The phase margin in the worst case is approximately 62°, which indicates a robust controller design since the phase lag is already accounted for.

2.3.4 Maximum Power Point Tracking for Photovoltaic Systems

Photovoltaic energy is an essential component of the energy transition (see Fig. 1.4). PV systems can be integrated into other infrastructures without additional land consumption, e.g. on residential buildings, in so-called agrivoltaics as a combination with agriculture, floating on lakes, or in transport infrastructures. The average solar irradiation in Germany is about 1115 kWh/m^2 per year [97]. A well-placed PV system can reach a performance ratio of approximately 80 to 90 %. It is defined by the ratio of generated electric energy to the solar irradiation within one year [20, 98]. The performance ratio must not be confused with the efficiency of a PV module. The efficiency considers the power that the module delivers under standard test conditions with an irradiation of 1000 W/m^2 and a module temperature of 25 °C. Currently, PV modules achieve an efficiency of about 20 to 25 % [99].

Photovoltaic cells can directly convert sunlight into electricity and are, therefore, unique. Other

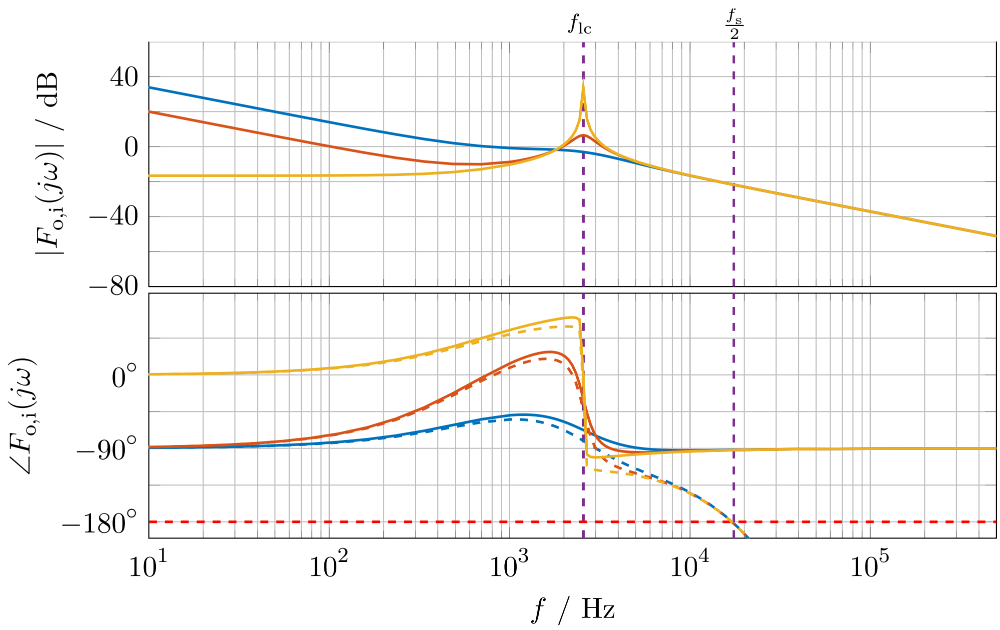

Figure 2.24: Frequency responses of the resulting open-loop transfer function $F_{\mathrm{o,i}}(s)$, with $R_{\mathrm{sec}} = 10\ \Omega$ [—], $R_{\mathrm{sec}} = 50\ \Omega$ [—] and $R_{\mathrm{sec}} \to \infty\ \Omega$ [—]. The influence of the delay on the phase is shown by the dashed line. The discussed frequencies are written on top corresponding to the dashed lines.

energy sources and conventional power plants, such as coal or nuclear power plants, require an intermediate mechanical step, whereby heat generated by combustion produces steam that drives a steam turbine. The turbine is connected to a generator to convert the mechanical power into electrical power. Wind turbines generate a rotating motion, which also drives a generator. PV systems have no mechanical moving parts and therefore do not generate noise, which makes them predestined for residential areas.

A PV cell is basically a silicon diode whose p–n junction is exposed to light [92]. When photons hit the surface of the PV cell, charge carriers are released from the semiconductor. A metal grid on top collects the electric charge and provides them to the terminal of the PV cell. The physical effect behind this was first explained by no other than Albert Einstein in [100], for which he was receiving the Nobel Prize and not for the theory of relativity, as many think [101].

A PV array can be modelled with a current source, a diode parallel to it and equivalent resistances, as shown in Figure 2.25. The output current i_{pv} of the PV array can be described

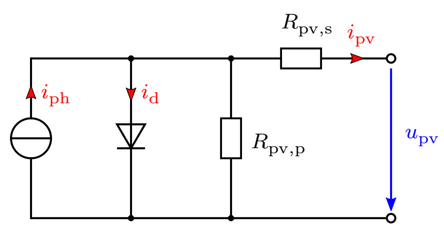

Figure 2.25: Equivalent circuit of a PV array.

by

$$i_{\mathrm{pv}} = i_{\mathrm{ph}} - \underbrace{i_{\mathrm{s}} \left(e^{\dfrac{q\,(u_{\mathrm{pv}} + R_{\mathrm{pv,s}}\, i_{\mathrm{pv}})}{N_{\mathrm{pv}}\, n_{\mathrm{d}}\, k_{\mathrm{b}}\, \vartheta}} - 1 \right)}_{=i_{\mathrm{d}}} - \frac{u_{\mathrm{pv}} + R_{\mathrm{pv,s}}\, i_{\mathrm{pv}}}{R_{\mathrm{pv,p}}}\,, \tag{2.62}$$

where i_{ph} is the cell's photocurrent, which is directly proportional to the solar radiation [92]. The current i_{d} through the diode is described by the Shockley diode equation, where i_{s} is the saturation current, q is the elementary charge, k_{b} is Boltzmann constant, ϑ is the temperature in Kelvin, n_{d} is the diode ideality factor and N_{pv} is the number of in series connected PV cells. The resistances $R_{\mathrm{pv,s}}$ and $R_{\mathrm{pv,p}}$ are the equivalent series and parallel resistances, respectively. Figure 2.26 shows exemplary current-voltage (I-V) and power-voltage (P-V) characteristics of a PV array with two different solar radiations. Manufacturers typically specify their PV panels with the open circuit voltage $u_{\mathrm{pv,oc}}$, the short circuit current $i_{\mathrm{pv,sc}}$, and the maximum power point (MPP) with u_{mpp} and i_{mpp}. There are some methods to approximate the parameters from equation (2.62) with the information from the datasheet [92], [102, Sec. 3.2.2].

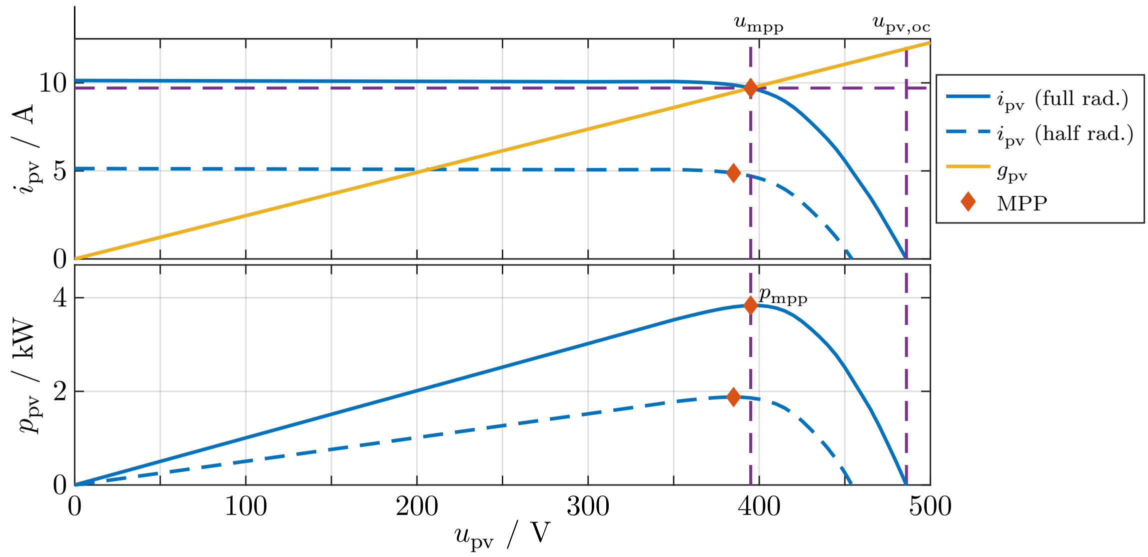

Figure 2.26: Exemplary current-voltage (I-V) in the upper and power-voltage (P-V) characteristics in the lower subplot of a PV array, each with full [—] and half [- - -] radiation and the respective MPPs [♦]. The resistive load characteristics of the proposed controller is shown by the yellow line [—]. The MPP voltage u_{mpp} and the open circuit voltage $u_{\mathrm{pv,oc}}$ are written on top corresponding to the dashed lines [- - -].

The PV power

$$p_{\mathrm{pv}} = u_{\mathrm{pv}}\, i_{\mathrm{pv}} \tag{2.63}$$

depends on many parameters. The temperature affects mostly the diode current i_{d} and is, therefore, the major cause that changes the voltage of the PV array. The lower the temperature, the higher the voltage and, consequently, the higher the power at the same irradiation. Since the photovoltaic current is proportional to solar radiation, it is very sensitive to changes in atmospheric conditions, like moving clouds, which can rapidly change the PV power. In contrast to this, the temperature change is rather slow. Due to the changing atmospheric conditions, continuous adjustment or tracking is necessary to extract the maximum power available.

For this purpose, several different algorithms have been developed. The perturb and observe (P&O) and incremental conductance (INC) are most widely used [103]. The P&O algorithm perturbs the actual operation point at specified intervals by changing the applied voltage. If the power increases compared to the previous operation point, the next perturbation goes in the same direction. Otherwise, the direction changes. The INC algorithm uses the approximated derivative $\frac{\mathrm{d}i_{\mathrm{pv}}}{\mathrm{d}u_{\mathrm{pv}}}$, which corresponds to the conductivity, and changes the reference value proportionally to it, which leads to a faster convergence [104]. P&O is chosen mainly due to its ease of implementation. The downside of the algorithm is that the perturbation in every cycle result in oscillations around the MPP. To reduce this oscillation, the perturbation step can be decreased if a subsequent change of direction is detected. However, this can slow down the algorithm, which can lead to power loss [104]. Nevertheless, the P&O is chosen here due to its simplicity and robustness. It will be shown that the convergence is also very fast, accompanied by low oscillations, if the algorithm is tuned correctly.

The conditions at its terminals need to be permanently adjusted to extract the maximum power from the PV array. A DC/DC converter connected to it can control either the current or the voltage to achieve the MPP. Fig 2.26 shows that the PV current is almost constant at voltages below the MPP, where a stable operation point can hardly be maintained with a current-controlled DC/DC converter. The MPP tracker (MPPT) can keep the operation point away from this flat region, but since solar radiation can change rapidly, this cannot be prevented. Thus, it is preferable to choose the voltage as the control variable [105].

As shown in Sec. 2.3.2, voltage control does not work for this DC/DC converter. Hence, another solution must be found. Generally, the stability of a DC/DC converter in voltage-mode in combination with a PV system must be investigated. A small-signal analysis of the PV system yields a dynamic and nonlinear source impedance, which eventually affects the stability of the converter. Therefore, precise tuning of the controller is required, which depends on the characteristics of the PV array and atmospheric conditions, like shading [106, 107].

A resistive control is introduced to overcome this system-specific tuning. Therefore, the inner control loop of the DC/DC converter is a current controller, as described in Section 2.3.3, and the reference current is derived from the output voltage. From the perspective of the PV module, this means that it is connected to an resistive load. The PV voltage is multiplied by a proportional gain, which represents a conductivity and defines the slope of the resistive load. Thus, the intersection with the I-V curve of the PV array is not as acute-angled as with a pure current controller. The resistive load is shown by the yellow line in Fig 2.26. The resistive controller yields a stable control system, and there is always just one defined intersection point, even with rapid changes in solar radiation or partial shading.

The controller and the MPP algorithm were tested with a PV array with twelve modules on the office roof, shown in Fig. 2.27. The PV string is connected to a phase of the DC/DC converter. The other two phases of the DC/DC converter are disabled. A bidirectional DC source is connected to the DC link to keep the DC link voltage u^{dc} constant at 800 V. The electricity generated is thereby fed into the grid.

The control variable of the MPPT is the conductivity g_{pv} of the outer voltage controller, meaning the proportional gain of the resistive control. After the perturbation, the new operation state needs to settle down before it can be decided if the output power is higher or lower than the previous one. The computed power needs to be filtered to reduce the influence of measurement noise. During the tests, it was found that the voltage measurement is very sensitive, and a 50 Hz noise signal, imposed by the grid voltage, with an amplitude of about 2 to 3 V overlays the PV voltage. Therefore, the cutoff frequency of the filter needs to be less than half of the grid frequency to remove its influence. This filter setting yields the period of the MPPT algorithm with $5\,\tau$ (see Appendix A.6).

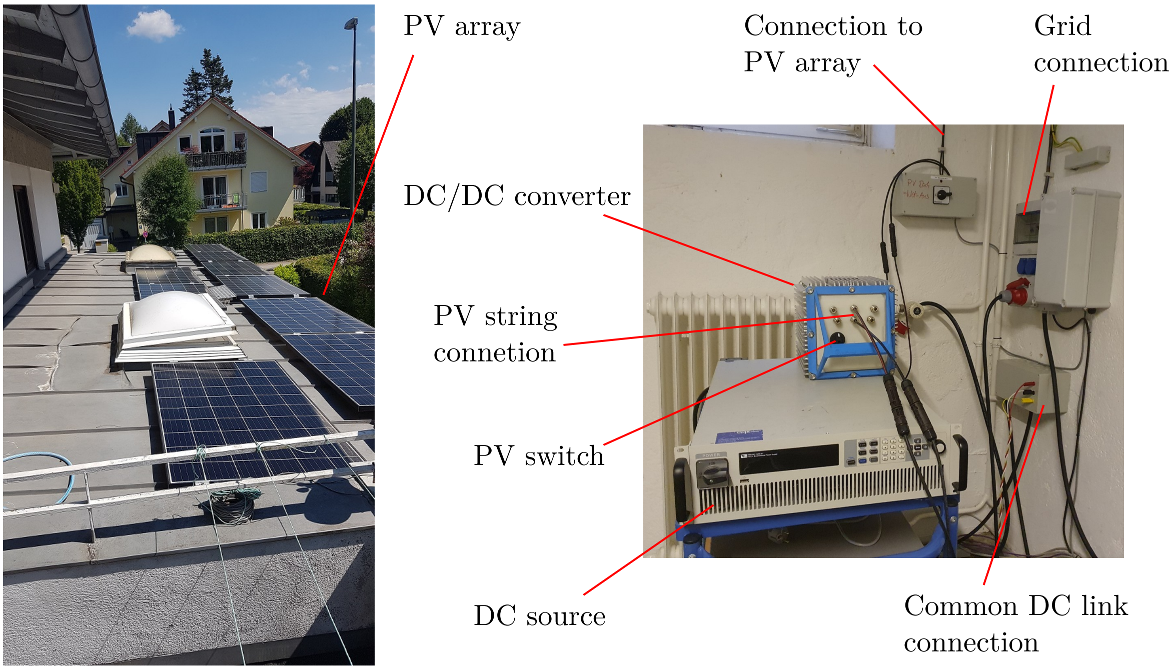

Figure 2.27: PV Test array with twelve modules on the roof of the office.

To reduce the oscillations around the MPP, the perturbation step is halved if a subsequent change of direction is detected. If more steps in the same direction are made, the step size is doubled to achieve a faster conversion. This compensates for the slowdown of the algorithm due to the smaller steps at the beginning. Fig. 2.28 shows the transient of the MPPT after the DC/DC converter is started. The blue lines show the P&O algorithm with constant step size, whereas the red lines show the result when the step size changes. In the first subplot, the conductivity g_{pv} is shown. Both methods converge at about the same time. In the beginning, the optimised P&O starts much slower, but due to the exponential growth, it overtakes the conventional one. In the second subplot, where the PV power p_{pv} is shown, it reveals that the MPP is even reached a bit faster. The third subplot shows the PV voltage u_{pv} where the 50 Hz noise signal from the grid voltage is evident. This noise would prevent the algorithm from converging if it is not filtered. Moreover, in the end, where the MPP is reached, the difference in the oscillations becomes apparent. Because of scaling, they do not show up so clearly in the power subplot. The voltage of the P&O algorithm with constant step size keeps oscillating around the MPP, whereas the optimised algorithm shows no more oscillations.

For this experiment, the algorithm starts with a PV current $i_{\mathrm{pv}} = 0$ A to demonstrate their difference. To speed up the algorithm and, thus, increase its efficiency, the initial point for the voltage can be set to about 80 % of the open circuit voltage, where the MPP is usually close by [106]. Therefore, the initial value of the optimised algorithm with variable step size is also chosen to be small since the MPP is reached quickly after DC/DC converter is started. If the initial step size were set to its maximum value for this experiment, the optimised algorithm would be significantly faster in comparison. This makes the advantage of the reduced oscillation even more valuable.

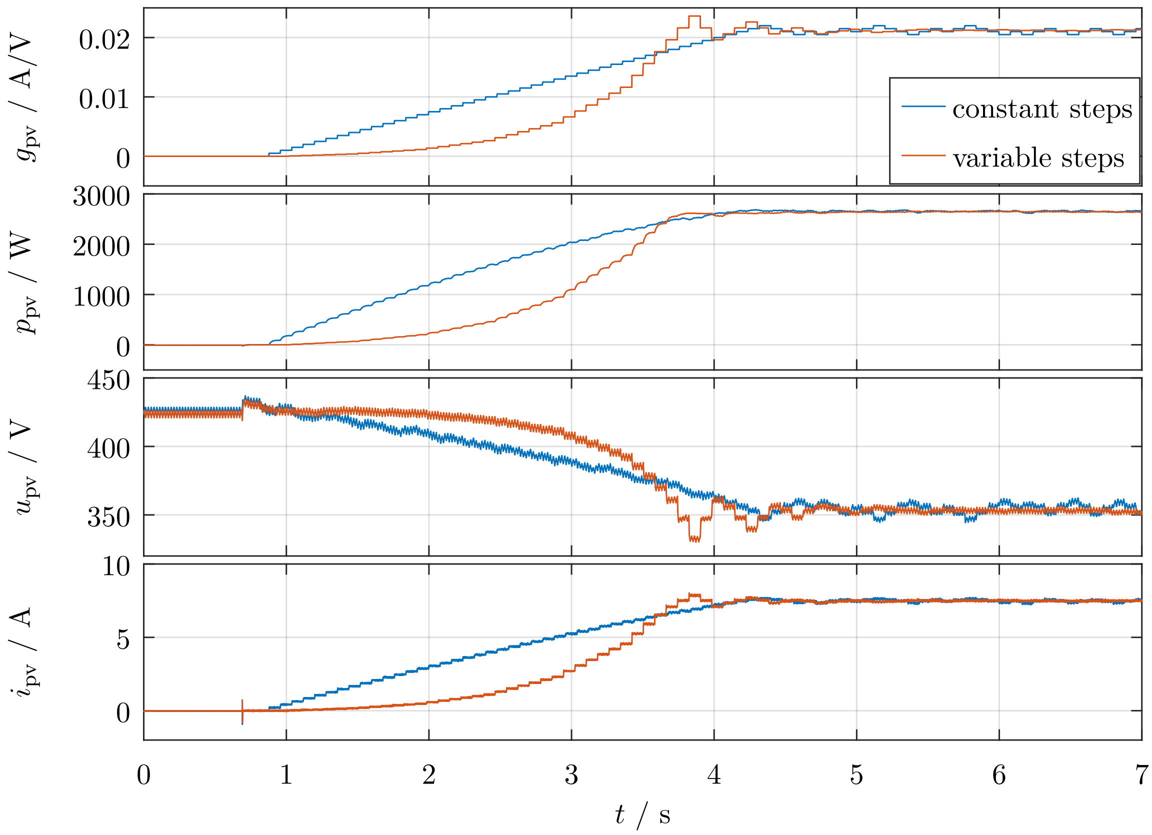

Figure 2.28: Transient response of the P&O algorithm with constant [—] and variable [—] step size after the DC/DC converter is started.

2.4 Generator Unit

The generator unit consists of a motor drive and an electrical machine (E-machine). With this unit, rotating energy sources can be integrated into the DC grid, enhancing Specification (S5). Its main applications are the wave energy converter and small wind turbines. Fig. 2.29 shows a photo of the motor drive and the designed permanent magnet synchronous machine (PMSM), which is also integrated into the same aluminium extruded profile. The power electronics is the basic three-phase voltage source inverter (VSI). It can be mechanically connected with the electrical machine to form the generator unit, as shown on the right side of the photo. It is also possible to mechanically connect several machines in series to increase the torque and, thus, the power on the shaft. At the end of the string, as many motor drives as electrical machines are mounted, each connected to one electrical machine. This offers maximum flexibility and modularity and thus contributes to fulfilling the Specification (S7).

In Sec. 2.4.1, a generic model of a synchronous machine is presented. Based on this model, a field-oriented control (FOC) is designed to control the stator currents and, thus, the machine's torque. According to Specification (S6), this enables a bidirectional drive system, which is necessary for optimum control of the WEC employing reactive power control. As stated in Sec. 1.2.3, a significant improvement can be achieved with every increase in the efficiency of the generator unit, even in the upper-efficiency range. For this reason, Specification (S8) is defined. It is achieved with a newly proposed measurement method to experimentally identify the current vector for an optimal feedforward torque control to maximise the efficiency of the generator unit. This is presented in the last section.

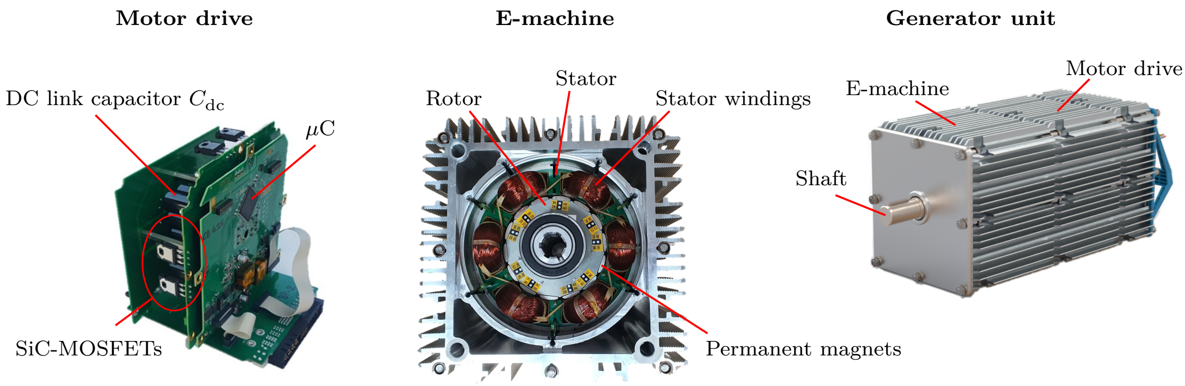

Figure 2.29: Photo of the motor drive, the electrical machine, and the generator unit.

2.4.1 Model of the Permanent Magnet Synchronous Machine

Figure 2.30 shows an illustration of the cross-section of a PMSM. For simplicity, the illustrated machine has only one pole pair and three stator windings a, b and c. This assumption does not restrict the validity of the model. The three stator windings are connected in star and spatially shifted by 120° to each other. By applying the space vector theory, described in Sec. 2.2.2, the stator-fixed (a,b,c)-reference frame can be transformed into the stator-fixed and orthogonal (α,β)-reference frame, whereby the α-axis is aligned with the a-axis.

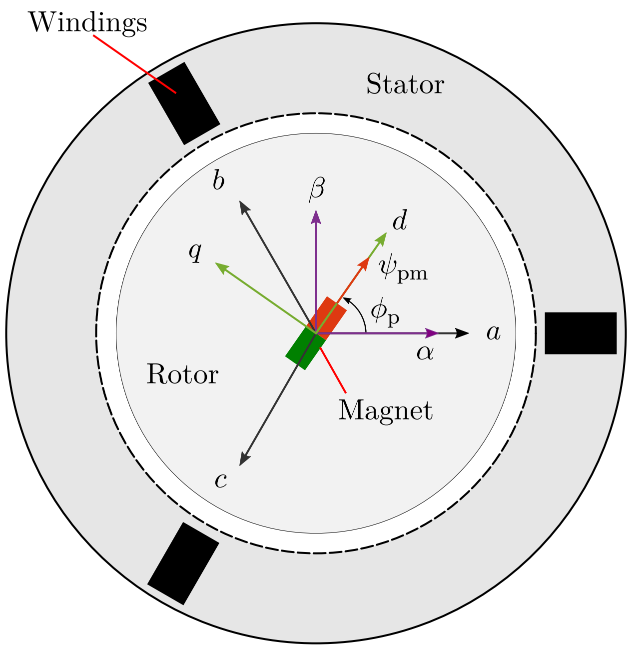

Figure 2.30: Illustration of the cross-section of a PMSM.

The stator-fixed (α,β)-reference frame is further transformed into the rotor-fixed (d,q)-reference frame by using the Park transformation matrices (see also Appendix A.2)

$$\boldsymbol{T}_\mathrm{p}(\phi_\mathrm{p}) = \begin{bmatrix} \cos(\phi_\mathrm{p}) & -\sin(\phi_\mathrm{p}) & 0 \\ \sin(\phi_\mathrm{p}) & \cos(\phi_\mathrm{p}) & 0 \\ 0 & 0 & 1 \end{bmatrix} \quad \text{and} \quad \boldsymbol{T}_\mathrm{p}^{-1}(\phi_\mathrm{p}) = \begin{bmatrix} \cos(\phi_\mathrm{p}) & \sin(\phi_\mathrm{p}) & 0 \\ -\sin(\phi_\mathrm{p}) & \cos(\phi_\mathrm{p}) & 0 \\ 0 & 0 & 1 \end{bmatrix}. \tag{2.64}$$

The d-axis is aligned with the permanent magnet flux linkage $\boldsymbol{\psi}_{\mathrm{pm}}^{dq} := (\psi_{\mathrm{pm}}^{d}, \psi_{\mathrm{pm}}^{q})^{\top}$ with the angle ϕ_{p} between the α-axis and the d-axis.

Since the windings are connected in star, the sum of all currents is zero, meaning

$$i_{\mathrm{s}}^{a} + i_{\mathrm{s}}^{b} + i_{\mathrm{s}}^{c} \stackrel{!}{=} 0 \text{ A} . \tag{2.65}$$

Hence, no γ-current flows into the machine. Therefore, all the γ-components can be neglected. The stator voltages $\boldsymbol{u}_{\mathrm{s}}^{dq} := (u_{\mathrm{s}}^{d}, u_{\mathrm{s}}^{q})^{\top}$ of a PMSM in the synchronously rotating orthogonal (d,q)-reference frame are given as [80, Sec. 6.9.2], [84, Sec. 14.3.2], [27]

$$\boldsymbol{u}_{\mathrm{s}}^{dq} = R_{\mathrm{s}}\, \boldsymbol{i}_{\mathrm{s}}^{dq} + \omega_{\mathrm{p}}\, \boldsymbol{J}\, \boldsymbol{\psi}_{\mathrm{s}}^{dq}\left(\boldsymbol{i}_{\mathrm{s,m}}^{dq}\right) + \frac{\mathrm{d}}{\mathrm{d}t}\, \boldsymbol{\psi}_{\mathrm{s}}^{dq}\left(\boldsymbol{i}_{\mathrm{s,m}}^{dq}\right) , \tag{2.66}$$

where R_{s} is the stator resistance, $\boldsymbol{i}_{\mathrm{s}}^{dq} := (i_{\mathrm{s}}^{d}, i_{\mathrm{s}}^{q})^{\top}$ are the stator currents and $\boldsymbol{\psi}_{\mathrm{s}}^{dq} := (\psi_{\mathrm{s}}^{d}, \psi_{\mathrm{s}}^{q})^{\top}$ is the stator flux linkage. In general, the flux linkage $\boldsymbol{\psi}_{\mathrm{s}}^{dq}\left(\boldsymbol{i}_{\mathrm{s,m}}^{dq}\right)$ depends on the machine temperature ϑ_{m} and is a nonlinear function of the magnetisation currents $\boldsymbol{i}_{\mathrm{s,m}}^{dq} := (i_{\mathrm{s,m}}^{d}, i_{\mathrm{s,m}}^{q})^{\top}$ with [80, Sec. 6.9.2], [108, 109]

$$\boldsymbol{i}_{\mathrm{s,m}}^{dq} = \boldsymbol{i}_{\mathrm{s}}^{dq} - \boldsymbol{i}_{\mathrm{s,Fe}}^{dq} , \tag{2.67}$$

where $\boldsymbol{i}_{\mathrm{s,Fe}}^{dq} := (i_{\mathrm{s,Fe}}^{d}, i_{\mathrm{s,Fe}}^{q})^{\top}$ are the iron loss currents. To clarify the equations, those arguments are omitted ($\boldsymbol{\psi}_{\mathrm{s}}^{dq} := \boldsymbol{\psi}_{\mathrm{s}}^{dq}\left(\boldsymbol{i}_{\mathrm{s,m}}^{dq}, \vartheta_{\mathrm{m}}\right)$). The $(2{\times}2)$-matrix $\boldsymbol{J}$ results from the differentiation of the Park matrix with

$$\frac{\mathrm{d}}{\mathrm{d}t}\boldsymbol{T}_{\mathrm{p}}(\phi_{\mathrm{p}}) = \omega_{\mathrm{p}}\, \boldsymbol{J}_0\, \boldsymbol{T}_{\mathrm{p}}(\phi_{\mathrm{p}}) = \omega_{\mathrm{p}} \begin{bmatrix} 0 & -1 & 0 \\ 1 & 0 & 0 \\ 0 & 0 & 0 \end{bmatrix} \boldsymbol{T}_{\mathrm{p}}(\phi_{\mathrm{p}}) , \tag{2.68}$$

where only the upper left $(2{\times}2)$-submatrix is used in (2.66). The electrical angular frequency ω_{p} is the mechanical angular frequency ω_{m} of the rotor multiplied by the pole pairs number n_{p} with

$$\omega_{\mathrm{p}} = n_{\mathrm{p}}\, \omega_{\mathrm{m}} . \tag{2.69}$$

The resistance R_{s} accounts for the copper losses and is assumed to be symmetrical in all three phases. The iron losses are indirectly included in (2.66) by the reference to the magnetisation currents $\boldsymbol{i}_{\mathrm{s,m}}^{dq}$. Iron losses are caused by the changing electromagnetic flux in the stator and rotor, which induces a voltage. As the stator and rotor material is electrically conductive, the voltage causes a current flow leading to ohmic losses, called eddy current losses in this context. They are proportional to the square of the electrical angular frequency ω_{p}. To reduce these losses, the stator and rotor have laminations consisting of many metal sheets that are insulated to each other to reduce the eddy current. There are also hysteresis losses, but as they have the same physical origin, they can be included in the eddy current losses [108]. Although the iron losses are much lower than the copper losses, they need to be considered to find the optimal operation strategy [110].

Fig. 2.31 shows the electrical equivalent circuit of the PMSM, where the iron losses can be accounted for by the in parallel connected resistances $\boldsymbol{R}_{\mathrm{s,Fe}}^{dq} := (R_{\mathrm{s,Fe}}^{d}, R_{\mathrm{s,Fe}}^{q})^{\top}$ [80, Sec. 6.9.2], [108]. From this, the voltages over the iron resistances $\boldsymbol{R}_{\mathrm{s,Fe}}^{dq}$ can be conducted with

$$\boldsymbol{R}_{\mathrm{s,Fe}}^{dq}\, \boldsymbol{i}_{\mathrm{s,Fe}}^{dq} = \omega_{\mathrm{p}}\, \boldsymbol{J}\, \boldsymbol{\psi}_{\mathrm{s}}^{dq} + \frac{\mathrm{d}}{\mathrm{d}t}\boldsymbol{\psi}_{\mathrm{s}}^{dq} . \tag{2.70}$$

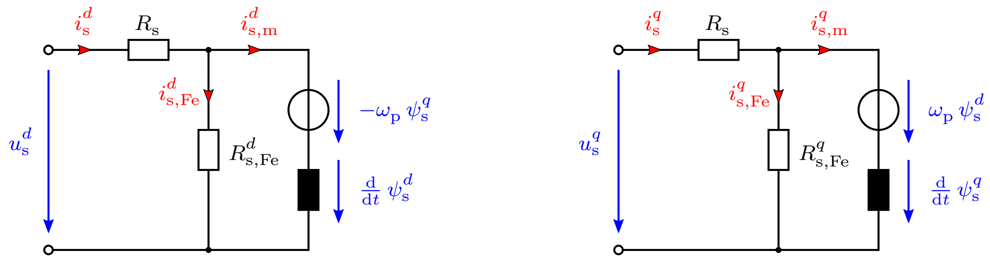

Figure 2.31: Electrical equivalent circuit of the PMSM.

The stator currents $\boldsymbol{i}_{\mathrm{s}}^{dq}$ split into the iron loss currents $\boldsymbol{i}_{\mathrm{s,Fe}}^{dq}$ through the iron resistances $\boldsymbol{R}_{\mathrm{s,Fe}}^{dq}$ and the magnetisation currents $\boldsymbol{i}_{\mathrm{s,m}}^{dq}$. The current component of the stator currents $\boldsymbol{i}_{\mathrm{s}}^{dq}$ that flows through the iron resistances $\boldsymbol{R}_{\mathrm{s,Fe}}^{dq}$, therefore, does not contribute to the generation of flux and torque. These currents are only virtual currents for the model and do not physically exist.

With an amplitude-correct Clarke transformation ($\kappa = \frac{2}{3}$), the electrical power is given by

$$
\begin{aligned}
p_{\mathrm{el}} &= \frac{3}{2}\,(\boldsymbol{u}_{\mathrm{s}}^{dq})^{\top}\,\boldsymbol{i}_{\mathrm{s}}^{dq} \\
&= \frac{3}{2}\left(R_{\mathrm{s}}\,\boldsymbol{i}_{\mathrm{s}}^{dq} + \omega_{\mathrm{p}}\,\boldsymbol{J}\,\boldsymbol{\psi}_{\mathrm{s}}^{dq} + \frac{\mathrm{d}}{\mathrm{d}t}\,\boldsymbol{\psi}_{\mathrm{s}}^{dq}\right)^{\top}\left(\boldsymbol{i}_{\mathrm{s,m}}^{dq} + \boldsymbol{i}_{\mathrm{s,Fe}}^{dq}\right) \\
&= \underbrace{\frac{3}{2}\,R_{\mathrm{s}}\,(\boldsymbol{i}_{\mathrm{s}}^{dq})^{\top}\boldsymbol{i}_{\mathrm{s}}^{dq}}_{=:p_{\mathrm{s,Cu}}} \\
&\quad + \underbrace{\frac{3}{2}\left(\omega_{\mathrm{p}}\,\boldsymbol{J}\,\boldsymbol{\psi}_{\mathrm{s}}^{dq} + \frac{\mathrm{d}}{\mathrm{d}t}\,\boldsymbol{\psi}_{\mathrm{s}}^{dq}\right)^{\top}\left(\boldsymbol{R}_{\mathrm{s,Fe}}^{dq}\right)^{-1}\left(\omega_{\mathrm{p}}\,\boldsymbol{J}\,\boldsymbol{\psi}_{\mathrm{s}}^{dq} + \frac{\mathrm{d}}{\mathrm{d}t}\,\boldsymbol{\psi}_{\mathrm{s}}^{dq}\right)}_{=:p_{\mathrm{s,Fe}}} \\
&\quad + \underbrace{\frac{3}{2}\left(\frac{\mathrm{d}}{\mathrm{d}t}\,\boldsymbol{\psi}_{\mathrm{s}}^{dq}\right)^{\top}\boldsymbol{i}_{\mathrm{s,m}}^{dq}}_{=:p_{\psi}} \quad + \quad \underbrace{\frac{3}{2}\left(\omega_{\mathrm{p}}\,\boldsymbol{J}\,\boldsymbol{\psi}_{\mathrm{s}}^{dq}\right)^{\top}\boldsymbol{i}_{\mathrm{s,m}}^{dq}}_{=:p_{\mathrm{m}}}
\end{aligned}
\tag{2.71}
$$

where $p_{\mathrm{s,Cu}}$ are the copper losses, $p_{\mathrm{s,Fe}}$ are the iron losses, p_{ψ} is magnetisation power and p_{m} is the mechanical power. From the mechanical power p_{m}, the (averaged) machine torque m_{m} can be derived with

$$
m_{\mathrm{m}} = \frac{p_{\mathrm{m}}}{\omega_{\mathrm{m}}} = \frac{3}{2}\,n_{\mathrm{p}}\left(\boldsymbol{i}_{\mathrm{s,m}}^{dq}\right)^{\top}\boldsymbol{J}\,\boldsymbol{\psi}_{\mathrm{s}}^{dq}\,. \tag{2.72}
$$

The difference between the machine torque m_{m} and the load torque m_{l}, scaled with the inverse moment of inertia Θ_{m}, gives the rotor acceleration $\frac{\mathrm{d}}{\mathrm{d}t}\,\omega_{\mathrm{m}}$. The nonlinear dynamics of the electrical machine can be summarised as

$$
\left.
\begin{aligned}
&\frac{\mathrm{d}}{\mathrm{d}t}\,\boldsymbol{\psi}_{\mathrm{s}}^{dq} = \boldsymbol{u}_{\mathrm{s}}^{dq} - R_{\mathrm{s}}\,\boldsymbol{i}_{\mathrm{s}}^{dq} - \omega_{\mathrm{p}}\,\boldsymbol{J}\,\boldsymbol{\psi}_{\mathrm{s}}^{dq} \\
&\frac{\mathrm{d}}{\mathrm{d}t}\,\omega_{\mathrm{m}} = \frac{1}{\Theta_{\mathrm{m}}}\left(\underbrace{\frac{3}{2}\,n_{\mathrm{p}}\left(\boldsymbol{i}_{\mathrm{s,m}}^{dq}\right)^{\top}\boldsymbol{J}\,\boldsymbol{\psi}_{\mathrm{s}}^{dq}}_{=m_{\mathrm{m}}} - m_{\mathrm{l}}\right) \\
&\frac{\mathrm{d}}{\mathrm{d}t}\,\phi_{\mathrm{p}} = \omega_{\mathrm{p}} = n_{\mathrm{p}}\,\omega_{\mathrm{m}}\,.
\end{aligned}
\right\}
\tag{2.73}
$$

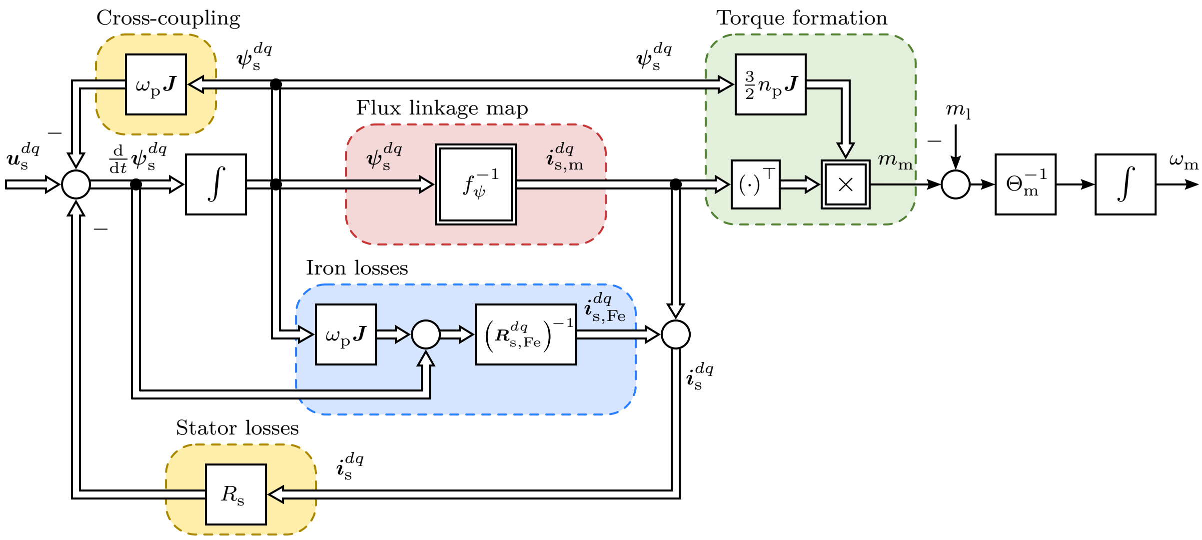

Figure 2.32: Signal flow diagram of the electrical machine.

The first equation in (2.73) describes the generation of the flux linkage, where the stator voltages $\boldsymbol{u}_{\mathrm{s}}^{dq}$ are applied externally by the VSI. The flux linkage $\boldsymbol{\psi}_{\mathrm{s}}^{dq}$ is a nonlinear function of the magnetisation currents $\boldsymbol{i}_{\mathrm{s,m}}^{dq}$ and can be defined as

$$\boldsymbol{\psi}_{\mathrm{s}}^{dq} = f_{\psi}\left(\boldsymbol{i}_{\mathrm{s,m}}^{dq}\right) . \tag{2.74}$$

This function is assumed to be a bijective assignment between the currents $\boldsymbol{i}_{\mathrm{s,m}}^{dq}$ and the flux linkage $\boldsymbol{\psi}_{\mathrm{s}}^{dq}$, which means that the function f_{ψ} can be inverted to obtain the currents with [67]

$$\boldsymbol{i}_{\mathrm{s,m}}^{dq} = f_{\psi}^{-1}\left(\boldsymbol{\psi}_{\mathrm{s}}^{dq}\right) . \tag{2.75}$$

Fig. 2.32 shows the signal flow diagram of the electrical machine. The function f_{ψ}^{-1} describes the essential characteristics of the electrical machine, like differential inductance, saturation, cross-coupling, or anisotropy. By adapting this function, the model can be used for different kinds of synchronous machines, even for reluctance synchronous machines (RSM), which do not have a permanent magnet.

2.4.2 Current Control

A current controller is required to control the stator currents $\boldsymbol{i}_{\mathrm{s}}^{dq}$ through the electrical machine and thus the torque at its shaft. The phase currents $\boldsymbol{i}_{\mathrm{s}}^{abc}$ are measured and fed to the controller, which calculates the required stator voltages $\boldsymbol{u}_{\mathrm{s,ref}}^{dq}$. This reference voltages are passed on to the modulation that drives the SiC-MOSFETs, according to the SVM (see Sec. 2.2.2).
The current dynamics must be derived to design a current controller for the electrical machine. For this purpose, the flux linkage is linearised around the operation point, which yields the well-known approximation [27, 111]

$$\boldsymbol{\psi}_{\mathrm{s}}^{dq} \approx \boldsymbol{L}_{\mathrm{s}}^{dq}\,\boldsymbol{i}_{\mathrm{s}}^{dq} + \boldsymbol{\psi}_{\mathrm{pm}}^{dq} = \begin{bmatrix} L_{\mathrm{s}}^{d} & L_{\mathrm{s,m}} \\ L_{\mathrm{s,m}} & L_{\mathrm{s}}^{q} \end{bmatrix} \boldsymbol{i}_{\mathrm{s}}^{dq} + \begin{pmatrix} \psi_{\mathrm{pm}} \\ 0 \end{pmatrix} , \tag{2.76}$$

where $\boldsymbol{L}_{\mathrm{s}}^{dq}$ are the differential stator inductances and $\boldsymbol{\psi}_{\mathrm{pm}}^{dq}$ is the permanent magnet flux linkage.

The inductances L_s^d and L_s^q are the differential inductances along the d- and q-axis, respectively. The coupling inductance $L_\mathrm{s,m}$ describes the cross-coupling between the two axes. Since it is very small compared to the differential inductances L_s^d and L_s^q, it is neglected for the controller design. Furthermore, the iron losses are also neglected, and it is assumed that the magnetisation currents $\boldsymbol{i}_\mathrm{s,m}^{dq}$ are equal to the stator currents $\boldsymbol{i}_\mathrm{s}^{dq}$ ($\boldsymbol{i}_\mathrm{s}^{dq} = \boldsymbol{i}_\mathrm{s,m}^{dq}$).
Inserting (2.76) into the first equation of (2.73) yields the current dynamics

$$\frac{\mathrm{d}}{\mathrm{d}t}\boldsymbol{i}_\mathrm{s}^{dq} = \left(\boldsymbol{L}_\mathrm{s}^{dq}\right)^{-1}\left(\boldsymbol{u}_\mathrm{s}^{dq} - R_\mathrm{s}\,\boldsymbol{i}_\mathrm{s}^{dq} \underbrace{-\omega_\mathrm{p}\,\boldsymbol{J}\left(\boldsymbol{L}_\mathrm{s}^{dq}\,\boldsymbol{i}_\mathrm{s}^{dq} + \boldsymbol{\psi}_\mathrm{pm}^{dq}\right)}_{=:\,\boldsymbol{u}_\mathrm{s,dist}^{dq}}\right)\,. \tag{2.77}$$

The disturbing voltages $\boldsymbol{u}_\mathrm{s,dist}^{dq}$ need to be compensated for by feedforward control, for which the voltages

$$\boldsymbol{u}_\mathrm{s,comp}^{dq} = -\boldsymbol{u}_\mathrm{s,dist}^{dq} = \begin{pmatrix} -\omega_\mathrm{p}\,L_\mathrm{s}^q\,i_\mathrm{s}^q \\ \omega_\mathrm{p}\,L_\mathrm{s}^d\,i_\mathrm{s}^d + \omega_\mathrm{p}\,\psi_\mathrm{pm} \end{pmatrix} \tag{2.78}$$

are added to the controller output voltages. This has the effect that the cross-coupling between the two currents is removed so that they can be controlled independently. This allows for the determination of the transfer functions

$$G_\mathrm{s}^{d/q}(s) = \frac{\frac{1}{R_\mathrm{s}}}{\left(1 + s\,\tau_\mathrm{s}^{d/q}\right)\left(1 + s\,\tau_\mathrm{avg}\right)}\,, \tag{2.79}$$

where τ_avg is the time constant of the modulation, as defined in (2.22). The time constants τ_s^d and τ_s^q of the stator are defined by

$$\tau_\mathrm{s}^{d/q} = \frac{L_\mathrm{s}^{d/q}}{R_\mathrm{s}}\,. \tag{2.80}$$

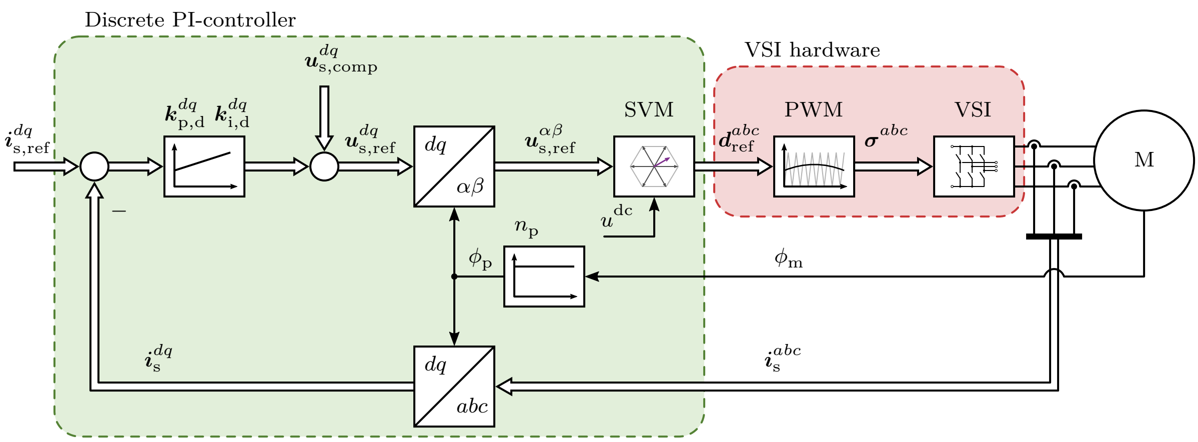

Figure 2.33: Block diagram of the current control loop for the electrical machine.

The control loop is shown in Fig. 2.33. The discrete PI controller with sampling time T_s and anti-windup is implemented as described in Sec. 2.3.3. The anti-windup is not explicitly shown for the sake of clarity. Like for the current controller of the DC/DC converter, the controller is tuned according to the symmetrical optimum (SO) because the large time constants $\tau_\mathrm{s}^{d/q}$ are much greater than τ_{avg} ($\tau_{\text{s}}^{d/q} \gg 4\,\tau_{\text{avg}}$). This leads to the control parameters

$$\left.\begin{aligned} \boldsymbol{k}_{\text{p,d}}^{dq} &= \frac{\left(L_{\text{s}}^{d}, L_{\text{s}}^{q}\right)}{2\,\tau_{\text{avg}}} \\ \boldsymbol{k}_{\text{i,d}}^{dq} &= \frac{\left(L_{\text{s}}^{d}, L_{\text{s}}^{q}\right)\,T_{\text{s}}}{8\,\tau_{\text{avg}}^{2}}\,. \end{aligned}\right\} \tag{2.81}$$

For strong nonlinear machines, adapting this controller parameter according to the currents can lead to more accurate tracking performance [112, 113].

Fig. 2.34 shows three step responses of the current i^{q}, where the controller is designed according to the magnitude optimum (MO; see [80, Sec. 1.3.1]), the symmetrical optimum (SO) and for an experimentally tuned controller. The controller designed according to MO does not reach the reference current as fast as the other controllers. Furthermore, the current shows more oscillations. The experimentally tuned controller is designed according to the SO, but the integral gain $\boldsymbol{k}_{\text{i,d}}^{dq}$ was halved, which reduced the overshoot compared to the SO controller design. Therefore, these controller settings are chosen. Moreover, a very fast response time, as demanded in Sec. 1.2.3, can be guaranteed, which leads to a more efficient WEC control.

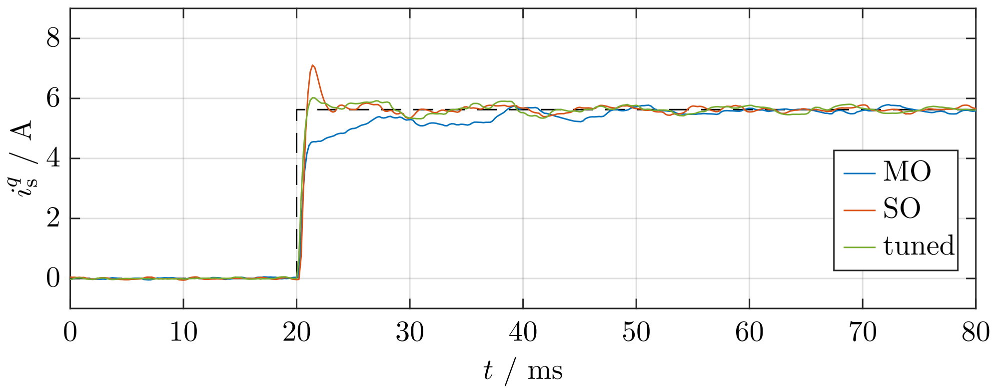

Figure 2.34: Step responses of the current controller designed according to MO [—], SO [—] and where the controller is experimentally tuned [—].

2.4.3 Optimal Feedforward Torque Control

This section is partially based on [1], where parts have already been published. The following measurements were made with the previous version of the generator unit, which has slightly different parameters. The main difference is that it contains a gearbox, and the electrical machine has an increased speed and less torque. Still, the power is about the same so that approximately the same conditions prevail at the shaft of the new generator unit. Moreover, the method is generally valid and can be applied to the newer version.

The torque of the electrical machine depends on both stator currents $\boldsymbol{i}_{\text{s}}^{dq}$. This gets clear by inserting the linearised flux linkage (2.76) into (2.72) and neglecting the cross-coupling inductance $L_{\mathrm{s,m}}$, which yields the linearised torque [80, Sec. 6.9.4], [27]

$$\begin{aligned} m_{\mathrm{m}} &\approx \frac{3}{2}\, n_{\mathrm{p}} \left(\boldsymbol{i}_{\mathrm{s,m}}^{dq}\right)^{\top} \boldsymbol{J} \left(\boldsymbol{L}_{\mathrm{s}}^{dq}\, \boldsymbol{i}_{\mathrm{s}}^{dq} + \boldsymbol{\psi}_{\mathrm{pm}}^{dq}\right) \\ &= \underbrace{\frac{3}{2}\, n_{\mathrm{p}}\, \psi_{\mathrm{pm}}\, i_{\mathrm{s}}^{q}}_{=:m_{\mathrm{el}}} \;+\; \underbrace{\frac{3}{2}\, n_{\mathrm{p}} \left(L_{\mathrm{s}}^{d} - L_{\mathrm{s}}^{q}\right) i_{\mathrm{s}}^{d}\, i_{\mathrm{s}}^{q}}_{=:m_{\mathrm{re}}} \,. \end{aligned} \tag{2.82}$$

The torque can be divided into electromagnetic torque m_{el} and reluctance torque m_{re}. The main torque results from the electromagnetic torque m_{el} with the q-component of the current vector. Since the d-axis of the rotating (d,q)-reference frame is aligned with the flux linkage of the permanent magnet, the current i_{s}^{q} is perpendicular to it and causes the Lorentz force. The reluctance torque only exists in anisotropic machines where the inductances are unequal ($L_{\mathrm{s}}^{d} \neq L_{\mathrm{s}}^{q}$). In general, a set of currents $\boldsymbol{i}_{\mathrm{s}}^{dq}$ can produce the same torque. The reluctance torque m_{re} can be incorporated to find an optimal current vector $\boldsymbol{i}_{\mathrm{s}}^{dq}$ for a given reference torque $m_{\mathrm{m,ref}}$ and thus maximise efficiency (Specification (S8)).

Depending on the operating point and limits, there are different optimisation targets. The strategies maximum-torque-per-current (MTPC) and maximum-torque-per-losses (MTPL) can be applied for normal operating points where no limits are reached. With MTPC, only the stator resistances are considered. MTPL is an extension of MTPC in which iron losses are also considered. The strategies maximum-current (MC), field-weakening (FW) and maximum-torque-per-voltage (MTPV) are used when reaching the current or voltage limits with [110]

$$\left\|\boldsymbol{i}_{\mathrm{s}}^{dq}\right\| = \sqrt{\left(i_{\mathrm{s}}^{d}\right)^{2} + \left(i_{\mathrm{s}}^{q}\right)^{2}} \leq i_{\max} \quad \text{and} \quad \left\|\boldsymbol{u}_{\mathrm{s}}^{dq}\right\| = \sqrt{\left(u_{\mathrm{s}}^{d}\right)^{2} + \left(u_{\mathrm{s}}^{q}\right)^{2}} \leq u_{\max} \,. \tag{2.83}$$

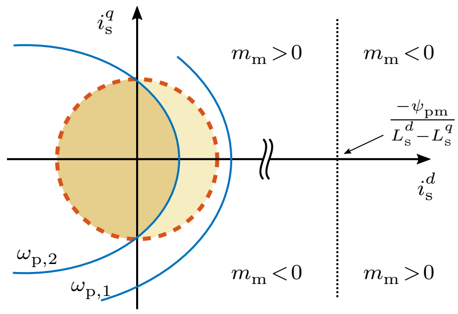

Figure 2.35: Illustration of the operation areas with the transient line [·····], the current limit [- - -] and the voltage limit [——] for two different speeds with $\omega_{\mathrm{p},1} < \omega_{\mathrm{p},2}$.

Fig. 2.35 illustrates the operation areas with the current and voltage limits for two different speeds. The voltage ellipse is derived by solving (2.77) for $\boldsymbol{u}_{\mathrm{s}}^{dq}$ and inserting it into the voltage limit in (2.83). Note that the maximum voltage $u_{\max}$ depends on the modulation technique (see Sec. 2.2) and should be smaller than the maximum feasible output voltage of the VSI to ensure dynamic adaptation of the controller.

In Fig. 2.35, the four quadrants with either positive or negative torque are also highlighted. They are divided by the transient lines

$$i_{\mathrm{s}}^{q} = 0 \text{ A} \quad \text{and} \quad i_{\mathrm{s}}^{d} = -\frac{\psi_{\mathrm{pm}}}{L_{\mathrm{s}}^{d} - L_{\mathrm{s}}^{q}} \,, \tag{2.84}$$

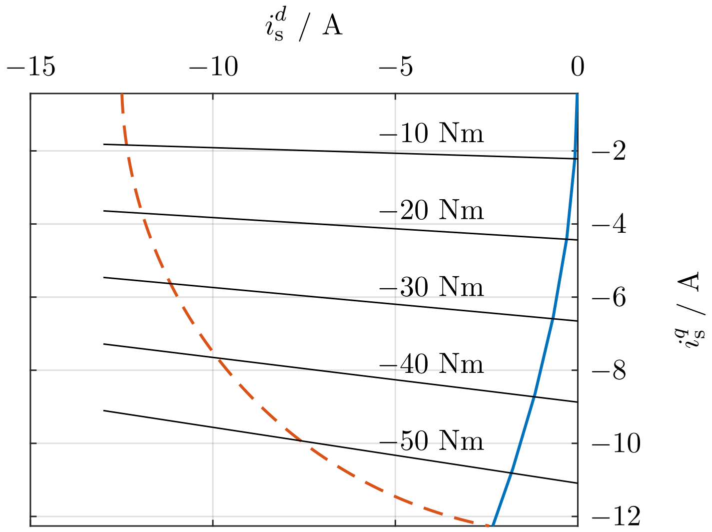

Figure 2.36: Illustration of the MTPC hyperbola [—], torque contour lines [—] and the current limit [- - -] with a linearised flux linkage.

which result from solving (2.82) with $m_\mathrm{m} = 0$ Nm. If the difference between the inductances L_s^d and L_s^q is small, this transient line is at a very high current, even beyond the current limit i_max. Since the entire system is designed to generate electricity from renewable energy sources and is well coordinated, the operating limits are only reached in a few exceptional cases, so the corresponding optimisations are not considered here. Only the application of MTPC and MTPL is discussed in the following.

Classical Maximum Torque per Current with Linearised Flux Linkages

The objective of MTPC is to find the current vector with minimum amplitude for a given reference torque $m_\mathrm{m,ref}$ to minimise the copper losses $p_\mathrm{s,Cu}$ in the stator windings [111]. Fig. 2.36 illustrates a resulting MTPC hyperbola with linearised flux linkages over the entire operating region, meaning $\boldsymbol{L}_\mathrm{s}^{dq}$ is assumed to be constant. The black lines are the contour lines, where the torque is constant for each line. They can be calculated with

$$i_\mathrm{s}^q = \frac{m_\mathrm{m,ref}}{\frac{3}{2} n_\mathrm{p} \left(\psi_\mathrm{pm} + \left(L_\mathrm{s}^d - L_\mathrm{s}^q \right) i_\mathrm{s}^d \right)}, \tag{2.85}$$

which is obtained by solving (2.82) for i_s^q. The points with the minimum current amplitude of each contour line result in the MTPC hyperbola.

Maximum Torque per Current with Nonlinear Flux Linkages

To increase the accuracy, the MTPC hyperbola can be obtained by inserting the nonlinear flux linkages into (2.72) and determining the current vector with minimal amplitude. The flux linkage can be measured in steady-state conditions. Solving (2.73) for the flux linkages $\boldsymbol{\psi}_\mathrm{s}^{dq}$ and

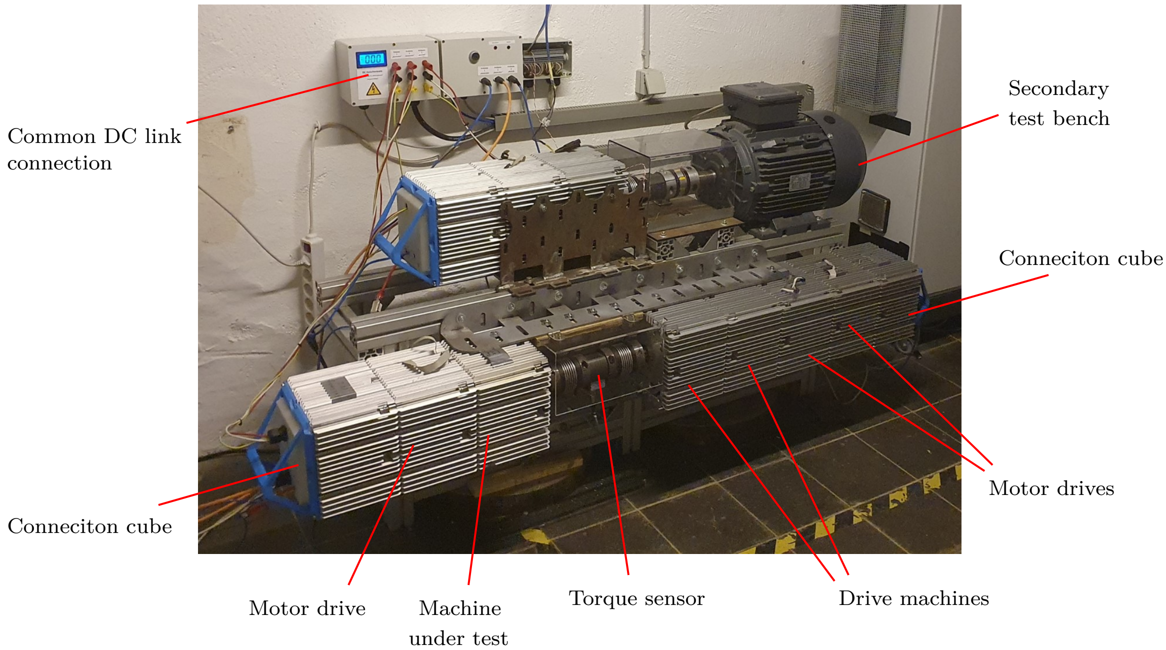

Figure 2.37: Photo of the test bench with the machine under test on the left side and the drive machine on the right, which consists of two electrical machines, each with a motor drive.

eliminating the time derivative due to the steady-state condition ($\frac{\mathrm{d}}{\mathrm{d}t}(\cdot) \stackrel{!}{=} 0$) yields

$$\boldsymbol{\psi}_\mathrm{s}^{dq} = \left(\omega_\mathrm{p}\, \boldsymbol{J}\right)^{-1} \left(\boldsymbol{u}_\mathrm{s}^{dq} - R_\mathrm{s}\, \boldsymbol{i}_\mathrm{s}^{dq}\right) = \frac{1}{\omega_\mathrm{p}} \begin{pmatrix} u_\mathrm{s}^q - R_\mathrm{s}\, i_\mathrm{s}^q \\ -u_\mathrm{s}^d - R_\mathrm{s}\, i_\mathrm{s}^d \end{pmatrix}. \tag{2.86}$$

Note that the voltage in q-direction is used to calculate the flux linkage ψ_s^d in d-direction and vice versa. To obtain the desired maps of the flux linkages, different current vectors $\boldsymbol{i}_\mathrm{s}^{dq}$ are approached in a sensible grid. The electrical machine under test is driven by an external machine with constant speed. At each point, the currents $\boldsymbol{i}_\mathrm{s}^{dq}$ and the voltages $\boldsymbol{u}_\mathrm{s}^{dq}$ are measured. Fig. 2.37 shows a photo of the test bench.

Fig. 2.38 shows the measured flux linkage map. In the upper subplots, the flux linkage ψ_s^d and in the lower subplot ψ_s^q is shown. The top view with the contour lines of constant flux for each flux linkage is shown on the left side. On the right side is the same flux linkage as a 3D plot. Inserting this nonlinear and measured flux linkage into (2.72) results in a torque map. The torque contour lines can be calculated, and the current vector with minimal amplitude can be picked. This leads to a more accurate representation of the produced torque in the machine and, thus, a better solution for the MTPC hyperbola.

The measurement of the flux linkage is susceptible and needs to be done accurately. The temperature has the most significant influence on the measurement as the stator resistance R_s and the permanent magnet flux linkage ψ_pm are strongly dependent on it [80, Sec. 6.9.3], [114]. The resistance R_s increases nearly proportional with the temperature, whereas the flux linkage ψ_pm decreases. Therefore, it is essential to make the measurements by almost constant machine temperature, which can be achieved by adding cooling and heating phases between the measurements. The iron losses also falsify the measurement because they lead to the fact that the stator current is not completely used for magnetisation, see Fig. 2.31. Since iron losses increase at high rotor speeds, the measurements should be carried out at lower speeds [115]. Alternatively,

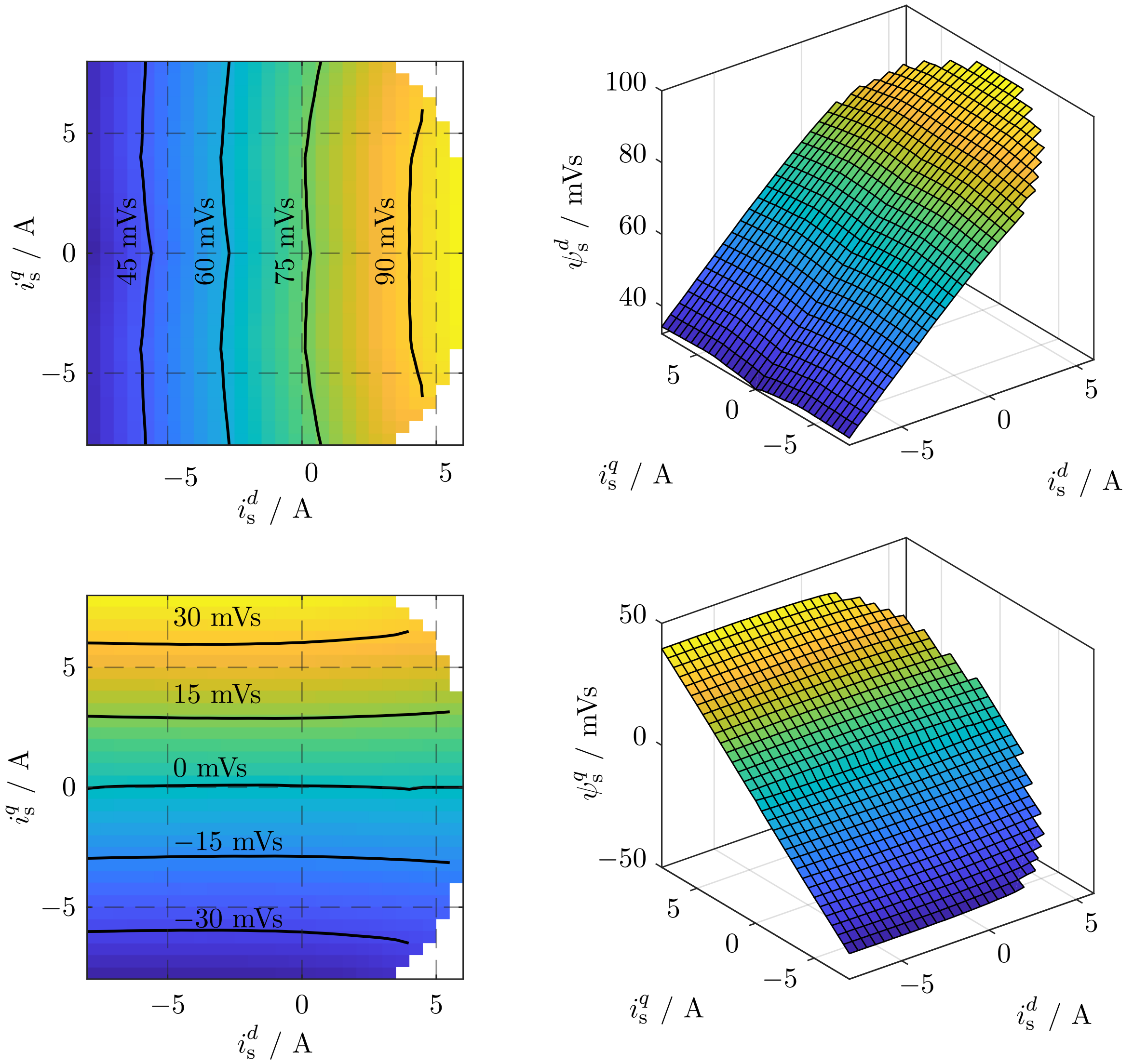

Figure 2.38: Measured flux linkage maps of ψ_s^d in the upper subplots and ψ_s^q in the lower subplots, where the top view with the black contour lines is shown on the left and the corresponding 3D plot is shown on the right.

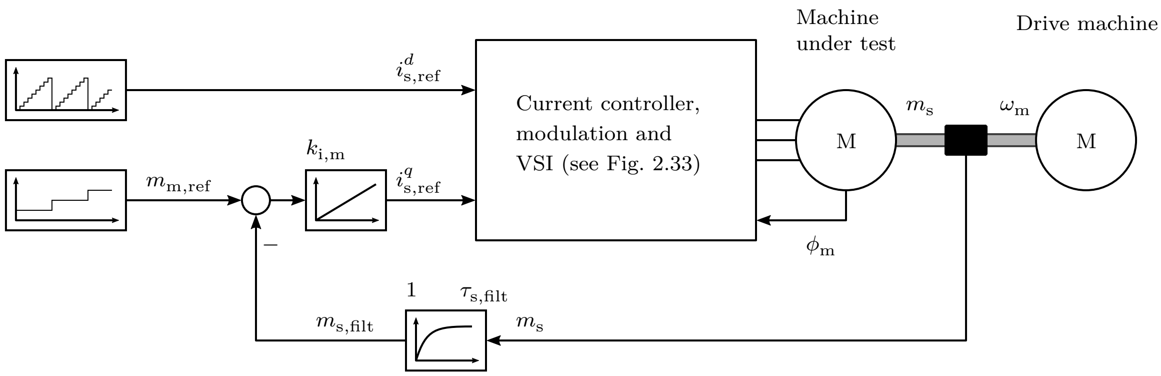

Figure 2.39: Block diagram of the cascaded torque control loop for the direct measurement of the current vector with maximum efficiency.

the iron losses can also be taken into account or can be identified by alternating between motor and generator operation with a corresponding flux linkage [108, 116]. To eliminate unwanted signals such as noise and spatial or inverter harmonics, averaging the signals is required. It is possible to obtain the stator voltages $\boldsymbol{u}_{\mathrm{s}}^{dq}$ from the reference voltages of the controller output. However, it is then essential to compensate for the dead time of the MOSFET half-bridge and the on-resistance of the MOSFETs, as described in Sec. 2.1.1. A detailed description of the measuring procedure can be found in [1, 117].

Direct Measurement of the Current Vector with the Maximum Efficiency

A new measurement method is proposed in [1] that allows for direct determination of the current vectors with maximum efficiency. The idea is to drive through the contour lines of constant torque in the (d,q)-plane and observe the DC link power p_{dc} of the motor drive. By observing the DC link power, consequently, all losses are considered, including the inverter and iron losses. The point of maximum output power during generator operation or minimum input power during motor operation determines the optimal current vector. For this purpose, a cascaded torque control loop is superimposed on the q-component of the current. The block diagram of this control system is shown in Fig. 2.39.

These measurements are also done in steady-state with an external machine that drives the machine under test with constant speed. The control loop maintains the reference torque $m_{\mathrm{m,ref}}$ at the shaft by adjusting the q-current i_{s}^q. The contour line of constant torque is traversed within the complete current range by changing the d-current i_{s}^d stepwise. At each point, the currents $\boldsymbol{i}_{\mathrm{s}}^{dq}$ and the DC link power p_{dc} are recorded and averaged over a certain period. Here, it is also very important that the machine temperature remains approximately constant, which can likewise be achieved by adding heating and cooling phases.

To remove torque harmonics, the signals must be averaged over multiple mechanical revolutions. To prevent the torque controller from compensating for these harmonics and frequently changing the current i_{s}^q, the feedback torque signal m_{s} from the torque sensor must also be averaged. This averaging is done with a first-order low-pass filter with the time constant $\tau_{\mathrm{s,filt}}$. The cutoff frequency must be very low to achieve a smooth torque signal, resulting in a very high time constant, which dominates the system dynamics. Therefore, the dynamics of the current control loop can be neglected, and an integrating controller with the transfer function

$$\frac{i^q_{\mathrm{s,ref}}(s)}{m_{\mathrm{m,ref}}(s) - m_{\mathrm{s,filt}}} = \frac{k_{\mathrm{i,m}}}{s} \tag{2.87}$$

is sufficient to control the torque. Note that the measured torque m_{s} at the shaft, given by

$$m_{\mathrm{s}} = m_{\mathrm{m}} - m_{\mathrm{f}}\,, \tag{2.88}$$

is the machine torque m_{m} minus the torque m_{f}, which is caused by friction. However, this does not influence the measurement results as the friction stays constant since the temperature and the speed are kept constant as well [84, Sec. 11.1.5]. According to [80, Sec. 1.3.3], the controller gain is chosen as

$$k_{\mathrm{i,m}} = \frac{1}{2\,\tau_{\mathrm{s,filt}}\,V_{\mathrm{m}}}\,, \tag{2.89}$$

where V_{m} is the ratio of the machine torque and the current i^q_{s}. It is derived from (2.82) with $i^d_{\mathrm{s}} = 0$ A, which yields

$$V_{\mathrm{m}} = \frac{m_{\mathrm{m}}}{i^q_{\mathrm{s}}} = \frac{3}{2}\,n_{\mathrm{p}}\psi_{\mathrm{pm}}\,. \tag{2.90}$$

Fig. 2.40(a) shows the results of the three discussed methods. The MTPC hyperbolas with linearised [—] and nonlinear [—] flux linkage are very similar since the machine under investigation is not very nonlinear. The black lines in the left subplot are the directly measured torque contour lines for which the proposed measurement routine is used. The yellow, violet, and green lines represent the trajectories with maximum efficiency for the shaft speeds 100 rpm, 200 rpm and 300 rpm, respectively. These trajectories deviate strongly from the MTPC trajectories and show an offset in the d-component of the current.

The dashed black line in Fig. 2.40(b) shows the measured efficiency

$$\eta_{\mathrm{m}} = \frac{p_{\mathrm{dc}}}{p_{\mathrm{m}}} = \frac{u^{\mathrm{dc}}\,i^{\mathrm{dc}}}{\omega_{\mathrm{m}}\,m_{\mathrm{s}}} \tag{2.91}$$

over the current i^d_{s} for a shaft speed of 300 rpm and a torque of -15 Nm. To determine the point with maximum efficiency, a polynomial of second order is fitted to the measured efficiency, shown by the green line. The efficiency is expected to be quadratically dependent on the current i^d_{s}, as the copper losses are also proportional to the square of the current, see (2.71). The point of maximum efficiency is marked with the red diamond [♦], which is significantly better than the estimated points of the MTPC methods with linearised [×] and nonlinear [×] flux linkage.

The difference is based on iron losses, which are not considered in the MTPC method. In steady-state, the iron losses are given by

$$p^{\star}_{\mathrm{s,Fe}} = \frac{3}{2}\,\omega_{\mathrm{p}}^2 \left(\boldsymbol{J}\,\boldsymbol{\psi}^{dq}_{\mathrm{s}}\right)^{\top} \left(\boldsymbol{R}^{dq}_{\mathrm{s,Fe}}\right)^{-1} \left(\boldsymbol{J}\,\boldsymbol{\psi}^{dq}_{\mathrm{s}}\right) = \frac{3}{2}\,\omega_{\mathrm{p}}^2 \left(\frac{\left(\psi^q_{\mathrm{s}}\right)^2}{R^d_{\mathrm{s,Fe}}} + \frac{\left(\psi^d_{\mathrm{s}}\right)^2}{R^q_{\mathrm{s,Fe}}}\right). \tag{2.92}$$

Since the angular frequency ω_{p} is constant, the iron losses are only affected by the flux linkage $\boldsymbol{\psi}^{dq}_{\mathrm{s}}$. A more negative stator current i^d_{s} reduces the flux linkage ψ^d_{s}, which can be seen in Fig. 2.38. This reduces the iron losses but increases the copper losses due to the greater current amplitude. However, it is shown here that it is more efficient to allow more copper losses if the iron losses are reduced. The high increase in efficiency has not been made possible because of strong nonlinearity, as the PMSM tested does not have any exceptionally nonlinear characteris-

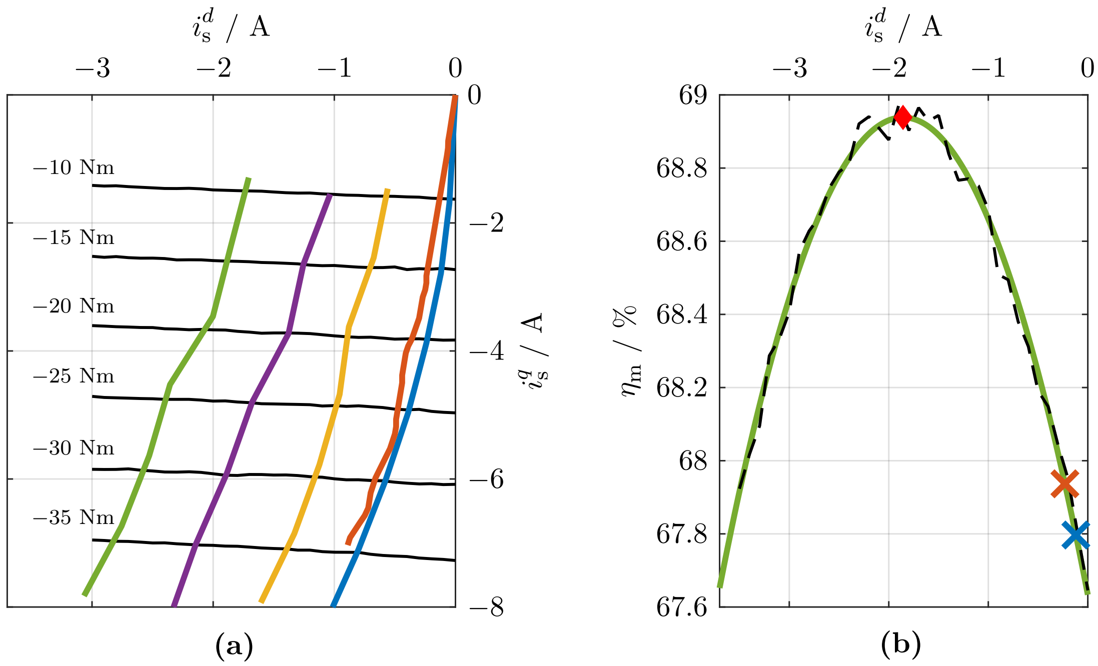

Figure 2.40: (a) Measured torque contour lines [—] and resulting trajectories for the two MTPC methods with linearised [—] and nonlinear [—] flux linkages and the measured trajectories with the maximum efficiency for different shaft speeds of 100 rpm [—], 200 rpm [—] and 300 rpm [—] in the (d,q)-plane. (b) Efficiency [—] for a shaft speed of 300 rpm and a constant torque of −15 Nm and the two points of MTPC for linear approximated [×] and nonlinear [×] flux linkages and the point of maximum efficiency [♦].

tics. The fact that the efficiency was directly optimised and thus all losses were considered makes the method very generally valid. This method allows the maximum efficiency to be determined for any machine.
For implementation, the optimal current vectors are stored in a lookup table. The desired torque and the actual rotor speed can be used to determine the optimal reference current vector $\boldsymbol{i}_{\mathrm{s,ref}}^{dq}$. A straightforward but less accurate implementation is to adjust the reference current $i_{\mathrm{s,ref}}^{d}$ proportionally to the speed. In this experiment, the influence of temperature was eliminated by keeping the machine temperature constant. The experiment must be repeated for different temperatures to determine the effect of temperature on the optimal current vector.
If all parameters of the electrical machine are known, including the iron resistance $\boldsymbol{R}_{\mathrm{s,Fe}}^{dq}$, it is preferable to use an analytical solution and compute the optimal current vector online. If the machine temperature is measured during regular operation, the parameters of the electrical machine can be adjusted with it. A fully generic and analytical solution for optimal feedforward torque control for all strategies, including MTPL, MTPV, FW and MC, is given in [110], [80, Sec. 6.9]. However, if the optimisation is sufficient for regular operation, where no or hardly any operating limits are exceeded, the method presented here offers an excellent and easy-to-implement alternative.

2.5 Grid Inverter

The grid inverter is the link between the proposed highly modular power electronics system and the public power grid. It allows for a power flow between the DC grid, into which the renewable energy sources are fed, and the low voltage AC grid. The number of inverters must be expandable as required to maintain the power electronics system's modularity according to the Specifications (S7) and (S9). This is ensured by the newly introduced topology that makes it possible to connect multiple grid inverters in full parallel and expand the feed-in power as desired. They can be simultaneously connected in parallel on both the AC and DC sides.

The novelty of the topology is the connection from the star-point of the filter capacitors to the midpoint M of the DC link, which enables the full parallel connection of multiple grid inverters, as will be shown later. This connection is only internal to the device and has no connection to the grid. In Section 2.5.2, it is shown that for classical topologies, the DC link potential with respect to ground strongly depends on the switching states of the MOSFETs. To realise a full parallel connection with these, each grid inverter needs a strong common-mode filter on the DC side or a 50 Hz transformer on the AC side. Both variants are costly and not energy-efficient, and the common-mode filter is very complex [118, Sec. 5]. This makes these solutions impractical. When the literature refers to a parallel connection of grid inverters, it often relates only to the common connection on the AC side. In this case, each inverter has its DC source, and the interference between the inverters and their influence on the grid or microgrid are analysed [119, 120]. In [121, 122], the inverters are fully connected in parallel with common AC and DC buses, but they only feed a passive load and are not connected to the grid.

A very well-studied and typical topology is the three-level inverter with neutral point clamping (NPC) [123–126]. This topology belongs to the group of multilevel inverters whose main propose is to overcome the voltage limitation of semiconductors [123]. It was introduced in [127] by Nabae, Magi and Takahashi in 1981. Compared to the classic two-level inverters, it offers improved switching stress due to lower voltage steps, which is advantageous for IGBTs [64, Sec. 2.3]. With the topology of multilevel inverters, the DC link capacitor is split into two parts and the midpoint is used as a third output level. Because of this connection, this topology is similar to the one presented here. The difference is that, in this case, the connection is not actively used but only serves to stabilise the DC link potential. With the NPC topology, the midpoint is connected to the grid, its voltage is actively controlled, and power flows over the connection into the grid. This does not eliminate the dependence of the DC link potential with respect to ground on the switching states, and a parallel connection is also only possible with additional measures.

Another notable characteristic of the inverter presented here is that only an LC filter is used instead of the far more common LCL filter [128]. The saving of the grid-side filter inductance is possible due to the very high switching frequency of 70 kHz. The rationale for this and the dimensioning of the filter are explained in Sec. 2.5.1.

Sec. 2.5.3 presents the model of the topology in the state-space representation. For optimum control performance, as required by Specification (S8), and good damping of the filter resonance, a PI state feedback controller (PI-SFC) is presented in Sec. 2.5.4. Since all states of the system are required for the controller, but not all of them can be measured, an observer is necessary, which is explained in Sec. 2.5.5. The controller must be implemented in the C programming language on a real-time embedded system. Since this does not allow direct matrix operations, such as those possible in MATLAB, the controller must be implemented element by element. The approach for this is shown in Sec. 2.5.6. In the section that follows, the measurement results of an experiment carried out in the laboratory are presented, which shows the advantages of the PI state feedback controller compared to a classical PI controller. Finally, the implementation of the full parallel connection of multiple inverters is discussed in Sec. 2.5.8. This section is partially based on [2] and [4], where parts have already been published.

2.5.1 Filter of the Grid Inverter

The DC/DC converter and the grid inverter need an inductance as a filtering element. The two MOSFETs of a half-bridge connect the corresponding phase either to the potential DC+ or DC−, which are huge voltage steps. To limit these voltage steps at the output and the resulting current slope, an inductor is connected to each output of the VSI. Due to the stricter requirements, the inductor is designed for the grid inverter. It can then also be used for the DC/DC converter, reducing the variety of components.

The filter must be designed to meet the requirements of standards and the specifications of the grid operator, documented in so-called grid-codes [64, Sec. 7]. In some cases, a simple inductance can be sufficient. However, a filter of a higher order is usually used. The most commonly used filter is the LCL filter, which has prevailed for various reasons. One of the main reasons for using this 3rd-order filter is its attenuation of 60 dB per decade at high frequencies, where the switching frequency is placed. Thus, better damping of the switching frequency and its harmonics can be achieved, which allows for a reduction of the size of the costly filter elements [129–133].

Nevertheless, only an LC filter is used in this topology, and the grid-side inductance of the filter is omitted. This can be justified by the high switching frequency. Advances in semiconductor technology, such as the here-used SiC-MOSFETs, have enabled higher switching frequencies. Here, the switching frequency f_{sw} is chosen to be 70 kHz, which is very high compared to other publications dealing with grid inverters. Typical switching frequencies are placed around 10 to 20 kHz, shown in the overview [128].

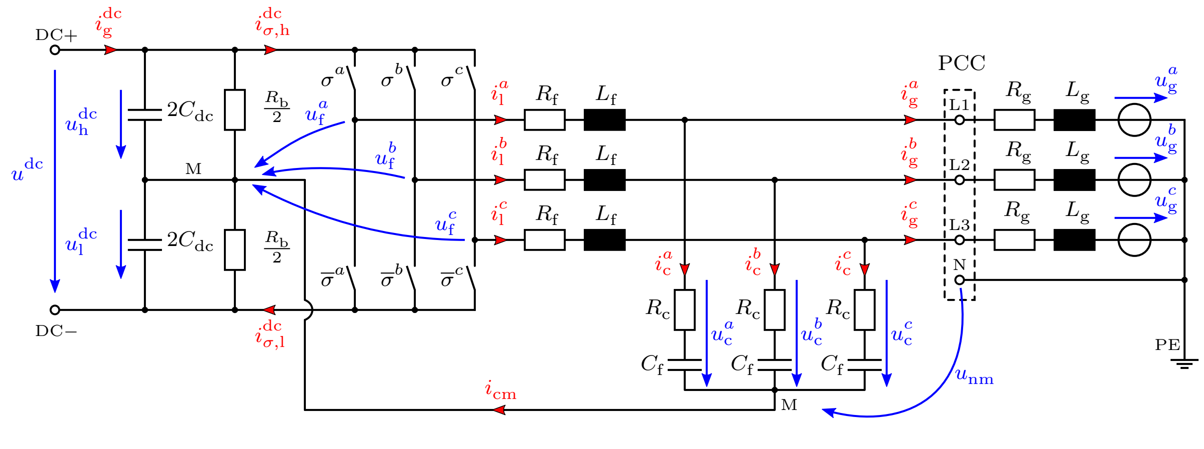

Figure 2.41: The electrical circuit of the grid inverter.

Fig. 2.41 shows the electrical circuit of the grid inverter, where the grid-side inductance L_{g} is present anyway, but it is not part of the inverter's installed filter. Instead, it should represent the grid impedance, indicated by being on the right side of the point of common coupling (PCC), which represents the connection point to the grid. The grid impedance is not a part of the inverter by itself. Still, from a control theory perspective, it is also a part of the filter and, therefore, an important parameter. That is why much research has been done on identifying the grid impedance [134–140]. In general, the grid has ohmic-inductive characteristics and can be approximated by its Thevenin equivalent circuit, consisting of an ideal voltage source $\boldsymbol{u}_{\mathrm{g}}^{abc}$ in series with an RL grid impedance [141, 142]. Up to a frequency of about 1 kHz, the grid impedance is pure ohmic-inductive with nearly constant parameters. These are the most significant characteristics of the power cables and the transformer, which is required for the connection to the medium voltage distribution grid [134–136, 139, 140, 143]. These transformers add the main contribution of the grid-side inductance L_{g} [130, 136, 144]. Above approximately 1 kHz, the grid

Table 2.2: The parameter of the power electronics.

Name	Parameter	Value
DC link capacitance	C_{dc}	810 μF
Balancing Resistors	R_{b}	495 kΩ
Filter resistance	R_{f}	130 mΩ
Filter inductance	L_{f}	820 μH
Equivalent series resistance	R_{c}	5 mΩ
Filter capacitance	C_{f}	9.4 μF
Grid frequency	f_{g}	50 Hz
Switching frequency	f_{sw}	70 kHz

impedance turns more complex, sometimes nonlinear, and, most importantly, load dependent. Thus, it changes permanently during the day, as shown in [130, 135, 138, 144]. In most cases, however, the grid keeps an inductive behaviour over the whole frequency spectrum, which is why the RL model remains valid. Nevertheless, grid impedances are becoming increasingly complex due to more decentralised grid feed-in. Therefore, the stability of the combined impedances of inverter and grid is an important research topic in literature [129, 135–137, 144, 145]. Likewise, the control algorithm must also be robust against variations in the grid impedance.

When designing a filter for a grid inverter, a major objective is to place the resonance frequency f_{res} of the filter below the switching frequency f_{sw} so that the resonance won't be excited by the switching, which would cause oscillations. The resonance frequency should also be higher than the fundamental frequency f_{g} of the grid so that it does not affect the fundamental waveform and challenge the control loop [131, 133, 144, 146]. The main steps for designing an LCL filter according to [129, 131] and [64, Sec. 11.3] are as follows.

- The inductance L_{f} on the inverter side is designed to reduce the current ripple to a desired value while complying with the standards. A reasonable estimate for the inductor ripple current is about 20 to 40 % of the nominal output current.
- The size of the capacitor C_{f} should be limited so that the reactive power consumption of the capacitors does not exceed 5 % of the inverter's rated power.
- A passive resistor R_{c} in series to the filter capacitor can optionally be introduced to dampen the resonance of the filter, avoiding oscillations.
- The resonance frequency f_{res} can be adjusted with the grid-side inductance. The resonance frequency f_{res} should be at least ten times higher than the grid frequency f_{g} and less than half of the switching frequency f_{sw}.

Following these steps, the range of the converter-side inductance L_{f} and the filter capacitor C_{f} can be derived from the given parameters. The parameters of the grid inverter components are listed in Table 2.2.

In systems with lower switching frequencies, the resonant frequency must be additionally damped to ensure stability. For this purpose, a resistor can be used in series with the filter capacitor. However, since this causes losses and does not allow online adaptation, a notch filter is sometimes integrated into the controller for active damping [132, 135, 137, 144, 147]. The resonance frequency can also be damped with a more sophisticated controller, like a state feedback controller [2, 128], which is also used here and presented in Sec. 2.5.4.

The parasitic resistances of the filter elements are also considered, which allows for a better controller design and loss calculation. The resistance R_f is a composition of the equivalent series resistance of the inductor and the drain-source on resistance $R_\mathrm{ds,on}$ of the MOSFETs (see Sec. 2.1.1). Here, the resistance R_c represents the capacitor's equivalent series resistance and is not an extra installed damping resistor. The resonance is only be addressed by a proper filter design and a robust state feedback controller. Nevertheless, R_c is considered in the model, but as the equivalent series resistance of modern film capacitors is very small, it can be set to zero to account for the worst case.

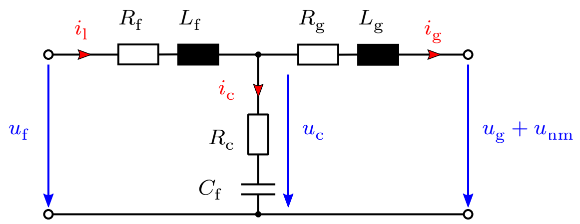

Figure 2.42: LCL filter of one phase with parasitic resistances.

To determine the range for the resonance frequency, the filter's transfer function is derived. In Figure 2.42, the LCL filter for one phase with the parasitic resistances is shown, which is used to derive the transfer functions. The superscripts of the quantities for the indication of the phase are omitted since the three phases are identical. Notice that the grid-side voltage is $u_\mathrm{g} + u_\mathrm{nm}$, and the star-point of the filter capacitors is actually not connected to the grid. This means, e.g., that the grid current i_g^a of phase A flows back through the filter components of the other two phases, B and C, because no γ-current can flow into the grid and

$$i_\mathrm{g}^a + i_\mathrm{g}^b + i_\mathrm{g}^c \overset{!}{=} 0 \text{ A} \tag{2.93}$$

holds. This affects the transfer function and should be considered if a more accurate model is required, which is often ignored in the literature. However, since the grid impedance is not known and the consideration of the return path has only a minor influence on the resonance, it is sufficient to consider only one phase for this analysis.

The transfer function from the switched voltage u_f to the grid-side current i_g is given by

$$\frac{i_\mathrm{g}(s)}{u_\mathrm{f}(s)} = \frac{1 + s\, R_\mathrm{c}\, C_\mathrm{f}}{a_0 + s\, a_1 + s^2\, a_2 + s^3\, a_3} \tag{2.94}$$

with

$$\left.\begin{aligned}
a_0 &= R_\mathrm{f} + R_\mathrm{g}\,,\\
a_1 &= L_\mathrm{f} + L_\mathrm{g} + C_\mathrm{f}\left(R_\mathrm{f} R_\mathrm{c} + R_\mathrm{f} R_\mathrm{g} + R_\mathrm{c} R_\mathrm{g}\right),\\
a_2 &= C_\mathrm{f}\,\left[\left(R_\mathrm{c} + R_\mathrm{g}\right) L_\mathrm{f} + \left(R_\mathrm{f} + R_\mathrm{c}\right) L_\mathrm{g}\right] \text{ and}\\
a_3 &= L_\mathrm{f}\, C_\mathrm{f}\, L_\mathrm{g}\,.
\end{aligned}\right\} \tag{2.95}$$

The transfer function from the inverter-side current i_l to the grid-side current i_g is given by

$$\frac{i_\mathrm{g}(s)}{i_\mathrm{l}(s)} = \frac{1 + s\, R_\mathrm{c}\, C_\mathrm{f}}{1 + s\left(R_\mathrm{c} + R_\mathrm{g}\right) C_\mathrm{f} + s^2\, L_\mathrm{g}\, C_\mathrm{f}}\,. \tag{2.96}$$

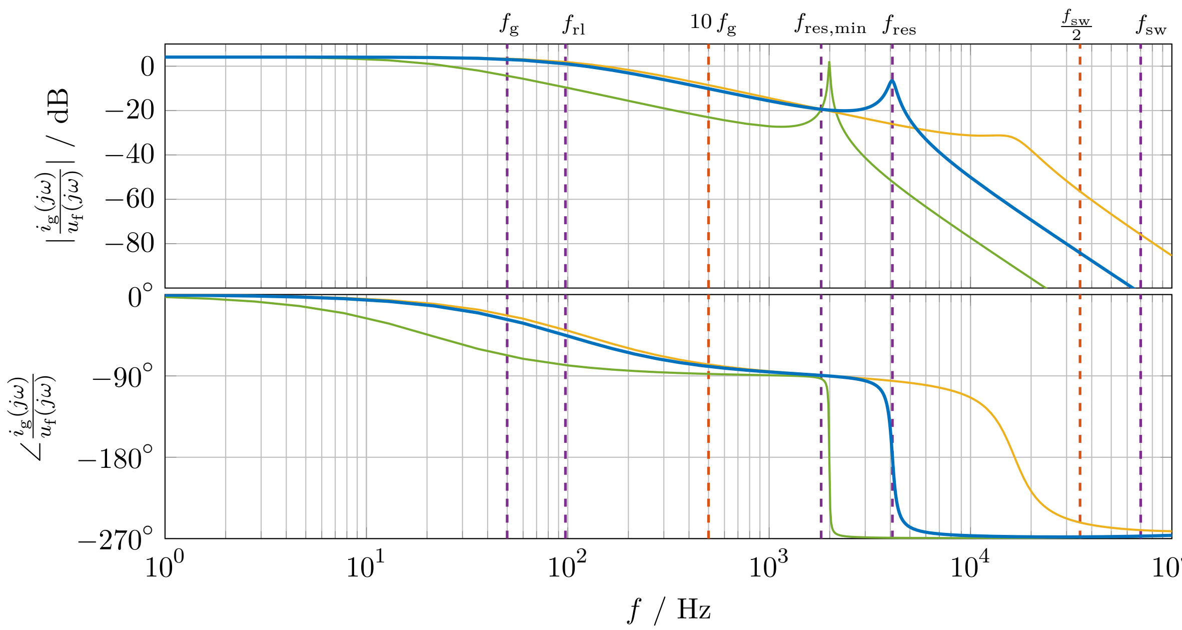

Figure 2.43: Frequency responses of the LCL filter with $L_g = 4$ mH [—], $L_g = 200$ μH [—] and $L_g = 10$ μH [—]. The discussed frequencies are written on top corresponding to the dashed lines, whereby f_{rl} and f_{res} are only marked for the blue line. The dashed red lines [- - -] are marking the range limits within the resonance frequency f_{res} should lie.

The resonant frequency results from the transfer function (2.94) by setting the parasitic resistances to zero. It is given by

$$f_{res} = \frac{1}{2\,\pi}\sqrt{\frac{L_f + L_g}{L_f\,C_f\,L_g}}\,. \tag{2.97}$$

As the converter-side inductance L_f and the filter capacitor C_f is already determined, the resonance frequency f_{res} can only be changed with the grid-side inductance L_g. The theoretical lower limit of the resonant frequency $f_{res,min}$ results as L_g approaches infinity, which yields

$$f_{res,min} = \lim_{L_g\to\infty} f_{res} = \frac{1}{2\pi\,\sqrt{L_f\,C_f}} \overset{!}{\geq} 10\,f_g\,. \tag{2.98}$$

The maximum resonant frequency that can be tolerated is

$$f_{res,max} = \frac{f_{sw}}{2}\,. \tag{2.99}$$

Rearranging (2.97) and inserting (2.99) determines the smallest feasible grid inductance $L_{g,min}$ with

$$L_{g,min} = \frac{L_f}{(\pi\,f_{sw})^2\,L_f\,C_f - 1}\,. \tag{2.100}$$

If the switching frequency f_{sw} is very high, L_g can become very small, and even so small, that the smallest possible grid impedance can be enough to guarantee a stable operation. With the parameters given in Tab. 2.2, the minimum required grid impedance is 2.21 μH. If the switching frequency is lower, the minimum grid inductance becomes greater, necessitating an extra grid-side inductor to be added to have a defined and known minimum inductance between the grid and the inverter.

In Fig. 2.43, the frequency responses of the transfer function (2.94) with three different values of L_g are shown. At the frequency

$$f_\mathrm{rl} = \frac{1}{2\pi}\,\frac{R_\mathrm{f}+R_\mathrm{g}}{L_\mathrm{f}+L_\mathrm{g}} \tag{2.101}$$

is the first pole of the transfer function, which usually is compensated for by a classical PI controller approach. Notice that this frequency depends on the grid impedance L_g, as well. To optimally design the PI controller, the grid impedance must be known.
With the parameters in Tab. 2.2, the recommended limits of the resonance frequency f_res can be computed. The dashed red lines mark them. The minimum resonance frequency $f_\mathrm{res,min}$ is greater than ten times the grid frequency f_g. The smallest feasible inductance $L_\mathrm{g,min}$ is about 2.2 μH, which is already achieved by only a few metres of cable. As a rule of thumb, a specific inductance between 0.2 and 1 $\frac{\mu\mathrm{H}}{\mathrm{m}}$ can be assumed, depending on the cable parameters [148]. Also, leakage inductances of the necessary EMI filter, e.g., from the common-mode choke, will contribute to the grid inductance so that this value is exceeded in any case. With the chosen parameters and due to the high switching frequency, the grid-side filter inductance can be saved and stable operation with only an LC filter can still be guaranteed.

2.5.2 Connection of the Filter Star-Point

The star-point of the filter capacitors can be connected in different ways. In many publications, this point is not connected at all and remains floating [129, 136–138]. This has the side effect that the DC link potential with respect to the protective earth (PE) potential changes with the switching states. This prevents the full parallel connection of several grid inverters, which will be shown later. Moreover, this common-mode voltage greatly influences the electromagnetic compatibility [149]. This is especially a problem in DC grids where the grid extends over larger distances. As a result, the common-mode voltage generates more interference and can be radiated over long lines like an antenna. In a so-called three-leg four-wire inverter, the filter star-point is connected to the neutral N of the grid and to the midpoint M of the DC link, whereby a fourth half-bridge is sometimes added to keep the DC link voltage balanced if an unsymmetrical load is to be connected, where load current flows via the neutral [150–155]. This brings the advantage that the potential of the DC link does not change during switching.
In [150], an inductance in the connection between the star-point and the midpoint is modelled to consider parasitic effects. It is shown that the common-mode voltage increases with this inductance, which degrades electromagnetic compatibility. In [151], on the other hand, such an inductor is introduced on purpose to reduce the overall size of the filter inductors. Therefore, the advantages and disadvantages of implementing such an inductor should be carefully weighed.
This topology is designed to allow full parallel connection simultaneously on the DC and AC sides of multiple grid-connected inverters. Therefore, the potential of the DC link with respect to PE must be independent of the switching states. The connection of the filter star-point to the midpoint M of the DC link capacitors makes this possible. However, this connection is not connected to the grid to prevent additional circulating currents. The connection must have the lowest possible impedance for the DC link potential to remain as constant as possible.
Considering Fig. 2.41, according to Kirchhoff's voltage law, the voltage equation

$$\boldsymbol{u}_\mathrm{f}^{abc} = R_\mathrm{f}\,\boldsymbol{i}_\mathrm{l}^{abc} + L_\mathrm{f}\frac{\mathrm{d}}{\mathrm{d}t}\boldsymbol{i}_\mathrm{l}^{abc} + R_\mathrm{g}\,\boldsymbol{i}_\mathrm{g}^{abc} + L_\mathrm{g}\frac{\mathrm{d}}{\mathrm{d}t}\boldsymbol{i}_\mathrm{g}^{abc} + \boldsymbol{u}_\mathrm{g}^{abc} + \mathbf{1}_3\,u_\mathrm{nm} \tag{2.102}$$

can be stated, where $\boldsymbol{u}_\mathrm{f}^{abc} := (u_\mathrm{f}^a, u_\mathrm{f}^b, u_\mathrm{f}^c)^\top$ are the voltages applied by the VSI, $\boldsymbol{i}_\mathrm{l}^{abc} := (i_\mathrm{l}^a, i_\mathrm{l}^b, i_\mathrm{l}^c)^\top$ are the currents flowing through the filter inductances L_f, $\boldsymbol{i}_\mathrm{g}^{abc} := (i_\mathrm{g}^a, i_\mathrm{g}^b, i_\mathrm{g}^c)^\top$ are the grid-side currents and $\boldsymbol{u}_{\mathrm{g}}^{abc} := (u_{\mathrm{g}}^{a}, u_{\mathrm{g}}^{b}, u_{\mathrm{g}}^{c})^{\top}$ are the grid voltages. This equation is generally valid regardless of the star-point connection, whereby the voltage u_{nm} is defined as the voltage from the neutral N to the midpoint M of the DC link. By rearranging (2.102), the voltage u_{nm} is given by

$$u_{\mathrm{nm}} = \frac{1}{3}\,\mathbf{1}_3^{\top}\left(\boldsymbol{u}_{\mathrm{f}}^{abc} - R_{\mathrm{f}}\,\boldsymbol{i}_{\mathrm{l}}^{abc} - L_{\mathrm{f}}\frac{\mathrm{d}}{\mathrm{d}t}\boldsymbol{i}_{\mathrm{l}}^{abc} - R_{\mathrm{g}}\,\boldsymbol{i}_{\mathrm{g}}^{abc} - L_{\mathrm{g}}\frac{\mathrm{d}}{\mathrm{d}t}\boldsymbol{i}_{\mathrm{g}}^{abc} - \boldsymbol{u}_{\mathrm{g}}^{abc}\right). \tag{2.103}$$

With

$$\mathbf{1}_3^{\top}\boldsymbol{x}^{abc} = \mathbf{1}_3^{\top}\boldsymbol{T}_{\mathrm{c}}^{-1}\,\boldsymbol{x}^{\alpha\beta\gamma} = \frac{3}{\sqrt{2}}\,x^{\gamma} \tag{2.104}$$

and inserting

$$\boldsymbol{u}_{\mathrm{f}}^{abc} = u^{\mathrm{dc}}\left(\boldsymbol{\sigma}^{abc} - \frac{1}{2}\right), \tag{2.105}$$

where it is assumed that the DC link is balanced $\left(u_{\mathrm{h}}^{\mathrm{dc}} = u_{\mathrm{l}}^{\mathrm{dc}}\right)$, (2.103) can be further simplified to

$$u_{\mathrm{nm}} = \frac{1}{3}\,u^{\mathrm{dc}}\left(\mathbf{1}_3^{\top}\,\boldsymbol{\sigma}^{abc} - \frac{1}{2}\right) - \frac{1}{\sqrt{2}}\left(R_{\mathrm{f}}\,i_{\mathrm{l}}^{\gamma} + L_{\mathrm{f}}\,\frac{\mathrm{d}}{\mathrm{d}t}i_{\mathrm{l}}^{\gamma} + u_{\mathrm{g}}^{\gamma}\right). \tag{2.106}$$

There, the terms which involve the current i_{g}^{γ} are already cancelled since the star connection of the grid transformer prohibits a γ-current component and (2.93) still holds.
Now, it should be assumed that the star-point is not connected and remains floating. This implies that no γ-current i_{l}^{γ} can flow either, which further reduces the previous equation to

$$u_{\mathrm{nm,f}} = \frac{1}{3}\,u^{\mathrm{dc}}\left(\mathbf{1_3}^{\top}\,\boldsymbol{\sigma}^{abc} - \frac{1}{2}\right) - \frac{1}{\sqrt{2}}\,u_{\mathrm{g}}^{\gamma}. \tag{2.107}$$

Here, $u_{\mathrm{nm,f}}$ denotes the voltage from the neutral N of the grid to the midpoint M of the DC link when the star-point of the filter capacitors is floating. It now only depends on the γ-component of the grid voltage, the DC link voltage u^{dc}, and the switching states. Under normal, symmetrical grid conditions, the voltage u_{g}^{γ} is zero as well. Assuming a slow rate of change for the DC link voltage u^{dc}, the voltage $u_{\mathrm{nm,f}}$ and, thus, the DC link potential with respect to N and PE changes mainly with the switching states. If this voltage differs between grid inverters connected in parallel, this leads to an unwanted current flow, which is not acceptable from a practical point of view.
Fig. 2.44 shows the results of a PLECS simulation of this voltage for a single grid inverter with a floating star-point. The DC link voltage u^{dc} is constant and set to 800 V. With every switching event, the voltage $u_{\mathrm{nm,f}}$ makes a step of $\frac{u^{\mathrm{dc}}}{3}$, which makes a full parallel connection of several grid inverters impractical. Since the modulation of the VSIs is not synchronised with each other, the switching events do not happen simultaneously. Also, parameter variations cause different controller outputs, which causes different duty cycles. This leads to a voltage difference between the parallel connected grid inverters, which in turn results in a circulating current flow.
Fig. 2.45 shows simulation results of two in parallel connected inverters with floating star-point. To model the asynchrony of the modulation, the switching frequency of one inverter was increased by 2 %. The upper subplot shows the currents $\boldsymbol{i}_{\mathrm{l},1/2}^{abc}$ and the lower subplot shows the corresponding γ-components, each for of both grid inverters. Although no γ-current i_{l}^{γ} could flow with the single grid inverter, it is possible with the parallel connection. Due to the different switch positions of the two VSIs, a γ-current circulates between them, whereby $i_{\mathrm{l},1}^{\gamma} = -i_{\mathrm{l},2}^{\gamma}$ holds. There is also a beat frequency that arises from the interference of the different switching frequencies. These currents cause large losses and already constitute a base load for the inverters, which limit the usable current. Therefore, a full parallel connection with floating star-point is not practical without further measure. In [121], a control method is proposed to

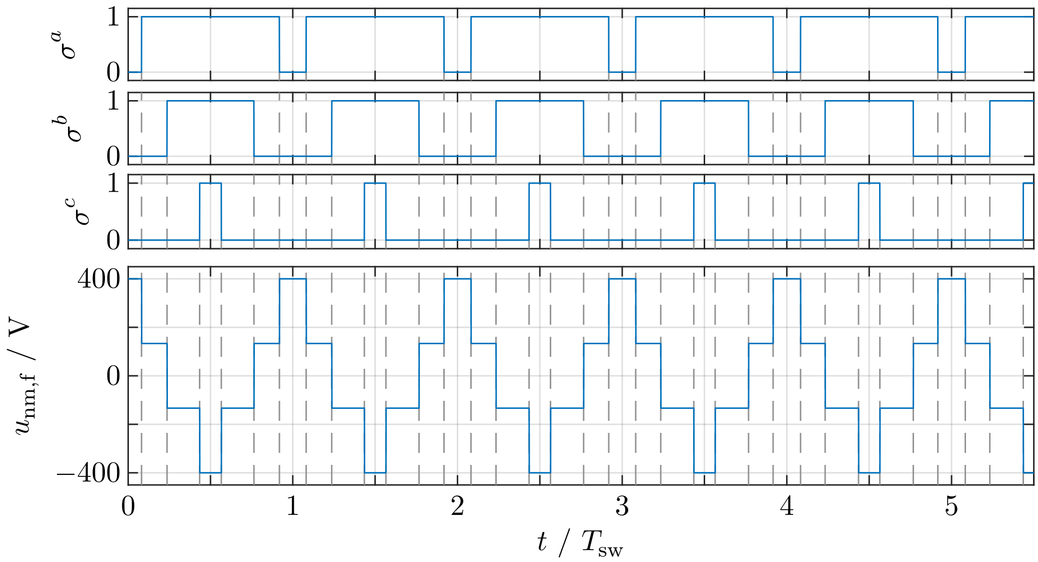

Figure 2.44: Simulation result of the voltage $u_{\mathrm{nm,f}}$ and the correlation with the switching states $\boldsymbol{\sigma}^{abc}$ for a single grid inverter with floating star-point.

suppress circulating-currents among parallel connected VSI with floating star-point. However, this does not solve the problem of the jumping DC link potential. Furthermore, the method was only examined on a passive load, not with a grid connection.

To prevent this dependency of the switching states, a connection between the star-point of the filter capacitors and the midpoint M of the split DC link capacitors is introduced. It is important to mention that this midpoint connection is not connected to the neutral N of the grid. This has the advantage that no ripple current flows over the neutral conductor, and still no γ-current can flow into the grid, which can cause other circulating currents.

This connection (see the current path of i_{cm} in Fig. 2.41) introduces the additional voltage condition

$$\boldsymbol{u}_{\mathrm{cf}}^{abc} + R_{\mathrm{c}}\, \boldsymbol{i}_{\mathrm{c}}^{abc} = R_{\mathrm{g}}\, \boldsymbol{i}_{\mathrm{g}}^{abc} + L_{\mathrm{g}} \frac{\mathrm{d}}{\mathrm{d}t} \boldsymbol{i}_{\mathrm{g}}^{abc} + \boldsymbol{u}_{\mathrm{g}}^{abc} + \mathbf{1}_3\, u_{\mathrm{nm}}\,, \tag{2.108}$$

where $\boldsymbol{u}_{\mathrm{cf}}^{abc} := (u_{\mathrm{cf}}^{a}, u_{\mathrm{cf}}^{b}, u_{\mathrm{cf}}^{c})^\top$ denotes the voltages across the filter capacitance C_{f}. Substituting the currents $\boldsymbol{i}_{\mathrm{c}}^{abc} := (i_{\mathrm{c}}^{a}, i_{\mathrm{c}}^{b}, i_{\mathrm{c}}^{c})^\top$ through the filter capacitance with

$$\boldsymbol{i}_{\mathrm{c}}^{abc} = \boldsymbol{i}_{\mathrm{l}}^{abc} - \boldsymbol{i}_{\mathrm{g}}^{abc}\,, \tag{2.109}$$

and rearranging leads to

$$u_{\mathrm{nm}} = \frac{1}{3} \mathbf{1}_3^\top \left(\boldsymbol{u}_{\mathrm{cf}}^{abc} + R_{\mathrm{c}}\, \boldsymbol{i}_{\mathrm{l}}^{abc} - (R_{\mathrm{c}} + R_{\mathrm{g}})\, \boldsymbol{i}_{\mathrm{g}}^{abc} - L_{\mathrm{g}} \frac{\mathrm{d}}{\mathrm{d}t} \boldsymbol{i}_{\mathrm{g}}^{abc} - \boldsymbol{u}_{\mathrm{g}}^{abc} \right). \tag{2.110}$$

Applying (2.93) and (2.104) yields the simplified relation

$$u_{\mathrm{nm}} = \frac{1}{\sqrt{2}} \left(u_{\mathrm{cf}}^{\gamma} + R_{\mathrm{c}}\, i_{\mathrm{l}}^{\gamma} - u_{\mathrm{g}}^{\gamma} \right)\,, \tag{2.111}$$

which shows that the voltage u_{nm} is no longer dependent on the switching states due to this connection. To keep the voltage u_{nm} as close to zero as possible, the current i_{l}^{γ} must be controlled

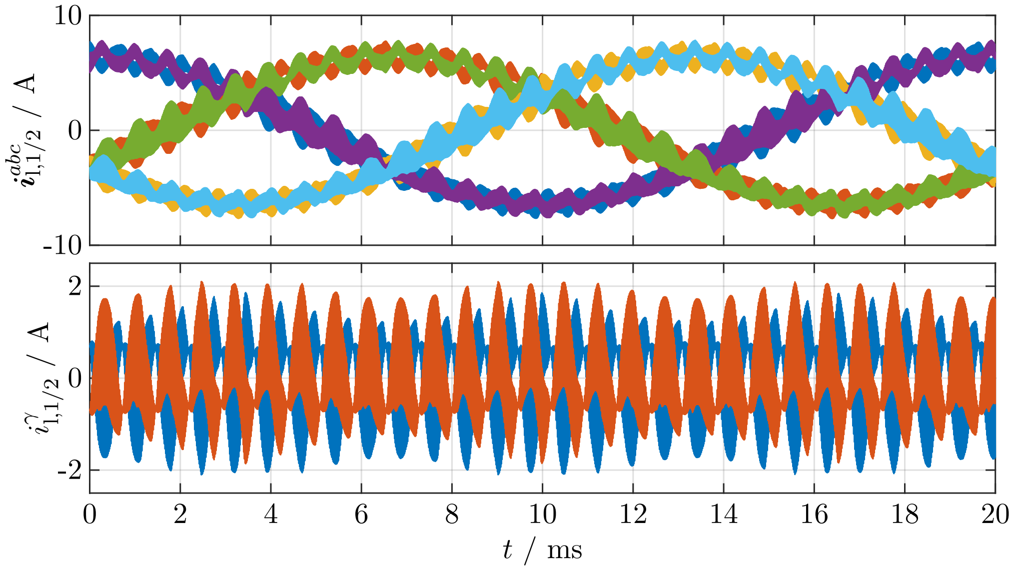

Figure 2.45: Simulation results of two parallel connected inverters with floating star-point with the currents $\boldsymbol{i}^{abc}_{1,1/2}$ in the first subplot and the circulating γ-current in the second subplot.

to zero. By keeping i^{γ}_{1} zero, and since

$$\frac{\mathrm{d}}{\mathrm{d}t}u^{\gamma}_{\mathrm{cf}} = \frac{1}{C_{\mathrm{f}}}i^{\gamma}_{\mathrm{c}} \tag{2.112}$$

where $i^{\gamma}_{\mathrm{c}} = i^{\gamma}_{1}$ for a single inverter, the voltage u_{nm} is only dependent on the voltage u^{γ}_{g}. However, since this is the same for all inverters connected in parallel, this has no further effect and does not lead to any undesired current flow.

However, the current can only be controlled within the given bandwidth of the controller. Meaning the resulting current ripple in i^{γ}_{1} cannot be controlled. As discussed in Sec. 2.2, each active voltage vector has a γ-component, resulting in a γ-current ripple through the filter capacitors.

Fig. 2.46 shows a comparison of the current ripples between a grid inverter with the newly introduced star-point connection and an inverter with floating star-point, each for a single grid inverter without a parallel connection. The first three subplots show the switching states $\boldsymbol{\sigma}^{abc}$, which are equal for both scenarios. In the following subplots, the results of the grid inverter with connected star-point are represented by the blue lines [—] and those of the inverter with floating star-point by the red lines [—]. The second subplot shows the ripple of the current i^{a}_{1} in phase A. With the extra connection of the star-point, the current ripple is only affected by its respective switching state. It differs from the case with a floating star-point, where the current ripple in one phase depends on all three switching states. An advantage of this is that the amplitude of the current ripple is approximately halved, which also reduces the losses. Or viewed differently, the inductance L_{f} can be halved while the amplitude of the current ripple remains the same.

The next subplot shows the currents i^{α}_{1} after applying the Clarke transformation. Apart from minor deviations, the currents show the same pattern. The same applies to the current i^{β}_{1}, which shows that the two topologies do not differ in the α- and β-components. They only differ due to the γ-current i^{γ}_{1}, which is shown in the last subplot. The current flow is caused by the proportion of γ-voltage in the active vectors once the star-point is connected.

The current i^{γ}_{c} through the filter capacitors also flows in the star-point connection and, thus,

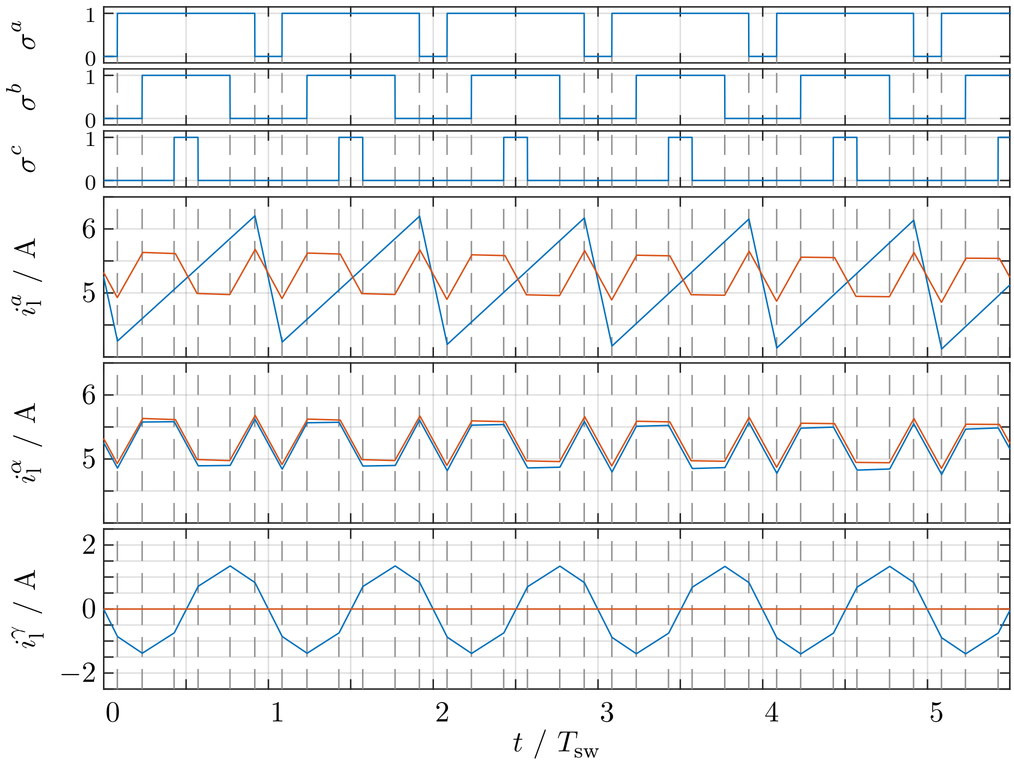

Figure 2.46: Comparison of the current ripples between a grid inverter with star-point connection [—] and with floating star-point [—].

into the DC link capacitance. The current i_{cm} in the connection is given by

$$i_{cm} = \mathbf{1}_3^\top \, \boldsymbol{i}_c^{abc} = \frac{3}{\sqrt{2}} \, i_c^\gamma \, . \tag{2.113}$$

This causes a change in the voltage $\Delta u^{dc} = u_h^{dc} - u_l^{dc}$ of the DC link (see Sec. 2.1.2). Since the current flows through both the filter capacitance C_f and the DC link capacitance C_{dc}, a relation between the voltages can be derived. By inserting (2.112) and (2.113) into the dynamics of the DC link voltage difference Δu^{dc} from (2.6) yields

$$\frac{d}{dt}\Delta u^{dc} = -\frac{1}{R_b C_{dc}}\Delta u^{dc} - \frac{3\, C_f}{2\sqrt{2}\, C_{dc}} \, \frac{d}{dt} u_{cf}^\gamma \, . \tag{2.114}$$

This differential equation can be transformed into the Laplace domain, which leads to the transfer function

$$\Delta u^{dc}(s) = -\frac{s\, R_b\, C_{dc}}{1 + \, s\, R_b\, C_{dc}} \, \frac{3\, C_f}{2\sqrt{2}\, C_{dc}} \, u_{cf}^\gamma(s) \, . \tag{2.115}$$

The first term represents a high-pass filter with the time constant $\tau_b = R_b\, C_{dc}$. Since both the resistance R_b and the capacitance C_{dc} are very high, the cutoff frequency

$$f_{c,dc} = \frac{1}{2\pi\, \tau_b} \quad \approx 0.40 \text{ mHz} \tag{2.116}$$

of the filter is very low so that practically every change in u_{cf}^{γ} is also reflected in the voltage Δu^{dc}. However, a constant DC-component of the voltage u_{cf}^{γ} is not transferred to the DC link voltage Δu^{dc}. Moreover, since $C_{\mathrm{dc}} \gg C_{\mathrm{f}}$, the voltage change in the DC link can be neglected, and, thus, the assumption $u_{\mathrm{h}}^{\mathrm{dc}} = u_{\mathrm{l}}^{\mathrm{dc}} = \frac{u^{\mathrm{dc}}}{2}$ still holds.

It is shown that the introduced connection between the star-point of the filter capacitors and the midpoint of the DC link allows for a full parallel connection simultaneously on the DC and AC side of multiple grid inverters. The connection ensures that the DC link potential with respect to PE is no longer dependent on the switching states. This prevents uncontrollable circulating currents among parallel connected inverters. The main difference of the new topology compared to a standard grid inverter with a floating star-point is that a γ-current can flow, which increases the amplitude of the current ripple. However, this disadvantage can be compensated for by the high switching frequency.

In addition to the γ-component of the ripple current, a current i_{l}^{γ} with lower frequency can also flow. This current flow must be prevented. Firstly, it can cause an unbalanced DC link voltage. Secondly, with parallel connected grid inverters, the current would circulate between them, and, thus, cause losses and already constitute a base load for the inverters. Therefore, it is mandatory to control the γ-current i_{l}^{γ} as well. The modelling and control of the grid inverter will be discussed in the following sections.

2.5.3 Modelling

The model of the grid inverter with LC filter can be derived from Fig. 2.41. It is connected to the grid at the point of common coupling (PCC). The grid impedance is approximated by an RL model, whereby its parameters R_{g} and L_{g} are uncertain. It is assumed that all component values are identical in each phase. The dynamics in the (a, b, c)-reference frame is governed by the differential equations

$$\left.\begin{aligned}
\frac{\mathrm{d}}{\mathrm{d}t}\boldsymbol{i}_{\mathrm{l}}^{abc} &= \frac{1}{L_{\mathrm{f}}}\left(\boldsymbol{u}_{\mathrm{f}}^{abc} - (R_{\mathrm{f}}+R_{\mathrm{c}})\,\boldsymbol{i}_{\mathrm{l}}^{abc} + R_{\mathrm{c}}\,\boldsymbol{i}_{\mathrm{g}}^{abc} - \boldsymbol{u}_{\mathrm{cf}}^{abc}\right)\\
\frac{\mathrm{d}}{\mathrm{d}t}\boldsymbol{u}_{\mathrm{cf}}^{abc} &= \frac{1}{C_{\mathrm{f}}}\left(\boldsymbol{i}_{\mathrm{l}}^{abc} - \boldsymbol{i}_{\mathrm{g}}^{abc}\right)\\
\frac{\mathrm{d}}{\mathrm{d}t}\boldsymbol{i}_{\mathrm{g}}^{abc} &= \frac{1}{L_{\mathrm{g}}}\left(\boldsymbol{u}_{\mathrm{cf}}^{abc} + R_{\mathrm{c}}\,\boldsymbol{i}_{\mathrm{l}}^{abc} - (R_{\mathrm{g}}+R_{\mathrm{c}})\,\boldsymbol{i}_{\mathrm{g}}^{abc} - \boldsymbol{u}_{\mathrm{g}}^{abc} - \mathbf{1}_3\,u_{\mathrm{nm}}\right)\,,
\end{aligned}\right\} \tag{2.117}$$

where $\boldsymbol{i}_{\mathrm{l}}^{abc} = (i_{\mathrm{l}}^{a}, i_{\mathrm{l}}^{b}, i_{\mathrm{l}}^{c})^{\top}$ are the filter currents through the inductances L_{f}, $\boldsymbol{u}_{\mathrm{cf}}^{abc} = (u_{\mathrm{cf}}^{a}, u_{\mathrm{cf}}^{b}, u_{\mathrm{cf}}^{c})^{\top}$ denotes the voltages across filter capacitances C_{f}, and $\boldsymbol{i}_{\mathrm{g}}^{abc} = (i_{\mathrm{g}}^{a}, i_{\mathrm{g}}^{b}, i_{\mathrm{g}}^{c})^{\top}$ are the grid-side currents. The voltage u_{nm} is defined in (2.111) and is the potential difference between the midpoint M of the DC link and the neutral N of the grid.

As with the generator unit, the Clarke and Park transformation is used to transform the system into a rotating reference frame (see Appendix A.1 and A.2). As described in the previous section, in this case, it is essential to apply the full transformations, including the γ-component. The angle ϕ_{g} of the grid voltages $\boldsymbol{u}_{\mathrm{g}}^{abc}$, which is necessary for the Park transformation, is estimated by means of a phase-locked loop (PLL) [80, Sec. 10.3.4],[156, 157]. Thereby, the d-axis is aligned with the grid voltage vector. The dynamics in the synchronously rotating (d, q, γ)-reference frame are given by (see Appendix A.3)

$$
\left.
\begin{aligned}
\frac{\mathrm{d}}{\mathrm{d}t}\boldsymbol{i}_\mathrm{l}^{dq\gamma} &= \frac{1}{L_\mathrm{f}}\Big(\boldsymbol{u}_\mathrm{f}^{dq\gamma} - \Big((R_\mathrm{f}{+}R_\mathrm{c})\,\boldsymbol{I}_3 + \omega_\mathrm{g}\,L_\mathrm{f}\,\boldsymbol{J}_0\Big)\,\boldsymbol{i}_\mathrm{l}^{dq\gamma} + R_\mathrm{c}\,\boldsymbol{i}_\mathrm{g}^{dq\gamma} - \boldsymbol{u}_\mathrm{cf}^{dq\gamma}\Big)\\
\frac{\mathrm{d}}{\mathrm{d}t}\boldsymbol{u}_\mathrm{cf}^{dq\gamma} &= \frac{1}{C_\mathrm{f}}\Big(\boldsymbol{i}_\mathrm{l}^{dq\gamma} - \omega_\mathrm{g}\,C_\mathrm{f}\,\boldsymbol{J}_0\,\boldsymbol{u}_\mathrm{cf}^{dq\gamma} - \boldsymbol{i}_\mathrm{g}^{dq\gamma}\Big)\\
\frac{\mathrm{d}}{\mathrm{d}t}\boldsymbol{i}_\mathrm{g}^{dq} &= \frac{1}{L_\mathrm{g}}\Big(\boldsymbol{u}_\mathrm{cf}^{dq} + R_\mathrm{c}\,\boldsymbol{i}_l^{dq} - \Big((R_\mathrm{c}{+}R_\mathrm{g})\,\boldsymbol{I}_2 + \omega_\mathrm{g}\,L_\mathrm{g}\,\boldsymbol{J}\Big)\,\boldsymbol{i}_\mathrm{g}^{dq} - \boldsymbol{u}_\mathrm{g}^{dq}\Big)\\
i_\mathrm{g}^{\gamma} &= 0\ \mathrm{A}\,,
\end{aligned}
\right\}
\tag{2.118}
$$

where ω_g denotes the angular grid frequency, and the coupling matrices are given by

$$
\boldsymbol{J}_0 \coloneqq \begin{bmatrix} 0 & -1 & 0\\ 1 & 0 & 0\\ 0 & 0 & 0 \end{bmatrix} \quad \text{and} \quad \boldsymbol{J} \coloneqq \begin{bmatrix} 0 & -1\\ 1 & 0 \end{bmatrix}. \tag{2.119}
$$

Notice that the voltage u_nm no longer appears. The voltage only influences the γ-component, but since $i_\mathrm{g}^{\gamma}{=}0$ A applies due to the star connection of the transformer, it does not need to be considered further.

With this, the state-space representation can be derived, which yields

$$
\left.
\begin{aligned}
\frac{\mathrm{d}}{\mathrm{d}t}\underbrace{\begin{pmatrix}\boldsymbol{i}_\mathrm{l}^{dq\gamma}\\ \boldsymbol{u}_\mathrm{cf}^{dq\gamma}\end{pmatrix}}_{=:\,\boldsymbol{x}_\mathrm{g}} &= \underbrace{\begin{bmatrix} -\dfrac{R_\mathrm{f}+R_\mathrm{c}}{L_\mathrm{f}}\boldsymbol{I}_3 - \omega_\mathrm{g}\,\boldsymbol{J}_0 & -\dfrac{1}{L_\mathrm{f}}\boldsymbol{I}_3\\ \dfrac{1}{C_\mathrm{f}}\boldsymbol{I}_3 & -\omega_\mathrm{g}\,\boldsymbol{J}_0 \end{bmatrix}}_{=:\,\boldsymbol{A}_\mathrm{g}} \begin{pmatrix}\boldsymbol{i}_\mathrm{l}^{dq\gamma}\\ \boldsymbol{u}_\mathrm{cf}^{dq\gamma}\end{pmatrix} + \underbrace{\begin{bmatrix} \dfrac{1}{L_\mathrm{f}}\boldsymbol{I}_3\\ \boldsymbol{O}_3 \end{bmatrix}}_{=:\boldsymbol{B}_\mathrm{g}} \boldsymbol{u}_\mathrm{f}^{dq\gamma} + \underbrace{\begin{bmatrix} \dfrac{R_\mathrm{c}}{L_\mathrm{f}}\boldsymbol{I}_3\\ -\dfrac{1}{C_\mathrm{f}}\boldsymbol{I}_3 \end{bmatrix}}_{=:\,\boldsymbol{E}_\mathrm{g}} \boldsymbol{i}_\mathrm{g}^{dq\gamma}\\
\underbrace{\begin{pmatrix} i_\mathrm{l}^{d}\\ i_\mathrm{l}^{q}\\ u_\mathrm{cf}^{\gamma}\end{pmatrix}}_{=:\,\boldsymbol{y}_\mathrm{g}} &= \underbrace{\begin{bmatrix} 1 & 0 & 0 & 0 & 0 & 0\\ 0 & 1 & 0 & 0 & 0 & 0\\ 0 & 0 & 0 & 0 & 0 & 1 \end{bmatrix}}_{=:\,\boldsymbol{C}_\mathrm{g}} \begin{pmatrix}\boldsymbol{i}_\mathrm{l}^{dq\gamma}\\ \boldsymbol{u}_\mathrm{cf}^{dq\gamma}\end{pmatrix}
\end{aligned}
\right\}
\tag{2.120}
$$

where $\boldsymbol{x}_\mathrm{g} \in \mathbb{R}^6$ is the state vector, $\boldsymbol{u}_\mathrm{f}^{dq\gamma} \in \mathbb{R}^3$ is the input vector and the voltages applied by the VSI, and $\boldsymbol{i}_\mathrm{g}^{dq\gamma} \in \mathbb{R}^3$ are the grid currents which is interpreted as a disturbance vector. The output vector $\boldsymbol{y}_\mathrm{g} \in \mathbb{R}^3$ is defined by the output matrix $\boldsymbol{C}_\mathrm{g}$. Since the currents i_l^{d} and i_l^{q} are to be controlled to set active and reactive power accordingly, these are defined as the outputs of the state-space model. In the previous section, it was already pointed out that the controller should prevent a current i_l^{γ} from flowing. However, it is not sufficient to control the current to zero due to measurement errors and especially an offset in the measured currents. The controller would keep the measured value at zero, but a current corresponding to the offset would flow. According to (2.112), this would cause the capacitor voltage u_cf^{γ} to drift away. By controlling this voltage to zero, the current i_l^{γ} is kept zero and prevented from flowing. Therefore, this voltage is defined as another output of the model so that a controller can be designed accordingly.

2.5.4 Proportional-Integral State Feedback Control

The advantage of the state-space representation is mainly based on the controller design. It allows for a state feedback controller of the generic form [94, Sec. 9.1]

$$\boldsymbol{u} = -\boldsymbol{K}\,\boldsymbol{x}\,, \tag{2.121}$$

where the states $\boldsymbol{x}$ are used to compute the input $\boldsymbol{u}$ of the system. Inserting this into the generic state-space representation leads to

$$\frac{\mathrm{d}}{\mathrm{d}t}\boldsymbol{x} = \underbrace{(\boldsymbol{A} - \boldsymbol{B}\,\boldsymbol{K})}_{=:\,\boldsymbol{A}_{\mathrm{cl}}}\,\boldsymbol{x}\,. \tag{2.122}$$

This results in a new closed-loop system with system matrix $\boldsymbol{A}_{\mathrm{cl}}$ whose eigenvalues and, thus, its dynamics can be determined as desired with the feedback matrix $\boldsymbol{K}$.

Here, the feedback matrix $\boldsymbol{K}$ is determined based on linear quadratic regulator (LQR) theory by solving the Riccati equation, which results from minimising the cost function [158, Sec. 10.4]

$$J = \int_0^\infty \boldsymbol{x}^\top \boldsymbol{Q}\,\boldsymbol{x} + \boldsymbol{u}^\top \boldsymbol{R}\,\boldsymbol{u}\;\mathrm{d}t\,, \tag{2.123}$$

where $\boldsymbol{Q}$ and $\boldsymbol{R}$ denotes the weighting matrices of the states $\boldsymbol{x}$ and the inputs $\boldsymbol{u}$, respectively. In the case of this grid inverter, the inputs are the three filter voltages $\boldsymbol{u}_{\mathrm{f}}^{dq\gamma}$.

Like the feedforward control in Sec. 2.4.2, which eliminates the cross-coupling between the d- and q-axes, a filter current decoupling controller $\boldsymbol{K}_{\mathrm{f}}$ is introduced here [159]. In addition, feedforward control is implemented with the capacitor voltages $\boldsymbol{u}_{\mathrm{cf}}^{dq}$. From (2.120), the cross-coupling terms can be identified, which leads to

$$\boldsymbol{K}_{\mathrm{f}} = L_{\mathrm{f}} \begin{bmatrix} 0 & -\omega_{\mathrm{g}} & 0 & \frac{1}{L_{\mathrm{f}}} & 0 & 0 \\ \omega_{\mathrm{g}} & 0 & 0 & 0 & \frac{1}{L_{\mathrm{f}}} & 0 \\ 0 & 0 & 0 & 0 & 0 & 0 \end{bmatrix}. \tag{2.124}$$

This decoupling matrix $\boldsymbol{K}_{\mathrm{f}}$ is multiplied with the system states $\boldsymbol{x}_{\mathrm{g}}$ and added to the system input voltages $\boldsymbol{u}_{\mathrm{f}}^{dq\gamma}$. This leads to the fact that the system matrix is modified to

$$\boldsymbol{A}_{\mathrm{g,m}} = \boldsymbol{A}_{\mathrm{g}} + \boldsymbol{B}_{\mathrm{g}}\,\boldsymbol{K}_{\mathrm{f}}\,. \tag{2.125}$$

For implementation on a real-time system, a discretisation of the controller must be carried out. The discrete state-space system is given by [78, Sec. 11.1.6]

$$\left.\begin{aligned} \boldsymbol{x}[k+1] &= \boldsymbol{A}_{\mathrm{g,d}}\,\boldsymbol{x}[k] + \boldsymbol{B}_{\mathrm{g,d}}\,\boldsymbol{u}_{\mathrm{f}}^{dq\gamma}[k] + \boldsymbol{E}_{\mathrm{g,d}}\,\boldsymbol{i}_{\mathrm{g}}^{dq\gamma}[k] \\ \boldsymbol{y}[k] &= \boldsymbol{C}_{\mathrm{g,d}}\,\boldsymbol{x}[k]\,, \end{aligned}\right\} \tag{2.126}$$

where $\boldsymbol{x}[k] \coloneqq \boldsymbol{x}(kT_{\mathrm{s}})$ denotes the quantities at the discrete instants of time, whereby $k \in \mathbb{N}$ and T_{s} is the sampling time. The discrete system matrices result from solving the differential equation of the continuous system by using the zero-order hold (ZOH) approximation of the system inputs. This approximation is sufficient for this case due to the high sampling rate. The discrete system matrices are given by [160, Sec. 4.3.3], [78, Sec. 11.1.6]

$$\left.\begin{aligned} \boldsymbol{A}_{\mathrm{g,d}} &= e^{\boldsymbol{A}_{\mathrm{g,m}}\,T_{\mathrm{s}}} \\ \boldsymbol{B}_{\mathrm{g,d}} &= \boldsymbol{A}_{\mathrm{g,m}}^{-1}\left(\boldsymbol{A}_{\mathrm{g,d}} - \boldsymbol{I}_6\right)\boldsymbol{B}_{\mathrm{g}} \\ \boldsymbol{E}_{\mathrm{g,d}} &= \boldsymbol{A}_{\mathrm{g,m}}^{-1}\left(\boldsymbol{A}_{\mathrm{g,d}} - \boldsymbol{I}_6\right)\boldsymbol{E}_{\mathrm{g}} \\ \boldsymbol{C}_{\mathrm{g,d}} &= \boldsymbol{C}_{\mathrm{g}}\,. \end{aligned}\right\} \tag{2.127}$$

In order to make the controller robust against the disturbances $\boldsymbol{i}_{\mathrm{g}}^{dq}$ and parameter uncertainties, an integral control action must be added. For this purpose, the system is extended by the integral state $\boldsymbol{z}_{\mathrm{g}} \in \mathbb{R}^3$ with [158, Sec. 8.6]

$$\begin{aligned} \boldsymbol{z}_{\mathrm{g}}[k+1] &= \boldsymbol{z}_{\mathrm{g}}[k] + T_{\mathrm{s}}\,\Big(\boldsymbol{y}_{\mathrm{g,ref}}[k] - \boldsymbol{y}_{\mathrm{g}}[k]\Big) \\ &= \boldsymbol{z}_{\mathrm{g}}[k] + T_{\mathrm{s}}\,\Big(\boldsymbol{y}_{\mathrm{g,ref}}[k] - \boldsymbol{C}_{\mathrm{g,d}}\,\boldsymbol{x}_{\mathrm{g}}[k]\Big)\,. \end{aligned} \tag{2.128}$$

Thus, the augmented and decoupled system is given by

$$\left.\begin{aligned} \underbrace{\begin{pmatrix} \boldsymbol{x}_{\mathrm{g}}[k+1] \\ \boldsymbol{z}_{\mathrm{g}}[k+1] \end{pmatrix}}_{=:\,\boldsymbol{\xi}_{\mathrm{g}}[k+1]} &= \underbrace{\begin{bmatrix} \boldsymbol{A}_{\mathrm{g,d}} & \boldsymbol{O}_{6\times 3} \\ -T_{\mathrm{s}}\,\boldsymbol{C}_{\mathrm{g,d}} & \boldsymbol{I}_3 \end{bmatrix}}_{=:\,\boldsymbol{A}_{\xi,\mathrm{d}}} \begin{pmatrix} \boldsymbol{x}_{\mathrm{g}}[k] \\ \boldsymbol{z}_{\mathrm{g}}[k] \end{pmatrix} + \underbrace{\begin{bmatrix} \boldsymbol{B}_{\mathrm{g,d}} \\ \boldsymbol{O}_3 \end{bmatrix}}_{=:\,\boldsymbol{B}_{\xi,\mathrm{d}}} \boldsymbol{u}_{\mathrm{f}}^{dq\gamma}[k] + \begin{bmatrix} \boldsymbol{E}_{\mathrm{g,d}} & \boldsymbol{O}_{6\times 3} \\ \boldsymbol{O}_3 & \boldsymbol{I}_3 \end{bmatrix} \begin{pmatrix} \boldsymbol{i}_{\mathrm{g}}^{dq\gamma}[k] \\ \boldsymbol{y}_{\mathrm{g,ref}}[k] \end{pmatrix} \\ \boldsymbol{y}_{\mathrm{g}}[k] &= \boldsymbol{C}_{\mathrm{g,d}}\,\boldsymbol{x}_{\mathrm{g}}[k]\,, \end{aligned}\right\} \tag{2.129}$$

where $\boldsymbol{\xi}_{\mathrm{g}} \in \mathbb{R}^9$ is the newly combined state vector.

To achieve a fast and direct response to a change of the reference $\boldsymbol{y}_{\mathrm{g,ref}}$, a proportional gain matrix $\boldsymbol{K}_{\mathrm{p}}$ is added. It can be derived from (2.129) if it is assumed that the disturbance is zero, and under steady-state conditions with $\boldsymbol{x}_{\mathrm{g}}[k+1] = \boldsymbol{x}_{\mathrm{g}}[k]$ and $\boldsymbol{y}_{\mathrm{g}}[k] = \boldsymbol{y}_{\mathrm{g,ref}}[k]$. This results in the state vector

$$\boldsymbol{x}_{\mathrm{g}}[k] = \left(\boldsymbol{I}_6 - \boldsymbol{A}_{\mathrm{g,d}}\right)^{-1}\,\boldsymbol{B}_{\mathrm{g,d}}\,\boldsymbol{u}_{\mathrm{f}}^{dq\gamma}[k]\,. \tag{2.130}$$

Inserting this into the output $\boldsymbol{y}_{\mathrm{g}}$ yields

$$\boldsymbol{u}_{\mathrm{f}}^{dq\gamma}[k] = \underbrace{\Big(\boldsymbol{C}_{\mathrm{g,d}}\,\left(\boldsymbol{I}_6 - \boldsymbol{A}_{\mathrm{g,d}}\right)^{-1}\,\boldsymbol{B}_{\mathrm{g,d}}\Big)^{-1}}_{=:\,\boldsymbol{K}_{\mathrm{p,d}}}\,\boldsymbol{y}_{\mathrm{g,ref}}[k]\,. \tag{2.131}$$

Combining all this yields the PI state feedback controller (PI-SFC)

$$\boldsymbol{u}_{\mathrm{f}}^{dq\gamma}[k] = \boldsymbol{K}_{\mathrm{p,d}}\,\Big(\boldsymbol{y}_{\mathrm{g,ref}}[k] - \boldsymbol{C}_{\mathrm{g,d}}\,\boldsymbol{x}_{\mathrm{g}}[k]\Big) + \boldsymbol{K}_{\mathrm{i,d}}\,\boldsymbol{z}_{\mathrm{g}}[k] - \underbrace{\left(\boldsymbol{K}_{\mathrm{x,d}} - \boldsymbol{K}_{\mathrm{f,d}}\right)}_{=:\,\boldsymbol{K}_{\mathrm{xf,d}}}\,\boldsymbol{x}_{\mathrm{g}}[k]\,, \tag{2.132}$$

where the decoupling matrix $\boldsymbol{K}_{\mathrm{f,d}}$ is the discretised matrix of $\boldsymbol{K}_{\mathrm{f}}$ with

$$\boldsymbol{K}_{\mathrm{f,d}} = \boldsymbol{A}_{\mathrm{g,m}}^{-1}\left(\boldsymbol{A}_{\mathrm{g,d}} - \boldsymbol{I}_6\right)\boldsymbol{K}_{\mathrm{f}}\,. \tag{2.133}$$

Rearranging and using the expanded state vector $\boldsymbol{\xi}_{\mathrm{g}}$ leads to

$$\boldsymbol{u}_{\mathrm{f}}^{dq\gamma}[k] = \boldsymbol{K}_{\mathrm{p,d}}\,\boldsymbol{y}_{\mathrm{g,ref}}[k] - \boldsymbol{K}_{\xi,\mathrm{d}}\,\boldsymbol{\xi}_{\mathrm{g}}[k] + \boldsymbol{K}_{\mathrm{f,d}}\,\boldsymbol{x}_{\mathrm{g}}[k]\,, \tag{2.134}$$

where $\boldsymbol{K}_{\xi,\mathrm{d}}$ is given by

$$\boldsymbol{K}_{\xi,\mathrm{d}} = \begin{bmatrix} \underbrace{(\boldsymbol{K}_{\mathrm{p,d}}\,\boldsymbol{C}_{\mathrm{g,d}} + \boldsymbol{K}_{\mathrm{x,d}})}_{=:\,\boldsymbol{K}_{\mathrm{px,d}}} & -\boldsymbol{K}_{\mathrm{i,d}} \end{bmatrix} . \tag{2.135}$$

Note that the decoupling matrix $\boldsymbol{K}_{\mathrm{f,d}}$ is not included in $\boldsymbol{K}_{\xi,\mathrm{d}}$ since it is already considered with the modified system matrix $\boldsymbol{A}_{\mathrm{g,m}}$. Therefore, it must not be considered in the controller design again.

The optimal feedback matrix $\boldsymbol{K}_{\xi,\mathrm{d}}$ can be determined by solving the Riccati equation for discrete systems, where a discrete form of (2.123) is used. A simple and reasonable choice for the matrices $\boldsymbol{Q}$ and $\boldsymbol{R}$ results from Bryson's rule [161, Sec. 5.2], [162, Sec. 21.7]. It recommends that the weighting matrices should be set as diagonal matrices with the diagonal elements

$$q_{ii} = \frac{1}{x_{i,\max}^2} \quad \text{and} \quad r_{jj} = \frac{1}{u_{j,\max}^2}\,, \tag{2.136}$$

with $i \in \{1, 2, \ldots, n_{\mathrm{g}}\}$, $j \in \{1, 2, \ldots, m_{\mathrm{g}}\}$, the number of states n_{g}, and the number of inputs m_{g}. $x_{i,\max}$ and $u_{j,\max}$ are the maximum expected values for the state i and the input j, respectively. Thus, the terms in the cost function (2.123) are such that the maximum expected value for each term is 1, making them all equivalent. This leads to a first good result for a controller. However, this should only be considered as a starting point. Further iterative changes to the weighting matrices combined with an understanding of the system dynamics will lead to good controller performance.

Once the feedback matrix $\boldsymbol{K}_{\xi,\mathrm{d}}$ has been determined, it can be split into the individual matrices $\boldsymbol{K}_{\mathrm{px,d}}$ and $\boldsymbol{K}_{\mathrm{i,d}}$ again. Note that $\boldsymbol{K}_{\xi,\mathrm{d}}$ contains the negative integral matrix $\boldsymbol{K}_{\mathrm{i,d}}$. The feedback matrix $\boldsymbol{K}_{\mathrm{xf,d}}$ used for the implementation can be calculated by

$$\boldsymbol{K}_{\mathrm{xf,d}} = \boldsymbol{K}_{\mathrm{x,d}} - \boldsymbol{K}_{\mathrm{f,d}} = \boldsymbol{K}_{\mathrm{px,d}} - \boldsymbol{K}_{\mathrm{p,d}}\,\boldsymbol{C}_{\mathrm{g,d}} - \boldsymbol{K}_{\mathrm{f,d}}\,. \tag{2.137}$$

To clarify the controller structure, a block diagram of the continuous PI-SFC is shown in Fig. 2.47. A more detailed block diagram for the discrete system is presented in the following section.

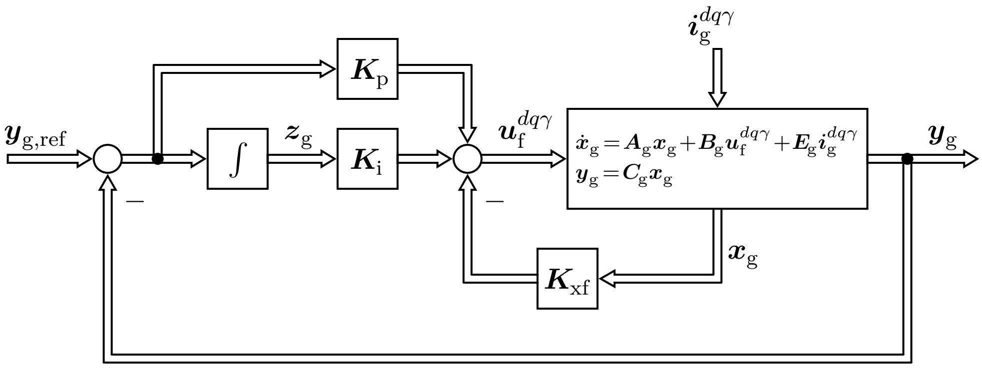

Figure 2.47: Block diagram of the continuous PI state feedback controller (PI-SFC).

2.5.5 Observer Design

For the PI-SFC, all system states $\boldsymbol{x}_{\mathrm{g}}$ are required. This includes all three currents $\boldsymbol{i}_{\mathrm{l}}^{dq\gamma}$ and voltages $\boldsymbol{u}_{\mathrm{cf}}^{dq\gamma}$. The currents are measured directly. The standard VDE-AR-N 4105 for grid inverters defines that the voltages $\boldsymbol{u}_{\mathrm{pcc}}^{abc}$ must be measured between the respective terminals of the phases and the neutral N [163, Sec. 6.5.1]. This is due to safety requirements. They are given by

$$\boldsymbol{u}_{\mathrm{pcc}}^{abc} = R_{\mathrm{g}}\,\boldsymbol{i}_{\mathrm{g}}^{abc} + L_{\mathrm{f}}\,\frac{\mathrm{d}}{\mathrm{d}t}\boldsymbol{i}_{\mathrm{g}}^{abc} + \boldsymbol{u}_{\mathrm{g}}^{abc}\,, \tag{2.138}$$

or in the (d, q, γ)-reference frame by

$$\boldsymbol{u}_{\mathrm{pcc}}^{dq\gamma} = R_{\mathrm{g}}\,\boldsymbol{i}_{\mathrm{g}}^{dq\gamma} + \omega_{\mathrm{g}}\,L_{\mathrm{f}}\,\boldsymbol{J}\,\boldsymbol{i}_{\mathrm{g}}^{dq\gamma} + L_{\mathrm{f}}\,\frac{\mathrm{d}}{\mathrm{d}t}\boldsymbol{i}_{\mathrm{g}}^{dq\gamma} + \boldsymbol{u}_{\mathrm{g}}^{dq\gamma}\,. \tag{2.139}$$

The voltages $\boldsymbol{u}_{\mathrm{cf}}^{dq\gamma}$ are not directly available for the controller, so they must be estimated with an observer. The proof of controllability and observability has already been published in [2] and [4].

Since the resistance R_{c} accounts for the equivalent series resistance of the capacitors, it is very small, and

$$\boldsymbol{u}_{\mathrm{cf}}^{dq\gamma} \approx \boldsymbol{u}_{\mathrm{c}}^{dq\gamma} \tag{2.140}$$

can be assumed. Furthermore, the line-to-line voltages of the capacitors and at the point of common coupling (PCC) are the same, which results in the fact that the d- and q-voltages are equal as well, meaning

$$\boldsymbol{u}_{\mathrm{pcc}}^{dq} = \boldsymbol{u}_{\mathrm{c}}^{dq}\,. \tag{2.141}$$

Therefore, only the γ-component u_{cf}^{γ} of $\boldsymbol{u}_{\mathrm{cf}}^{dq\gamma}$ needs to be estimated. This is achieved by a simplified Luenberger observer [78, Sec. 8.2]

$$\left.\begin{aligned}
\frac{\mathrm{d}}{\mathrm{d}t}\underbrace{\begin{pmatrix}\hat{u}_{\mathrm{cf}}^{\gamma}\\ \hat{i}_{\mathrm{l}}^{\gamma}\end{pmatrix}}_{=:\,\hat{\boldsymbol{x}}_{\mathrm{g}}} &= \underbrace{\begin{bmatrix}0 & \dfrac{1}{C_{\mathrm{f}}}\\ -\dfrac{1}{L_{\mathrm{f}}} & -\dfrac{R_{\mathrm{f}}+R_{\mathrm{c}}}{L_{\mathrm{f}}}\end{bmatrix}}_{=:\,\boldsymbol{A}_{\mathrm{o}}}\begin{pmatrix}\hat{u}_{\mathrm{cf}}^{\gamma}\\ \hat{i}_{\mathrm{l}}^{\gamma}\end{pmatrix} + \underbrace{\begin{pmatrix}0\\ \dfrac{1}{L_{\mathrm{f}}}\end{pmatrix}}_{=:\,\boldsymbol{B}_{\mathrm{o}}} u_{\mathrm{f}}^{\gamma} + \boldsymbol{L}\left(\boldsymbol{y}_{\mathrm{g}} - \hat{\boldsymbol{y}}_{\mathrm{g}}\right)\\
\hat{\boldsymbol{y}}_{\mathrm{g}} &= \underbrace{\begin{bmatrix}0 & 1\end{bmatrix}}_{=:\,\boldsymbol{C}_{\mathrm{o}}}\hat{\boldsymbol{x}}_{\mathrm{g}}\,,
\end{aligned}\right\} \tag{2.142}$$

where $\hat{\boldsymbol{x}}_{\mathrm{g}} \in \mathbb{R}^2$ are the estimated system states, $\boldsymbol{L} \in \mathbb{R}^{2\times1}$ is the observer feedback matrix, and $\hat{\boldsymbol{y}}_{\mathrm{g}} \in \mathbb{R}$ is estimated system output by the observer that will be compared to the measured system output $\boldsymbol{y}_{\mathrm{g}}$. With the feedback matrix $\boldsymbol{L}$, the dynamics of the observer can be influenced. This becomes clear when (2.142) is rearranged to

$$\frac{\mathrm{d}}{\mathrm{d}t}\hat{\boldsymbol{x}}_{\mathrm{g}} = \underbrace{(\boldsymbol{A}_{\mathrm{o}} - \boldsymbol{L}\,\boldsymbol{C}_{\mathrm{o}})}_{=:\,\boldsymbol{A}_{\mathrm{o,cl}}}\,\hat{\boldsymbol{x}} + \boldsymbol{B}_{\mathrm{o}}\,u_{\mathrm{f}}^{\gamma} + \boldsymbol{L}\,\boldsymbol{y}_{\mathrm{g}}\,. \tag{2.143}$$

The eigenvalues of the closed-loop system and, thus, the dynamics of the observer can be determined as desired with the feedback matrix $\boldsymbol{L}$, analogue to the state feedback controller. Note that the position of the feedback matrix $\boldsymbol{L}$ in the closed-loop system matrix $\boldsymbol{A}_{\mathrm{o,cl}}$ is different from (2.122). To be able to use known synthesis methods like LQR to determine the feedback matrix $\boldsymbol{L}$, the transposed form [158, Sec. 8.8.2]

$$(\boldsymbol{A}_{\mathrm{o}} - \boldsymbol{L}\,\boldsymbol{C}_{\mathrm{o}})^{\top} = \boldsymbol{A}_{\mathrm{o}}^{\top} - \boldsymbol{C}_{\mathrm{o}}^{\top}\,\boldsymbol{L}^{\top} \tag{2.144}$$

can be used. Finally, for the implementation of the observer, the system must be discretised by means of (2.127), which leads to

$$\hat{\boldsymbol{x}}[k+1] = \boldsymbol{A}_{\mathrm{o,cl,d}}\,\hat{\boldsymbol{x}}[k] + \boldsymbol{B}_{\mathrm{o,d}}\,u_{\mathrm{f}}^{\gamma}[k] + \boldsymbol{L}_{\mathrm{d}}\,i_{\mathrm{l}}^{\gamma}[k]\,. \tag{2.145}$$

The block diagram of the discrete PI-SFC in combination with the discrete observer is shown in Fig. 2.48.

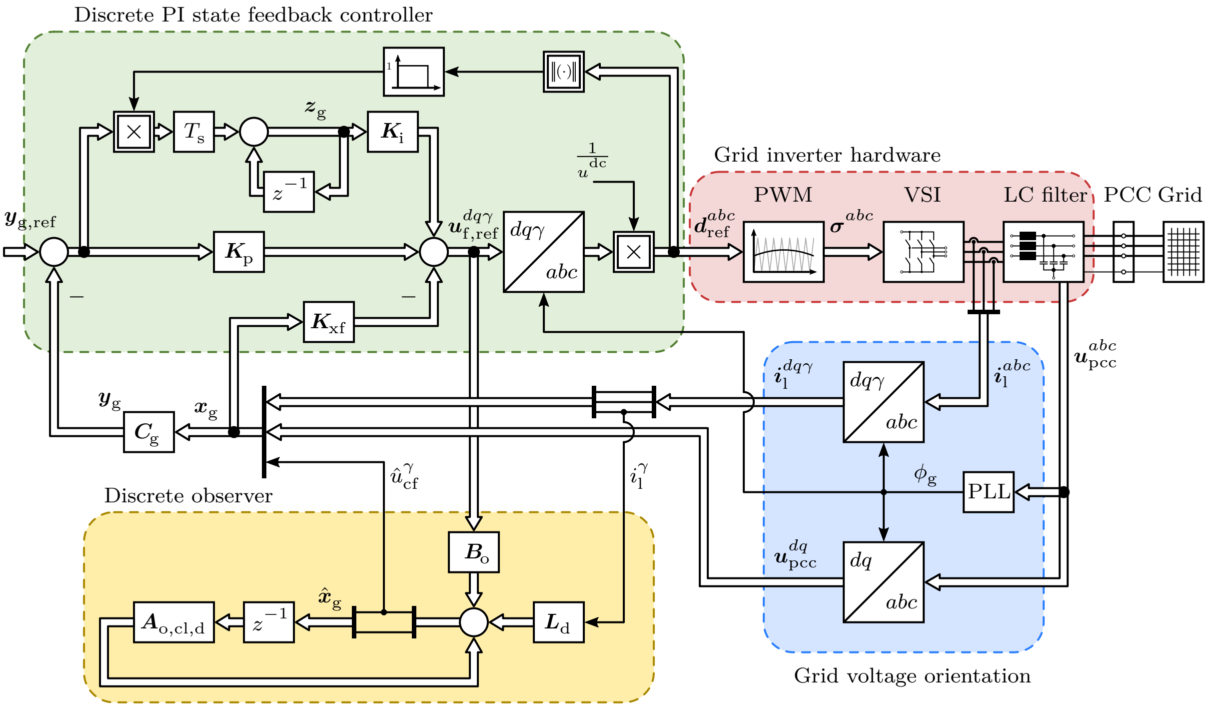

Figure 2.48: Block diagram of the control loop with PI state feedback controller (PI-SFC) and observer.

2.5.6 Implementation

The computation of the feedback matrix using the Riccati equation is complex and usually performed offline. It is also not easy to include the computation in the preprocessor environment of the integrated development environment (IDE) of the microcontroller. Therefore, MATLAB is used to compute the elements of the controller matrices $\boldsymbol{K}_{\mathrm{p,d}}$, $\boldsymbol{K}_{\mathrm{i,d}}$, and $\boldsymbol{K}_{\mathrm{xf,d}}$, as well as the matrices $\boldsymbol{A}_{\mathrm{o,cl,d}}$, $\boldsymbol{B}_{\mathrm{o,d}}$, and $\boldsymbol{L}_{\mathrm{d}}$, which are required for the observer.
First, the previously derived system matrices $\boldsymbol{A}_{\xi,\mathrm{d}}$ and $\boldsymbol{B}_{\xi,\mathrm{d}}$ and the weighting matrices $\boldsymbol{Q}$ and $\boldsymbol{R}$ must be defined. With the MATLAB command *dlqr*, the discrete feedback matrix $\boldsymbol{K}_{\xi,\mathrm{d}}$ can be designed from the discrete system as follows [164].

```
Q = diag(q_i,q_i,q_i,q_u,q_u,q_u,q_int,q_int,q_int);
R = diag(r_u,r_u,ru);

K_xi_d = dlqr(A_xi_d, B_xi_d, Q, R, T_s);
```

To split the matrix $\boldsymbol{K}_{\xi,\mathrm{d}}$, the matrices $\boldsymbol{K}_{\mathrm{p,d}}$ and $\boldsymbol{K}_{\mathrm{f,d}}$ are required. With (2.131), (2.135) and (2.137), the three required matrices can be computed as follows.

```
[num_x,num_u] = size(B_d);
[num_y,~] = size(C_d);
[~,num_e] = size(E_d);
```

```
K_p_d  = inv( C_d / (eye(size(A_d)) - A_d) * B_d );
K_xf_d =  K_xi_d(:,1:num_x)  -  K_p_d * C_d  -  K_f_d;
K_i_d  = -K_xi_d(:,(num_x+1):end);
```

To implement the PI-SFC for the embedded system in the C programming language, the matrix multiplications must be performed element by element. This can be achieved by a cascaded for-loop. However, not every multiplication is necessary since many elements in the matrices are zero or very small. By omitting them, a lot of computing time can be spared. For this purpose, an automated code generation is implemented, where matrix multiplication is performed element-wise, and coefficients smaller than a certain tolerance (e.g. 10^{-7}) are neglected. This can be implemented with the function *fprintf* to write the code to a file, which results in the following structure.

```
for row = 1:num_u

   fprintf('u_f_dqga_ref[%i] = 0.0;\n', row-1);

   for col = 1:num_y
      if abs(K_p_d(row,col)) > tol
         fprintf('u_f_dqga_ref[%i] += %e * e[%i];\n',...
            row-1, K_p_d(row,col), col-1);
      end
   end

   for col = 1:num_y
      if abs(K_i_d(row,col)) > tol
         fprintf('u_f_dqga_ref[%i] += %e * z[%i];\n',...
            row-1, K_i_d(row,col), col-1);
      end
   end

   for col = 1:num_x
      if abs(K_xf_d(row,col)) > tol
         fprintf('u_f_dqga_ref[%i] -= %e * x[%i];\n', ...
            row-1, K_xf_d(row,col), col-1);
      end
   end

end
```

The code for the observer can be generated in the same way. The resulting code can be copied to the correct place. However, it is more practical to include the remaining code of the controller in the code generation so that a separate C-file can be created. This avoids copying errors when adapting or tuning the controller.
The integration for the added integral states is implemented by means of the rectangular rule, which yields

$$\left.\begin{aligned} e_{\mathrm{g},i}[k] &= y_{\mathrm{g,ref},i}[k] - y_{\mathrm{g},i}[k] \\ z_{\mathrm{g},i}[k] &= z_{\mathrm{g},i}[k-1] + f_{\mathrm{aw}}\left(0, \left\| \boldsymbol{u}_{\mathrm{f,ref}}^{dq\gamma}[k-1] \right\|, \tfrac{u^{\mathrm{dc}}}{2}\right) T_{\mathrm{s}}\, e_{\mathrm{g},i}[k]\,. \end{aligned}\right\} \tag{2.146}$$

The anti-windup function is defined by

$$f_{\mathrm{aw}}(u_{\min}, u, u_{\max}) = \begin{cases} 1 & , u_{\min} \leq u_{\sigma,\mathrm{ref}} \leq u_{\max} \\ 0 & , \text{otherwise}\,. \end{cases} \tag{2.147}$$

2.5.7 Experimental Results

In this section, measurement results with the described PI-SFC are presented and compared to a classical PI controller for various grid conditions. The classical PI controller is similarly implemented as the controller for the generator unit introduced in Sec. 2.4.2. Also, a feedforward control with the capacitor voltages $\boldsymbol{u}_{\mathrm{pcc}}^{dq\gamma}$ is implemented. The block diagram of the experimental setup is shown in Fig. 2.49. The DC link of the grid inverter is connected to a bidirectional DC source that holds the DC link voltage u^{dc} constant at 800 V. A grid simulator with six additional inductors is used to simulate different grid conditions. The inductors are connected between the grid simulator and the grid inverter. With the grid simulator, the grid voltages $\boldsymbol{u}_{\mathrm{g}}^{abc}$ can be set as desired. One inductor has an inductance of 1000 μH and a resistance of 25 mΩ. To vary the impedance, two inductors per phase can be used to simulate a grid inductance of 500 μH or 2000 μH by connecting them in parallel or series, respectively. Additional current and voltage sensors are installed between the grid impedance and the grid inverter to measure the currents $\boldsymbol{i}_{\mathrm{g}}^{dq}$ and the voltages $\boldsymbol{u}_{\mathrm{pcc}}^{abc}$. The analogue sensor signals are converter by a dSPACE box and sent to a computer, which records the data. The computer is also connected to the grid inverter from which the reference currents $\boldsymbol{i}_{l,\mathrm{ref}}^{dq}$ can be set, and the resulting inductance currents $\boldsymbol{i}_{\mathrm{l}}^{dq\gamma}$ can be recorded as well.

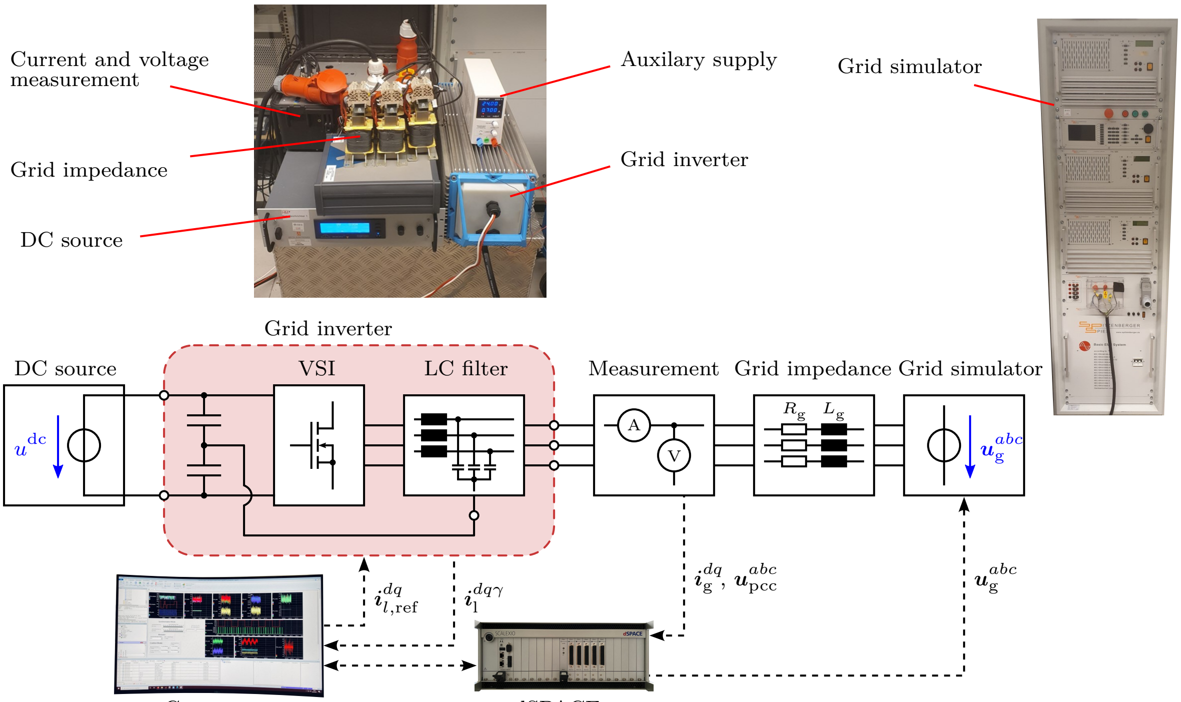

Figure 2.49: Block diagram of the experimental setup.

The parameters of the grid inverter, the elements of the weighting matrices, and the control parameter for the classical PI controller are shown in Table 2.3. The diagonal elements in the weighting matrices $\boldsymbol{Q}$ and $\boldsymbol{R}$ are chosen according to Bryson's rule and subsequently tuned.
Figure 2.50 show the measurement results for the PI [—] and the PI-SFC [—] under normal grid conditions with a grid inductance of 500 μH and a grid resistance of 12.5 mΩ. The first subplot shows the measured grid voltages $\boldsymbol{u}_{\mathrm{g}}^{abc}$ provided by the grid simulator. In this case, normal grid conditions with symmetrical and ideal sinusoidal voltages are provided.
The next three subplots show the currents $\boldsymbol{i}_{\mathrm{l}}^{dq\gamma}$. The reference current vector $\boldsymbol{i}_{l,\mathrm{ref}}^{dq}$ is chosen such that each quadrant occurs once and only one reference step occurs at a time. This allows for analysis of the control performance in steady-state and transient conditions as well as the cross-coupling behaviour. The current i_{l}^{γ} is shown in the fourth subplot. By controlling the voltage u_{c}^{γ} to zero, it is also indirectly controlled to be zero according (2.112). The observed

Table 2.3: Parameter of the grid inverter, the PI-SFC and the classical PI controller.

Name	Parameter	Value
DC link voltage	u^{dc}	800 V
Nominal current	$i_{\mathrm{l,nom}}$	7.5 A
Nominal power	$p_{\mathrm{ac,nom}}$	5.2 kW
Filter resistance	R_{f}	130 mΩ
Filter inductance	L_{f}	820 μH
Equivalent series resistance	R_{c}	5 mΩ
Filter capacitance	C_{f}	9.4 μF
Grid frequency	f_{g}	50 Hz
RMS grid voltage	U_{g}	230 V
Grid resistance	R_{g}	{12.5 mΩ, 25 mΩ, 50 mΩ}
Grid inductance	L_{g}	{500 μH, 1000 μH, 2000 μH}
Switching frequency	f_{sw}	70 kHz
Sampling frequency	$f_{\mathrm{s}} = \frac{1}{T_{\mathrm{s}}}$	35 kHz
Current weighting	q_{i}	$0.25/i_{\mathrm{max}}^2$
Voltage weighting	q_{u}	$0.01/u_{\mathrm{max}}^2$
Integral weighting	q_{int}	10^5
Input weighting	r_{u}	$10/u_{\mathrm{max}}^2$
Maximum current	i_{max}	12 A
Maximum voltage	u_{max}	350 V
P-gain of the PI controller	$\boldsymbol{k}_{\mathrm{p,d}}^{dq\gamma}$	7.175 $\frac{\mathrm{V}}{\mathrm{A}}$
I-gain of the PI controller	$\boldsymbol{k}_{\mathrm{i,d}}^{dq\gamma}$	0.448 $\frac{\mathrm{V}}{\mathrm{A}}$

voltage $\hat{u}_{\mathrm{cf}}^{\gamma}$ is shown in the fifth subplot. As it has not been implemented for the PI controller, it is only shown for the PI-SFC [—].

The PI-SFC shows less overshoot in both the d- and q- components of the inductor currents $\boldsymbol{i}_l^{dq}$ compared to the PI controller. It also shows improved decoupling capability, visible at 50 ms. In addition, ringing in i_{l}^{γ} can be damped significantly better with the LQR design. Notice that the current i_{l}^{γ} is not zero stationary, which is based on the offset in the current measurement. To avoid drifting in the voltage u_{c}^{γ}, the current i_{l}^{γ} must indeed be zero. This is not possible by simply controlling the current to zero since there is always a little offset in the current measurement. This would always cause a small γ-current, leading to a drift in the γ-voltage. Hence, it is essential to control the voltage u_{c}^{γ} to zero. The voltage can be well controlled to zero, which can be seen from the observed voltage $\hat{u}_{\mathrm{cf}}^{\gamma}$, as it only shows minimal fluctuations of less than 5 V.

The grid currents $\boldsymbol{i}_{\mathrm{g}}^{dq}$ are shown in the lower two subplots. The classical PI controller also shows a larger overshoot here than the LQR, which is even larger than for the inductance currents $\boldsymbol{i}_l^{dq}$. As the inductance currents $\boldsymbol{i}_l^{dq}$ are controlled, the grid currents $\boldsymbol{i}_{\mathrm{g}}^{dq}$ results from the inductance currents $\boldsymbol{i}_l^{dq}$ minus the capacitor currents $\boldsymbol{i}_{\mathrm{c}}^{dq}$. In the controller design, the grid currents are interpreted as a disturbance. Hence, a static deviation between the inductance currents $\boldsymbol{i}_l^{dq}$ and the grid currents $\boldsymbol{i}_{\mathrm{g}}^{dq}$ are caused by the capacitor currents $\boldsymbol{i}_{\mathrm{c}}^{dq}$. This becomes clear by considering

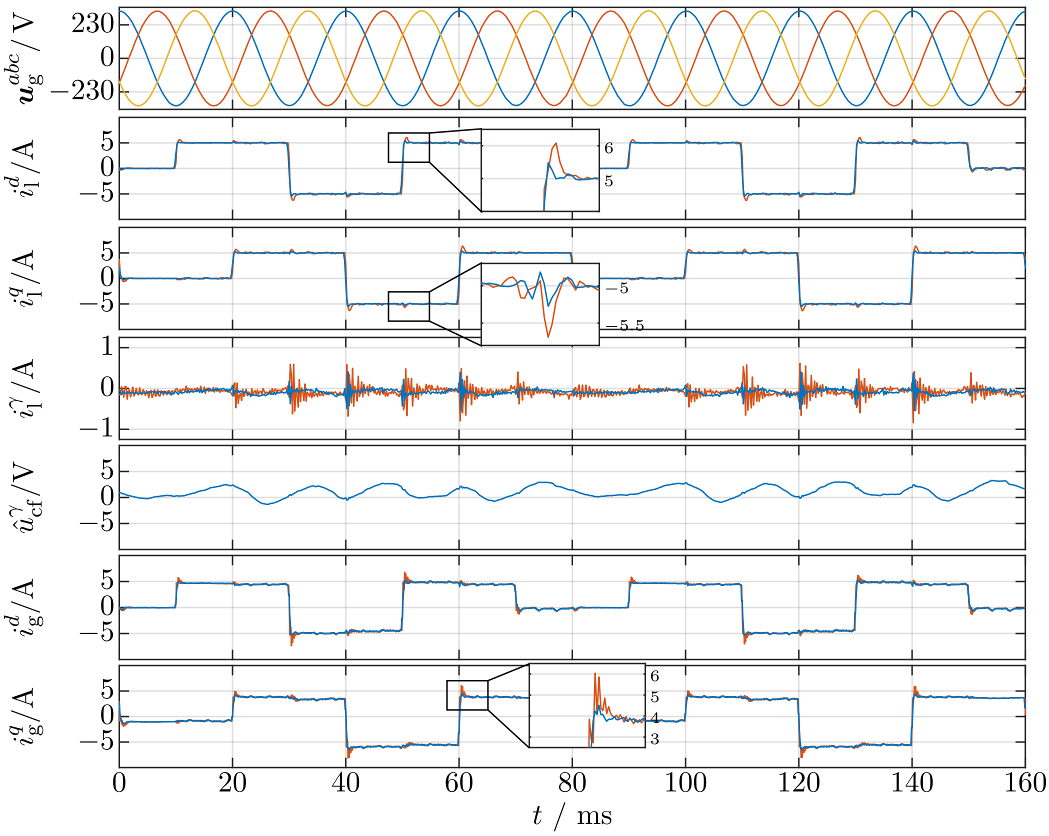

Figure 2.50: Measurement results of the PI controller [—] and the PI-SFC [—] under normal grid conditions with a grid inductance of 500 μH.

the steady-state in (2.118) with $\boldsymbol{i}_l^{dq} = 0$ A and $R_c = 0$ mΩ, which leads to

$$\boldsymbol{i}_c^{dq} = -\boldsymbol{i}_g^{dq} = \omega_g\, C_f\, \boldsymbol{J} \left(\boldsymbol{u}_g^{dq} + R_g\, \boldsymbol{i}_g^{dq} + \omega_g\, L_g\, \boldsymbol{J}\, \boldsymbol{i}_g^{dq} \right) . \tag{2.148}$$

Inserting the steady-state condition of the voltages $\boldsymbol{u}_{pcc}^{dq\gamma}$ from (2.139) leads to

$$\boldsymbol{i}_c^{dq} = \omega_g\, C_f\, \boldsymbol{J}\, \boldsymbol{u}_{pcc}^{dq} . \tag{2.149}$$

The steady-state capacitor currents $\boldsymbol{i}_c^{dq}$ are therefore mainly dependent on the voltages $\boldsymbol{u}_{pcc}^{dq}$. Note that due to the voltage orientation, the q-component of this voltage is zero under normal conditions, which leads to

$$i_c^q = \omega_g\, C_f\, u_{pcc}^d . \tag{2.150}$$

This reactive current will flow constantly. This is also the current that must be compensated for by adding it to the reference currents $\boldsymbol{i}_{l,\mathrm{ref}}^{dq}$ for the practical application.

In the next measurements, the grid voltages are no longer ideal and symmetrically. Instead, harmonic distortion, Fault-ride-through (FRT) condition, and a combination of both are to be emulated. The harmonic distortion is generated by adding the 5th harmonic with an amplitude of 5 % of the nominal voltage to the grid voltage. It is intended to imitate a non-perfect grid. During FRT conditions, a single-phase failure is emulated by setting one of the three grid voltages $\boldsymbol{u}_g^{abc}$ to zero. Such voltage dips can occur in the event of a fault in the grid, for example, due to short circuits in the transformer station or lightning strikes. In such a case, decentralised generation units must support the grid by continuing to supply electricity and not disconnect from the grid.

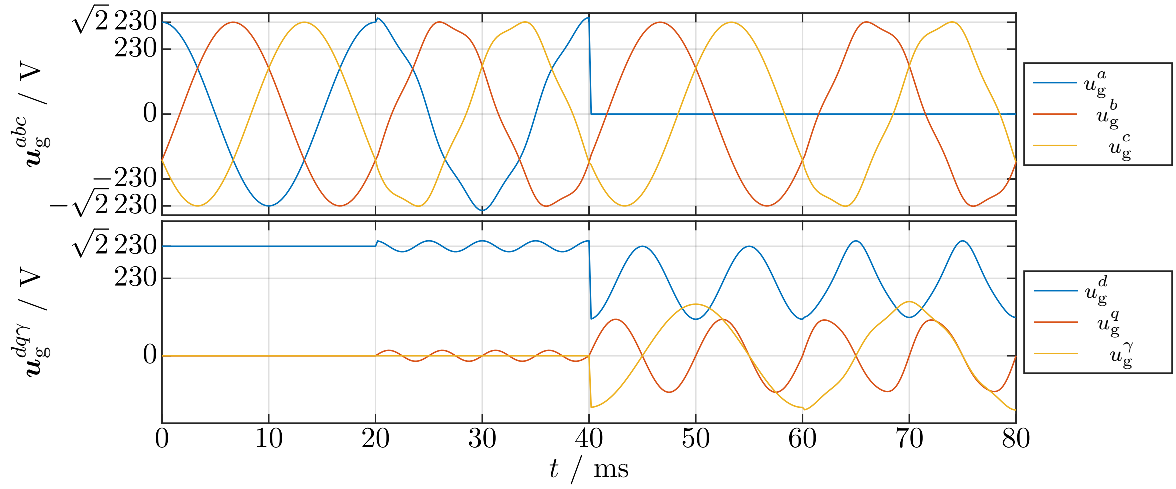

Figure 2.51: Illustration of the emulated scenarios of the grid voltages $\boldsymbol{u}_{\mathrm{g}}^{abc}$ in the first subplot, and the corresponding grid voltages $\boldsymbol{u}_{\mathrm{g}}^{dq\gamma}$ in the second subplot.

For the controller, these are additional disturbances against which it must be robust. Fig. 2.51 shows the four different scenarios, with the first subplot representing the voltages $\boldsymbol{u}_{\mathrm{g}}^{abc}$ in the (a, b, c)-reference frame, and the corresponding voltages $\boldsymbol{u}_{\mathrm{g}}^{dq\gamma}$ in the second subplot in the (d, q, γ)-reference frame. In the first period, the grid voltages are ideally sinusoidal. The (d, q, γ)-reference frame is voltage orientated, meaning that the d-axis is aligned with the grid voltage vector. Therefore, only the d-component of the voltages $\boldsymbol{u}_{\mathrm{g}}^{dq\gamma}$ is different from zero. During the subsequent period, harmonic distortion is enabled. This results in the voltages $\boldsymbol{u}_{\mathrm{g}}^{dq\gamma}$ also being superimposed with a sine wave. Note that the frequency of the harmonic in the (d, q, γ)-reference frame is reduced by the fundamental and is only 200 Hz due to the rotating reference frame. The FRT condition occurs in the third period, where the oscillations in the voltages $\boldsymbol{u}_{\mathrm{g}}^{dq\gamma}$ become larger, and it also affects the γ-component. The last section shows the combined scenario, which is the superposition of harmonic distortion and FRT for both reference frames.
Figure 2.52 shows the results of both controllers with the same grid impedance of 500 μH as the first results but under FRT conditions. Compared to the first measurement, the overshoot in the inductance currents $\boldsymbol{i}_{l}^{dq}$ is even higher for the PI controller under these conditions than before. In addition, the classical PI controller cannot keep the current i_{l}^{γ} steady. In contrast, the PI-SFC shows no significant difference from the previous results. The grid currents $\boldsymbol{i}_{l}^{dq}$ show small oscillations for both cases. According to the relation between the grid voltages $\boldsymbol{u}_{\mathrm{g}}^{dq}$ and the capacitor currents $\boldsymbol{i}_{\mathrm{c}}^{dq}$ from (2.149), the capacitor currents are oscillating as well. Since the inductance currents $\boldsymbol{i}_{l}^{dq}$ are controlled and therefore steady, the oscillations have to occur in the grid currents $\boldsymbol{i}_{\mathrm{g}}^{dq}$. It would be possible to control the grid currents $\boldsymbol{i}_{\mathrm{g}}^{dq}$ by employing an observer, but this is not desired here. It is intended to connect multiple grid inverters in parallel, and it is not possible for all inverters to simultaneously control the grid currents. Therefore, each inverter must primarily control its inductance currents $\boldsymbol{i}_{l}^{dq}$.
Figure 2.53 shows the results of FRT when the voltage of a phase is set to zero abruptly for 160 ms and then returns. The reference currents are constant with $i_{\mathrm{l,ref}}^{d} = -5$ A and $i_{\mathrm{l,ref}}^{q} = 0$ A. The voltage drop does not significantly affect the d- and q-components of the inductance currents for both controllers. However, they differ drastically in the γ-current i_{l}^{γ}. The PI-SFC is able to

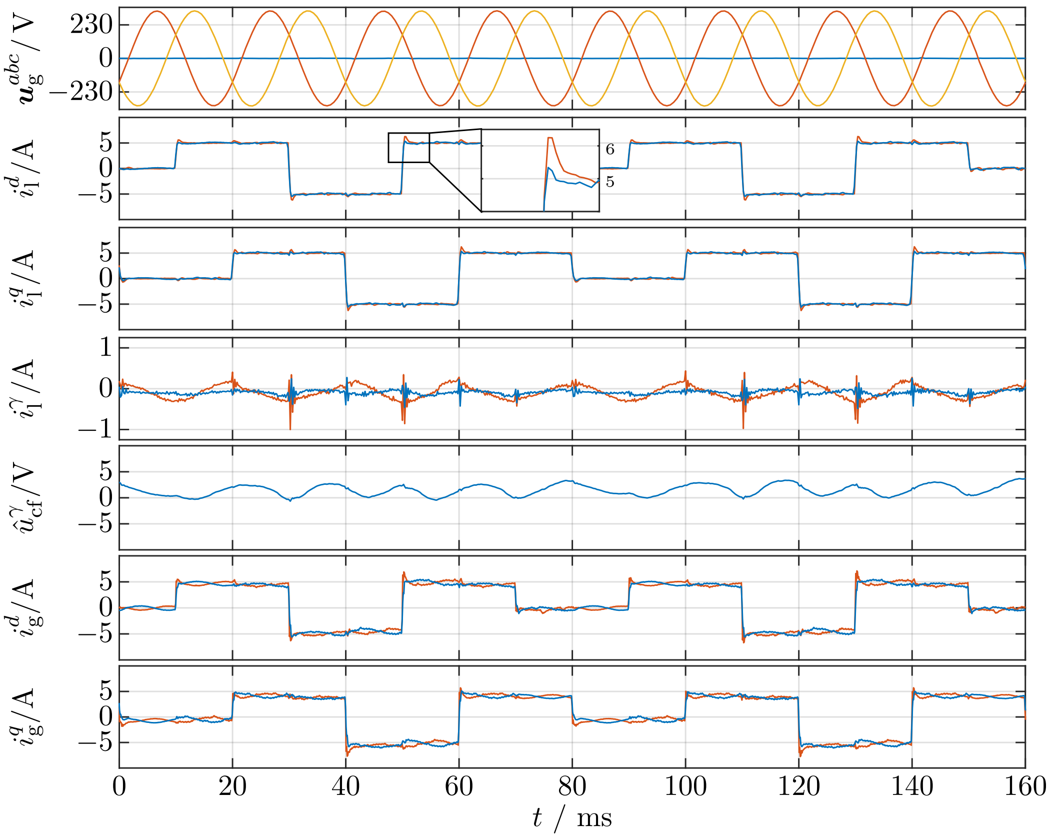

Figure 2.52: Measurement results of the PI controller [—] and the PI-SFC [—] under FRT conditions with a grid inductance of 500 μH.

keep the current stable, whereas the current shows an overshot with the classical PI controller. Moreover, during the FRT, the current keeps oscillating due to the introduced harmonics by the phase failure. For the grid currents $\boldsymbol{i}_g^{dq}$, both controllers show the same behaviour.
For the results in Fig. 2.54, the grid impedance is increased to 2000 μH, and the combined scenario with harmonic distortion and FRT conditions is applied. The PI-SFC again shows almost no change in the inductance currents $\boldsymbol{i}_1^{dq\gamma}$ compared to the previous measurements. This differs from the classical PI controller, whose overshoot has increased drastically. This can cause the overcurrent protection to trip, interrupting the grid inverter and causing it to stop operating. To avoid this, the permissible reference current has to be limited. Moreover, the midpoint current i_1^γ is affected by the harmonic distortion. This also has a significant effect on the grid currents. Due to the high grid impedance, the overshoot in the grid currents $\boldsymbol{i}_g^{dq}$ has increased again compared to the previous measurements. As with the inductance currents, hardly anything has changed in the case of the PI-SFC with the grid currents $\boldsymbol{i}_g^{dq}$. This shows the high robustness against variations of the grid impedance and disturbances on the grid voltages $\boldsymbol{u}_g^{dq\gamma}$.

2.5.8 Full Parallel Connection of Multiple Grid Inverters

The main purpose of the newly proposed grid inverter topology is to allow full parallel connection of the grid inverters. This means that they can be connected simultaneously on both the AC and DC sides. This feature is essential to ensure the modularity of the entire system. It is made possible by the unique connection between the star-point of the filter capacitors and the midpoint M of the DC link. In Section 2.5.2, it is shown that the dependence of the potential

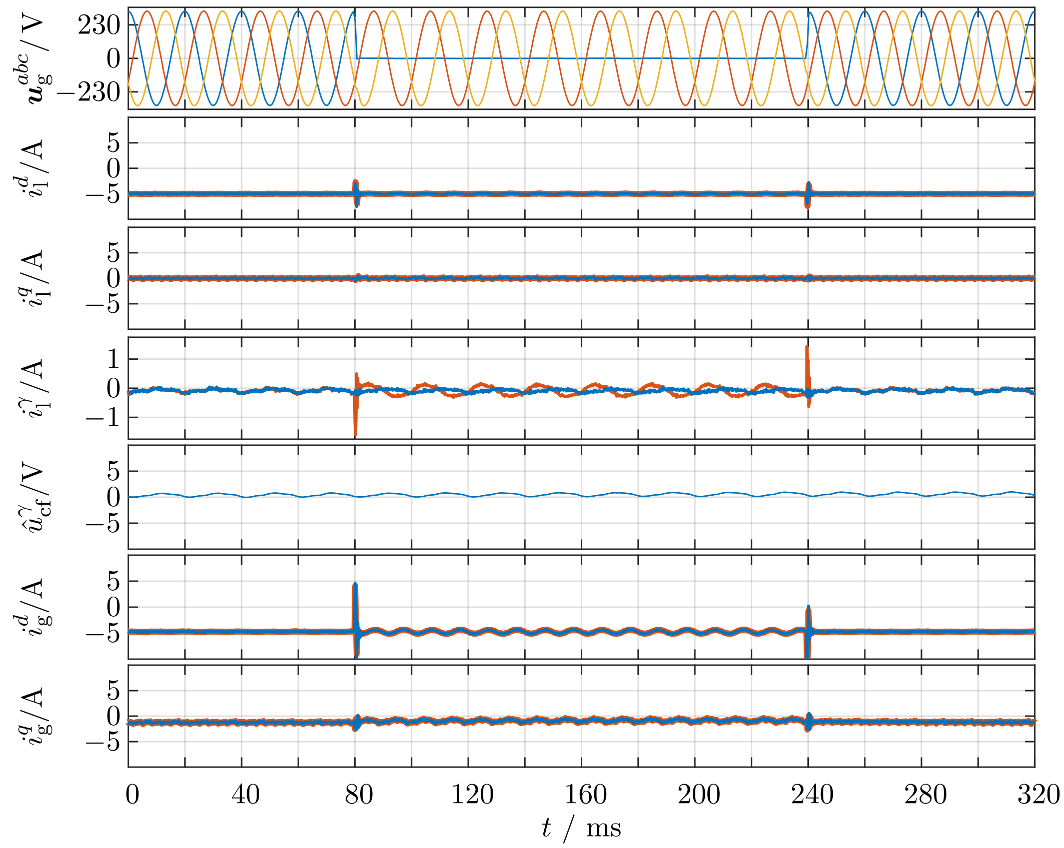

Figure 2.53: Measurement results of the PI controller [—] and the PI-SFC [—] with FRT condition and a grid inductance of 1000 μH.

between DC link and ground on the switching states of the MOSFETs is cancelled. With other topologies, this potential changes constantly according to the switching states, which makes a full parallel connection impossible due to an uncontrollable high current flow. A parallel connection could only be realised with further measures. For example, one transformer for each grid inverter on the grid side would be necessary to create galvanic isolation and thus compensate for the potential difference among the inverters. These 50 Hz transformers cost extra, are inefficient, heavy and take up a lot of installation space [118, Sec. 5], which makes this solution impractical.

Fig. 2.55 shows the topology of multiple in parallel connected grid inverters. Each inverter is connected to the DC link terminals DC+ and DC−, as well as to the PCC. Since the grid inverters are directly connected to each other in the aluminium profile or are near to each other, the impedances of the connections can be neglected.

Due to the star-point connection, the grid inverters can operate independently of each other. Therefore, the inductance currents $\boldsymbol{i}_l^{dq}$ can be controlled as with a single grid inverter since no external components were considered in the controller design. It is only necessary to ensure that the reference currents $\boldsymbol{i}_{l,\mathrm{ref}}^{dq}$ and, thus, the load are properly distributed. This is done using the DC link voltage u^{dc}, which is discussed in the next chapter. Likewise, the DC link voltage difference Δu_i^{dc} of the individual grid inverters is only depending on their respective voltage $u_{\mathrm{cf},i}^\gamma$ because the star-point connection is only internal to the device and is not connected to other devices. The transfer function (2.115) gives the relationship of the voltages, which still holds for the case of multiple parallel-connected grid inverters.

The only difference compared to the single grid inverter is that the voltage $u_{\mathrm{cf},i}^\gamma$ can now be

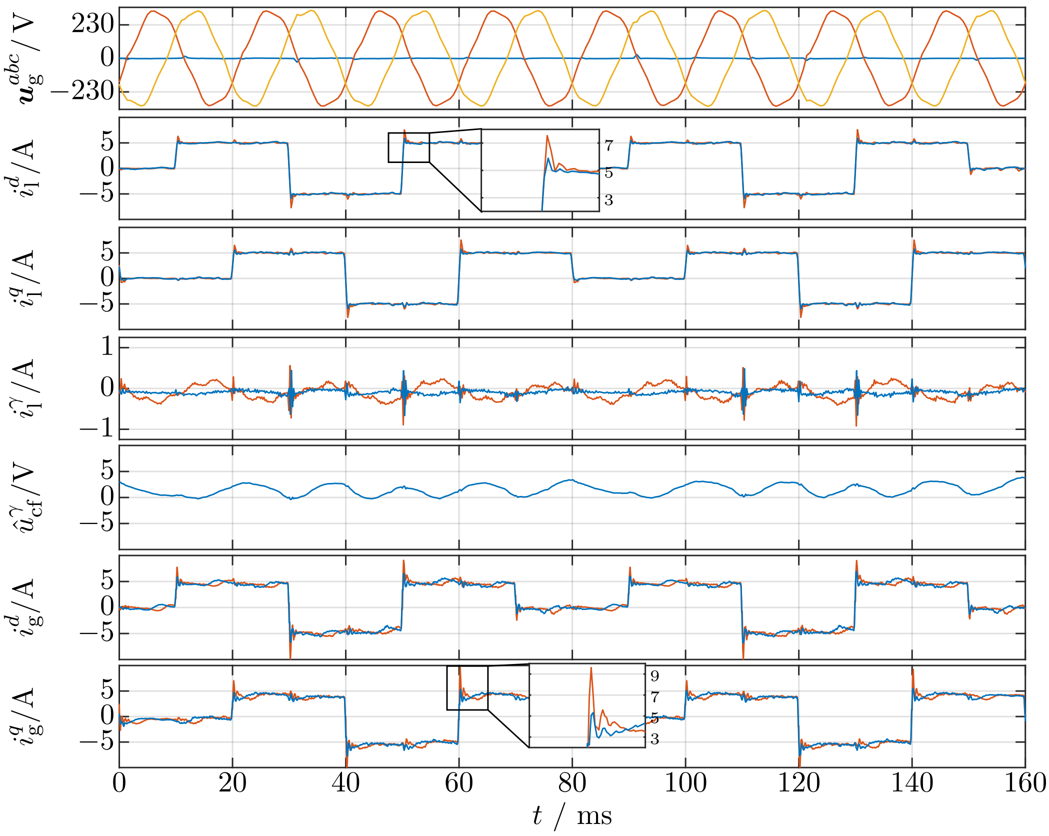

Figure 2.54: Measurement results of the PI controller [—] and the PI-SFC [—] with harmonic distortion and FRT condition and a grid inductance of 2000 μH.

influenced by all other grid inverters. Since no γ-current can flow into the grid ($i_g^\gamma = 0$ A), it can only flow between the grid inverters, which then affects the voltage $u_{cf,i}^\gamma$. The d- and q-components of the inductance currents $\boldsymbol{i}_1^{dq\gamma}$ can flow into the grid, so controlling those currents works without any further measures.

To prevent a γ-current flow, the capacitor's γ-voltage u_{cf}^γ is controlled in the case of a single inverter as described in Sec. 2.5.3. With current control, the current becomes not precisely zero due to the measurement error, which leads in a voltage drift. This problem is avoided by voltage control. However, when connected in parallel, not all inverters can control the voltage as they interfere, causing an undefined γ-current flow between them. The resulting current flows in a circle from one grid inverter to another and back via the DC link, which is why it is also called circulating current. To avoid this circulating current and its immense losses, only one grid inverter must take over the voltage control. All others must then control the γ-component of the inductance currents to zero.

In contrast, if they all control the γ-current, a residual current flows again due to the current offset in the measurement, as in the case of the single grid inverter. The only path for the residual current is through the filter capacitors, which would cause the voltage $u_{cf,i}^\gamma$ to drift.

With this control strategy, the inverter with voltage control must, therefore, compensate for the current of all other inverters. Since this current results only from minor offset errors, it can be ruled out that this inverter will reach its current limit. In addition, the offset error of the individual inverters is stochastically distributed around zero. This means that the current is also partially cancelled out between the inverters.

The correct control strategies can be selected automatically when the system is started. When the system is initialised, the communication system identifies the first grid inverter. This one can switch to voltage control during the initialisation process. The others then control the γ-current i_{l}^{γ} instead of the γ-voltage u_{cf}^{γ}. The design of the controller is the same as described in the previous section, except that the system output matrix $\boldsymbol{C}$ must be adjusted accordingly. This control keeps all γ-voltages $u_{\mathrm{cf},i}^{\gamma}$ of the filter capacitors C_{f} zero and prevents a circulation current. Thus, the assumption

$$i_{\mathrm{cm},i} = 0\ \mathrm{A} \tag{2.151}$$

holds, and

$$u_{\mathrm{h},i}^{\mathrm{dc}} = u_{\mathrm{l},i}^{\mathrm{dc}} = \frac{u^{\mathrm{dc}}}{2} \tag{2.152}$$

is still valid in the case of multiple parallel-connected grid inverters so that the DC link can be considered symmetrical. This is a relevant assumption for the DC link voltage and droop control described in the next chapter. A detailed model of the parallel connected grid inverters, a stability analyses and experimental results can be found in [4].

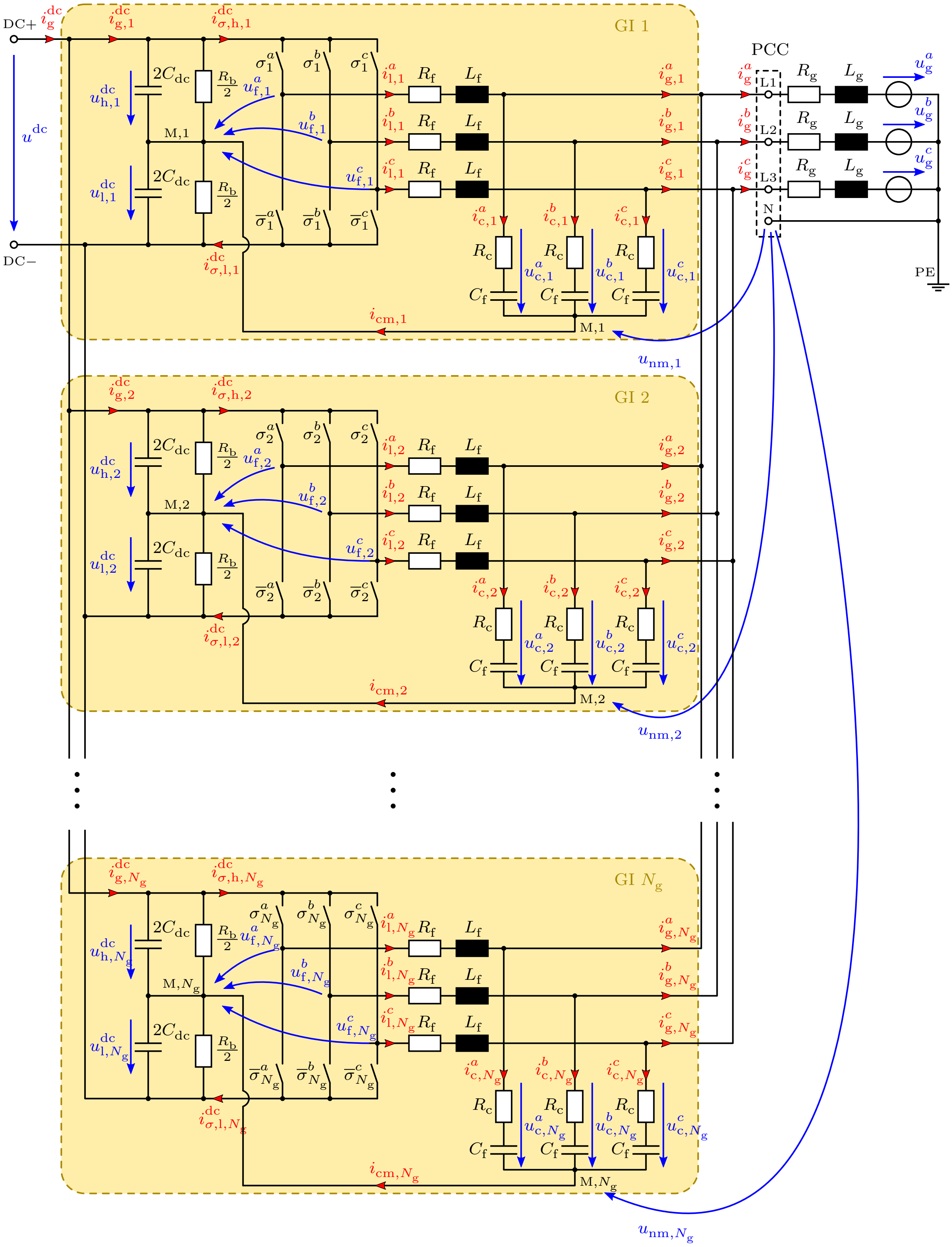

Figure 2.55: The electrical circuit of multiple parallel-connected grid inverters.

Chapter 3

Control of the Modular DC Grid

Most of our devices require direct current (DC), e.g., battery-powered devices such as laptops, LED lighting, monitors, information technology (IT) infrastructure, electric vehicles, etc. Traditional electrical grids, such as the synchronous grid in Continental Europe, use alternating current (AC) and distribute electricity over large areas. DC grids can help improve energy efficiency and reduce CO2 emissions by saving AC/DC conversions while ensuring excellent power quality [165]. When the term grid is mentioned here, it refers to the traditional distribution AC grid. DC link and DC grid are used interchangeably.

The interest in DC grids is also growing in the industry. The association ZVEI e.V., representing the economic, technological and environmental interests of the German electrical and digital industry, has developed a system concept for industrial DC grids within the projects “DC-INDUSTRIE” and “DC-INDUSTRIE2” [118].

In production facilities, many drives are required for machine tools, conveyor systems or robots, which are usually controlled via a frequency converter. These frequency converters, whether with diode rectifiers or in back-to-back converter configurations, already have an internal DC link [27]. Combining these individual DC links into a DC grid and incorporating energy storage systems (ESS), renewable energy sources (RES), and a connection to the AC grid brings many benefits. Recuperation energy from drives that would otherwise be dissipated in resistors can be stored or utilised directly by other loads. The energy storage in the DC grid can be used to bridge grid outages.

These projects aim to drive forward the energy supply of industrial facilities via an intelligent DC grid. Essential topics such as voltage levels or protection and earthing concepts are described, as well as the development of standards. The results of the projects are incorporated and further developed by the ZVEI working party “Open DC Alliance (ODCA)”, founded in November 2022 [166].

These DC grids are used as microgrids. A microgrid or minigrid – there is no clear distinction between those [167] – is a group of interconnected loads and generating units within clearly defined electrical boundaries that act as a single controllable unit for the distribution grid [168]. An essential advantage of microgrids is that they can operate grid-connected and in island mode. In case of a grid outage, the microgrid switches to island mode, disconnects from the grid and supplies the connected loads from the integrated energy storage units. When the grid is working again, the inverters synchronise and reconnect [167]. This offers the microgrid operator increased supply reliability.

Microgrids are seen as crucial elements for integrating renewable and decentralised energy. Energy generation will be increasingly decentralised through photovoltaic (PV) systems and wind turbines [167, 169]. Thus, power electronics will dominate grid dynamics instead of synchronous machines. In Sec. 3.1.1, it is discussed that decentralised generation can lead to stability problems in the grid, as its control concept is based on the presence of large synchronous machines that add inertia to the system. Microgrids are becoming increasingly crucial as generation, energy storage, consumption, control and management can be combined and decentralised while supporting the grid simultaneously [167, 170]. Microgrids can be realised as AC or DC grid, and both have pros and cons.

AC grids have prevailed over DC grids for the distribution grids in the past. The main reason for this was the simple realisation of transformers to generate higher voltages for the transmission of electrical energy [148]. AC grids are generally characterised by their simple design and operation. Plugs, sockets, switches and fuses are more straightforward because the direction of current changes with the grid frequency and, therefore, periodically crosses zero, thus avoiding dangerous arcing. The safety of users and components is guaranteed by proven protection concepts and protective devices. In DC grids, the problem is that arcs do not extinguish automatically when an active load is switched off. Active switching with an additional semiconductor is necessary for safe switching. Furthermore, protection and earthing concepts still need to be developed, standardised and extensively tested [118, 165].

For microgrids, however, DC offers significant advantages and gained popularity. The DC nature of renewable energy sources such as PV, fuel cells, wind turbines (connected via a voltage source inverter), and storage elements favours a DC microgrid as they can be integrated easily [118, Sec. 5], [170, 171].

The investment costs for establishing a DC grid can be higher than for an AC grid, as special equipment such as grid inverters, DC/DC converters and a new infrastructure are required. While DC is efficient for specific devices, converting DC to other voltages can be difficult and expensive, especially for transmission systems. For large offshore wind farms, however, there is a break-even distance at which high-voltage direct current (HVDC) transmission lines become cheaper. The break-even distance is currently around 50 km, and this technology will become increasingly lucrative as development continues [172]. A similar development can be expected for DC microgrids. Although the investment costs are higher, the return on investment is also achieved more quickly due to the higher system efficiency [118].

A DC grid has the advantage that renewable energies can be easily integrated, and the power supply to devices can be improved. The internal supplies of the individual functional components are already provided with DC, so a DC grid makes countless conversions obsolete and leads to lower material consumption and losses. In contrast to AC grids, no synchronisation is required, there is no reactive power flow, and the grid quality is better due to the possibility of continuous power flow [165, 169, 171]. The absence of reactive power flow also results in more efficient energy transmission. Moreover, the existing wire cross-sections can be utilised more efficiently as the skin effect is less pronounced [173, 174]. The skin effect describes the phenomenon of the magnetic field in the conductor forcing the charge carriers to the conductor's surface. This reduces the effective cross-section of the conductor, which is why the effective resistance increases approximately with the square root of the frequency [63, Sec. 10.4.1].

The DC grid developed here for integrating renewable energy sources (RES), particularly wave energy, is shown in Fig. 3.1. It consists of the highly modular power electronics system presented in the previous chapter. In Sec. 3.1, the droop control strategies to control AC and DC microgrids are presented. In Sec. 3.2, a detailed nonlinear model of the DC grid in the state-space representation is derived. Finally, a comprehensive stability and sensitivity analysis is carried out using the root locus method. The last Sec. 3.3 introduces power smoothing, which is crucial for sensible wave energy utilisation. According to Specification (S11), the DC grid should be able to smooth the fluctuating power of the WEC so that the power fed into the AC grid is as constant as possible.

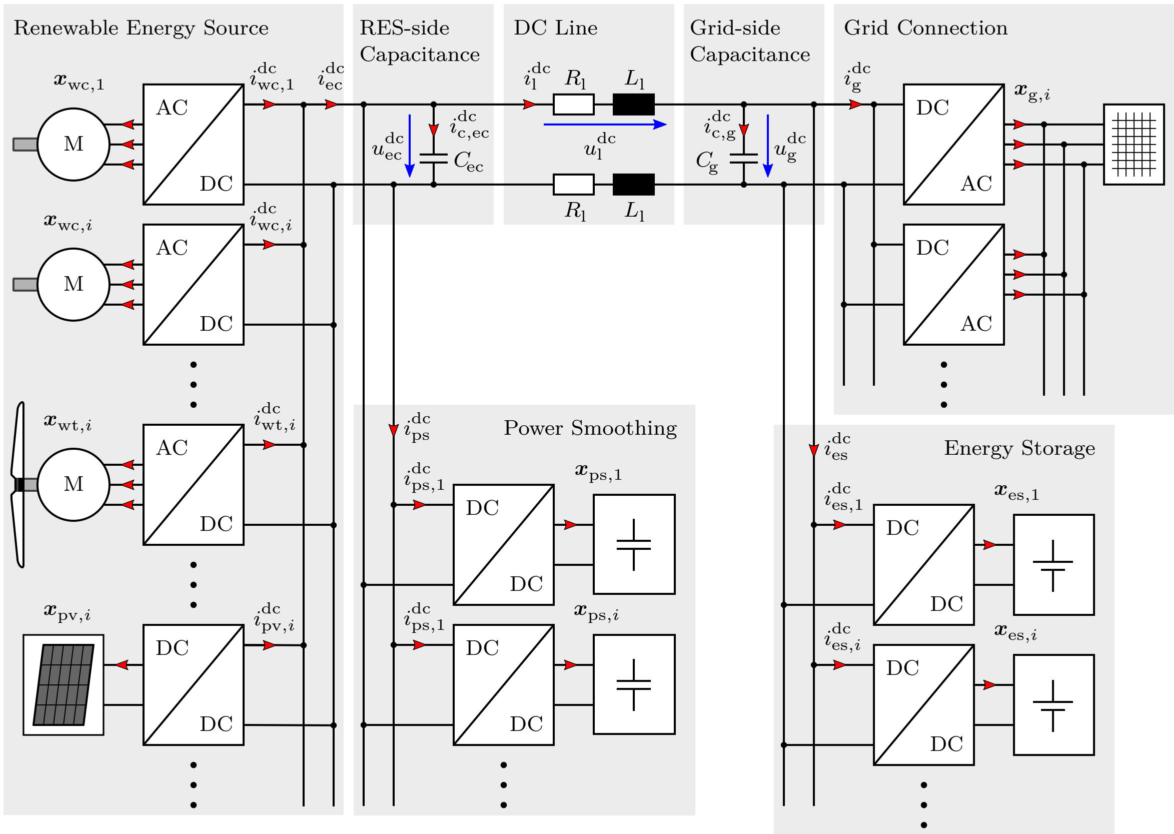

Figure 3.1: Electrical circuit of the developed DC grid for the integration of renewable energy sources, particularly wave energy.

3.1 Droop Control

Droop control, a control method for power sharing between generating units in grids, is pivotal in maintaining grid stability. The power is distributed among the units to ensure equal loading. This control method is derived from the inherent behaviour of traditional electrical grids, where a power imbalance can disrupt the grid frequency [169, 175]. For instance, if the power demand exceeds the generation capacity, the grid frequency decreases, and vice versa.
Droop control is a well-known control strategy for both AC and DC microgrids [167, 176]. It is used, for example, for uninterruptible power supplies (UPS) in DC grids for data centres where high reliability and power quality are required [170, 177–179]. UPS are used for IT systems to overcome a grid outage or to guarantee a reasonable time for a controlled shutdown.
In PV systems, the inverters must also adjust the power depending on the grid frequency. In the past, PV systems had to stop feeding into the grid abruptly at a frequency above 50.2 Hz and under 49.5 Hz. The massive installation of photovoltaic systems could have led to severe stability problems if all PV systems were to disconnect simultaneously. The term “50.2 Hz problem” was commonly used, as a disconnection is more likely due to overfrequency, as there is an excess of electrical energy on very sunny days [180]. Since 2011, the connection guidelines have stipulated that decentralised generating units, in general, must be able to reduce their power proportionally to the grid frequency above a frequency of 50.2 Hz, imitating the droop behaviour of the synchronous machines [181]. In addition, a law on retrofitting existing systems was passed in 2012 [182]. Fig. 3.2 shows a characteristic curve according to the current standard VDE-AR-N 4105 [163, Sec. 5.7.4.3].

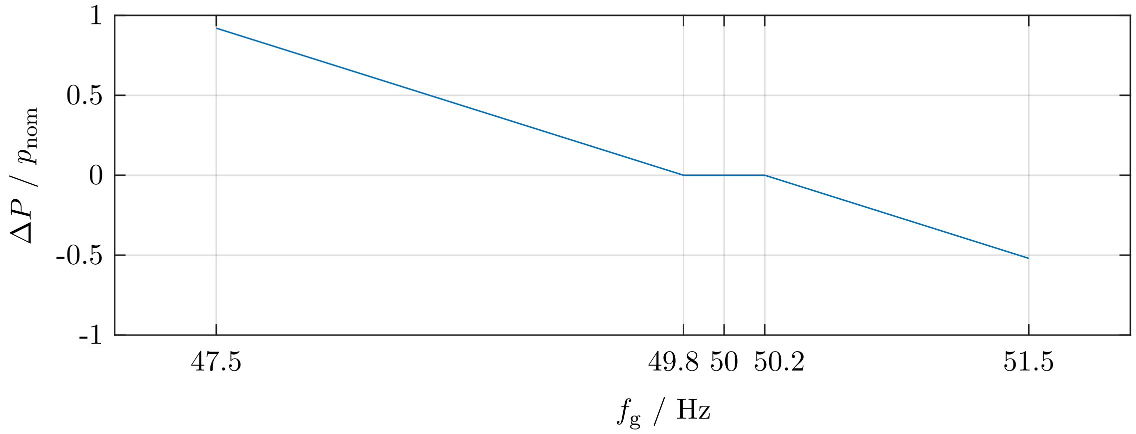

Figure 3.2: An exemplary characteristic droop curve for adjusting the active power in the event of over- or underfrequency according to the current standard VDE-AR-N 4105 [163, Sec. 5.7.4.3].

In the case of an overfrequency, there is an excess of generation power. Therefore, all generating units must reduce the active power to a maximum of 51.5 Hz. At grid frequencies $f_{\mathrm{g}} > 51.5$ Hz, the generating units must disconnect from the grid when they still deliver energy. The grid operator can specify the gradient of the curve so that, for example, a reduction of 100 % at 51.5 Hz can also be possible.
In the case of underfrequency, there is a deficit of generation power. All generating units must increase the currently generated active power at frequencies below 49.8 Hz with a gradient of $0.4\,p_{\mathrm{nom}}$ / Hz up to their technically possible maximum value. This is only possible with decentralised renewable energy sources if an energy storage systems (ESS) is integrated. At grid frequencies $f_{\mathrm{g}} < 47.5$ Hz, the generating and storage units must disconnect from the grid.
For distributed grids, a decentralised control strategy is essential. If the devices only use local measurements, it increases modularity, reliability and flexibility. It is desired that no communication system is required for grid control. Communication with the devices must generally be available for data analysis or software updates, but it should not be necessary for control. The failure of a necessary communication connection can lead to the failure of the corresponding unit, overloading other units, which can lead to the instability of the entire grid [167, 171]. In the literature, attempts are generally made to avoid the need for communication [169, 175, 179, 183–185].
With droop control, the frequency or voltage serves as the communication medium between the generating units and carries the information about the power flow [175, 179]. An additional, non-critical communication system can be integrated to improve system performance. As with distribution grids, a hierarchical control structure is generally adopted to operate microgrids, where several cascaded controllers are used [167, 171, 176, 186]. The controller on the first level, the primary controller, performs the most essential and time-critical control task. The higher the controller level, the slower the speed of the controller and the less critical its failure.
The primary controller is implemented locally and takes over voltage or current control and load sharing. The secondary control adjusts the voltage or frequency deviation by changing the reference values of the primary controller. The tertiary control system manages the power flow between the grid, the ESS and the microgrid. It is responsible for economic decisions and power scheduling. In [118, Sec. 9], four levels of droop control for DC grids with increasing system complexity are proposed.

(i) The **basic compound** is a complete decentralised system without grid control and communication. The generating units provide a DC voltage, and all other devices follow their control strategy according to their intended purpose. An example of this compound would be one or more parallel-connected uncontrolled diode rectifiers to supply several motor drives. The power flow cannot be controlled, and power sharing can only be permanently set passively for the rectifiers.

(ii) With the **decentralised droop control**, the devices react according to their locally measured DC voltage. The reference current of the unit is specified or limited using a predefined characteristic droop curve, and passive devices are considered a disturbance. The operation can take place without additional communication. Only the DC link voltage serves as the information carrier.

(iii) The **extended droop control** is like the decentralised droop control with an additional communication system between the devices. Usually, there is also a superordinate control unit that monitors the status of the grid and the devices. This control unit allows for adjustment of the droop control parameters during operation to optimise the power flow.

(iv) **Centralised control** is when a central unit controls the system via communication. It transmits all reference values for current, DC link voltage or power to the devices. This requires a real-time communication system. Due to its bandwidth, the number of devices is also limited. This design makes the system very flexible and allows any adjustments during operation. The disadvantage is that the entire system fails in the event of a communication failure.

The control strategy implemented here can be categorised as an extended droop control. The devices operate autonomously, and power flows can be adjusted via communication. As the primary controller, i.e. the current controller and the droop controller, is implemented locally on each device, the control tasks necessary for grid stability can also be accomplished without communication.
The following section presents the origin of droop control in AC grids. Given Specification (S10), the need for droop control for decentralised generation units is emphasised to enable off-grid applications and ensure the stability of the future structure of the distribution grid. Afterwards, droop control in DC grids is discussed, followed by the control strategy implemented here.

3.1.1 Droop Control in AC Grids and the Low-Inertia Problem

In traditional electrical grids, synchronous machines constitute the generating units, including the typically used steam turbines. As all generators are synchronised, the grid frequency can be considered the same throughout the grid. The frequency is controlled by the grid operators and is kept almost constant during regular operation. Depending on the region, the nominal grid frequency f_g is either 50 or 60 Hz. A change in the grid frequency reflects a discrepancy between generated and consumed power.
Since it can be assumed that the frequency is the same at every point in the grid, all power plants can be combined into a single unit. Neglecting the grid topology and its impedance, the dynamics of the power system can be represented in a very simplified way with [187, Sec. 16.2],[188]

$$\Theta_\mathrm{m} \frac{\mathrm{d}}{\mathrm{d}t}\omega_\mathrm{g} = m_\mathrm{m} - m_\mathrm{el}\,, \tag{3.1}$$

where Θ_m is the combined system inertia, $\omega_\mathrm{g} = 2\pi\, f_\mathrm{g}$ is the angular frequency of the grid, m_m the mechanical torque supplied by the turbines and m_el the electrical torque induced by the connected load. In power systems, expressing this swing equation in terms of power rather than torque is more common, which can be achieved by multiplying (3.1) with ω_g [189], resulting in

$$\Theta_\mathrm{m}\,\omega_\mathrm{g}\,\frac{\mathrm{d}}{\mathrm{d}t}\omega_\mathrm{g} = p_\mathrm{m} - p_\mathrm{el}\,. \tag{3.2}$$

In addition, a per-unit representation is often chosen to better compare quantities and parameters of generating units of different sizes. A per-unit representation is derived by dividing the quantities by their nominal value. Therefore, (3.2) is divided by the nominal apparent power S_nom, which leads to [189]

$$2\,H_\mathrm{m}\,\frac{\mathrm{d}}{\mathrm{d}t}\omega_\mathrm{g,pu} = p_\mathrm{m,pu} - p_\mathrm{el,pu}\,, \tag{3.3}$$

where $\omega_\mathrm{g,pu} \approx 1$ is used. The inertia constant H_m is defined as

$$H_\mathrm{m} = \frac{\frac{1}{2}\Theta_\mathrm{m}\,\omega_\mathrm{g}^2}{S_\mathrm{nom}}\,. \tag{3.4}$$

It is the combined moment of inertia from the generators and turbines, whereby the turbine usually gives the main part of the inertia.

Equation (3.3) describes how a power imbalance affects the grid frequency. If the electrical load $p_\mathrm{el,pu}$ increases, the frequency drops at the first moment. If the load decreases, the frequency rises. Thereby, the rate of change is given by the inertia constant H_m. The droop control methods described below are developed based on this phenomenon.

In traditional grids, the kinetic rotational energy of the generators and turbines is used to compensate for imbalances in generation and load at the first instant by providing or absorbing the power difference. This behaviour is essential for stability as it bridges the time until the primary frequency controller intervenes by adjusting the power of the generators. A hierarchical control strategy is established to ensure stable operations. The primary controller is activated after about 5 s. After a few tens of seconds, secondary control takes over, followed by tertiary control and generator rescheduling, whose time scales are in the range of minutes and hours, respectively [188, 190].

Due to the climate crisis, there is a massive global effort to replace conventional fossil energy with sustainable and renewable energy sources. Hence, the share of wind and solar has increased drastically in the past years (see Fig. 1.4 in Sec. 1.1.3). Since conventional power plants with their synchronous machines as generators are now replaced by grid inverters, the system's inertia will decrease [188–191], leading to a so-called low-inertia system. Since inertia is crucial for grid stability, other measures must be taken. With PV systems, there is no rotating mass that could contribute to the system's stability. In power plants such as wind turbines, whose electrical machine is connected to the grid via a back-to-back converter, the inertia is decoupled from the grid [189].

Wind turbines have various drive systems. In onshore wind turbines, double-fed induction machines are predominantly used in about 60 % of the turbines [192]. There, the stator windings are directly connected to the grid voltage, and the three-phase rotor windings are connected to the grid via a back-to-back converter that allows to adjust the rotor voltage. Thus, the wind turbine can operate at variable speed in a range of ±30 % of its synchronous speed [192, 193]. In the other part of onshore wind turbines, the generator is connected to the grid exclusively via a back-to-back converter, whereby synchronous or squirrel-cage induction machines are used as generators. In offshore wind turbines, however, almost all generators in new plants are connected to the grid via a power converter [194]. These systems must require as little maintenance as possible. Gearboxes and brushless topologies can be dispensed with in this drive train [195].

In addition, offshore wind farms are increasingly connected to the grid via HVDC transmission lines [172, 173], decoupling their inertia from the grid.

Alongside their high inertia, directly grid-connected synchronous machines also have a damping effect to suppress frequency oscillations. An additional damper winding achieves this damping effect. Hence, they contribute significantly to grid stability and serve as a protective measure against faults and disturbances. In addition to the reduction in inertia, renewable energy sources are more volatile, meaning a power imbalance will occur more frequently [188]. Thus, if synchronous machines disappear, grid inverters will inevitably have to contribute to grid stability in the future [190, 191].

The DC link capacitor is an energy storage device that can be used as a counterpart to inertia for stabilisation. However, it is often stated that the energy of the DC link is negligible compared to the actual inertia of the power system [188, 191]. Typically, the inertia constant H_{m}, as defined in (3.4), lies between 2 and 9 s [189, 196]. It is the time equivalent during which the generating unit can provide its rated power only from the stored kinetic energy. Therefore, the stored kinetic energy ratio to its nominal power is between 2000 and 9000 $\frac{\mathrm{J}}{\mathrm{kW}}$. In comparison, for the power electronic system presented here, the stored energy in the DC link capacitance is

$$\frac{E_{\mathrm{dc}}}{p_{\mathrm{nom}}} = \frac{C_{\mathrm{dc}}\left(u^{\mathrm{dc}}\right)^2}{2\,p_{\mathrm{nom}}} \approx 51.8\ \frac{\mathrm{J}}{\mathrm{kW}}\,. \tag{3.5}$$

However, in both cases, not all stored energy can be used to stabilise the grid, as certain limits must be respected. The DC link voltage of the grid inverter must remain within its boundaries, and the speed of the synchronous machines must stay in the specified grid frequency. In Europe, the permissible frequency deviation Δf_{g} within which the primary control of the generating units is active is ±200 mHz around the nominal grid frequency of 50 Hz. Outside this tolerance band, a critical system state is present, usually caused by a fault in the grid [197, Sec. 10.2], [198]. The energy difference ΔE_{m} between the nominal frequency $f_{\mathrm{g,nom}}$ and the permissible deviation can be calculated with

$$\frac{\Delta E_{\mathrm{m}}}{S_{\mathrm{nom}}} = H_{\mathrm{m}}\left(1 - \left(\frac{f_{\mathrm{g,nom}} - \Delta f_{\mathrm{g}}}{f_{\mathrm{g,nom}}}\right)^2\right) = H_{\mathrm{m}}\left(1 - \left(\frac{49.8\ \mathrm{Hz}}{50\ \mathrm{Hz}}\right)^2\right)\,. \tag{3.6}$$

This gives an energy-to-power ratio between 16.0 and 71.9 $\frac{\mathrm{J}}{\mathrm{kW}}$, which can be used to balance load fluctuations until the primary control of the generating units takes effect. For example, if a deviation from the nominal DC link voltage of ±50 V is permitted in the range from 750 V to 850 V, the energy-to-power ratio for this system is 13.0 $\frac{\mathrm{J}}{\mathrm{kW}}$. Under this consideration, the energy difference stored in the synchronous machines and the DC link capacitor tends to converge. This is because the DC link voltage allows for more variability than the rotational speed of the synchronous machine, which must always be synchronous with the grid frequency. Of course, they are not identical, but it is incorrect that the DC link capacitor's energy can be neglected to contribute to grid stability. In addition, the DC link voltage can be further increased with newer generations of semiconductors, increasing the stored energy over-proportionally. The energy-to-power ratio for a voltage range from 1350 V to 1450 V is 22.7 $\frac{\mathrm{J}}{\mathrm{kW}}$.

Stored energy must also be available outside the frequency band to keep the grid stable in the event of a fault. Another energy storage device must be utilised if the DC link voltage is already at its limits. The energy in the DC link capacitor can primarily provide a first and foremost fast response and can be supplemented by secondary energy storage. This is particularly relevant if, for example, no 100 V reserve is available, as discussed above. However, suppose the inevitable reduction of inertia in the grid makes every energy storage facility necessary to contribute to stability. In that case, this is undoubtedly a good option which meets the dynamic requirements. In addition, the increased provision of DC link energy could be given more significant consideration or even mandated in the design of inverters. This would also have the advantage of contributing to the stability of the DC grid, which is addressed in Sec. 3.2.5. However, this contradicts the trend that the DC link capacitor is increasingly being reduced due to cost and space [128].

In microgrids, the droop control strategy can be used to distribute power between multiple inverters that supply the microgrid. Power sharing is essential as the load should be distributed evenly across the grid inverters. This distributes the heat generated by losses in the devices evenly. Consequently, the thermal load on the electrical components, such as the DC link capacitors, is reduced, and the lifetime of the devices is extended.

Microgrids differ from transmission grids in many aspects. Differences are, for example, in the voltage levels, line characteristics, and the grid topology, which require different control strategies. The coupling between active and reactive power has more impact and must be compensated for [188, 199, 200]. Considering this in a full-state feedback control design leads to better controller performance [200]. In [201], the grid impedance is estimated to adjust the controller to compensate for the strong coupling between active and reactive power flow.

Another challenge in AC microgrids is the supply of nonlinear loads, such as uncontrolled diode rectifiers. The harmonic currents they require are often not evenly distributed across the inverters, which can lead to an overload of individual inverters [167]. Adding integral and differential terms to the droop controller can increase its dynamics and improve the harmonic distribution [175, 183].

In recent years, literature has addressed using droop control to support the distribution grid's stability due to low inertia [200, 202]. Distributed inverters do not currently contribute to grid stability in the nominal frequency range of 50 Hz ± 200 mHz, as given by the flat part of the curve in Fig. 3.2.

Besides droop control, other grid-stabilizing control strategies have been developed, and all of them rely on some form of energy storage to support grid stability. Energy storage can be batteries, supercapacitors or flywheels. However, the inertia of a connected wind turbine can also be used [189, 190, 196, 203].

Most of the strategies require a PLL that also provides the rate of change of frequency (RoCoF), meaning the time derivative of the frequency $\frac{\mathrm{d}}{\mathrm{d}t}\omega_\mathrm{g}$. This can be achieved by an additional low-pass filter (see Appendix A.6), often used to pre-filter the input voltage [204]. The PLL can be modelled with [190]

$$\left.\begin{aligned} &\frac{\mathrm{d}}{\mathrm{d}t}\widehat{\phi}_\mathrm{g} = \widehat{\omega}_\mathrm{g} \\ &\frac{\mathrm{d}}{\mathrm{d}t}\widehat{\omega}_\mathrm{g} = -\frac{1}{\tau_\mathrm{pll}}\left(\widehat{\omega}_\mathrm{g} + k_\mathrm{p,pll}\, u^q_\mathrm{pcc} + k_\mathrm{i,pll}\int u^q_\mathrm{pcc}\,\mathrm{d}t\right)\,. \end{aligned}\right\} \tag{3.7}$$

A favoured approach for grid inverters is to emulate a synchronous machine [205–207]. Synchronous machines have advantageous properties such as self-synchronisation with the grid, rotational inertia and damping of oscillations. Therefore, a virtual synchronous machine model is implemented to emulate the beneficial behaviour of the synchronous machine with its inertia. In addition to the grid-stabilising effect, the inverters can switch to island mode without interrupting the supply during a grid outage. Of course, the resulting microgrid must also have a corresponding energy storage system. The virtual inertia can only supply a small amount of energy for a short time. A larger energy storage must be utilised for a long-term supply. Interestingly, the virtual inertia does not have to correspond to the available energy connected to the inverter due to decoupling [189]. This results in greater flexibility for the controller parameters. Another significant advantage is that the requirements in the standards for the dynamic behaviour of inverters are based on the behaviour of synchronous machines. This is because synchronous machines in conventional power plants still dominate the grid. The standard VDE-AR-N 4110, therefore, require similar behaviour for inverters, e.g., during a low-voltage ride-through (LVRT) [197, Sec. 10.2]. However, it has been shown that droop control and virtual synchronous machines have strong similarities and are even equal under certain conditions [202, 208]. The matching control strategy takes advantage of the inverter's and synchronous machine's structural similarities and takes the DC link voltage as an additional feedback signal for the controller [191, 209]. Other strategies are hybrid angle control [210] or power synchronisation control [211, 212].

3.1.2 Droop Control in DC grids

Just as the frequency changes in AC grids in the event of a power imbalance, the voltage changes in DC grids. The capacitance of the DC link serves as a counterpart to the inertia of the synchronous machines in AC grids. It absorbs or releases power when the DC link voltage changes. All devices must react to this and take appropriate measures to keep the voltage within the permissible range.

In practice, DC grids are only realised as subsystems to the AC grid in form of microgrids. Therefore, the literature on droop control for DC grids concentrates exclusively on these [167, 169–171]. Great attention is paid to the self-sufficiency of the system, and efforts are made to ensure stand-alone operation. Since the natural fluctuation of renewable energy sources needs to be compensated for in island mode, energy storage systems must be added.

A permanent power imbalance would lead to a rapid change in the DC link voltage and, thus, to a critical state in the system or even to the damage of the power electronics. Therefore, maintaining the DC link voltage within the specified voltage range must have the highest priority. The secondary control objective is power sharing or maximum power point tracking (MPPT) for grid inverters and DC/DC converters with batteries or generating units, respectively. Suppose the energy storages are fully charged, and more power is generated than the loads required. Then, the renewable energy sources must change from the MPPT control strategy to DC link voltage control [171].

Two methods have been established for droop control in DC grids. Both methods require an inner current or voltage control loop to which the droop control is cascaded [167, 179]. One method is based on a characteristic curve, similar to the frequency droop curve for decentralised generating units, as shown in Fig. 3.2. Depending on the DC link voltage, the reference current of the respective current-controlled unit is changed. Thus, the units become a voltage-dependent current source [179]. From a control theory perspective, this is equivalent to a P-controller of the superimposed voltage control. This method is also used here for the grid inverter and the generating units and is presented in the next section.

The second and most frequently discussed method in the literature is using a virtual resistor. The idea originates from the electrical considerations when connecting voltage sources in parallel [184]. Theoretically, connecting ideal voltage sources in parallel is impossible because a minimal voltage difference between the sources would cause an infinitely high current. A parallel connection can only be realised with real voltage sources with an internal resistance, i.e. a resistance in series with the ideal voltage source, as shown in Fig. 3.3. This droop control method is combined with the first method for power smoothing with the DC/DC converters, presented in Sec. 3.3.

Droop control with virtual resistance mimics this behaviour by proportionally reducing the

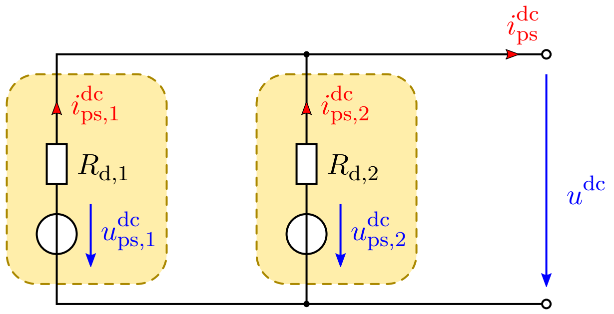

Figure 3.3: Equivalent circuit of two voltage controlled units using droop control with virtual resistances $R_{\mathrm{d,1}}$ and $R_{\mathrm{d,2}}$.

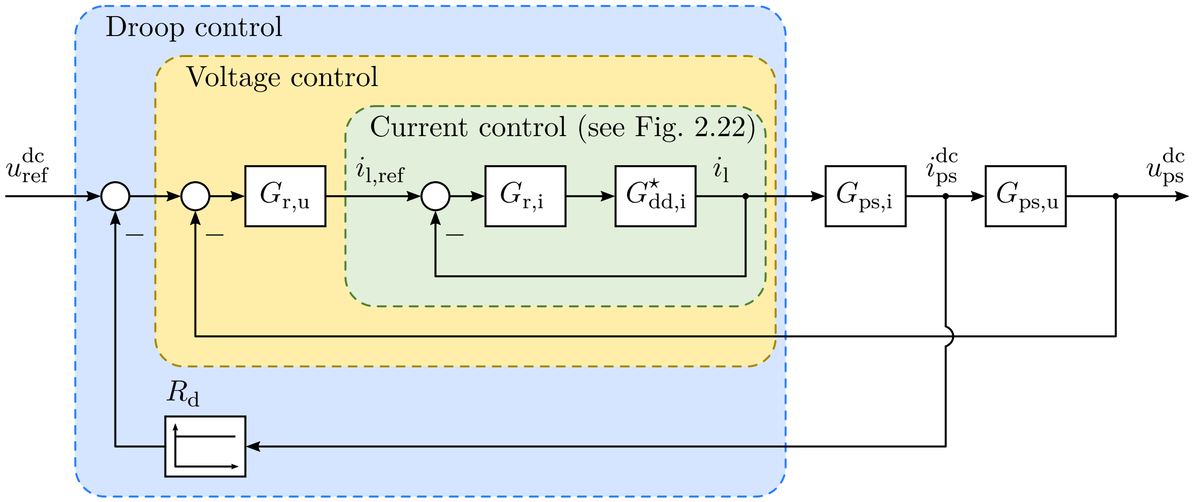

Figure 3.4: Block diagram of the droop controller with cascaded current and voltage control loops.

controlled output voltage to the current. The output current of the unit is fed back via the virtual droop resistance R_{d} and subtracted from the reference voltage, as shown in Fig. 3.4. There, $G_{\mathrm{ps,i}}(s)$ and $G_{\mathrm{ps,u}}(s)$ are the transfer functions from i_{l} to $i^{\mathrm{dc}}_{\mathrm{ps}}$ and from $i^{\mathrm{dc}}_{\mathrm{ps}}$ to $u^{\mathrm{dc}}_{\mathrm{ps}}$, respectively.
Droop control with virtual resistance requires DC link voltage control, either cascaded to an inner current controller, as shown in Fig. 3.4, or directly, as described in Sec. 2.3.2. However, to design a proper DC link voltage controller, the dynamics of the DC link must be known. This is hardly possible for arbitrary microgrids, as it depends heavily on their configuration, the individual devices and the spatial expansion, i.e. the line impedance. Therefore, the voltage controller must be conservatively designed to achieve acceptable performance for all possible microgrid configurations.
The choice of the value of the virtual droop resistance is a trade-off between power sharing and voltage tracking. In general, a large droop resistance leads to better power sharing, and a small droop resistance is better for voltage tracking [171]. Power sharing with a constant droop resistance is susceptible to the impedances of the transmission lines and differences between the units, which can cause circulating currents [169, 171]. Therefore, the droop resistance should be varied depending on the system states to adjust the power sharing between the units. This can be used, for example, to equalise the state of charge (SOC) of several battery storage units [169]. The overall SOC is usually managed by the tertiary control system, which mainly

makes economic decisions. The tertiary control transmits the reference values to the secondary control, which adapts the virtual resistance accordingly. During island mode, where the grid inverters are on standby, the DC/DC converters of the storage units take over the droop control of the grid inverter.
In [170] and [184] decentralised fuzzy control is used to adapt the droop resistance to achieve a good energy balance among several ESS and prevent deep discharge while minimising the deviation from the reference voltage. Fuzzy control can also be combined with gain scheduling so that voltage control and balancing of the stored energy also work for an unknown system [170].

3.1.3 Implemented Droop Control with Characteristic Curve

Droop control with virtual resistance is advantageous when the permissible voltage range is small since adjusting the virtual resistance allows for better voltage tracking [167]. If voltage tracking is not strictly required and a wider voltage range can be used, droop control with a characteristic curve is a viable alternative [179]. It is generally more flexible and easier to implement than the virtual resistance method.
The DC link voltage must also remain within a specific range here. The component with the smallest rated voltage gives the maximum permissible voltage. These are usually the power semiconductors or the DC link capacitors. If the maximum voltage is exceeded, they will be destroyed. A safety distance should also be maintained in case of a voltage overshoot. Moreover, the lifetime is reduced if they are constantly operated at their voltage limits [69] (see Sec. 2.1.2).
The connected RES and the AC grid voltage determine the minimum DC link voltage. The RES, i.e. the electrical machines, the PV modules or the storage systems, must generate a lower voltage than the DC link voltage. For PV systems, the number of PV modules connected in series must be limited, as the open-circuit voltage must be lower than the minimum DC link voltage (see Sec. 2.3.1). The maximum speed of electric machines must be limited accordingly, as their induced voltage is proportional to the rotational speed (see Sec. 2.4.1).
The same applies to the grid. The DC link voltage must be high enough for the grid inverter to apply a sufficiently large phase voltage to control the desired current. This minimum voltage also depends on the modulation technique. Classic pulse width modulation (PWM) is used here, with which an average amplitude of up to $\frac{u^{\mathrm{dc}}}{2}$ can be generated (see Sec. 2.2). For the grid of continental Europe, the absolute minimum DC link voltage for this grid inverter with PWM is

$$u^{\mathrm{dc}}_{\mathrm{min}} > 2\sqrt{2}\, U_{\mathrm{g}} \cdot 1.1 = 2\sqrt{2} \cdot 230\ \mathrm{V} \cdot 1.1 = 715.6\ \mathrm{V} \quad , \tag{3.8}$$

where $U_{\mathrm{g}} = 230$ V is the nominal root mean square (RMS) value of the grid voltage. The amplitude is $\sqrt{2}$ times the RMS value for sinusoidal signals [63, Sec. 20.2]. Factor 1.1 accounts for the grid voltage range under normal operating conditions, which must not deviate by more than ±10 % from the nominal voltage as defined in the standard IEC 60038:2009 for standard voltages [213]. It is impractical to utilise the absolute voltage limits, as a certain voltage reserve is also required for current control. Therefore,

$$u^{\mathrm{dc}}_{\mathrm{min}} \coloneqq 750\ \mathrm{V} \leq u^{\mathrm{dc}} \leq 875\ \mathrm{V} \eqqcolon u^{\mathrm{dc}}_{\mathrm{max}} \tag{3.9}$$

are chosen for this system.
Lower minimum DC link voltages are permissible in industrial environments. Uncontrolled diode rectifiers (B6 bridges) are also considered there, which work with a much lower DC link voltage of about 540 V [118, Sec. 6.1]. They work passively and charge the DC grid if its voltage is lower than the grid voltage. They are, therefore, easy to implement and also very cost-effective. However, they are a highly nonlinear load to the grid and induce current harmonics [81, Sec. 2.6].

Moreover, they only work unidirectionally, which does not allow to feed energy into the grid. This is especially relevant given the low inertia problem discussed in Sec. 3.1.1, where it was noted that newly installed systems should be able to ensure grid stability. In particular, systems as large as those required in industry should be able to be used for this purpose.

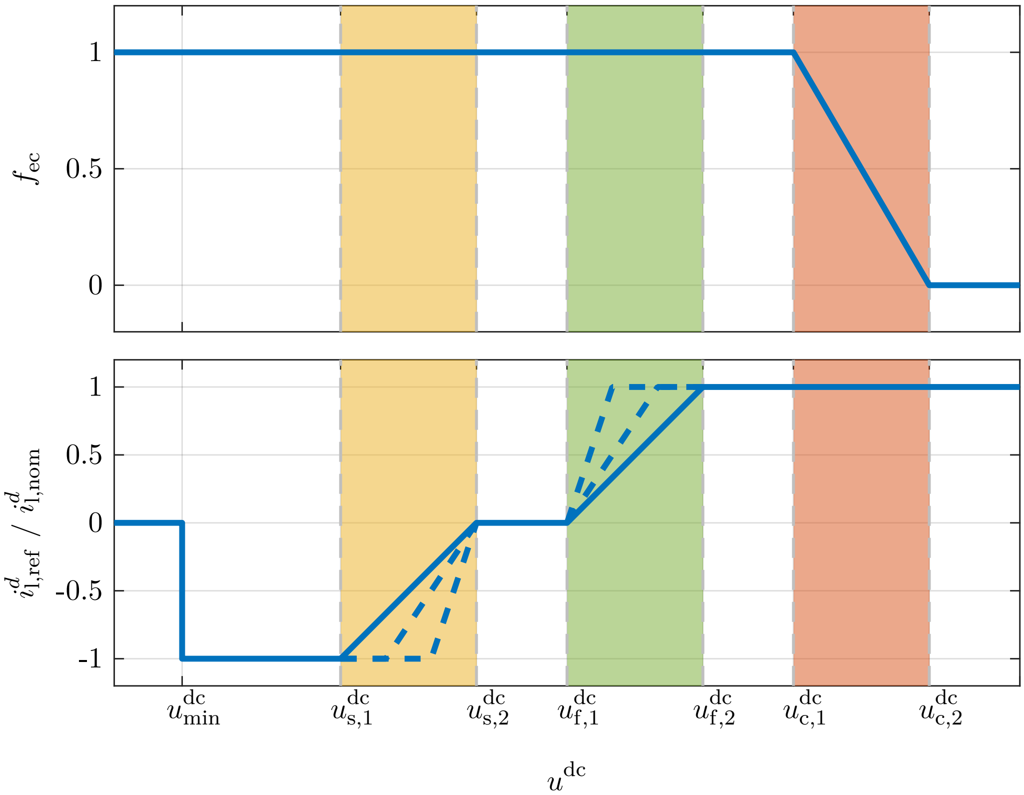

Figure 3.5: Implemented droop control curves for the RES in the first subplot and for the grid inverters in the second subplot.

Fig. 3.5 shows the implemented characteristic curves for droop control. The first subplot shows the derating curve for the RES or, in general, for all energy conversion (EC) systems that feed current into the DC link. Limiting the current injected into the DC link in the red range is required when the voltage becomes too high. The voltage can become too high if the RES generates more power than can currently be consumed or fed into the grid. Usually, this is not reached, as the maximum available power should be utilised as much as possible. It can happen, for example, if a grid inverter fails or a grid outage occurs. Sometimes, dimensioning the installed RES power larger than the grid inverter power can be economically more beneficial. The surplus power can no longer be utilised at times of high yield. The resulting financial loss over the entire lifetime should be less than the investment costs saved on the grid inverters.
The derating curve f_{ec}, as shown in the first subplot in Fig. 3.5, is defined as

$$f_{\mathrm{ec}}(u^{\mathrm{dc}}) = \begin{cases} 1 & , u^{\mathrm{dc}} \leq u^{\mathrm{dc}}_{\mathrm{c},1} \\ 1 - \dfrac{u^{\mathrm{dc}} - u^{\mathrm{dc}}_{\mathrm{c},1}}{u^{\mathrm{dc}}_{\mathrm{c},2} - u^{\mathrm{dc}}_{\mathrm{c},1}} & , u^{\mathrm{dc}}_{\mathrm{c},1} < u^{\mathrm{dc}} \leq u^{\mathrm{dc}}_{\mathrm{c},2} \\ 0 & , u^{\mathrm{dc}} > u^{\mathrm{dc}}_{\mathrm{c},2} \, . \end{cases} \tag{3.10}$$

Generally, the reference current for the RES is provided by a MPPT. The MPPT is specific for each type of RES, e.g. for PV systems as described in Sec. 2.3.4, for an ideal energy output for wind turbines as described in [27], or an algorithm for the optimal control of a WEC as introduced in Sec. 1.2.3. The optimal current $i_{\mathrm{l,opt}}$ from the MPPT is multiplied by the function f_{ec} which yields the actual reference current $i_{\mathrm{l,ref}}$ for the current controller, as shown in Fig. 3.6. Thus, the reference current $i_{\mathrm{l,ref}}$ is reduced accordingly if the voltage is too high.

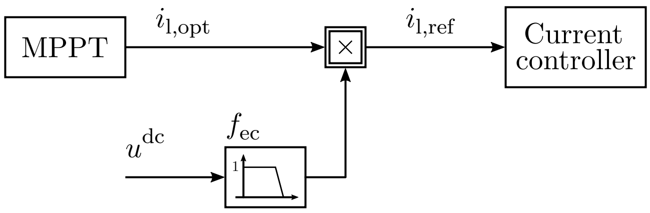

Figure 3.6: Block diagram of the droop controller for derating the reference current of renewable energy sources.

This derating curve reduces the power output of RES. Depending on the type of RES, this can lead to uncontrolled behaviour and damage. For wind turbines, for example, the rotor speed would increase rapidly, which means that safe operation cannot be guaranteed. For the WEC, the point absorber would drive into the mechanical limit without braking and cause drastic damage. Therefore, appropriate measures must be taken to guarantee safe operation despite this. For example, the excess power can be dissipated, brakes can be installed, or pitch control can be implemented in the case of wind turbines.

The second subplot in Fig. 3.5 shows the droop control curve implemented in the grid inverters. The reference current $i^{d}_{\mathrm{l,ref}}$ of the grid inverter is specified according to this curve. As shown in Sec. 3.2, the d-component of the inductance currents $\boldsymbol{i}_l^{dq}$ decisively determines the active power flow from the DC link into the grid. The q-component determines the reactive power flow, which minimally influences the DC link dynamics.

The voltage from which the reference current is derived is measured by each inverter at its terminals. This allows for a decentralised control system. As several inverters are connected in full parallel, meaning they are connected in parallel simultaneously on both the AC as well as on the DC side, proper power sharing is crucial. As the inverters are positioned near each other, it can be assumed that the respective terminal voltage is equal. Furthermore, the curves in all parallel-connected inverters are the same, resulting in the same inductance current. Thus, ideal power sharing can be guaranteed.

In the green voltage range between $u^{\mathrm{dc}}_{\mathrm{f,1}}$ and $u^{\mathrm{dc}}_{\mathrm{f,2}}$, the RES generate power, which causes the voltage to rise and the grid inverters to feed power into the grid. The grid inverters have reached their rated current at voltage $u^{\mathrm{dc}}_{\mathrm{f,2}}$, which remains constant also with higher voltages. The RES reduce its output power once the critical voltage $u^{\mathrm{dc}}_{\mathrm{c,1}}$ is exceeded. The voltage gap between $u^{\mathrm{dc}}_{\mathrm{f,1}}$ and $u^{\mathrm{dc}}_{\mathrm{c,1}}$ accounts for the transmission line losses. For example, if the power from the RES is equal to the rated power of the inverters, the DC link voltage $u^{\mathrm{dc}}_{\mathrm{g}}$ at the inverter terminals is equal to $u^{\mathrm{dc}}_{\mathrm{f,2}}$. The voltage $u^{\mathrm{dc}}_{\mathrm{ec}}$ at the terminals of the RES is higher, corresponding to the voltage drop along the transmission line impedance. The gap is inserted here so that the power of the RES is only reduced after the grid inverters have reached their rated power. Sec. 3.2.3 shows that the voltage drop along the transmission line is limited to 3 % of the maximum voltage. Accordingly, it is sufficient if the distance between $u^{\mathrm{dc}}_{\mathrm{f,1}}$ and $u^{\mathrm{dc}}_{\mathrm{c,1}}$ is also 3 % of $u^{\mathrm{dc}}_{\mathrm{c,1}}$.

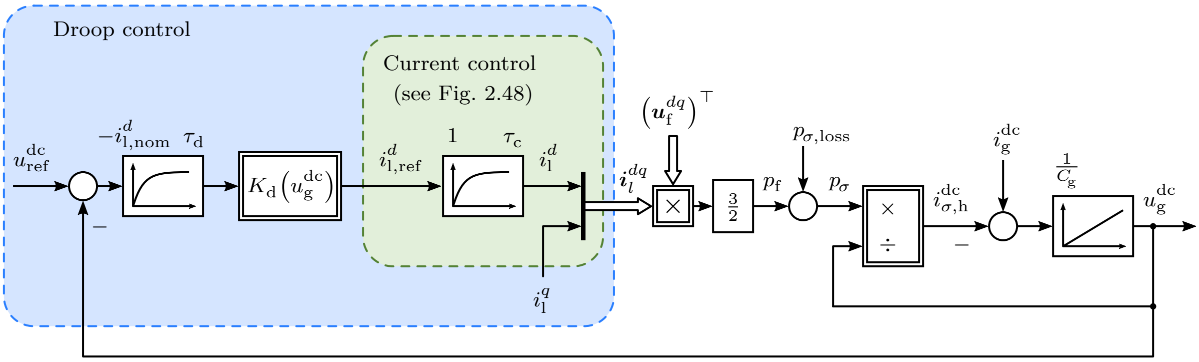

Figure 3.7: Block diagram of the droop controller with characteristic droop curve for the grid inverters.

In the yellow range between $u^{\mathrm{dc}}_{\mathrm{s},1}$ and $u^{\mathrm{dc}}_{\mathrm{s},2}$, more power is required in the DC grid than is generated by the RES. This causes the voltage to fall below $u^{\mathrm{dc}}_{\mathrm{s},2}$, which means that the grid inverters draw power from the grid to supply the DC grid. A voltage gap is also inserted between the voltage $u^{\mathrm{dc}}_{\mathrm{s},2}$ and $u^{\mathrm{dc}}_{\mathrm{f},1}$. As no current flows here, there is also no voltage drop on the transmission line that needs to be considered. However, this gap is necessary to separate the two sections and prevent circulating currents. Due to tolerances in the voltage measurement, the locally measured DC link voltage at the individual devices differs slightly.

Suppose there is no gap, i.e. $u^{\mathrm{dc}}_{\mathrm{s},2} = u^{\mathrm{dc}}_{\mathrm{f},1}$, and the generated power of the RES is zero. In this case, one grid inverter may measure a voltage less than $u^{\mathrm{dc}}_{\mathrm{s},2}$ and supply the DC link from the AC grid. Another inverter measures a voltage greater than $u^{\mathrm{dc}}_{\mathrm{f},1}$ and feeds power into the AC grid. This results in a circulating current between these two grid inverters. This circulating current does not contribute to the DC link control and only dissipates power. Therefore, it should be avoided.

This can be prevented by inserting this voltage gap. It only needs to be greater than twice the maximum expected measurement error to account for the worst case where one inverter has a maximum voltage error and another a minimum. Here, the voltage gap is set to 10 V, which is more than sufficient. Since the slopes and the respective voltage range of the droop control curve can be adapted, it is essential that the two voltages, $u^{\mathrm{dc}}_{\mathrm{s},2}$ and $u^{\mathrm{dc}}_{\mathrm{f},1}$, remain the same for each unit. Otherwise, circulating current can occur again.

If the voltage drops below the yellow range, more power is required in the DC grid than the grid inverters can provide. In this case, the loads must be reduced or switched off. If this does not happen, the voltage drops further until the minimum DC link voltage $u^{\mathrm{dc}}_{\mathrm{min}}$ is reached, where the grid inverters cannot control the grid-side inductance currents $\boldsymbol{i}^{dq}_{l}$ anymore and must disconnect from the grid. The RES can still try to supply the required power and are not limited, as indicated by $f_{\mathrm{ec}} = 1$ in the upper subplot of Fig. 3.5. However, they must disconnect and stop operation if the DC link voltage drops below their limit. The system will shut down until the central control unit decides that the power consumption can be satisfied and restarts the system.

The block diagram of the droop control for the grid inverters is shown in Fig. 3.7. A detailed explanation of the model is given in the next section. The reference current $i^{d}_{\mathrm{l,ref}}$ in ratio to the nominal current $i^d_{\mathrm{l,nom}}$ is given as

$$\frac{i^d_{\mathrm{l,ref}}(u^{\mathrm{dc}}_{\mathrm{g}})}{i^d_{\mathrm{l,nom}}} = \begin{cases} 0 & , u^{\mathrm{dc}}_{\mathrm{g}} \leq u^{\mathrm{dc}}_{\mathrm{min}} \\ -1 & , u^{\mathrm{dc}}_{\mathrm{min}} < u^{\mathrm{dc}}_{\mathrm{g}} \leq u^{\mathrm{dc}}_{\mathrm{s,1}} \\ \dfrac{u^{\mathrm{dc}} - u^{\mathrm{dc}}_{\mathrm{s,2}}}{u^{\mathrm{dc}}_{\mathrm{s,2}} - u^{\mathrm{dc}}_{\mathrm{s,1}}} & , u^{\mathrm{dc}}_{\mathrm{s,1}} < u^{\mathrm{dc}}_{\mathrm{g}} \leq u^{\mathrm{dc}}_{\mathrm{s,2}} \\ 0 & , u^{\mathrm{dc}}_{\mathrm{s,2}} < u^{\mathrm{dc}}_{\mathrm{g}} \leq u^{\mathrm{dc}}_{\mathrm{f,1}} \\ \dfrac{u^{\mathrm{dc}} - u^{\mathrm{dc}}_{\mathrm{f,1}}}{u^{\mathrm{dc}}_{\mathrm{f,2}} - u^{\mathrm{dc}}_{\mathrm{f,1}}} & , u^{\mathrm{dc}}_{\mathrm{f,1}} < u^{\mathrm{dc}}_{\mathrm{g}} \leq u^{\mathrm{dc}}_{\mathrm{f,2}} \\ 1 & , u^{\mathrm{dc}}_{\mathrm{g}} > u^{\mathrm{dc}}_{\mathrm{f,2}} \, . \end{cases} \tag{3.11}$$

From a control theory perspective, this results in a nonlinear P-controller for the DC link voltage $u^{\mathrm{dc}}_{\mathrm{g}}$ at the terminals of the grid inverter. Considering the green or yellow sections with a gradient, the reference current can be given in the known controller structure

$$i^d_{\mathrm{l,ref}} = -K_{\mathrm{d}} \left(u^{\mathrm{dc}}_{\mathrm{g}}\right) i^d_{\mathrm{l,nom}} \left(u^{\mathrm{dc}}_{\mathrm{ref}} - u^{\mathrm{dc}}_{\mathrm{g}}\right) , \tag{3.12}$$

where $u^{\mathrm{dc}}_{\mathrm{ref}} = u^{\mathrm{dc}}_{\mathrm{s,2}}$ or $u^{\mathrm{dc}}_{\mathrm{ref}} = u^{\mathrm{dc}}_{\mathrm{f,1}}$ for the yellow and green sections, respectively. The proportional gain K_{d} is defined by the distance between the respective voltages. Thus, the droop gain is given as

$$K_{\mathrm{d}} \left(u^{\mathrm{dc}}_{\mathrm{g}}\right) := \begin{cases} 0 & , u^{\mathrm{dc}}_{\mathrm{g}} \leq u^{\mathrm{dc}}_{\mathrm{min}} \\ \dfrac{1}{u^{\mathrm{dc}}_{\mathrm{s,2}} - u^{\mathrm{dc}}} & , u^{\mathrm{dc}}_{\mathrm{min}} < u^{\mathrm{dc}}_{\mathrm{g}} \leq u^{\mathrm{dc}}_{\mathrm{s,1}} \\ \dfrac{1}{u^{\mathrm{dc}}_{\mathrm{s,2}} - u^{\mathrm{dc}}_{\mathrm{s,1}}} & , u^{\mathrm{dc}}_{\mathrm{s,1}} < u^{\mathrm{dc}}_{\mathrm{g}} \leq u^{\mathrm{dc}}_{\mathrm{s,2}} \\ 0 & , u^{\mathrm{dc}}_{\mathrm{s,2}} < u^{\mathrm{dc}}_{\mathrm{g}} \leq u^{\mathrm{dc}}_{\mathrm{f,1}} \\ \dfrac{1}{u^{\mathrm{dc}}_{\mathrm{f,2}} - u^{\mathrm{dc}}_{\mathrm{f,1}}} & , u^{\mathrm{dc}}_{\mathrm{f,1}} < u^{\mathrm{dc}}_{\mathrm{g}} \leq u^{\mathrm{dc}}_{\mathrm{f,2}} \\ \dfrac{-1}{u^{\mathrm{dc}}_{\mathrm{s,2}} - u^{\mathrm{dc}}} & , u^{\mathrm{dc}}_{\mathrm{g}} > u^{\mathrm{dc}}_{\mathrm{f,2}} \, . \end{cases} \tag{3.13}$$

For reasons of symmetry, the distances are generally chosen to be equal. An additional first-order low-pass filter with the time constant τ_{d} is added to the nonlinear P-controller. This allows the damping of fluctuations and noise in the DC link voltage. This filter is also essential for power smoothing, as described in Sec. 3.3.

3.2 Modelling and Stability Analysis of the DC Link Dynamics

To assess system stability and determine the system limits, this section presents a nonlinear system model in state-space and analyses it for stability. The DC link voltage control through grid inverters whose grid-side current is controlled results in a strongly nonlinear and non-minimum-phase system, which can challenge the controller design [214].

The voltage control in the DC link has been the subject of numerous studies. An adaptive controller design leads to excellent control performance for a back-to-back inverter, where no line impedance between the inverters has to be considered. If a PI-controller with constant controller parameters is used, these must be chosen conservatively, severely limiting the bandwidth [214].

In [179], [148], and [215], the stability assessment of a DC grid is accomplished by experimentally identifying the output impedance of the power converters and the impedance of the DC grid in the frequency domain. If the measurement results fulfil the passivity criteria, the DC grid is stable. This is particularly suitable if the DC grid is very complex and many different kinds of converters come into use. An analytical assessment is time-consuming for those arbitrary DC grids and only applies to the particular grid being analysed. However, only linear systems can be studied in this way.

Here, identical power electronic components are always used, and general assumptions and simplifications can be made, which allows for a generic analytical analysis of the stability. This approach offers several advantages, including the ability to make precise statements about system stability, understand general dynamic behaviour, and assess the effects of component tolerances.

Since the DC link is also used for power transmission, the impedance of the transmission line needs to be considered for a proper system model. In small DC grid configurations, the line impedance is assumed to be resistive [167, 170, 175]. More accurate models consider the inductance of the transmission line as well [171, 179, 186]. A complex impedance model of the transmission line in a π-structure is assumed to achieve an accurate system model here.

The model is derived by considering the RES and multiple parallel-connected grid inverters. Passive devices and loads are seen as disturbances to the control system and are not explicitly considered. A small-signal stability analysis is achieved by linearisation of the nonlinear system around the operation point. The root locus method is used for the stability and sensitivity analysis. It is particularly suitable for this case [169, 183].

3.2.1 Nonlinear Grid-Side DC Link Dynamics of a Single Grid Inverter

To assess the DC link's stability, the dynamics of the grid-side DC link voltage $u_{\mathrm{g}}^{\mathrm{dc}}$ must be determined. The subscript g refers to the grid inverter side. Firstly, the dynamics for a single grid inverter are determined. In the next section, this is then extended for an arbitrary number of fully parallel-connected grid inverters.

Considering the single grid inverter in Fig. 3.8, the DC link dynamics are given by the currents

$$\left.\begin{aligned} i_{\mathrm{c,h}}^{\mathrm{dc}} &= i_{\mathrm{g}}^{\mathrm{dc}} - i_{\sigma,\mathrm{h}}^{\mathrm{dc}} - \frac{u_{\mathrm{g,h}}^{\mathrm{dc}}}{\frac{R_{\mathrm{b}}}{2}} \quad \text{and} \\ i_{\mathrm{c,l}}^{\mathrm{dc}} &= i_{\mathrm{g}}^{\mathrm{dc}} - i_{\sigma,\mathrm{l}}^{\mathrm{dc}} - \frac{u_{\mathrm{g,l}}^{\mathrm{dc}}}{\frac{R_{\mathrm{b}}}{2}} \end{aligned}\right\} \tag{3.14}$$

through the higher and lower DC link capacitances, respectively. The subscript c refers to the capacitance, while the subscripts h and l refer to the high and low sides of the voltage source inverter (VSI), respectively. As defined in 2.2, the current $i_{\sigma,\mathrm{h}}^{\mathrm{dc}}$ is the sum of the switched phase currents $\boldsymbol{i}_{\mathrm{l}}^{abc}$ with $\left(\boldsymbol{\sigma}^{abc}\right)^{\top} \boldsymbol{i}_{\mathrm{l}}^{abc}$ through the high-side MOSFETs, where $\boldsymbol{\sigma}^{abc}$ are the switching

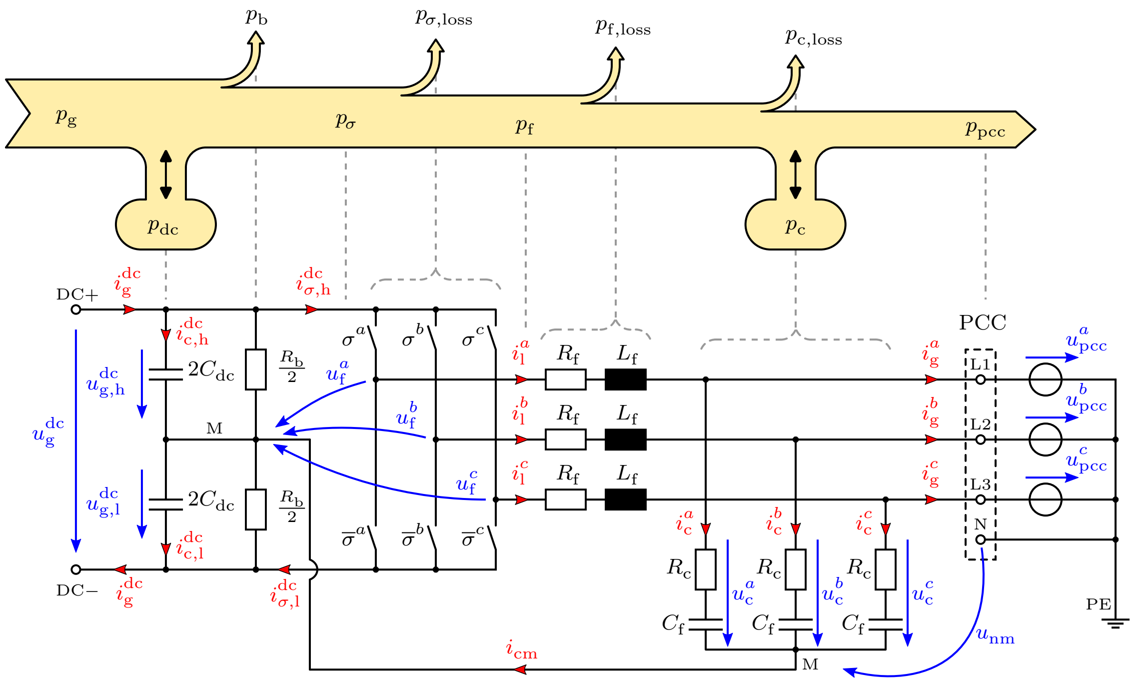

Figure 3.8: Electrical circuit of a single grid inverter with a qualitative power flow diagram on top.

states (see Sec. 2.1.1). This yields the DC link dynamics

$$\left.\begin{aligned}
\frac{\mathrm{d}}{\mathrm{d}t}u_{\mathrm{g,h}}^{\mathrm{dc}} &= \frac{i_{\mathrm{c,h}}^{\mathrm{dc}}}{2C_{\mathrm{dc}}} = \frac{1}{2C_{\mathrm{dc}}}\left(i_{\mathrm{g}}^{\mathrm{dc}} - i_{\sigma,\mathrm{h}}^{\mathrm{dc}} - \frac{u_{\mathrm{g,h}}^{\mathrm{dc}}}{\frac{R_\mathrm{b}}{2}}\right)\\
\frac{\mathrm{d}}{\mathrm{d}t}u_{\mathrm{g,l}}^{\mathrm{dc}} &= \frac{i_{\mathrm{c,l}}^{\mathrm{dc}}}{2C_{\mathrm{dc}}} = \frac{1}{2C_{\mathrm{dc}}}\left(i_{\mathrm{g}}^{\mathrm{dc}} - i_{\sigma,\mathrm{l}}^{\mathrm{dc}} - \frac{u_{\mathrm{g,l}}^{\mathrm{dc}}}{\frac{R_\mathrm{b}}{2}}\right).
\end{aligned}\right\} \tag{3.15}$$

The dynamics of the DC link voltage u_g^dc results from the sum of both voltages, which gives

$$\frac{\mathrm{d}}{\mathrm{d}t}u_{\mathrm{g}}^{\mathrm{dc}} = \frac{\mathrm{d}}{\mathrm{d}t}u_{\mathrm{g,h}}^{\mathrm{dc}} + \frac{\mathrm{d}}{\mathrm{d}t}u_{\mathrm{g,l}}^{\mathrm{dc}} = \frac{1}{C_{\mathrm{dc}}}\left(i_{\mathrm{g}}^{\mathrm{dc}} - \frac{i_{\sigma,\mathrm{h}}^{\mathrm{dc}} + i_{\sigma,\mathrm{l}}^{\mathrm{dc}}}{2} - \frac{u_{\mathrm{g}}^{\mathrm{dc}}}{R_\mathrm{b}}\right). \tag{3.16}$$

Considering Kirchhoff's current law at the midpoint M of the DC link results in

$$i_{\mathrm{c,h}}^{\mathrm{dc}} + \frac{u_{\mathrm{g,h}}^{\mathrm{dc}}}{\frac{R_\mathrm{b}}{2}} + i_{\mathrm{cm}} = i_{\mathrm{c,l}}^{\mathrm{dc}} + \frac{u_{\mathrm{g,l}}^{\mathrm{dc}}}{\frac{R_\mathrm{b}}{2}}. \tag{3.17}$$

Inserting the currents $i_{\mathrm{c,h}}^{\mathrm{dc}}$ and $i_{\mathrm{c,l}}^{\mathrm{dc}}$ from (3.14) yields

$$i_{\mathrm{cm}} = i_{\sigma,\mathrm{h}}^{\mathrm{dc}} - i_{\sigma,\mathrm{l}}^{\mathrm{dc}} \overset{(2.113)}{=} \frac{3}{\sqrt{2}}\, i_\mathrm{c}^{\gamma}. \tag{3.18}$$

Note that the currents $i_{\sigma,\mathrm{h}}^{\mathrm{dc}}$ and $i_{\sigma,\mathrm{l}}^{\mathrm{dc}}$ that flow into the VSI are stated here, not the capacitor currents. This relation shows that the difference between the currents $i_{\sigma,\mathrm{h}}^{\mathrm{dc}}$ and $i_{\sigma,\mathrm{l}}^{\mathrm{dc}}$ is the current i_{cm} through the star-point connection, which flows back into the DC link via the filter capacitors. For a grid inverter topology without this connection, the currents $i_{\sigma,\mathrm{h}}^{\mathrm{dc}}$ and $i_{\sigma,\mathrm{l}}^{\mathrm{dc}}$ are equal. Inserting (3.18) into the DC link dynamics (3.16) leads to

$$\frac{\mathrm{d}}{\mathrm{d}t} u_{\mathrm{g}}^{\mathrm{dc}} = \frac{\mathrm{d}}{\mathrm{d}t} u_{\mathrm{g,h}}^{\mathrm{dc}} + \frac{\mathrm{d}}{\mathrm{d}t} u_{\mathrm{g,l}}^{\mathrm{dc}} = \frac{1}{C_{\mathrm{dc}}} \left(i_{\mathrm{g}}^{\mathrm{dc}} - i_{\sigma,\mathrm{h}}^{\mathrm{dc}} + \frac{i_{\mathrm{cm}}}{2} - \frac{u_{\mathrm{g}}^{\mathrm{dc}}}{R_{\mathrm{b}}} \right) . \tag{3.19}$$

Since the current $i_{\mathrm{g}}^{\mathrm{dc}}$ is given by the energy sources, the grid inverter can only influence the DC link voltage $u_{\mathrm{g}}^{\mathrm{dc}}$ using the current $i_{\sigma,\mathrm{h}}^{\mathrm{dc}}$. The current $i_{\sigma,\mathrm{h}}^{\mathrm{dc}}$ depends on the inductance current $\boldsymbol{i}_{\mathrm{l}}^{dq\gamma}$, which is controlled by the grid inverter (see Sec. 2.5.4). Accordingly, the current references $\boldsymbol{i}_{l,\mathrm{ref}}^{dq}$ are the control signals for the DC link voltage controller. The relation between these two currents can be derived from the power balance

$$p_\sigma = p_{\mathrm{f}} + p_{\sigma,\mathrm{loss}} \, . \tag{3.20}$$

As shown by the qualitative power flow diagram in Fig. 3.8, the power p_σ flows from the DC link capacitors into the half-bridges of the VSI, the power p_{f} on the AC side that flows into the filter inductance L_{f}, and $p_{\sigma,\mathrm{loss}}$ are the switching losses. Note that the conduction losses of the MOSFETs are already considered with the resistance R_{f} (see Sec. 2.1.1).

Calculating the power p_σ is not trivial, because it is wrong to simply multiply the voltage $u_{\mathrm{g}}^{\mathrm{dc}}$ by the current $i_{\sigma,\mathrm{h}}^{\mathrm{dc}}$. It is essential that the current i_{cm} flowing back into the DC link via the star-point connection is also considered. To clarify this, the power p_σ is to be derived from the power balance

$$p_\sigma = p_{\mathrm{g}} - p_{\mathrm{dc}} - p_{\mathrm{b}} \, , \tag{3.21}$$

where p_{g} is the input power flowing into the grid inverter, p_{dc} is the power flowing into and out of the DC link capacitors C_{dc}, and p_{b} is the dissipated power of the balancing resistors. With (3.14) and $u_{\mathrm{g}}^{\mathrm{dc}} = u_{\mathrm{g,h}}^{\mathrm{dc}} + u_{\mathrm{g,l}}^{\mathrm{dc}}$, the power p_σ can be given as

$$\begin{aligned} p_\sigma &= \underbrace{u_{\mathrm{g}}^{\mathrm{dc}} \, i_{\mathrm{g}}^{\mathrm{dc}}}_{=p_{\mathrm{g}}} - \underbrace{\left(u_{\mathrm{g,h}}^{\mathrm{dc}} \, i_{\mathrm{c,h}}^{\mathrm{dc}} + u_{\mathrm{g,l}}^{\mathrm{dc}} \, i_{\mathrm{c,l}}^{\mathrm{dc}} \right)}_{=p_{\mathrm{dc}}} - \underbrace{\frac{\left(u_{\mathrm{g,h}}^{\mathrm{dc}}\right)^2 + \left(u_{\mathrm{g,l}}^{\mathrm{dc}}\right)^2}{\frac{R_{\mathrm{b}}}{2}}}_{=p_{\mathrm{b}}} \\ &\overset{(3.14)}{=} \left(\cancel{u_{\mathrm{g,h}}^{\mathrm{dc}}} + \cancel{u_{\mathrm{g,l}}^{\mathrm{dc}}} \right) i_{\mathrm{g}}^{\mathrm{dc}} \\ &\quad - u_{\mathrm{g,h}}^{\mathrm{dc}} \left(\cancel{i_{\mathrm{g}}^{\mathrm{dc}}} - i_{\sigma,\mathrm{h}}^{\mathrm{dc}} - \cancel{\frac{u_{\mathrm{g,h}}^{\mathrm{dc}}}{\frac{R_{\mathrm{b}}}{2}}} \right) - u_{\mathrm{g,l}}^{\mathrm{dc}} \left(\cancel{i_{\mathrm{g}}^{\mathrm{dc}}} - i_{\sigma,\mathrm{l}}^{\mathrm{dc}} - \cancel{\frac{u_{\mathrm{g,l}}^{\mathrm{dc}}}{\frac{R_{\mathrm{b}}}{2}}} \right) \\ &\quad \cancel{- \frac{\left(u_{\mathrm{g,h}}^{\mathrm{dc}}\right)^2 + \left(u_{\mathrm{g,l}}^{\mathrm{dc}}\right)^2}{\frac{R_{\mathrm{b}}}{2}}} \\ &= u_{\mathrm{g,h}}^{\mathrm{dc}} \, i_{\sigma,\mathrm{h}}^{\mathrm{dc}} + u_{\mathrm{g,l}}^{\mathrm{dc}} \, i_{\sigma,\mathrm{l}}^{\mathrm{dc}} \, . \end{aligned} \tag{3.22}$$

With (3.18), the power p_σ results in

$$p_\sigma = u_{\mathrm{g}}^{\mathrm{dc}} \, i_{\sigma,\mathrm{h}}^{\mathrm{dc}} - u_{\mathrm{g,l}}^{\mathrm{dc}} \, i_{\mathrm{cm}} \, , \tag{3.23}$$

where the first term describes the main power flow and the second term considers the oscillating power caused by the current i_{cm} through the midpoint connection.

The power p_{f} that flows into the filter results from the product of the voltages $\boldsymbol{u}_{\mathrm{f}}^{abc}$ and the inductance currents $\boldsymbol{i}_{\mathrm{l}}^{abc}$. Since the controller is designed in the synchronously rotating (d, q, γ)-reference frame, the power shall also be calculated with the associated quantities, which results in

$$p_{\mathrm{f}} = \left(\boldsymbol{u}_{\mathrm{f}}^{abc}\right)^{\top} \boldsymbol{i}_{\mathrm{l}}^{abc} = \frac{3}{2} \left(\boldsymbol{u}_{\mathrm{f}}^{dq\gamma}\right)^{\top} \boldsymbol{i}_{\mathrm{l}}^{dq\gamma} . \tag{3.24}$$

The voltages $\boldsymbol{u}_{\mathrm{f}}^{dq\gamma}$ can be derived by applying the amplitude-correct Clarke ($\kappa = \frac{2}{3}$) and Park transformation to (2.102), which yields

$$\boldsymbol{u}_{\mathrm{f}}^{dq\gamma} = R_{\mathrm{f}}\, \boldsymbol{i}_{\mathrm{l}}^{dq\gamma} + L_{\mathrm{f}} \frac{\mathrm{d}}{\mathrm{d}t} \boldsymbol{i}_{\mathrm{l}}^{dq\gamma} + \omega_{\mathrm{g}}\, L_{\mathrm{f}}\, \boldsymbol{J}_0\, \boldsymbol{i}_{\mathrm{l}}^{dq\gamma} + \boldsymbol{u}_{\mathrm{pcc}}^{dq\gamma} + \boldsymbol{T}_{\mathrm{c}}\, \mathbf{1}_3\, u_{\mathrm{nm}} . \tag{3.25}$$

Note that the grid-side impedances are included in the voltage sources $\boldsymbol{u}_{\mathrm{pcc}}^{abc}$. This does not mean that the impedance can be neglected. However, since these are usually unknown and the power flowing into the grid is measured at the point of common coupling (PCC), it is sufficient for this power consideration to use only the voltages $\boldsymbol{u}_{\mathrm{pcc}}^{dq\gamma}$. This combination implies that the voltages $\boldsymbol{u}_{\mathrm{pcc}}^{dq\gamma}$ depend on the gird currents $\boldsymbol{i}_{\mathrm{g}}^{dq}$ according to (2.139).

Inserting (3.25) into (3.24) yields

$$\begin{aligned} p_{\mathrm{f}} &= \frac{3}{2} \left(R_{\mathrm{f}}\, \boldsymbol{i}_{\mathrm{l}}^{dq\gamma} + L_{\mathrm{f}} \frac{\mathrm{d}}{\mathrm{d}t} \boldsymbol{i}_{\mathrm{l}}^{dq\gamma} + \omega_{\mathrm{g}}\, L_{\mathrm{f}}\, \boldsymbol{J}_0\, \boldsymbol{i}_{\mathrm{l}}^{dq\gamma} + \boldsymbol{u}_{\mathrm{pcc}}^{dq\gamma} + \boldsymbol{T}_{\mathrm{c}}\, \mathbf{1}_3\, u_{\mathrm{nm}} \right)^{\top} \boldsymbol{i}_{\mathrm{l}}^{dq\gamma} \\ &= \frac{3}{2} \left(R_{\mathrm{f}} \left\| \boldsymbol{i}_{\mathrm{l}}^{dq\gamma} \right\|^2 + L_{\mathrm{f}} \left(\frac{\mathrm{d}}{\mathrm{d}t} \boldsymbol{i}_{\mathrm{l}}^{dq\gamma} \right)^{\top} \boldsymbol{i}_{\mathrm{l}}^{dq\gamma} + \omega_{\mathrm{g}}\, L_{\mathrm{f}} \underbrace{\left(\boldsymbol{J}_0\, \boldsymbol{i}_{\mathrm{l}}^{dq\gamma} \right)^{\top} \boldsymbol{i}_{\mathrm{l}}^{dq\gamma}}_{=0} + \left(\boldsymbol{u}_{\mathrm{pcc}}^{dq\gamma} + \boldsymbol{T}_{\mathrm{c}}\, \mathbf{1}_3\, u_{\mathrm{nm}} \right)^{\top} \boldsymbol{i}_{\mathrm{l}}^{dq\gamma} \right) . \end{aligned} \tag{3.26}$$

Thus, the current $i_{\sigma,\mathrm{h}}^{\mathrm{dc}}$ can be given by (3.20) and (3.23)

$$\begin{aligned} i_{\sigma,\mathrm{h}}^{\mathrm{dc}} &= \frac{p_{\mathrm{f}} + p_{\sigma,\mathrm{loss}} + u_{\mathrm{g,l}}^{\mathrm{dc}}\, i_{\mathrm{cm}}}{u_{\mathrm{g}}^{\mathrm{dc}}} \\ &\overset{(3.26)}{=} \frac{3}{2\, u_{\mathrm{g}}^{\mathrm{dc}}} \left(R_{\mathrm{f}} \left\| \boldsymbol{i}_{\mathrm{l}}^{dq\gamma} \right\|^2 + L_{\mathrm{f}} \left(\frac{\mathrm{d}}{\mathrm{d}t} \boldsymbol{i}_{\mathrm{l}}^{dq\gamma} \right)^{\top} \boldsymbol{i}_{\mathrm{l}}^{dq\gamma} + \left(\boldsymbol{u}_{\mathrm{pcc}}^{dq\gamma} \right)^{\top} \boldsymbol{i}_{\mathrm{l}}^{dq\gamma} \right) + \frac{p_{\sigma,\mathrm{loss}} + u_{\mathrm{g,l}}^{\mathrm{dc}}\, i_{\mathrm{cm}}}{u_{\mathrm{g}}^{\mathrm{dc}}} . \end{aligned} \tag{3.27}$$

Note that also the voltage u_{nm} disappeared, as it only affects the γ-component since

$$\boldsymbol{T}_{\mathrm{c}}\, \mathbf{1}_3 = \begin{pmatrix} 0 \\ 0 \\ \sqrt{2} \end{pmatrix} . \tag{3.28}$$

The dynamics of the current control loops are approximated by the first-order transfer function

$$\boldsymbol{i}_{l}^{dq} = \frac{1}{1 + s\, \tau_{\mathrm{c}}}\, \boldsymbol{i}_{l,\mathrm{ref}}^{dq} \quad \bullet\!\!-\!\!\circ \quad \frac{\mathrm{d}}{\mathrm{d}t} \boldsymbol{i}_{l}^{dq} = \frac{1}{\tau_{\mathrm{c}}} \left(\boldsymbol{i}_{l,\mathrm{ref}}^{dq} - \boldsymbol{i}_{l}^{dq} \right) , \tag{3.29}$$

where τ_{c} is the time constant. This typical assumption holds for high switching and control frequencies [80, Sec. 10.3], [179, 214]. Inserting this into (3.27) leads to

$$i_{\sigma,\mathrm{h}}^{\mathrm{dc}} = \frac{3}{2\, u_{\mathrm{g}}^{\mathrm{dc}}} \left(\left(R_{\mathrm{f}} - \frac{L_{\mathrm{f}}}{\tau_{\mathrm{c}}} \right) \left\| \boldsymbol{i}_{l}^{dq} \right\|^2 + \frac{L_{\mathrm{f}}}{\tau_{\mathrm{c}}} \left(\boldsymbol{i}_{l,\mathrm{ref}}^{dq} \right)^{\top} \boldsymbol{i}_{l}^{dq} + \left(\boldsymbol{u}_{\mathrm{pcc}}^{dq} \right)^{\top} \boldsymbol{i}_{l}^{dq} \right) + \frac{p_{\sigma,\mathrm{loss}} + u_{\mathrm{g,l}}^{\mathrm{dc}}\, i_{\mathrm{cm}}}{u_{\mathrm{g}}^{\mathrm{dc}}} . \tag{3.30}$$

The nonlinear DC link dynamics are obtained by inserting (3.30) into (3.19), which yields

$$\frac{\mathrm{d}}{\mathrm{d}t}u_{\mathrm{g}}^{\mathrm{dc}} = \frac{1}{C_{\mathrm{dc}}}\Bigg[i_{\mathrm{g}}^{\mathrm{dc}} - \frac{3}{2\,u_{\mathrm{g}}^{\mathrm{dc}}}\left(\left(R_{\mathrm{f}} - \frac{L_{\mathrm{f}}}{\tau_{\mathrm{c}}}\right)\left\|\boldsymbol{i}_{l}^{dq}\right\|^{2} + \frac{L_{\mathrm{f}}}{\tau_{\mathrm{c}}}\left(\boldsymbol{i}_{l,\mathrm{ref}}^{dq}\right)^{\top}\boldsymbol{i}_{l}^{dq} + \left(\boldsymbol{u}_{\mathrm{pcc}}^{dq}\right)^{\top}\boldsymbol{i}_{l}^{dq}\right) \\ - \frac{p_{\sigma,\mathrm{loss}}}{u_{\mathrm{g}}^{\mathrm{dc}}} - \frac{u_{\mathrm{g,l}}^{\mathrm{dc}}\,i_{\mathrm{cm}}}{u_{\mathrm{g}}^{\mathrm{dc}}} + \frac{i_{\mathrm{cm}}}{2} - \frac{u_{\mathrm{g}}^{\mathrm{dc}}}{R_{\mathrm{b}}}\Bigg]\,. \tag{3.31}$$

3.2.2 Nonlinear Grid-Side DC Link Dynamics with Multiple Grid Inverters

When connecting several grid inverters in parallel, it is assumed that the connection between them is very short, so the impedance between them can be neglected. Thus, the DC link voltage at the terminals of each grid inverter i are the same, i.e.

$$u_{\mathrm{g},1}^{\mathrm{dc}} = u_{\mathrm{g},2}^{\mathrm{dc}} = \ldots = u_{\mathrm{g},N_{\mathrm{g}}}^{\mathrm{dc}} \stackrel{!}{=} u_{\mathrm{g}}^{\mathrm{dc}}\,, \tag{3.32}$$

where $N_{\mathrm{g}} \in \mathbb{N}$ is the number of fully parallel-connected grid inverters. This implies that the DC link capacitors C_{dc} of all grid inverters are directly connected in parallel, so they can be combined to one capacitance

$$C_{\mathrm{g}} \coloneqq N_{\mathrm{g}}\,C_{\mathrm{dc}}\,. \tag{3.33}$$

The current $i_{\mathrm{g}}^{\mathrm{dc}}$ is the sum of the currents $i_{\mathrm{g},i}^{\mathrm{dc}}$, flowing into the grid inverters with

$$i_{\mathrm{g}}^{\mathrm{dc}} = i_{\mathrm{g},1}^{\mathrm{dc}} + i_{\mathrm{g},2}^{\mathrm{dc}} + \ldots + i_{\mathrm{g},N_{\mathrm{g}}}^{\mathrm{dc}} = \sum_{i=1}^{N_{\mathrm{g}}} i_{\mathrm{g},i}^{\mathrm{dc}}\,. \tag{3.34}$$

Analogue to (3.19), the DC link dynamics on the grid side can be given by

$$\frac{\mathrm{d}}{\mathrm{d}t}u_{\mathrm{g}}^{\mathrm{dc}} = \frac{1}{C_{\mathrm{g}}}\left(i_{\mathrm{g}}^{\mathrm{dc}} + \sum_{i=1}^{N_{\mathrm{g}}}\left(-i_{\sigma,i}^{\mathrm{dc}} + \frac{i_{\mathrm{cm},i}}{2} - \frac{u_{\mathrm{g},i}^{\mathrm{dc}}}{R_{\mathrm{b}}}\right)\right)\,. \tag{3.35}$$

Inserting the current $i_{\sigma,\mathrm{h},i}^{\mathrm{dc}}$ from (3.30) leads to

$$\frac{\mathrm{d}}{\mathrm{d}t}u_{\mathrm{g}}^{\mathrm{dc}} = \frac{1}{C_{\mathrm{g}}}\Bigg[i_{\mathrm{g}}^{\mathrm{dc}} - \frac{3}{2\,u_{\mathrm{g}}^{\mathrm{dc}}}\Bigg(\left(R_{\mathrm{f}} - \frac{L_{\mathrm{f}}}{\tau_{\mathrm{c}}}\right)\sum_{i=1}^{N_{\mathrm{g}}}\left\|\boldsymbol{i}_{\mathrm{l},i}^{dq}\right\|^{2} + \frac{L_{\mathrm{f}}}{\tau_{\mathrm{c}}}\sum_{i=1}^{N_{\mathrm{g}}}\left(\boldsymbol{i}_{\mathrm{l,ref},i}^{dq}\right)^{\top}\boldsymbol{i}_{\mathrm{l},i}^{dq} \\ + \left(\boldsymbol{u}_{\mathrm{pcc}}^{dq}\right)^{\top}\sum_{i=1}^{N_{\mathrm{g}}}\boldsymbol{i}_{\mathrm{l},i}^{dq}\Bigg) - \sum_{i=1}^{N_{\mathrm{g}}}\left(\frac{p_{\sigma,\mathrm{loss},i}}{u_{\mathrm{g}}^{\mathrm{dc}}} + \frac{u_{\mathrm{g,l},i}^{\mathrm{dc}}\,i_{\mathrm{cm},i}}{u_{\mathrm{g}}^{\mathrm{dc}}} - \frac{i_{\mathrm{cm},i}}{2} + \frac{u_{\mathrm{g},i}^{\mathrm{dc}}}{R_{\mathrm{b}}}\right)\Bigg]\,. \tag{3.36}$$

As stated in (3.32), the DC link voltage $u_{\mathrm{g}}^{\mathrm{dc}}$ is assumed to be the same at each grid inverter. Thus, the reference currents $\boldsymbol{i}_{\mathrm{l,ref},i}^{dq}$ are also the same, as they are derived from the DC link voltage according to (3.11), leading to

$$\boldsymbol{i}_{\mathrm{l,ref},1}^{dq} = \boldsymbol{i}_{\mathrm{l,ref},2}^{dq} = \ldots = \boldsymbol{i}_{\mathrm{l,ref},N_{\mathrm{g}}}^{dq} \stackrel{!}{=} \boldsymbol{i}_{l,\mathrm{ref}}^{dq}\,. \tag{3.37}$$

Moreover, since the reference currents $\boldsymbol{i}_{\mathrm{l,ref},i}^{dq}$ are the same, the resulting currents $\boldsymbol{i}_{\mathrm{l},i}^{dq}$ can also be assumed to be the same due to the identical control parameters and hardware. This leads to the assumptions

$$\boldsymbol{i}_{\mathrm{l},1}^{dq} = \boldsymbol{i}_{\mathrm{l},2}^{dq} = \ldots = \boldsymbol{i}_{\mathrm{l},N_{\mathrm{g}}}^{dq} \stackrel{!}{=} \boldsymbol{i}_{l}^{dq}\,, \tag{3.38}$$

and thus further to

$$\sum_{i=1}^{N_\mathrm{g}} \left\| \boldsymbol{i}_{\mathrm{l},i}^{dq} \right\|^2 = N_\mathrm{g} \left\| \boldsymbol{i}_{l}^{dq} \right\|^2 \quad \text{and} \quad \sum_{i=1}^{N_\mathrm{g}} \left(\boldsymbol{i}_{\mathrm{l,ref},i}^{dq} \right)^\top \boldsymbol{i}_{\mathrm{l},i}^{dq} = N_\mathrm{g} \left(\boldsymbol{i}_{l,\mathrm{ref}}^{dq} \right)^\top \boldsymbol{i}_{l}^{dq} . \tag{3.39}$$

In Section 2.5, it is shown that the grid inverters hardly interact with fully parallel-connected grid inverters due to well-tuned PI state feedback control. Therefore, each inverter can be considered independent when connected in parallel, especially for the dq-components. In comparison to the previous consideration with only one grid inverter, the γ-current i_l^γ can flow not only via the internal star-point connection as current i_cm, but also to the grid inverters connected in parallel. The γ-component of the induction currents $\boldsymbol{i}_\mathrm{l}^{dq\gamma}$ is controlled to zero since there is no practical purpose, and it would otherwise only cause losses. As a result, the current i_cm is indirectly controlled to zero. Only the current ripple of the inductance current flows via the star-point connection, but it is zero on average, as analysed in Fig. 2.46. Since these components do not contribute to the power flow or significantly influence the dynamics of the DC link voltage u_g^dc, they are substituted with the current

$$i_{\mathrm{loss},i} := \frac{p_{\sigma,\mathrm{loss},i}}{u_\mathrm{g}^\mathrm{dc}} + \frac{u_\mathrm{g,l}^\mathrm{dc}\, i_{\mathrm{cm},i}}{u_\mathrm{g}^\mathrm{dc}} - \frac{i_{\mathrm{cm},i}}{2} + \frac{3}{2\, u_\mathrm{g}^\mathrm{dc}} \left(R_\mathrm{f} \left(i_{\mathrm{l},i}^\gamma \right)^2 + L_\mathrm{f} \frac{\mathrm{d}}{\mathrm{d}t} i_{\mathrm{l},i}^\gamma\, i_{\mathrm{l},i}^\gamma + u_\mathrm{pcc}^\gamma\, i_{\mathrm{l},i}^\gamma \right) . \tag{3.40}$$

Since the current $i_{\mathrm{loss},i}$ is very small and partly undefined,

$$\sum_{i=1}^{N_\mathrm{g}} i_{\mathrm{loss},i} = N_\mathrm{g}\, i_\mathrm{loss} \tag{3.41}$$

is assumed.

Thus, the nonlinear DC link dynamics for multiple fully parallel-connection grid inverters can be given by

$$\begin{aligned} \frac{\mathrm{d}}{\mathrm{d}t} u_\mathrm{g}^\mathrm{dc} = \frac{1}{C_\mathrm{g}} \Bigg[& i_\mathrm{g}^\mathrm{dc} - \frac{3\, N_\mathrm{g}}{2\, u_\mathrm{g}^\mathrm{dc}} \left(\left(R_\mathrm{f} - \frac{L_\mathrm{f}}{\tau_\mathrm{c}} \right) \left\| \boldsymbol{i}_l^{dq} \right\|^2 + \frac{L_\mathrm{f}}{\tau_\mathrm{c}} \left(\boldsymbol{i}_{l,\mathrm{ref}}^{dq} \right)^\top \boldsymbol{i}_l^{dq} + \left(\boldsymbol{u}_\mathrm{pcc}^{dq} \right)^\top \boldsymbol{i}_l^{dq} \right) \\ & - N_\mathrm{g}\, i_\mathrm{loss} - \frac{N_\mathrm{g}\, u_\mathrm{g}^\mathrm{dc}}{R_\mathrm{b}} \Bigg] . \end{aligned} \tag{3.42}$$

3.2.3 DC Link Dynamics on the Side of the Renewable Energy Sources

The introduced highly modular power electronics system allows the integration of any renewable energy source (RES). To model the RES, the generator units for wave energy converters (WEC), wind turbines (WT) and photovoltaic (PV) are combined into one current source, as shown in Fig. 3.9. Since the generated power depends strongly on the natural conditions and fluctuates accordingly, the sum of the generated currents

$$i_\mathrm{ec}^\mathrm{dc} := \sum_{i=1}^{N_\mathrm{wc}} i_{\mathrm{wc},i}^\mathrm{dc} + \sum_{i=1}^{N_\mathrm{wt}} i_{\mathrm{wt},i}^\mathrm{dc} + \sum_{i=1}^{N_\mathrm{pv}} i_{\mathrm{pv},i}^\mathrm{dc} \tag{3.43}$$

from the energy conversion (EC) systems is interpreted as a disturbance for the system.

As for the grid side in the previous section, the capacitances of the generating units are combined to one capacitance

$$C_\mathrm{ec} := N_\mathrm{ec}\, C_\mathrm{dc} . \tag{3.44}$$

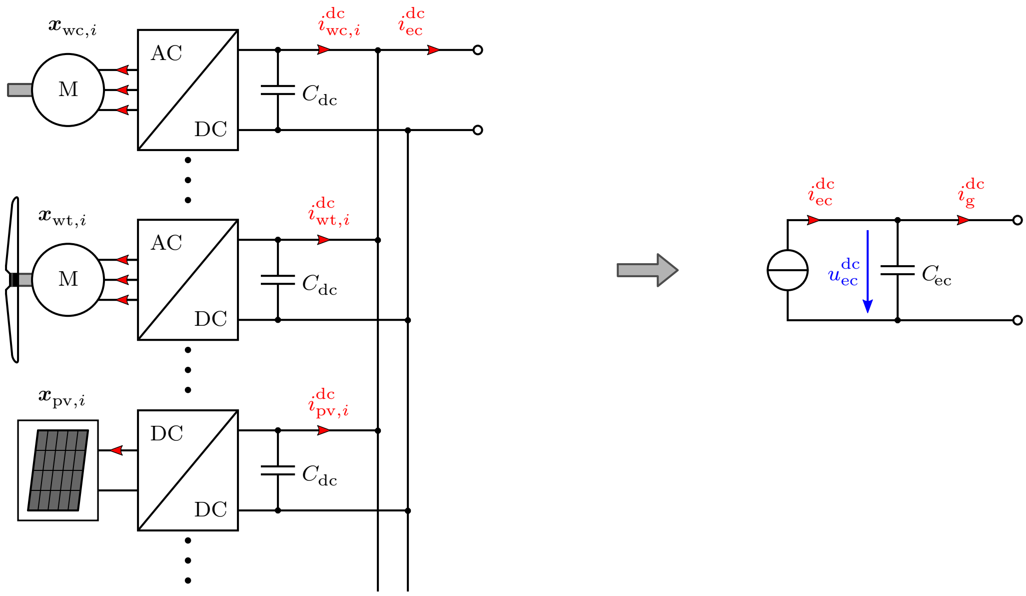

Figure 3.9: Illustration of the combination of the generating units for wave energy converters (WEC), wind turbines (WT) and photovoltaics (PV) into one current source.

Thus, the RES-side voltage $u_{\mathrm{ec}}^{\mathrm{dc}}$ dynamics is given by

$$\frac{\mathrm{d}}{\mathrm{d}t} u_{\mathrm{ec}}^{\mathrm{dc}} = \frac{1}{C_{\mathrm{ec}}} \left(i_{\mathrm{ec}}^{\mathrm{dc}} - i_{\mathrm{g}}^{\mathrm{dc}} \right) , \tag{3.45}$$

where $i_{\mathrm{g}}^{\mathrm{dc}}$ is the current that flows to the grid inverters.

The DC link is chosen as the transmission system to overcome the distance between the generating units and the PCC. Its voltage is higher than the AC grid's. Hence, the transmission losses are lower. The transmission losses $p_{\mathrm{l},\Omega}$ are given by

$$p_{\mathrm{l},\Omega} = 2\, R_{\mathrm{l}} \left(i_{\mathrm{g}}^{\mathrm{dc}} \right)^2 , \tag{3.46}$$

where R_{l} is the ohmic resistance of the transmission line of one wire. The resistance R_{l} is a combination of the resistance $R_{\mathrm{l},c}$ of the cable and the contact resistance $R_{\mathrm{l},0}$ with

$$R_{\mathrm{l}} = R_{\mathrm{l},c} + R_{\mathrm{l},0} \, . \tag{3.47}$$

As there is a forward and return line, the resistance for the losses must be considered two times. For cables, the resistance can be calculated with

$$R_{\mathrm{l},c} = \rho \, \frac{l_{\mathrm{l}}}{A_{\mathrm{l}}}, \tag{3.48}$$

where l_{l} is the length of the cable in m, and A_{l} is the cross-section in mm^2. ρ is the resistivity of the material used, usually copper or aluminium. The resistivity for soft-annealed copper and aluminium is given by [216], [63, Sec. 10.3.2]

$$\rho_{\mathrm{Cu}} \approx 17.3 \, \frac{\mathrm{m}\Omega\,\mathrm{mm}^2}{\mathrm{m}} \qquad \text{and} \qquad \rho_{\mathrm{Al}} \approx 26.5 \, \frac{\mathrm{m}\Omega\,\mathrm{mm}^2}{\mathrm{m}} \, , \tag{3.49}$$

respectively.
The resistance $R_{1,0}$ is the non-vanishing resistance of R_1 for $l_1 = 0$ m that accounts for the contact resistance of the terminals and the fuses installed at the output of the power electronic devices to protect the transmission line. The resistance of the fuse determines the amount of energy required to melt the fusing element and, thus, the fuse's current rating. The fuses used here have a resistance of approximately 5 mΩ [217]. For long transmission lines, this resistance is insignificant and can be neglected. However, for short distances below 1 m, this component is essential to the system's damping, as shown in Sec. 3.2.5.
For a specific generated power p_{ec}, the generated current is

$$i_{ec}^{dc} = \frac{p_{ec}}{u_{ec}^{dc}}, \tag{3.50}$$

i.e. the higher the voltage u_{ec}^{dc}, the lower the current. Consequently, according to (3.46), the transmission losses $p_{1,\Omega}$ decrease more than proportionally with increasing voltage. Further advantages of a DC transmission system are the absence of reactive power flow and the fact that synchronisation of the generating units is not required [173, 174].
A transmission line is characterised by the so-called primary line constants, whereby the DC-resistance R_1 is one of them. The others are the line inductance L_1, the insulator capacitance C_1 and the insulator conductivity G_1 [218, Sec. 39]. They depend on the cross-section, construction and insulation type of the cable. They are usually given per unit length so that they can be multiplied by the cable length l_1 to calculate the actual values.

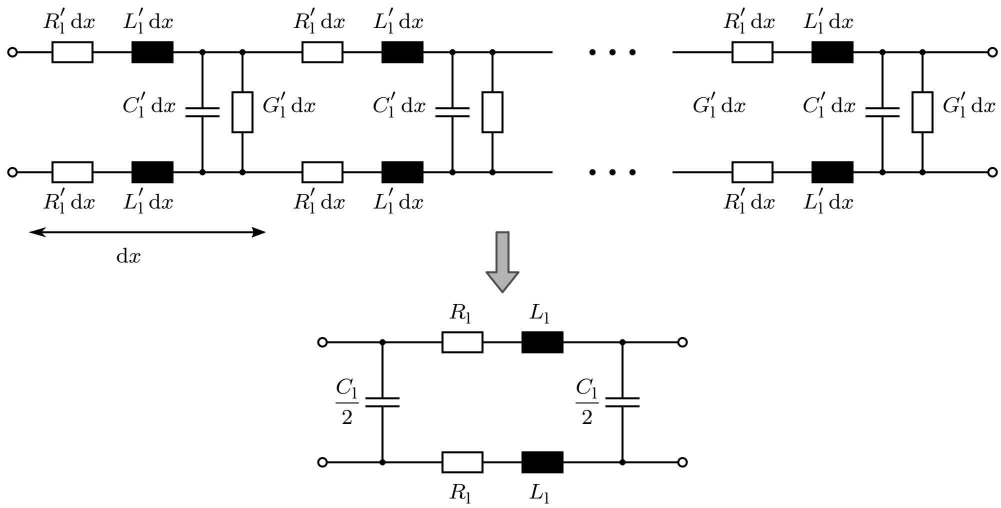

Figure 3.10: Model simplification for short transmission lines.

To achieve an accurate representation of the transmission line, the impedances must be distributed continuously along the line with infinitesimally small sections dx [218, Sec. 39], as shown at the top in Fig. 3.10. The apostrophe on the line constants indicates that they represent the specific values per unit length. However, lumped elements can be assumed if the sections are short enough. The impedances are arranged in a π-structure, whereby the capacitance is evenly distributed at both ends [148], as shown at the bottom in Fig. 3.10.
For AC transmission lines with a grid frequency of 50 Hz, a single π-section of up to 250 km can be assumed [187, Sec. 6.4]. The sections must be shorter if higher frequencies are present to obtain a more accurate model. In [219], a long transmission cable is modelled to analyse the stability of power converters in DC distribution systems. It is shown that more π-sections in

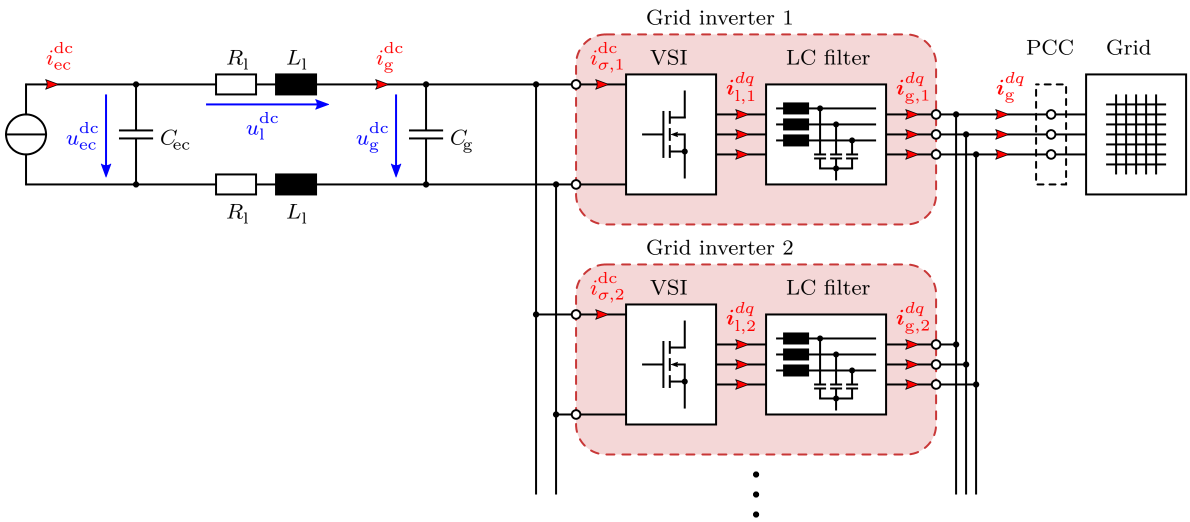

Figure 3.11: Electrical circuit with the simplified transmission line model.

series increase the accuracy of the transmission line model. A section length of 20 km provides a good balance between accuracy and complexity.

For this system, cables with cross-sections up to 35 mm^2 can be used. Based on the standard DIN VDE 0100-520 [220], the voltage drop along the cable should be limited to 3 % of the maximum DC link voltage $u^{\mathrm{dc}}_{\mathrm{max}}$ at steady-state conditions, i.e.

$$\frac{2\,R_{\mathrm{l}}\,i^{\mathrm{dc}}_{\mathrm{g,max}}}{u^{\mathrm{dc}}_{\mathrm{max}}} \overset{!}{\leq} 3\ \%\,. \tag{3.51}$$

This also limits the transmission losses $p_{\mathrm{l},\Omega}$ to 3 % of the generated power p_{ec}, as

$$\frac{p_{\mathrm{l},\Omega}}{p_{\mathrm{ec}}} \overset{(3.46)}{=} \frac{2\,R_{\mathrm{l}}\left(i^{\mathrm{dc}}_{\mathrm{g}}\right)^2}{u^{\mathrm{dc}}_{\mathrm{ec}}\,i^{\mathrm{dc}}_{\mathrm{g}}} = \frac{2\,R_{\mathrm{l}}\,i^{\mathrm{dc}}_{\mathrm{g}}}{u^{\mathrm{dc}}_{\mathrm{ec}}} \overset{(3.51)}{\leq} 3\ \%\,. \tag{3.52}$$

The cross-section and voltage drop parameters limit the maximum system power and transmission line length. If more power is required, the overall system must be divided into subsystems, which are then coupled on the AC side. Suppose the distances are very long, e.g. from the floating platform to the shore. In that case, the grid transformer can be placed closer to the generating units, i.e. on the platform, to overcome the long distances with medium voltage. The longest DC link transmission line is reached with the smallest possible system size and a maximum cross-section of 35 mm^2. The smallest system configuration consists of one grid inverter with 5 kW. The permissible cable length is then about 4 km. Therefore, a single π-section is sufficient to model the DC link transmission line [148, 219].

The inductance L_{l} depends strongly on the design of the cable. The cross-section, the thickness of the insulation and the wires' twisting are decisive factors. There are various formulas for estimating the cable inductance [218, Sec. 39], [187, Sec. 6.4]. However, if the actual value of a particular cable is required, it must be measured. It is often also specified by the manufacturer. As a rule of thumb, a specific inductance of

$$0.2\,\frac{\mu\mathrm{H}}{\mathrm{m}} \;\leq\; L'_{\mathrm{l}} \;\leq\; 1\,\frac{\mu\mathrm{H}}{\mathrm{m}} \tag{3.53}$$

can be assumed [148].

Fig. 3.11 shows the overall system model with the simplified transmission line model. The specific value for the insulator capacitance C_l is in the order of 100 to 300 $\frac{\mathrm{nF}}{\mathrm{km}}$ [148]. In this model, the insulator capacitance is parallel to the DC link capacitances C_ec and C_g. The insulator capacitance C_l is many times smaller than the DC link capacitances and can, therefore, be neglected [148]. Thus, the dynamics of the current i_g^dc that flows in the DC link transmission line is given by

$$\frac{\mathrm{d}}{\mathrm{d}t} i_\mathrm{g}^\mathrm{dc} = \frac{1}{2\,L_\mathrm{l}} \left(u_\mathrm{ec}^\mathrm{dc} - 2\,R_\mathrm{l}\, i_\mathrm{g}^\mathrm{dc} - u_\mathrm{g}^\mathrm{dc} \right) . \tag{3.54}$$

Fig. 3.11 shows the block diagram of the resulting DC link dynamics of the energy conversion (EC) system.

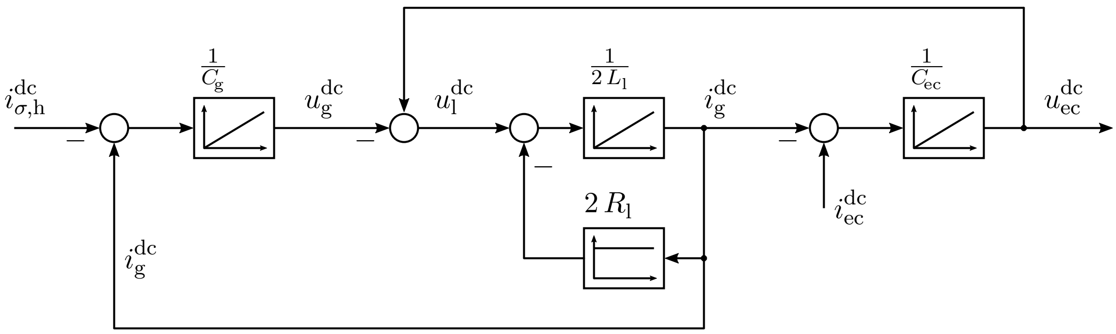

Figure 3.12: Block diagram of the DC link dynamics of the resulting DC link dynamics of the energy conversion (EC) system.

3.2.4 Linearisation in the State-Space Representation

A linearised system is required for the stability analysis in the next section. With the dynamics of the DC link voltage u_g^dc from (3.42), the current dynamics of the current controller as defined in (3.29), the dynamics of the transmission line (3.54), and the dynamics of the RES-side voltage $u_\mathrm{ec}^\mathrm{dc}$ from (3.45), the nonlinear dynamics of the system shown in Fig. 3.11 are determined by

$$\left.\begin{aligned}
\frac{\mathrm{d}}{\mathrm{d}t} u_\mathrm{g}^\mathrm{dc} &= \frac{1}{C_\mathrm{g}} \Bigg[i_\mathrm{g}^\mathrm{dc} - \frac{3\,N_\mathrm{g}}{2\,u_\mathrm{g}^\mathrm{dc}} \left(\left(R_\mathrm{f} - \frac{L_\mathrm{f}}{\tau_\mathrm{c}} \right) \left\| \boldsymbol{i}_l^{dq} \right\|^2 + \frac{L_\mathrm{f}}{\tau_\mathrm{c}} \left(\boldsymbol{i}_{l,\mathrm{ref}}^{dq} \right)^\top \boldsymbol{i}_l^{dq} \right.\\
&\qquad \left. + \left(\boldsymbol{u}_\mathrm{pcc}^{dq} \right)^\top \boldsymbol{i}_l^{dq} \right) - N_\mathrm{g}\, i_\mathrm{loss} - \frac{N_\mathrm{g}\, u_\mathrm{g}^\mathrm{dc}}{R_\mathrm{b}} \Bigg] \\
\frac{\mathrm{d}}{\mathrm{d}t} \boldsymbol{i}_l^{dq} &= \frac{1}{\tau_\mathrm{c}} \left(\boldsymbol{i}_{l,\mathrm{ref}}^{dq} - \boldsymbol{i}_l^{dq} \right) \\
\frac{\mathrm{d}}{\mathrm{d}t} i_\mathrm{g}^\mathrm{dc} &= \frac{1}{2\,L_\mathrm{l}} \left(u_\mathrm{ec}^\mathrm{dc} - 2\,R_\mathrm{l}\, i_\mathrm{g}^\mathrm{dc} - u_\mathrm{g}^\mathrm{dc} \right) \\
\frac{\mathrm{d}}{\mathrm{d}t} u_\mathrm{ec}^\mathrm{dc} &= \frac{1}{C_\mathrm{ec}} \left(i_\mathrm{ec}^\mathrm{dc} - i_\mathrm{g}^\mathrm{dc} \right) .
\end{aligned}\right\} \tag{3.55}$$

The dynamics of the DC link can be given by the generic state-space representation with [221, Sec. 2.5.2]

$$\left.\begin{aligned} \frac{\mathrm{d}}{\mathrm{d}t}\boldsymbol{x}_{\mathrm{dc}} &= \boldsymbol{f}_{\mathrm{dc}}(\boldsymbol{x}_{\mathrm{dc}}, \boldsymbol{u}_{\mathrm{dc}}, \boldsymbol{d}_{\mathrm{dc}}) \\ \boldsymbol{y}_{\mathrm{dc}} &= \boldsymbol{g}_{\mathrm{dc}}(\boldsymbol{x}_{\mathrm{dc}})\ , \end{aligned}\right\} \tag{3.56}$$

where $\boldsymbol{x}_{\mathrm{dc}}$ is the system's state vector, $\boldsymbol{u}_{\mathrm{dc}}$ is the input vector, and $\boldsymbol{d}_{\mathrm{dc}}$ is the disturbance vector. They affect the system's dynamics as described by the state function $\boldsymbol{f}_{\mathrm{dc}}$. The output vector $\boldsymbol{y}_{\mathrm{dc}}$ is determined from the system states $\boldsymbol{x}_{\mathrm{dc}}$ according to the output function $\boldsymbol{g}_{\mathrm{dc}}$.

A small-signal analysis around the operating points $\boldsymbol{x}^{\star}_{\mathrm{dc}}$ is performed to obtain a linear state-space representation of the DC link dynamics. If the deviations from the operating points are small, the nonlinear equation (3.56) can be approximated very well with the first-order Taylor series [221, Sec. 2.5.2], [93, Sec. 3.2.3]. In the following, the quantities that depend on the operating points are marked with a superscript star ($\square^{\star}$), and a delta ($\Delta\square$) indicates the deviations from the operating point. Thus, the linear approximation of (3.56) can be given by [221, Sec. 2.5.2]

$$\begin{aligned} \frac{\mathrm{d}}{\mathrm{d}t}\left(\boldsymbol{x}^{\star}_{\mathrm{dc}} + \Delta\boldsymbol{x}_{\mathrm{dc}}\right) = \boldsymbol{f}_{\mathrm{dc}}(\boldsymbol{x}^{\star}_{\mathrm{dc}}, \boldsymbol{u}^{\star}_{\mathrm{dc}}, \boldsymbol{d}^{\star}_{\mathrm{dc}}) &+ \left.\frac{\partial \boldsymbol{f}_{\mathrm{dc}}(\boldsymbol{x}_{\mathrm{dc}}, \boldsymbol{u}_{\mathrm{dc}}, \boldsymbol{d}_{\mathrm{dc}})}{\partial \boldsymbol{x}_{\mathrm{dc}}}\right|_{\boldsymbol{x}^{\star}_{\mathrm{dc}}, \boldsymbol{u}^{\star}_{\mathrm{dc}}, \boldsymbol{d}^{\star}_{\mathrm{dc}}} \Delta\boldsymbol{x}_{\mathrm{dc}} \\ &+ \left.\frac{\partial \boldsymbol{f}_{\mathrm{dc}}(\boldsymbol{x}_{\mathrm{dc}}, \boldsymbol{u}_{\mathrm{dc}}, \boldsymbol{d}_{\mathrm{dc}})}{\partial \boldsymbol{u}_{\mathrm{dc}}}\right|_{\boldsymbol{x}^{\star}_{\mathrm{dc}}, \boldsymbol{u}^{\star}_{\mathrm{dc}}, \boldsymbol{d}^{\star}_{\mathrm{dc}}} \Delta\boldsymbol{u}_{\mathrm{dc}} \\ &+ \left.\frac{\partial \boldsymbol{f}_{\mathrm{dc}}(\boldsymbol{x}_{\mathrm{dc}}, \boldsymbol{u}_{\mathrm{dc}}, \boldsymbol{d}_{\mathrm{dc}})}{\partial \boldsymbol{d}_{\mathrm{dc}}}\right|_{\boldsymbol{x}^{\star}_{\mathrm{dc}}, \boldsymbol{u}^{\star}_{\mathrm{dc}}, \boldsymbol{d}^{\star}_{\mathrm{dc}}} \Delta\boldsymbol{d}_{\mathrm{dc}}\,. \end{aligned} \tag{3.57}$$

The system definition (3.56) also applies to the operating points. Since the linearised system is analysed around the operating points,

$$\frac{\mathrm{d}}{\mathrm{d}t}\boldsymbol{x}^{\star}_{\mathrm{dc}} = \boldsymbol{f}_{\mathrm{dc}}(\boldsymbol{x}^{\star}_{\mathrm{dc}}, \boldsymbol{u}^{\star}_{\mathrm{dc}}, \boldsymbol{d}^{\star}_{\mathrm{dc}}) \ = 0 \tag{3.58}$$

holds. This leads to the generic small-signal state-space representation

$$\begin{aligned} \frac{\mathrm{d}}{\mathrm{d}t}\Delta\boldsymbol{x}_{\mathrm{dc}} = &\left.\frac{\partial \boldsymbol{f}_{\mathrm{dc}}(\boldsymbol{x}_{\mathrm{dc}}, \boldsymbol{u}_{\mathrm{dc}}, \boldsymbol{d}_{\mathrm{dc}})}{\partial \boldsymbol{x}_{\mathrm{dc}}}\right|_{\boldsymbol{x}^{\star}_{\mathrm{dc}}, \boldsymbol{u}^{\star}_{\mathrm{dc}}, \boldsymbol{d}^{\star}_{\mathrm{dc}}} \Delta\boldsymbol{x}_{\mathrm{dc}} \\ &+ \left.\frac{\partial \boldsymbol{f}_{\mathrm{dc}}(\boldsymbol{x}_{\mathrm{dc}}, \boldsymbol{u}_{\mathrm{dc}}, \boldsymbol{d}_{\mathrm{dc}})}{\partial \boldsymbol{u}_{\mathrm{dc}}}\right|_{\boldsymbol{x}^{\star}_{\mathrm{dc}}, \boldsymbol{u}^{\star}_{\mathrm{dc}}, \boldsymbol{d}^{\star}_{\mathrm{dc}}} \Delta\boldsymbol{u}_{\mathrm{dc}} \\ &+ \left.\frac{\partial \boldsymbol{f}_{\mathrm{dc}}(\boldsymbol{x}_{\mathrm{dc}}, \boldsymbol{u}_{\mathrm{dc}}, \boldsymbol{d}_{\mathrm{dc}})}{\partial \boldsymbol{d}_{\mathrm{dc}}}\right|_{\boldsymbol{x}^{\star}_{\mathrm{dc}}, \boldsymbol{u}^{\star}_{\mathrm{dc}}, \boldsymbol{d}^{\star}_{\mathrm{dc}}} \Delta\boldsymbol{d}_{\mathrm{dc}}\,. \end{aligned} \tag{3.59}$$

Linearisation of the nonlinear system dynamics (3.55) leads to the system's small-signal state-space representation

$$\left.\begin{aligned}
\frac{\mathrm{d}}{\mathrm{d}t}\underbrace{\begin{pmatrix}\Delta u_{\mathrm{g}}^{\mathrm{dc}}\\ \Delta i_{\mathrm{l}}^{d}\\ \Delta i_{\mathrm{g}}^{\mathrm{dc}}\\ \Delta u_{\mathrm{ec}}^{\mathrm{dc}}\end{pmatrix}}_{=:\,\Delta \boldsymbol{x}_{\mathrm{dc}}} &= \underbrace{\begin{bmatrix} a_{11}^{\star} & a_{12}^{\star} & \frac{1}{C_{\mathrm{g}}} & 0\\ 0 & -\frac{1}{\tau_{\mathrm{c}}} & 0 & 0\\ -\frac{1}{2\,L_{\mathrm{l}}} & 0 & -\frac{R_{\mathrm{l}}}{L_{\mathrm{l}}} & \frac{1}{2\,L_{\mathrm{l}}}\\ 0 & 0 & -\frac{1}{C_{\mathrm{ec}}} & 0\end{bmatrix}}_{=:\,\boldsymbol{A}_{\mathrm{dc}}}\begin{pmatrix}\Delta u_{\mathrm{g}}^{\mathrm{dc}}\\ \Delta i_{\mathrm{l}}^{d}\\ \Delta i_{\mathrm{g}}^{\mathrm{dc}}\\ \Delta u_{\mathrm{ec}}^{\mathrm{dc}}\end{pmatrix} + \underbrace{\begin{bmatrix} -\kappa_{\mathrm{dc}}^{\star}\, i_{\mathrm{l}}^{d\star}\frac{L_{\mathrm{f}}}{\tau_{\mathrm{c}}}\\ \frac{1}{\tau_{\mathrm{c}}}\\ 0\\ 0\end{bmatrix}}_{=:\,\boldsymbol{B}_{\mathrm{dc}}}\underbrace{\Delta i_{\mathrm{l,ref}}^{d}}_{=:\,\Delta \boldsymbol{u}_{\mathrm{dc}}}\\
&+\underbrace{\begin{bmatrix} -\kappa_{\mathrm{dc}}^{\star}\frac{L_{\mathrm{f}}}{\tau_{\mathrm{c}}}\, i_{\mathrm{l}}^{q\star} & -\kappa_{\mathrm{dc}}^{\star}\, i_{\mathrm{l}}^{d\star} & -\kappa_{\mathrm{dc}}^{\star}\, i_{\mathrm{l}}^{q\star} & -\frac{N_{\mathrm{g}}}{C_{\mathrm{g}}} & 0\\ 0 & 0 & 0 & 0 & 0\\ 0 & 0 & 0 & 0 & 0\\ 0 & 0 & 0 & 0 & \frac{1}{C_{\mathrm{ec}}}\end{bmatrix}}_{=:\,\boldsymbol{E}_{\mathrm{dc}}}\underbrace{\begin{pmatrix}\Delta i_{\mathrm{l,ref}}^{q}\\ \Delta u_{\mathrm{pcc}}^{d}\\ \Delta u_{\mathrm{pcc}}^{q}\\ \Delta i_{\mathrm{loss}}\\ \Delta i_{\mathrm{ec}}^{\mathrm{dc}}\end{pmatrix}}_{=:\,\Delta \boldsymbol{d}_{\mathrm{dc}}}\\
\underbrace{\begin{pmatrix}\Delta u_{\mathrm{g}}^{\mathrm{dc}}\\ \Delta u_{\mathrm{ec}}^{\mathrm{dc}}\end{pmatrix}}_{=:\,\Delta \boldsymbol{y}_{\mathrm{dc}}} &= \underbrace{\begin{bmatrix}1 & 0 & 0 & 0\\ 0 & 0 & 0 & 1\end{bmatrix}}_{=:\,\boldsymbol{C}_{\mathrm{dc}}}\begin{pmatrix}\Delta u_{\mathrm{g}}^{\mathrm{dc}}\\ \Delta i_{\mathrm{l}}^{d}\\ \Delta i_{\mathrm{g}}^{\mathrm{dc}}\\ \Delta u_{\mathrm{ec}}^{\mathrm{dc}}\end{pmatrix}\,.
\end{aligned}\right\} \tag{3.60}$$

The, the coefficients a_{11} and a_{12} of the system matrix $\boldsymbol{A}_{\mathrm{dc}}$ are given by

$$\left.\begin{aligned}
a_{11}^{\star} &:= \frac{\kappa_{\mathrm{dc}}^{\star}}{u_{\mathrm{g}}^{\mathrm{dc}\star}}\left(\left(R_{\mathrm{f}} - \frac{L_{\mathrm{f}}}{\tau_{\mathrm{c}}}\right)\left\|\boldsymbol{i}_{\mathrm{l}}^{dq\star}\right\|^{2} + \frac{L_{\mathrm{f}}}{\tau_{\mathrm{c}}}\left(\boldsymbol{i}_{\mathrm{l,ref}}^{dq\star}\right)^{\top}\boldsymbol{i}_{\mathrm{l}}^{dq\star} + \left(\boldsymbol{u}_{\mathrm{pcc}}^{dq\star}\right)^{\top}\boldsymbol{i}_{\mathrm{l}}^{dq\star} - \frac{2\left(u_{\mathrm{g}}^{\mathrm{dc}\star}\right)^{2}}{3\,R_{\mathrm{b}}}\right)\\
a_{12}^{\star} &:= -\kappa_{\mathrm{dc}}^{\star}\left(\left(R_{\mathrm{f}} - \frac{L_{\mathrm{f}}}{\tau_{\mathrm{c}}}\right)2\, i_{\mathrm{l}}^{d\star} + \frac{L_{\mathrm{f}}}{\tau_{\mathrm{c}}}\, i_{\mathrm{l,ref}}^{d\star} + u_{\mathrm{pcc}}^{d\star}\right)\,,
\end{aligned}\right\} \tag{3.61}$$

where

$$\kappa_{\mathrm{dc}}^{\star} := \frac{3\,N_{\mathrm{g}}}{2\,u_{\mathrm{g}}^{\mathrm{dc}\star}\,C_{\mathrm{g}}} \overset{(3.33)}{=} \frac{3}{2\,u_{\mathrm{g}}^{\mathrm{dc}\star}\,C_{\mathrm{dc}}}\,. \tag{3.62}$$

The reference current $i_{\mathrm{l,ref}}^{d}$ determines the active power p_{f} and, thus, the power p_{σ} that flows from the DC link via the grid inverters into the grid, as indicated in (3.20). It is governed by the droop controller dynamics in the time domain of the DC link voltage $u_{\mathrm{g}}^{\mathrm{dc}}$ with

$$\frac{\mathrm{d}}{\mathrm{d}t} i_{\mathrm{l,ref}}^{d} = \frac{1}{\tau_{\mathrm{d}}}\left(-K_{\mathrm{d}}\left(u_{\mathrm{g}}^{\mathrm{dc}}\right) i_{\mathrm{l,nom}}^{d}\left(u_{\mathrm{g,ref}}^{\mathrm{dc}} - u_{\mathrm{g}}^{\mathrm{dc}}\right) - i_{\mathrm{l,ref}}^{d}\right)\,. \tag{3.63}$$

Since the active power p_{f} should increase with the DC link voltage $u_{\mathrm{g}}^{\mathrm{dc}}$, the droop gain K_{d} needs to be positive, and

$$K_{\mathrm{d}} > 0 \tag{3.64}$$

must hold. To modify the dynamics of the controller, a first-order low-pass filter with the time constant τ_{d} is inserted. This is essential for the power smoothing presented in Sec. 3.3, as it suppresses the effects of fluctuations in the DC link voltage $u_{\mathrm{g}}^{\mathrm{dc}}$ on the current i_{l}^{d}.

The nonlinear droop gain K_{d} depends on the grid-side DC link voltage $u_{\mathrm{g}}^{\mathrm{dc}}$ according to (3.13) and as shown in Fig. 3.5. However, for the small-signal system, the gain K_{d} is considered to be constant for small deviations $\Delta u_{\mathrm{g}}^{\mathrm{dc}}$ around the operating point $u_{\mathrm{g}}^{\mathrm{dc}\star}$.

Extending the small-signal state-space system (3.60) by the controller yields the closed-loop system

$$
\begin{aligned}
\frac{\mathrm{d}}{\mathrm{d}t}\begin{pmatrix}\Delta u_{\mathrm{g}}^{\mathrm{dc}}\\ \Delta i_{\mathrm{l}}^{d}\\ \Delta i_{\mathrm{g}}^{\mathrm{dc}}\\ \Delta u_{\mathrm{ec}}^{\mathrm{dc}}\\ \Delta i_{\mathrm{l,ref}}^{d}\end{pmatrix} = {} & \underbrace{\begin{bmatrix} a_{11}^{\star} & a_{12}^{\star} & \frac{1}{C_{\mathrm{g}}} & 0 & -\kappa_{\mathrm{dc}}^{\star}\, i_{\mathrm{l}}^{d\star}\frac{L_{\mathrm{f}}}{\tau_{\mathrm{c}}}\\ 0 & -\frac{1}{\tau_{\mathrm{c}}} & 0 & 0 & \frac{1}{\tau_{\mathrm{c}}}\\ -\frac{1}{2\,L_{\mathrm{l}}} & 0 & -\frac{1}{\tau_{\mathrm{l}}} & \frac{1}{2\,L_{\mathrm{l}}} & 0\\ 0 & 0 & -\frac{1}{C_{\mathrm{ec}}} & 0 & 0\\ \frac{K_{\mathrm{d}}\, i_{\mathrm{l,nom}}^{d}}{\tau_{\mathrm{d}}} & 0 & 0 & 0 & -\frac{1}{\tau_{\mathrm{d}}}\end{bmatrix}}_{=:\boldsymbol{A}_{\mathrm{dc,cl}}}\begin{pmatrix}\Delta u_{\mathrm{g}}^{\mathrm{dc}}\\ \Delta i_{\mathrm{l}}^{d}\\ \Delta i_{\mathrm{g}}^{\mathrm{dc}}\\ \Delta u_{\mathrm{ec}}^{\mathrm{dc}}\\ \Delta i_{\mathrm{l,ref}}^{d}\end{pmatrix}\\
& + \begin{bmatrix} K_{\mathrm{d}}\, i_{\mathrm{l,nom}}^{d}\,\kappa_{\mathrm{dc}}^{\star}\, i_{\mathrm{l}}^{d\star}\frac{L_{\mathrm{f}}}{\tau_{\mathrm{c}}}\\ -\frac{K_{\mathrm{d}}\, i_{\mathrm{l,nom}}^{d}}{\tau_{\mathrm{c}}}\\ 0\\ 0\\ -\frac{K_{\mathrm{d}}\, i_{\mathrm{l,nom}}^{d}}{\tau_{\mathrm{d}}}\end{bmatrix}\Delta u_{\mathrm{g,ref}}^{\mathrm{dc}}\\
& + \underbrace{\begin{bmatrix} -\kappa_{\mathrm{dc}}^{\star}\frac{L_{\mathrm{f}}}{\tau_{\mathrm{c}}}\, i_{\mathrm{l}}^{q\star} & -\kappa_{\mathrm{dc}}^{\star}\, i_{\mathrm{l}}^{d\star} & -\kappa_{\mathrm{dc}}^{\star}\, i_{\mathrm{l}}^{q\star} & -\frac{N_{\mathrm{g}}}{C_{\mathrm{g}}} & 0\\ 0 & 0 & 0 & 0 & 0\\ 0 & 0 & 0 & 0 & 0\\ 0 & 0 & 0 & 0 & \frac{1}{C_{\mathrm{ec}}}\\ 0 & 0 & 0 & 0 & 0\end{bmatrix}}_{=:\boldsymbol{E}_{\mathrm{dc,cl}}}\underbrace{\begin{pmatrix}\Delta i_{\mathrm{l,ref}}^{q}\\ \Delta u_{\mathrm{pcc}}^{d}\\ \Delta u_{\mathrm{pcc}}^{q}\\ \Delta i_{\mathrm{loss}}\\ \Delta i_{\mathrm{ec}}^{\mathrm{dc}}\end{pmatrix}}_{=:\Delta\boldsymbol{d}_{\mathrm{dc}}},
\end{aligned}
\tag{3.65}
$$

where

$$
\tau_{\mathrm{l}} := \frac{L_{\mathrm{l}}}{R_{\mathrm{l}}} \tag{3.66}
$$

is the time constant of the transmission line, $\boldsymbol{d}_{\mathrm{dc}}$ is the disturbance vector and $\boldsymbol{E}_{\mathrm{dc,cl}}$ is the disturbance matrix.

The root locus method is used in the next section to analyse the system's stability. Here, the poles and zeros of the transfer functions are evaluated for varying values of specific system parameters. The transfer functions of both the open- and the closed-loop are required for the start and end points of the root locus plots (see Appendix A.5).

The open-loop transfer functions can be derived from the open-loop state-space system (3.60) with (see Appendix A.4)

$$\frac{\boldsymbol{y}_{\mathrm{dc}}(s)}{\boldsymbol{u}_{\mathrm{dc}}(s)} = \boldsymbol{C}_{\mathrm{dc}}\,\left(s\,\boldsymbol{I}_4 - \boldsymbol{A}_{\mathrm{dc}}\right)^{-1}\boldsymbol{B}_{\mathrm{dc}}\,, \tag{3.67}$$

which yields

$$\begin{pmatrix} \Delta u_{\mathrm{g}}^{\mathrm{dc}}(s) \\ \Delta u_{\mathrm{ec}}^{\mathrm{dc}}(s) \end{pmatrix} = \begin{pmatrix} F_{\mathrm{o,g}}(s) \\ F_{\mathrm{o,ec}}(s) \end{pmatrix} \Delta i_{\mathrm{l,ref}}^{d}(s)$$

$$= \begin{pmatrix} \dfrac{\left(\kappa_{\mathrm{dc}}^{\star}\, i_{\mathrm{l}}^{d\star} \frac{L_{\mathrm{f}}}{\tau_{\mathrm{c}}} - a_{12}^{\star} + s\,\kappa_{\mathrm{dc}}^{\star}\, i_{\mathrm{l}}^{d\star}\, L_{\mathrm{f}}\right)\left(1 + s\,2\,R_{\mathrm{l}}\,C_{\mathrm{ec}} + s^2\,2\,L_{\mathrm{l}}\,C_{\mathrm{ec}}\right)}{(1+s\,\tau_{\mathrm{c}})\left[a_{11}^{\star} + s\left(2\,R_{\mathrm{l}}\,C_{\mathrm{ec}}\,a_{11}^{\star} - \frac{C_{\mathrm{ec}}}{C_{\mathrm{g}}} - 1\right) + s^2\left(-2\,R_{\mathrm{l}}\,C_{\mathrm{ec}} + 2\,L_{\mathrm{l}}\,C_{\mathrm{ec}}\,a_{11}^{\star}\right) - s^3\,2\,L_{\mathrm{l}}\,C_{\mathrm{ec}}\right]} \\[2ex] \dfrac{\kappa_{\mathrm{dc}}^{\star}\, i_{\mathrm{l}}^{d\star} \frac{L_{\mathrm{f}}}{\tau_{\mathrm{c}}} - a_{12}^{\star} + s\,\kappa_{\mathrm{dc}}^{\star}\, i_{\mathrm{l}}^{d\star}\, L_{\mathrm{f}}}{(1+s\,\tau_{\mathrm{c}})\left[a_{11}^{\star} + s\left(2\,R_{\mathrm{l}}\,C_{\mathrm{ec}}\,a_{11}^{\star} - \frac{C_{\mathrm{ec}}}{C_{\mathrm{g}}} - 1\right) + s^2\left(-2\,R_{\mathrm{l}}\,C_{\mathrm{ec}} + 2\,L_{\mathrm{l}}\,C_{\mathrm{ec}}\,a_{11}^{\star}\right) - s^3\,2\,L_{\mathrm{l}}\,C_{\mathrm{ec}}\right]} \end{pmatrix} \Delta i_{\mathrm{l,ref}}^{d}(s)\,. \tag{3.68}$$

The system is primarily stimulated by the current $i_{\mathrm{ec}}^{\mathrm{dc}}$ from the generation units. Therefore, the transfer behaviour from the current $i_{\mathrm{ec}}^{\mathrm{dc}}$ to the DC link voltages $u_{\mathrm{g}}^{\mathrm{dc}}$ and $u_{\mathrm{ec}}^{\mathrm{dc}}$ should be investigated. Since the current $i_{\mathrm{ec}}^{\mathrm{dc}}$ is uncertain and depends strongly on the natural conditions such as wind, sun and waves, it is introduced as a disturbance to the system in Sec. 3.2.3. Consequently, the disturbance transfer function must be determined. It can be derived with

$$\frac{\boldsymbol{y}_{\mathrm{dc}}(s)}{\boldsymbol{d}_{\mathrm{dc}}(s)} = \boldsymbol{C}_{\mathrm{dc}}\,\left(s\,\boldsymbol{I}_5 - \boldsymbol{A}_{\mathrm{dc,cl}}\right)^{-1}\boldsymbol{E}_{\mathrm{dc,cl}}\,, \tag{3.69}$$

which yields

$$\begin{pmatrix} \Delta u_{\mathrm{g}}^{\mathrm{dc}}(s) \\ \Delta u_{\mathrm{ec}}^{\mathrm{dc}}(s) \end{pmatrix} = \frac{1}{2\,C_{\mathrm{ec}}\,C_{\mathrm{g}}\,L_{\mathrm{l}}\,\tau_{\mathrm{c}}\,\tau_{\mathrm{d}}} \begin{pmatrix} \frac{(1+s\,\tau_{\mathrm{c}})(1+s\,\tau_{\mathrm{d}})}{\chi_{\mathrm{dc}}(s)} \\[1ex] \frac{\mathcal{N}_{\mathrm{ec}}(s)}{\chi_{\mathrm{dc}}(s)} \end{pmatrix} \Delta i_{\mathrm{ec}}^{\mathrm{dc}}(s)\,, \tag{3.70}$$

with the numerator

$$\mathcal{N}_{\mathrm{ec}}(s) = b_0 + b_1\,s + b_2\,s^2 + b_3\,s^3 + b_4\,s^4\,, \tag{3.71}$$

and its coefficients

$$\left.\begin{aligned} b_0 &= 1 + \frac{2\,C_{\mathrm{g}}\,L_{\mathrm{l}}}{\tau_{\mathrm{l}}}\left(K_{\mathrm{d}}\,i_{\mathrm{l,nom}}^{d}\left(-a_{12}^{\star} + \kappa_{\mathrm{dc}}^{\star}\,i_{\mathrm{l}}^{d\star}\frac{L_{\mathrm{f}}}{\tau_{\mathrm{c}}}\right) - a_{11}^{\star}\right) \\ b_1 &= \tau_{\mathrm{c}} + \tau_{\mathrm{d}} \\ &\quad + 2\,C_{\mathrm{g}}\,L_{\mathrm{l}}\left[\frac{1}{\tau_{\mathrm{l}}} - a_{11}^{\star}\left(1 + \frac{\tau_{\mathrm{c}}}{\tau_{\mathrm{l}}} + \frac{\tau_{\mathrm{d}}}{\tau_{\mathrm{l}}}\right) + K_{\mathrm{d}}\,i_{\mathrm{l,nom}}^{d}\left(-a_{12}^{\star} + L_{\mathrm{f}}\,\kappa_{\mathrm{dc}}^{\star}\,i_{\mathrm{l}}^{d\star}\left(\frac{1}{\tau_{\mathrm{l}}} + \frac{1}{\tau_{\mathrm{c}}}\right)\right)\right] \\ b_2 &= \tau_{\mathrm{c}}\,\tau_{\mathrm{d}} + 2\,C_{\mathrm{g}}\,L_{\mathrm{l}}\left(1 + \frac{\tau_{\mathrm{c}}}{\tau_{\mathrm{l}}} + \frac{\tau_{\mathrm{d}}}{\tau_{\mathrm{l}}} - a_{11}^{\star}\left(\frac{\tau_{\mathrm{c}}\,\tau_{\mathrm{d}}}{\tau_{\mathrm{l}}} + \tau_{\mathrm{c}} + \tau_{\mathrm{d}}\right) + K_{\mathrm{d}}\,i_{\mathrm{l,nom}}^{d}\,\kappa_{\mathrm{dc}}^{\star}\,i_{\mathrm{l}}^{d\star}\,L_{\mathrm{f}}\right) \\ b_3 &= 2\,C_{\mathrm{g}}\,L_{\mathrm{l}}\left(\frac{\tau_{\mathrm{c}}\,\tau_{\mathrm{d}}}{\tau_{\mathrm{l}}} + \tau_{\mathrm{c}} + \tau_{\mathrm{d}} - a_{11}^{\star}\,\tau_{\mathrm{c}}\,\tau_{\mathrm{d}}\right) \\ b_4 &= 2\,C_{\mathrm{g}}\,L_{\mathrm{l}}\,\tau_{\mathrm{c}}\,\tau_{\mathrm{d}}\,. \end{aligned}\right\} \tag{3.72}$$

The characteristic polynomial is given by

$$\chi_{\mathrm{dc}}(s) = \det\left(s\,\boldsymbol{I}_5 - \boldsymbol{A}_{\mathrm{dc,cl}}\right) = a_0 + a_1\,s + a_2\,s^2 + a_3\,s^3 + a_4\,s^4 + a_5\,s^5\,, \tag{3.73}$$

where

$$\left.\begin{aligned}
a_0 &= \frac{1}{2\,C_{\mathrm{ec}}\,L_{\mathrm{l}}\,\tau_{\mathrm{c}}\,\tau_{\mathrm{d}}}\left(-a_{11}^{\star} + K_{\mathrm{d}}\,i_{\mathrm{l,nom}}^{d}\left(\kappa_{\mathrm{dc}}^{\star}\,i_{\mathrm{l}}^{d\star}\,\frac{L_{\mathrm{f}}}{\tau_{\mathrm{c}}} - a_{12}^{\star}\right)\right)\\
a_1 &= \frac{C_{\mathrm{g}} + C_{\mathrm{ec}}}{2\,C_{\mathrm{g}}\,C_{\mathrm{ec}}\,L_{\mathrm{l}}\,\tau_{\mathrm{c}}\,\tau_{\mathrm{d}}} - \frac{a_{11}^{\star}}{\tau_{\mathrm{c}}\,\tau_{\mathrm{d}}\,\tau_{\mathrm{l}}}\left(1 + \frac{(\tau_{\mathrm{c}} + \tau_{\mathrm{d}})\,\tau_{\mathrm{l}}}{2\,C_{\mathrm{ec}}\,L_{\mathrm{l}}}\right)\\
&\quad + \frac{K_{\mathrm{d}}\,i_{\mathrm{l,nom}}^{d}}{\tau_{\mathrm{c}}\,\tau_{\mathrm{d}}\,\tau_{\mathrm{l}}}\left(-a_{12}^{\star} + \kappa_{\mathrm{dc}}^{\star}\,i_{\mathrm{l}}^{d\star}\,\frac{L_{\mathrm{f}}}{\tau_{\mathrm{c}}}\left(1 + \frac{\tau_{\mathrm{l}}\,\tau_{\mathrm{c}}}{2\,C_{\mathrm{ec}}\,L_{\mathrm{l}}}\right)\right)\\
a_2 &= \frac{(C_{\mathrm{g}} + C_{\mathrm{ec}})\,(\tau_{\mathrm{c}} + \tau_{\mathrm{d}})}{2\,C_{\mathrm{g}}\,C_{\mathrm{ec}}\,L_{\mathrm{l}}\,\tau_{\mathrm{c}}\,\tau_{\mathrm{d}}} - a_{11}^{\star}\left(\frac{1}{\tau_{\mathrm{c}}\,\tau_{\mathrm{d}}} + \frac{1}{\tau_{\mathrm{c}}\,\tau_{\mathrm{l}}} + \frac{1}{\tau_{\mathrm{d}}\,\tau_{\mathrm{l}}} + \frac{1}{2\,C_{\mathrm{ec}}\,L_{\mathrm{l}}}\right)\\
&\quad + \frac{1}{\tau_{\mathrm{c}}\,\tau_{\mathrm{d}}\,\tau_{\mathrm{l}}}\left(1 + K_{\mathrm{d}}\,i_{\mathrm{l,nom}}^{d}\left(\kappa_{\mathrm{dc}}^{\star}\,i_{\mathrm{l}}^{d\star}\,L_{\mathrm{f}}\left(1 + \frac{\tau_{\mathrm{l}}}{\tau_{\mathrm{c}}}\right) - a_{12}^{\star}\,\tau_{\mathrm{l}}\right)\right)\\
a_3 &= \frac{1}{\tau_{\mathrm{c}}\,\tau_{\mathrm{d}}\,\tau_{\mathrm{l}}}\left(\tau_{\mathrm{c}} + \tau_{\mathrm{d}} + \tau_{\mathrm{l}} + K_{\mathrm{d}}\,i_{\mathrm{l,nom}}^{d}\,\kappa_{\mathrm{dc}}^{\star}\,i_{\mathrm{l}}^{d\star}\,L_{\mathrm{f}}\,\tau_{\mathrm{l}}\right)\\
&\quad - a_{11}^{\star}\left(\frac{1}{\tau_{\mathrm{c}}} + \frac{1}{\tau_{\mathrm{d}}} + \frac{1}{\tau_{\mathrm{l}}}\right) + \frac{C_{\mathrm{g}} + C_{\mathrm{ec}}}{2\,C_{\mathrm{g}}\,C_{\mathrm{ec}}\,L_{\mathrm{l}}}\\
a_4 &= \frac{1}{\tau_{\mathrm{c}}} + \frac{1}{\tau_{\mathrm{d}}} + \frac{1}{\tau_{\mathrm{l}}} - a_{11}^{\star}\\
a_5 &= 1\,.
\end{aligned}\right\} \tag{3.74}$$

3.2.5 Stability Analysis of the DC Link Dynamics

The root locus method is particularly suitable for investigating the influence of variations in the system parameters on the transfer behaviour. With this method, the poles $s_{\mathrm{p},i}$ of the closed-loop transfer function (3.70), i.e., the solutions (roots) of the characteristic equation

$$\chi_{\mathrm{dc}}(s) = 0\,, \tag{3.75}$$

are displayed graphically on the complex s-plane for varying system parameters. In particular, these are the droop gain K_{d}, the droop controller time constant τ_{d}, the DC link capacitance C_{dc} and the transmission line length l_{l}. The solutions of the characteristic equation are also the eigenvalues of the system matrix $\boldsymbol{A}_{\mathrm{dc,cl}}$. The system is locally stable if all poles $s_{\mathrm{p},i}$ have negative real parts with

$$\Re\left\{s_{\mathrm{p},i}\right\} < 0\,, \tag{3.76}$$

i.e., they are located to the left of the imaginary axis [94, Sec. 3.2], [93, Sec. 6.3]. The system's stability can be assessed, and a qualitative statement can also be made about the dominant poles, the damping and the oscillation behaviour [84, Sec. 6.1.2].
Typically, the controller gain is varied, which in this case is K_{d}. Various simulation software, such as MATLAB, provide functions that are suitable for this case. The transfer function of the open-loop is passed to the function, and the poles of the closed-loop system for different values of K_{d} are returned [222]. If the variation of another parameter is to be analysed, the transfer function can be changed accordingly so that the existing software functions can also be used

(see Appendix A.5). However, this is only possible if the parameter only occurs at one position in the transfer function. If the parameter appears more than once, as is the case here, the root locus plot can only be determined by numerically evaluating the characteristic equation for each parameter value. The influence of various system parameters is to be analysed here, which is why all root locus plots are calculated numerically.

Fig. 3.13 shows the root locus with varying droop gain K_d for three operating points. There, the transmission line material is set to copper, and the length is set to $l_\mathrm{l} = 1000$ m, which is specified as the greatest possible length for this system. The DC transmission line is not suitable for longer distances at this voltage. The specific inductance is set to $L'_\mathrm{l} = 1\ \frac{\mu\mathrm{H}}{\mathrm{m}}$ to account for the worst case.

The current $i_\mathrm{l}^{d\star}$ has the most significant influence on the root locus plot among the operating points $\boldsymbol{x}_\mathrm{dc}^\star$. Therefore, three subplots, (a), (b), and (c), are shown below for $i_\mathrm{l}^{d\star} = i_\mathrm{l,nom}^{d}$, $i_\mathrm{l}^{d\star} = 0$ A, and $i_\mathrm{l}^{d\star} = -i_\mathrm{l,nom}^{d}$, respectively. A positive current i_l^{d} means power flows from the DC link into the grid. If the current i_l^{d} is negative, the DC link is supplied by the grid. All other operating points are set to the corresponding nominal value.

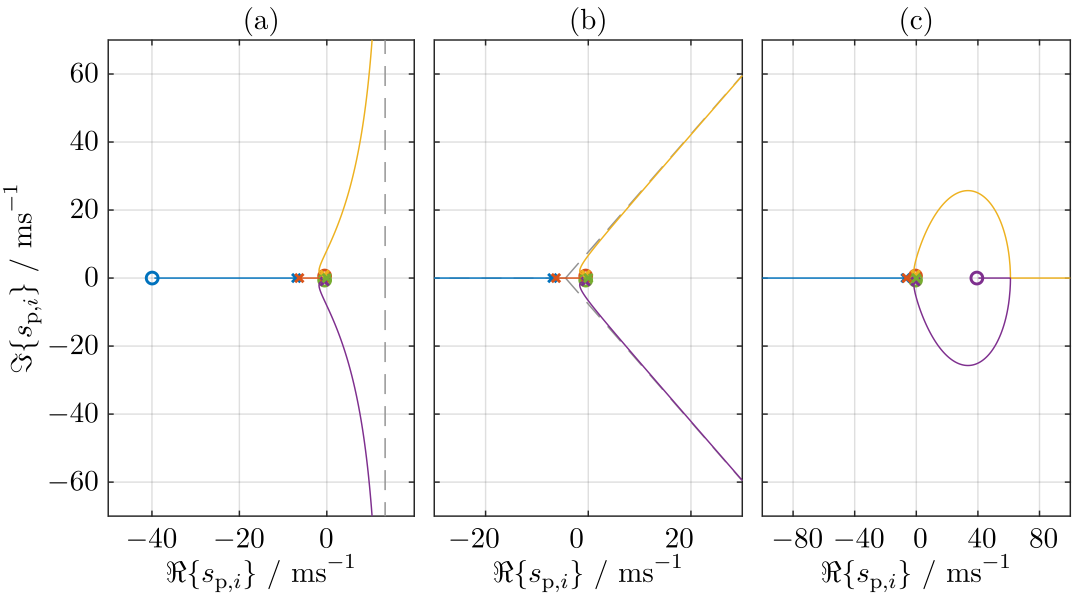

Figure 3.13: Root locus plot with varying droop gain K_d for the operating points (a) $i_\mathrm{l}^{d\star} = i_\mathrm{l,nom}^{d}$, (b) $i_\mathrm{l}^{d\star} = 0$ A, and (c) $i_\mathrm{l}^{d\star} = -i_\mathrm{l,nom}^{d}$.

For $K_\mathrm{d} = 0\ \mathrm{V}^{-1}$, the root locus plots start at the poles $s_{\mathrm{p},i}$ of the open-loop transfer function $F_\mathrm{o,g}(s)$ and end at its zeros $s_{\mathrm{z},i}$ for $K_\mathrm{d} \to \infty$ [94, Sec. 5.3]. In the figures, the open-loop poles are marked with a cross [✕] and the zeros with a circle [**O**]. This means that with increasing droop gain K_d, the poles move from the crosses to the circles (✕→**O**). Additionally, the dashed lines indicate the asymptotes of the root locus curves that go to infinity. The asymptotes intersect on the real axis in the root locus centre σ_rl, given by [84, Sec. 5.4.10], [93, Sec. 6.4.3.4]

$$\sigma_\mathrm{rl} = \frac{1}{n-m}\left(\sum_{i=1}^{n} \Re\left\{s_{\mathrm{p},i}\right\} - \sum_{i=1}^{m} \Re\left\{s_{\mathrm{z},i}\right\}\right), \tag{3.77}$$

where n is the number of poles $s_{\mathrm{p},i}$ and m is the number of zeros $s_{\mathrm{z},i}$ of the open-loop transfer function. For rationale transfer functions, $n > m$ holds. The angles of the asymptotes are given by [93, Sec. 6.4.3.5]

$$\phi_{\mathrm{rl}} = \frac{\pi}{n-m}\,(2\,i-1)\;, \tag{3.78}$$

with $i \in \{1, \ldots, n-m\}$.
The zeros of the open-loop transfer function $F_{\mathrm{o,g}}(s)$ from (3.68) can be given by

$$\left.\begin{aligned} s_{\mathrm{z},1} &= -\frac{1}{\tau_{\mathrm{c}}} + \frac{a_{12}^{\star}}{\kappa_{\mathrm{dc}}^{\star}\, i_{\mathrm{l}}^{d\star}\, L_{\mathrm{f}}} \\ s_{\mathrm{z},2/3} &= \frac{1}{2\,\tau_{\mathrm{l}}}\left(-1 \pm \sqrt{1 - \frac{2\,\tau_{\mathrm{l}}}{R_{\mathrm{l}}\,C_{\mathrm{ec}}}}\right)\;. \end{aligned}\right\} \tag{3.79}$$

For $i_{\mathrm{l}}^{d\star} = 0$ A, the zero $s_{\mathrm{z},1}$ approaches infinity, meaning only the two zeros $s_{\mathrm{z},2/3}$ of the open-loop transfer function $F_{\mathrm{o,g}}(s)$ remain. Depending on the operating point $i_{\mathrm{l}}^{d\star}$, the zero $s_{\mathrm{z},1}$ is either on the left half-plane or on the right half-plane. This means the system is non-minimum-phase if the DC link is supplied from the grid ($i_{\mathrm{l}}^{d\star} < 0$ A), which can challenge the controller design. Since the poles approach the zeros of the open-loop transfer function for $K_{\mathrm{d}} \to \infty$, they inevitably cross the imaginary axis at a certain gain, thus making the system unstable. In addition, the behaviour of the initially reversed step response known from non-minimum-phase systems can occur under certain conditions [214].

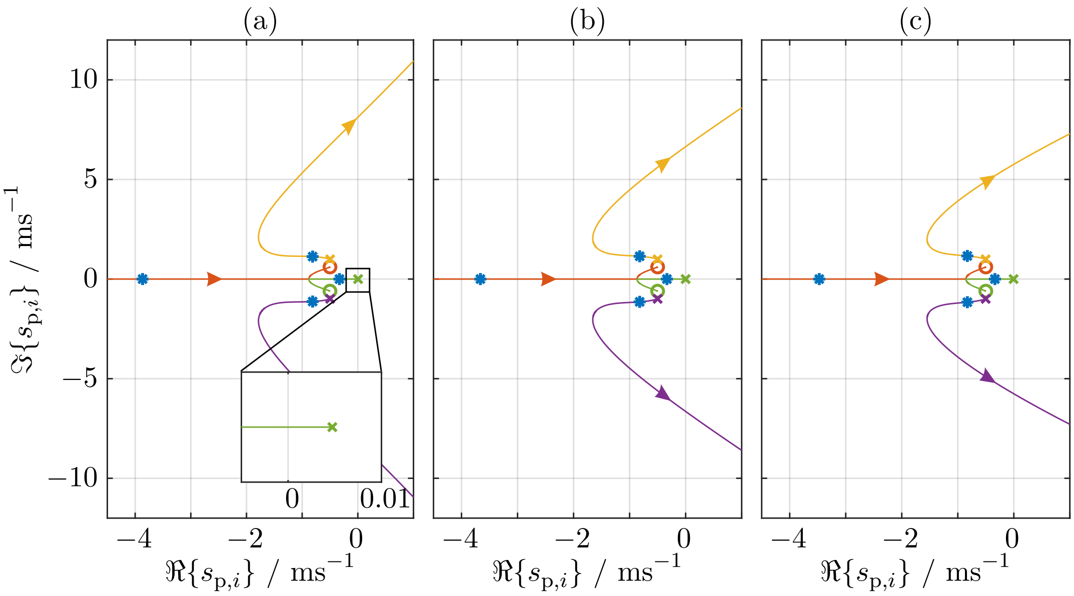

Figure 3.14: Zoomed area around the centre of the root locus plot with varying droop gain K_{d} for the operating points (a) $i_{\mathrm{l}}^{d\star} = i_{\mathrm{l,nom}}^{d}$, (b) $i_{\mathrm{l}}^{d\star} = 0$ A, and (c) $i_{\mathrm{l}}^{d\star} = -i_{\mathrm{l,nom}}^{d}$. The poles for $K_{\mathrm{d}} = (10\ \mathrm{V})^{-1}$ are marked with a blue asterisk [$\ast$].

Although a non-minimum-phase system only arises in case (c), in all three cases, the poles move to the right half-plane as the gain K_{d} increases, making the system unstable. Fig. 3.14 shows the zoomed area of the root locus plot around the centre σ_{rl} from the previous Fig. 3.13. The curve of the blue pole from the previous figure, located on the far left of the real axis, is outside this range, as it is irrelevant to the stability analysis. In this area, the shape of the root locus plots looks quite similar for the three operating points. They only differ in a few nuances. The poles cross the imaginary axis when $K_{\mathrm{d}} > (0.39\ \mathrm{V})^{-1}$, $K_{\mathrm{d}} > (0.59\ \mathrm{V})^{-1}$, and $K_{\mathrm{d}} > (0.78\ \mathrm{V})^{-1}$ for the operating points (a), (b), and (c), respectively. The gain K_d is given here inversely, as this makes it easier to recognise the voltage range of the droop curve in which the power increases from zero to the nominal value (see Fig. 3.5). The smaller the voltage range, the greater the gain K_d.

In this case, the system becomes unstable if the voltage range is less than 0.39 V, in which the active power p_f increases from 0 W to the nominal value. This range is very small and, therefore, not practicable. Due to measurement tolerances and errors, the measured DC link voltages of the individual inverters differ. The deviations are less than one volt, but if the voltage range is so small, the influence of the measurement errors increases. As a result, the power distribution between the inverters is also very unbalanced. For this reason, the voltage range should not be less than 10 V. The poles for $K_\mathrm{d} = (10\ \mathrm{V})^{-1}$ are marked with a blue asterisk [$\ast$]. With increasing voltage range, the gain K_d decreases and the poles move towards the open-loop poles [$\times$].

The red and green poles that start on the real axis are turning conjugate complex when $K_\mathrm{d} > (5.18\ \mathrm{V})^{-1}$, $K_\mathrm{d} > (5.28\ \mathrm{V})^{-1}$, and $K_\mathrm{d} > (5.38\ \mathrm{V})^{-1}$ for the operating points (a), (b), and (c), respectively. This additional conjugate complex pole pair increases the oscillation behaviour of the system, which can lead to increased overshoot. By keeping the voltage range greater than 10 V, these poles remain real.

In the case of operating point (a), at which power flows from the DC link into the grid, one pole of the open-loop transfer function, where the root locus curve for $K_\mathrm{d} = 0\ \mathrm{V}^{-1}$ begins, lies on the right half-plane. Therefore, the system is also unstable for gains that are too small, i.e. voltage ranges that are too large. It becomes stable for $K_\mathrm{d} > (823.8\ \mathrm{V})^{-1}$. In practical terms, this means that the power is not fed into the grid as quickly as it is fed into the DC link by the RES, causing the DC link voltage to rise steadily. This does not occur in the normal operating range of the droop curve. The theoretical maximum voltage range is the difference between the maximum and minimum permissible DC link voltage, which results in a range of 100 V.

However, the implemented droop curve from Fig. 3.5 is divided into different sections, separated by plateaus where $K_\mathrm{d} = 0\ \mathrm{V}^{-1}$. The operating points on these plateaus are unstable, and a steady-state can not be reached there. As described in Sec. 3.1.2, these plateaus only serve to separate the section and avoid circulating currents. The operating point slides over the plateau during the transition from one section to another, and the new operating point stabilises again in the next section of the droop curve.

The second droop control parameter is the filter time constant τ_d. Fig. 3.15 shows the root locus plot with varying droop time constant τ_d for the three operating points (a) $i_\mathrm{l}^{d\star} = i_\mathrm{l,nom}^{d}$, (b) $i_\mathrm{l}^{d\star} = 0$ A, and (c) $i_\mathrm{l}^{d\star} = -i_\mathrm{l,nom}^{d}$. The droop gain is set to $K_\mathrm{d} = (10\ \mathrm{V})^{-1}$. Again, the three plots differ only very slightly. Only for the first operating point (a) do the poles cross the imaginary axis if the time constant $\tau_\mathrm{d} > 268.8$ ms, corresponding to a cutoff frequency of $f_\mathrm{d} < 0.5921$ Hz. For power smoothing, the cutoff frequency must be low so that the fluctuations in the DC link voltage u_g^dc caused by the wave energy can be sufficiently suppressed. In Sec. 3.3, it is shown that power smoothing can be achieved with this limit and that the system remains stable.

The DC link capacitance C_dc is an important parameter in the system design and usually has the most significant impact on the lifetime of power electronic devices [69] (see Sec. 2.1.2). It essentially determines the dynamics of the DC link and, therefore, sets the limits of the droop controller. The greater the DC link capacitance C_dc, the slower the dynamics, allowing the control parameters to be selected more conservatively.

On the other hand, DC link capacitors are expensive and take up a lot of installation space. For this reason, the capacitance should not be arbitrarily oversized. Therefore, the influence of the DC link capacitance C_dc on system stability will be analysed here.

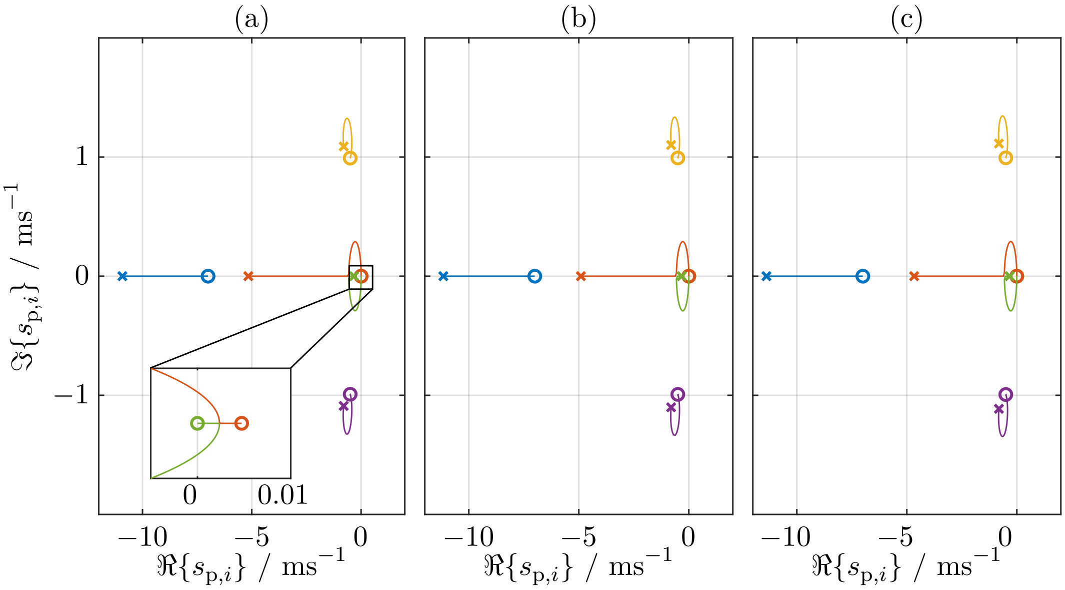

Figure 3.15: Root locus plot with varying droop time constant τ_d and with $K_\mathrm{d} = (10\ \mathrm{V})^{-1}$ for the operating points (a) $i_\mathrm{l}^{d\star} = i_{\mathrm{l,nom}}^{d}$, (b) $i_\mathrm{l}^{d\star} = 0$ A, and (c) $i_\mathrm{l}^{d\star} = -i_{\mathrm{l,nom}}^{d}$.

Fig. 3.16 shows the root locus plot with varying DC link capacitance C_dc and with $K_\mathrm{d} = (10\ \mathrm{V})^{-1}$ for the three operating points (a) $i_\mathrm{l}^{d\star} = i_{\mathrm{l,nom}}^{d}$, (b) $i_\mathrm{l}^{d\star} = 0$ A, and (c) $i_\mathrm{l}^{d\star} = -i_{\mathrm{l,nom}}^{d}$. In the area of the centre of the root locus plot where the poles intersect the imaginary axis, the difference between the three operating points is barely visible. The poles cross the imaginary axis when $C_\mathrm{dc} < 39.4\ \mu$F, $C_\mathrm{dc} < 54.6\ \mu$F, and $C_\mathrm{dc} < 70.5\ \mu$F for the operating points (a), (b), and (c), respectively.

With the implemented DC link capacitance of $C_\mathrm{dc} = 810\ \mu$F, marked with the blue asterisk [$\ast$], only one conjugate complex pole pair exists. The first conjugate complex pole pair on the yellow and violet curves already occurs when the capacitance is less than 4810.8 μF. This corresponds to five times the actual capacity and is therefore unreasonable to implement. The second conjugate complex pole pair arises on the red and green curves if the DC link capacitance is less than 409.5 μF, corresponding to about half of the implemented capacitance.

Even if a significantly lower capacity could be used due to the stability limit, the additional oscillation behaviour should be avoided, which can lead to increased overshoot. Fig. 3.17 shows two step responses with a DC link capacitance of $C_\mathrm{dc} = 810\ \mu$F [—] and $C_\mathrm{dc} = 200\ \mu$F [—]. The top subplot shows the current $i_\mathrm{ec}^\mathrm{dc}$ [—] of the RES and the current i_g^dc that flows into the grid inverter. It should be noted that the current $i_\mathrm{ec}^\mathrm{dc}$ from the RES can become negative, meaning that power is drawn from the DC link. This is necessary, e.g. for the reactive control of the WEC (see Sec. 1.2.3). The second and third subplot shows the resulting voltages $u_\mathrm{ec}^\mathrm{dc}$ and u_g^dc at the RES side and the grid inverter side, respectively. The current $i_\mathrm{ec}^\mathrm{dc}$ was selected so the grid inverter reaches its rated power in steady-state conditions. This is shown by the fact that the voltage u_g^dc reaches the limit of the droop curve and increases or decreases accordingly by 10 V ($K_\mathrm{d} = (10\ \mathrm{V})^{-1}$). The voltage $u_\mathrm{ec}^\mathrm{dc}$ on the RES side is higher or lower due to the voltage drop on the transmission line resistance R_l.

The reduced DC link capacitance causes the voltages on both sides of the transmission line to overshoot. This is due to the additional conjugate complex pole pair. With the capacitance implemented, no overshoot occurs, although a conjugate complex pole pair is still present. The overshoot could be tolerated in principle. However, it becomes critical if the system limits are to

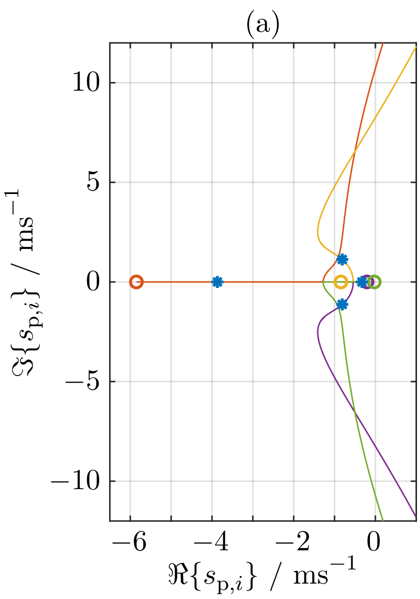

Figure 3.16: Root locus plot with varying DC link capacitance C_{dc} and with $K_{\mathrm{d}} = (10\ \mathrm{V})^{-1}$ for the operating points (a) $i_{\mathrm{l}}^{d\star} = i_{\mathrm{l,nom}}^{d}$, (b) $i_{\mathrm{l}}^{d\star} = 0$ A, and (c) $i_{\mathrm{l}}^{d\star} = -i_{\mathrm{l,nom}}^{d}$. The poles for the implemented DC link capacitance with $C_{\mathrm{dc}} = 810\ \mu$F are marked with a blue asterisk [$\ast$].

be fully utilised. A corresponding safety margin must be maintained as the overshoot increases due to component degradation. As the voltage range of the droop controller is very close to the upper voltage limits, the overshoot cannot be tolerated here.

Given the component tolerances combined with the degradation during the lifetime, the capacitance can drop by around 40 % of its nominal value at the end of its lifetime (see Sec. 2.1.2). Therefore, twice the capacitance should be selected at which the poles do not become complex, i.e. approximately twice 409.5 μF. The selected capacity of $C_{\mathrm{dc}} = 810\ \mu$F is, therefore, already an optimum value.

Finally, the influence of the transmission line length l_{l} will be analysed. The length influences the line resistance R_{l} and inductance L_{l} according to (3.48) and (3.53). Fig. 3.18 shows the root locus plot with varying droop gain K_{d} for three different transmission line lengths: (a) $l_{\mathrm{l}} = 1$ m, (b) $l_{\mathrm{l}} = 100$ m, and (c) $l_{\mathrm{l}} = 1000$ m. The poles cross the imaginary axis when $K_{\mathrm{d}} > (0.18\ \mathrm{V})^{-1}$, $K_{\mathrm{d}} > (0.43\ \mathrm{V})^{-1}$, and $K_{\mathrm{d}} > (0.40\ \mathrm{V})^{-1}$ for the cable length (a), (b), and (c), respectively. For short distances in subplot (a), the red and green curves intersect the imaginary axis before returning to the left half-plane. However, the first intersection at which the system becomes unstable is at a droop gain $K_{\mathrm{d}} > (0.18\ \mathrm{V})^{-1}$. As previously discussed, these voltage ranges are too small for a practical implementation. Accordingly, no instability will occur due to the cable length.

It can also be observed that the conjugate complex pole pair moves further away from the centre for shorter lengths l_{l}. Here, the non-vanishing resistance $R_{\mathrm{l},0}$ that accounts for the contact resistance and fuses is decisive for damping these poles. If the resistance $R_{\mathrm{l},0} = 0$ mΩ, the transmission line resistance disappears completely for $l_{\mathrm{l}} = 0$ m. Fig. 3.19 shows the root locus plot with varying transmission line length l_{l} with $i_{\mathrm{l}}^{d\star} = i_{\mathrm{l,nom}}^{d}$ and $K_{\mathrm{d}} = (10\ \mathrm{V})^{-1}$. For the first subplot (a), the resistance $R_{\mathrm{l},0} = 0$ mΩ. This causes the complex poles to move parallel to the imaginary axis, which leads to an ever-decreasing attenuation for shorter lengths l_{l}. The second subplot (b) shows the root locus plot with a small resistance of $R_{\mathrm{l},0} = 10$ mΩ, which is already given by the resistance of the fuses. As a result, the paths of the conjugate complex poles bend to the left for decreasing lengths l_{l}, which maintains the damping. From a length greater than

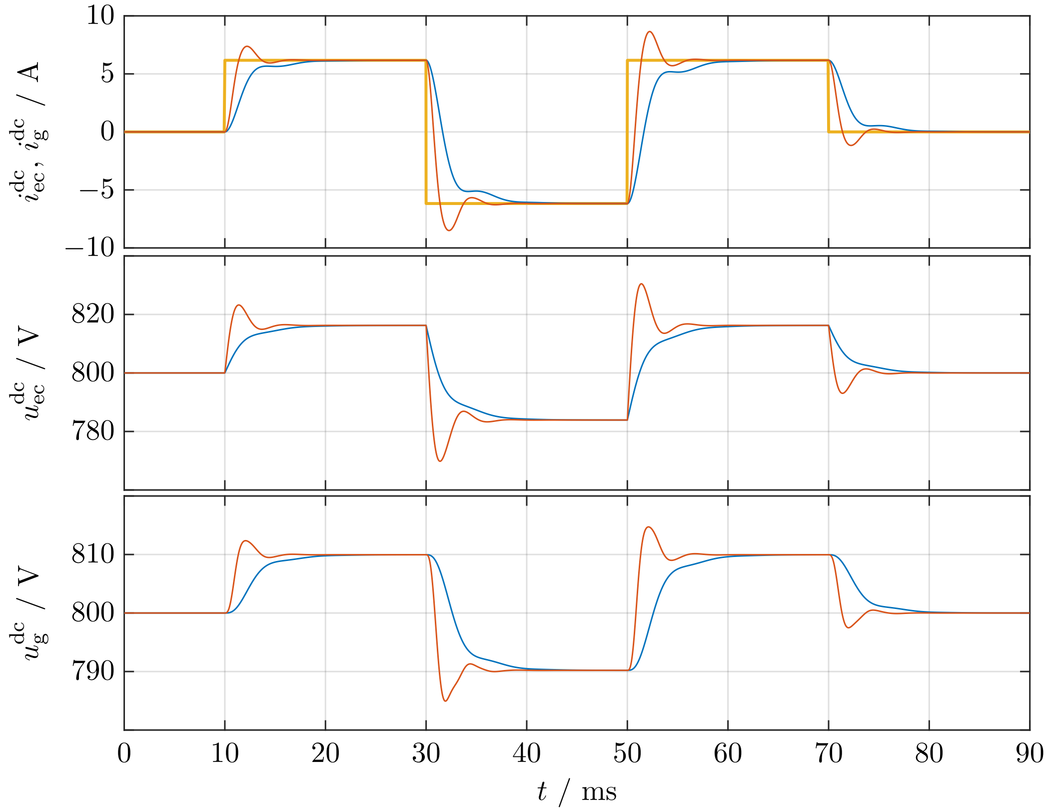

Figure 3.17: Step responses with a DC link capacitance of $C_{dc} = 810\ \mu F$ [—] and $C_{dc} = 200\ \mu F$ [—], where the input signal is the current i_{ec}^{dc} [—] of the RES.

8189 m, the conjugate complex pool pair becomes a real pole. However, as shown in Sec. 3.2.3, this length cannot be attained in practice.

To illustrate the behaviour concerning the damping, Fig. 3.20 shows two step responses with $R_{l,0} = 0\ m\Omega$ [—] and $R_{l,0} = 10\ m\Omega$ [—]. The top subplot shows the current i_{ec}^{dc} [—] of the RES and the current i_g^{dc} that flows into the grid inverter. The second and third subplots show the resulting voltages u_{ec}^{dc} and u_g^{dc} at the RES side and the grid inverter side, respectively.

The effect of the lack of damping can be recognised in the current, which begins to oscillate strongly. At shorter lengths, the oscillation decays more and more slowly. However, according to the stability definition, the system remains stable. Even if very short transmission line lengths are irrelevant for this system, this oscillation should be avoided. These analyses show that the resistance $R_{l,0}$ is sufficient to dampen these oscillations. Although this resistance only results from parasitic effects, it is essential for the damping of the system and its accurate modelling. The resistance $R_{l,0} = 10\ m\Omega$ assumed here is based solely on the fuses and will be higher in practice due to the contact resistances of several connections between the units. Therefore, even very short distances can be realised without strong oscillations.

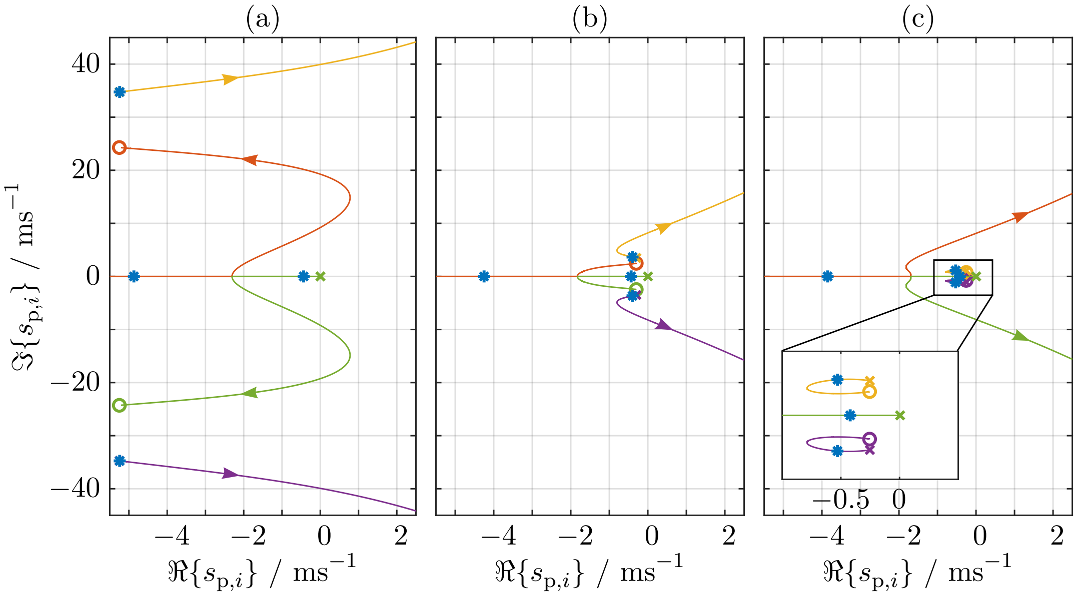

Figure 3.18: Root locus plot with varying droop gain K_d with $i_\mathrm{l}^{d\star} = i_\mathrm{l,nom}^{d}$ for the transmission line length (a) $l_\mathrm{l} = 1$ m, (b) $l_\mathrm{l} = 100$ m, and (c) $l_\mathrm{l} = 1000$ m. The poles for $K_\mathrm{d} = (10\ \mathrm{V})^{-1}$ are marked with a blue asterisk [∗].

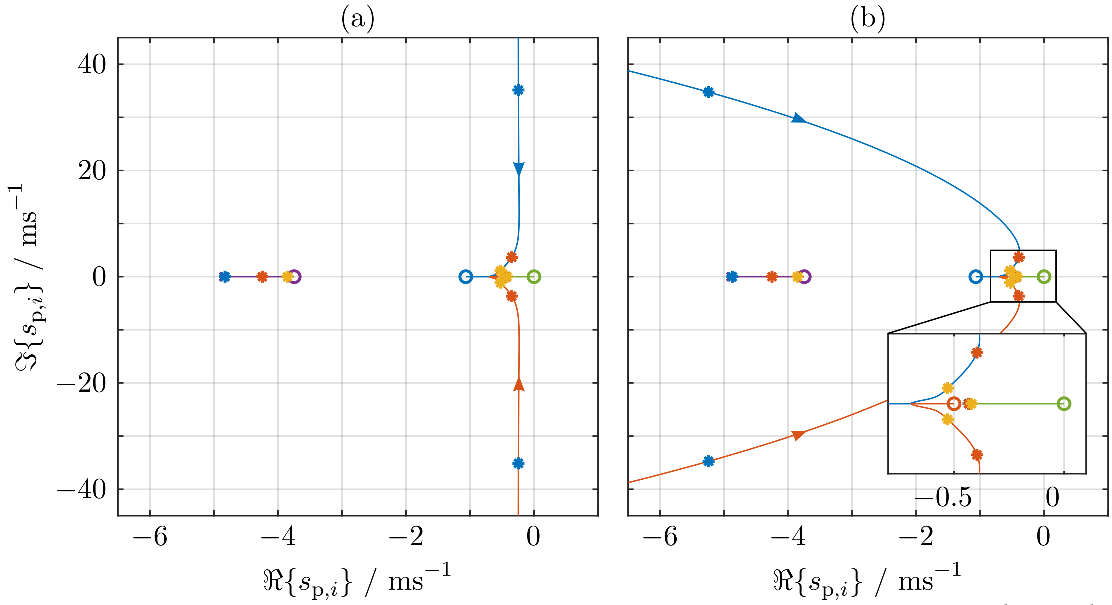

Figure 3.19: Root locus plot with varying transmission line length l_l with $i_\mathrm{l}^{d\star} = i_\mathrm{l,nom}^{d}$ and $K_\mathrm{d} = (10\ \mathrm{V})^{-1}$ for (a) $R_\mathrm{l,0} = 0$ mΩ and (b) $R_\mathrm{l,0} = 10$ mΩ. The lengths $l_\mathrm{l} = 1$ m, $l_\mathrm{l} = 100$ m, and $l_\mathrm{l} = 1000$ m are marked with a blue [∗], red [∗], and yellow [∗] asterisk, respectively.

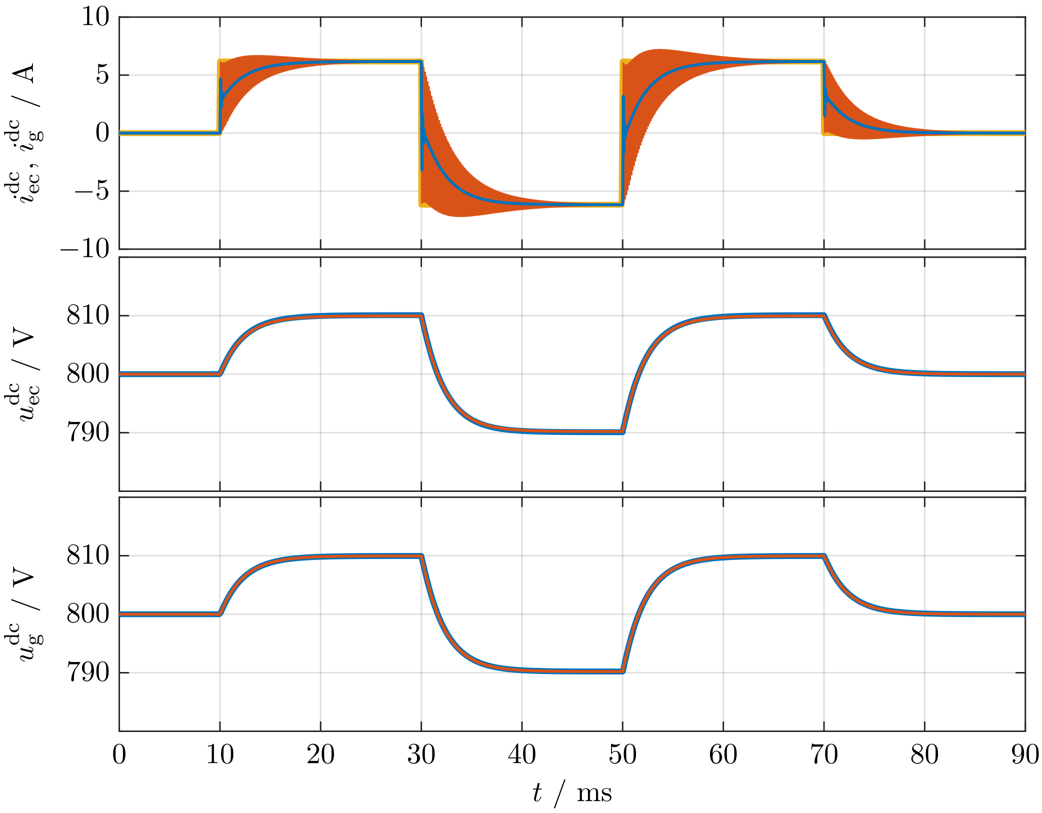

Figure 3.20: Step response with $R_{l,0} = 0$ mΩ [—] and $R_{l,0} = 10$ mΩ [—].

3.3 Power Smoothing

A common challenge for wave energy converters is power smoothing (see Specification (S11)). The generated electrical power fluctuates with the waves' movement with a period of a few seconds, depending on the prevailing sea state. The power peaks generated are many times higher than the average power. If these power peaks were fed directly into the grid, this could lead to severe voltage and frequency fluctuations and harmonics [223, Sec. 1.3], [224, 225]. This can cause damage to other devices connected to the grid or even lead to a power failure. These power peaks must be stored in a short-term storage system and continuously released when the power generated is below the average power.
The optimised positioning of the WEC modules in a WEC array can achieve an additional smoothing effect. The time delay of the waves at the individual WEC modules leads to a more evenly distributed total power [226–228]. It can be shown that the standard deviation of the power generated decreases significantly with the number of modules [229]. This means that the ratio between the peak and average power becomes smaller, which requires a lower short-term storage capacity per installed WEC power. This applies, in particular, to the WEC presented in Sec. 1.2. In the following, power smoothing is analysed for just one module. As the peak-to-average power ratio is the highest here, it represents the most demanding case. If the number of WEC modules is increased, the control strategy does not need to be adapted. It is only a major advantage for power smoothing as the ratio of the short-term storage capacity to the number of modules can be significantly reduced, according to the standard deviation of the power output.
The following section introduces the supercapacitor unit, which is used here as the short-term energy storage. In Sec. 3.3.2, the control system and the measurement results of the full-sized WEC prototype are presented. The last section describes power smoothing for the power electronics system presented, in which the supercapacitors are connected to the DC grid via the bidirectional DC/DC converter.

3.3.1 Short-Term Energy Storage

Energy storage systems are necessary when energy is not immediately required but is needed later. They are particularly essential for renewable energies due to their natural fluctuation. The transition in mobility to electric drives also requires extensive and powerful energy storage systems. Electric vehicles connected to the grid are not always considered as loads. If electric vehicles are not needed immediately, they can be used as a flexible energy storage system. This so-called vehicle-to-grid (V2G) technology supports their integration into a smart grid and the transition to decentralised energy generation [230].
Energy storage systems can be classified into different categories. A categorisation can be made according to the stored energy's form or its dynamics, meaning how fast the energy can be extracted or stored. The energy from short-term storage units is available within milliseconds and typically at high power. Long-term storage systems are suitable for providing energy over a longer period, but their dynamic behaviour is slower. Their strength lies in the amount of energy they can store.
Purely electrical storage devices are capacitors and inductors storing energy in the electric or magnetic field, respectively. They are designed for short-term storage purposes. Batteries are long-term and electrochemical storage devices consisting of various chemicals, such as lithium-ion (Li-ion), lithium iron phosphate battery ($LiFePO_4$), lead-acid (Pb), nickel-metal hydride (NiMH) and others.
Pump storages are also long-term energy storage systems, but the energy is stored mechanically as potential energy. Another mechanical energy storage system is the flywheel, where the energy is contained in a rotating mass as kinetic energy. Electrical machines are connected to the

rotating mass and convert between electrical and kinetic energy. They are typically used as short-term storage units. The rotating synchronous machines used as generators in the traditional electrical grid are to be considered in their secondary function as flywheel storage units. As discussed in Sec. 3.1.1, the energy stored in their rotating mass compensates for the power imbalance within the first few seconds. In [231–233], flywheels are considered to smooth the output power of wave energy converters.

Two essential parameters for categorising energy storage systems are the specific energy

$$E_{\text{spec}} := \frac{E_{\text{es,nom}}}{m_{\text{es}}} \tag{3.80}$$

and the specific power

$$p_{\text{spec}} := \frac{p_{\text{es,nom}}}{m_{\text{es}}}\,, \tag{3.81}$$

where the nominal energy $E_{\text{es,nom}}$ and the nominal power $p_{\text{es,nom}}$ are set in ratio to its mass m_{es}, respectively. The Ragone diagram in Fig. 3.21 shows the various storage technologies according to their specific energy and specific power. The specific energy of lithium-ion batteries is the highest, while electrolytic capacitors have the highest specific power. The diagonal lines mark a constant ratio between E_{spec} and p_{spec}. They indicate the time until the storage can be charged or discharged completely with its nominal power $p_{\text{es,nom}}$. This indicates that the short-term storage units are located at the bottom right and the long-term storage units at the top left.

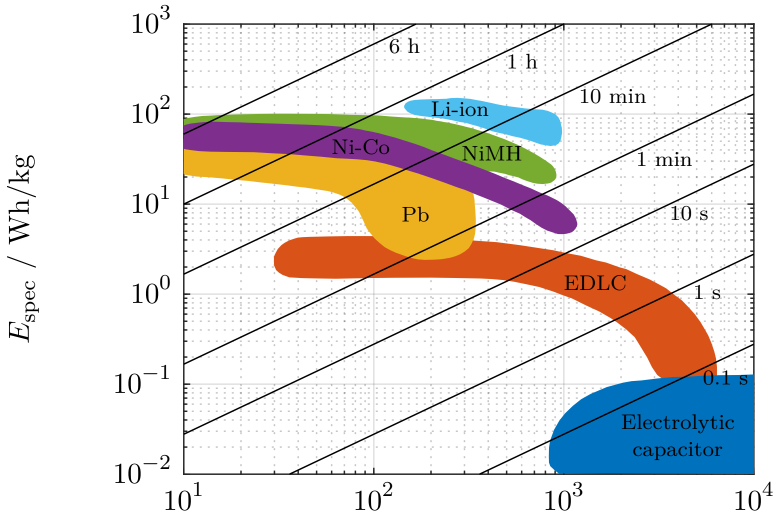

Figure 3.21: Ragone diagram of the specific energy and power of batteries and capacitors [234, Sec. 2.1.2].

The electrochemical double-layer capacitor (EDLC), also referred to as supercapacitors or ultra-capacitors, forms the link between capacitors and batteries. EDLCs are characterised by a very high capacitance of up to several thousand farads, and their cycle stability is significantly higher than that of batteries. On the other hand, their voltage rating is relatively low and usually less than 3 V. To achieve higher voltage ratings, supercapacitor cells have to be connected in series. Due to component tolerances and ageing, different voltages can occur at the single capacitor cells during charging and discharging, which requires a balancing system [235, 236].

Their low energy density compared to batteries and relatively high self-discharge rate make them unsuitable for long-term storage. However, they are ideal for short-term storage, which is why they are used here as storage units for power smoothing. In renewable energy applications, supercapacitors are used to smooth the power variations and to fulfil the grid requirements, such as the low voltage ride-through (LVRT) capability [237–239]. Because of their simplicity, supercapacitors are often chosen for the short-term energy storage system in WECs [225, 240–243].

Batteries are not suitable for this purpose due to their lower cycle stability. The cyclic lifetime of lithium-ion batteries ranges from several hundred to several thousand cycles [244, Sec. 12.3]. Supercapacitors, on the other hand, can last from several hundred thousand to several million cycles [245]. With a typical wave period of 10 seconds, several thousand cycles can occur daily. In addition, the short-term storage must absorb a high power level within a short period of the wave cycle. Batteries are, therefore, unsuitable for this purpose. A hybrid system consisting of batteries and supercapacitors can combine the advantages of both technologies. The supercapacitor, with its high power density, can withstand high power peaks, while the batteries, with their high energy density, can provide or store energy over a long period [237, 246, 247].

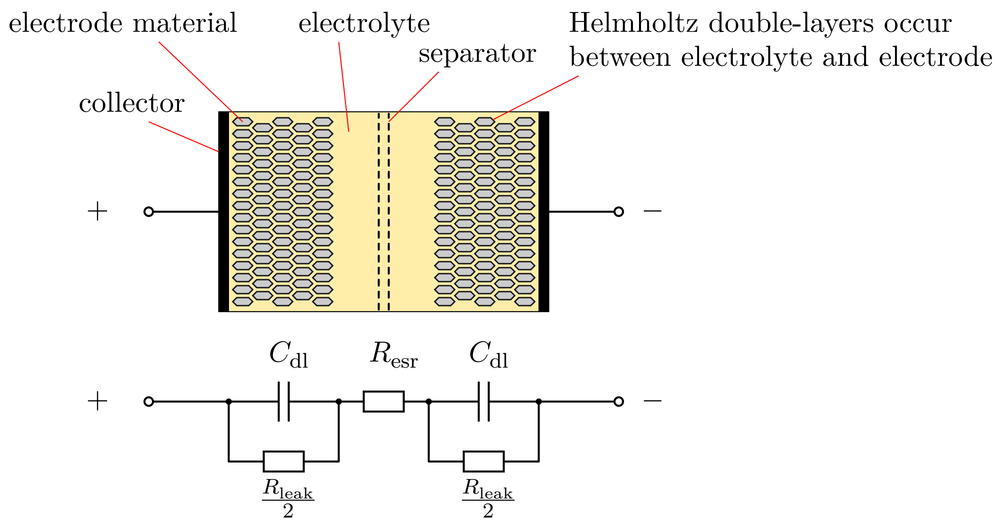

Figure 3.22: Schematic structure of an electrochemical double-layer capacitor and the equivalent circuit beneath.

Supercapacitors also combine the technology from conventional capacitors and batteries, as the energy is stored in electrical and chemical forms. The physicist Hermann von Helmholtz discovered this capacitor's functional principle in 1853 [248]. Fig. 3.22 shows the schematic structure of an electrochemical double-layer capacitor and its equivalent circuit. The EDLC has two electrodes that are mechanically separated by a separator but electrically connected via an electrolyte. Two so-called Helmholtz double-layers occur at the boundary layers between the electrode material and the electrolyte. This layer constitutes the dielectric and consists of a few molecular layers, about 0.3 to 0.5 nm thin [249, Sec. 3.4].

The high capacitance of supercapacitors is due to the double-layer effect and the electrode material. In general, a capacitance C of a capacitor is given by [250, Sec. 21]

$$C = \epsilon_{\mathrm{r}}\, \epsilon_0\, \frac{A}{d}\,, \tag{3.82}$$

where ϵ_{r} is the relative permittivity, ϵ_0 is the vacuum permittivity, A is the area of the electrodes, and d is the distance between them. The supercapacitor's electrodes consist of a sponge-like

activated carbon with a vast surface area. This area can be utilised with the liquid electrolyte. In addition, the double-layer is extremely thin. According to (3.82), these two factors result in a very large capacitance, ranging from a few farads to several thousand farads per cell [251].
Some ions from the electrolyte can overcome the double-layer and make direct contact with the surface of the electrode. These transfer electrons to the electrodes, creating a pseudo-capacitance. The pseudo-capacitance always occurs together with the double-layer capacitance, adding up inseparably to a total capacitance. The term pseudo-capacitance is used because it is a chemical reaction instead of the electrostatic storage of a classic capacitance. The high cycle stability of supercapacitors is due to these reactions being highly reversible [244, Sec. 6.1.2].
The high self-discharge rate compared to batteries and classic capacitors is due to the finite resistance of the double-layer. This is modelled in the equivalent circuit by the resistance R_{leak}. In addition, chemical equalisation processes in the electrolyte also reduce the charge. The equivalent series resistance (ESR) R_{esr} is also significantly higher compared to classic capacitors. The conductivity of the electrolyte and the separator primarily determines it. A more detailed description of the technical details of supercapacitors can be found in [244, Sec. 6.1.2] and [249, Sec. 3.4].
Although supercapacitors are electrochemical storage units, they can be modelled with a simple RC model, as shown in Fig. 3.23(a). This is possible due to the high reversibility of the chemical reaction. However, if the supercapacitor is charged or discharged rapidly, the entire capacity cannot be utilised due to the limited penetration depth into the activated carbon. In a subsequent rest phase, recharging processes occur, leading to a change in the terminal voltage [244, Sec. 6.1.3].
For such highly dynamic applications, a three-branch model, as shown in Fig. 3.23(b), can account for these effects. Each branch has a separate time constant. The first branch dominates the immediate behaviour, where a voltage-dependent capacitance $C_{\mathrm{iu}}(u_{\mathrm{i}})$ is added. The second branch accounts for the short-term effects in the range of some minutes, and the third branch accounts for long-term behaviour after more than ten minutes [252]. A more detailed model with multiple RC branches can be considered to further increase the accuracy of the dynamic behaviour [253, 254]. However, the simple RC model is sufficient for the application in the WEC, where moderate charging and discharging are given, and short-term storage of a few seconds is required [255].

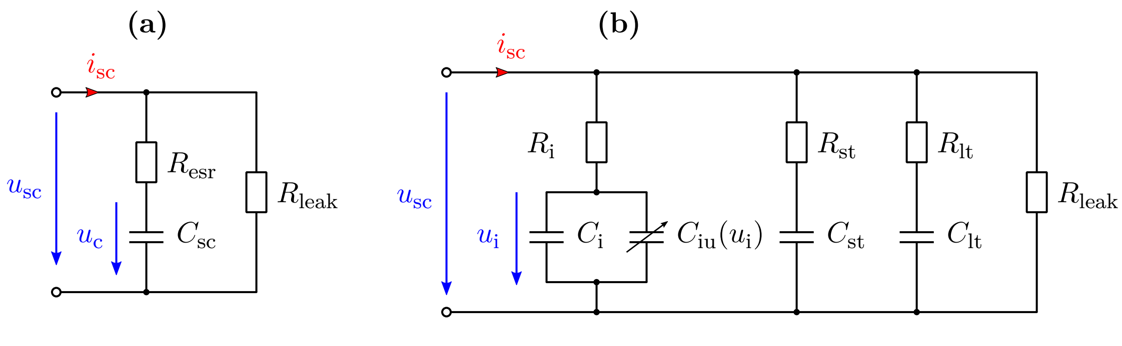

Figure 3.23: (a) RC model and (b) three-branch model for highly dynamic applications of supercapacitors.

The state of charge (SoC) of the energy storage system is crucial for controlling and monitoring the system. In general, the SoC is defined as [256, Sec. 7.1.3]

$$\mathrm{SoC} = \mathrm{SoC}_0 + \frac{q_{\mathrm{es}}}{Q_{\mathrm{nom}}}\,, \tag{3.83}$$

where SoC_0 is the initial state of charge for $t = 0$ s, Q_{nom} is the nominal charge of the storage when it is fully charged, and

$$q_{\mathrm{es}} = \int_{t=0\ \mathrm{s}}^{t} i_{\mathrm{es}}\,\mathrm{d}t \tag{3.84}$$

is the charge that flows into the storage unit. Note that the current i_{es} flows into the energy storage here, and the SoC increases if the current i_{es} is positive. When the storage is fully charged, $\mathrm{SoC} = 1$ applies.
Using the SoC for battery systems is standard practice, as it correlates with the energy they contain. This is because the terminal voltage of a battery hardly changes or only changes slightly with the SoC. This is not the case with supercapacitors. The energy E_{sc} depends on the voltage u_{c} and can be given by

$$E_{\mathrm{sc}} = \frac{1}{2}\,C_{\mathrm{sc}}\,u_{\mathrm{c}}^2\,, \tag{3.85}$$

where C_{sc} is the capacitance of the supercapacitor.
Therefore, introducing a state of energy (SoE) analogue to the SoC is much more practical. It is defined as [257, 258]

$$\mathrm{SoE} = \frac{\Delta E_{\mathrm{es}}}{\Delta E_{\mathrm{es,nom}}}\,, \tag{3.86}$$

where $\Delta E_{\mathrm{es,nom}}$ is the nominal energy of the supercapacitor when it is fully charged. The supercapacitor's maximum and minimum permissible voltage $u_{\mathrm{sc,max}}$ and $u_{\mathrm{sc,min}}$ determines the usable energy with

$$\Delta E_{\mathrm{es,nom}} = \frac{1}{2} C_{\mathrm{sc}} \left(u_{\mathrm{sc,max}}^2 - u_{\mathrm{sc,min}}^2\right)\,. \tag{3.87}$$

Accordingly, the actually stored energy ΔE_{es} is determined starting from the minimum voltage $u_{\mathrm{sc,min}}$. Inserting (3.87) into (3.86), the state of energy depends only on the voltages with

$$\mathrm{SoE} = f_{\mathrm{soe}}(u_{\mathrm{c}}) = \frac{u_{\mathrm{c}}^2 - u_{\mathrm{sc,min}}^2}{u_{\mathrm{sc,max}}^2 - u_{\mathrm{sc,min}}^2}\,. \tag{3.88}$$

When the supercapacitor is fully charged, $\mathrm{SoE} = 1$ and $u_{\mathrm{c}} = u_{\mathrm{sc,max}}$.

3.3.2 Control of the Electrical System of a Wave Energy Converter

In the following, the control of the electrical system of the WEC module prototype is presented. The test site of the full-sized prototype of the point absorber was located in Heraklion on the Greek island of Crete. Since it was only a single module and not an entire floating WEC consisting of several modules, the prototype had to be mounted on the harbour wall, as shown in Fig. 1.9. This section is partially based on [3], where parts have already been published.

Electrical System of the WEC Module Prototype

In this experimental setup, the supercapacitor is connected directly to the DC link because the development of the bidirectional DC/DC converter presented in Sec. 2.3 had not yet been completed at the time the prototype had to be installed.
As there is no sufficient grid connection at the harbour wall, the energy generated by the WEC is used to charge batteries. For this purpose, a purchased unidirectional DC/DC converter is used to charge a battery storage unit. The energy in the batteries is used for various peripheral devices to ensure that the batteries are not fully charged so that the energy generated by the WEC can always be stored. Power smoothing is also required here to reduce the battery's load

and thus ensure a longer lifetime. The high power peaks in the upward movement of the floating buoy are to be absorbed by the supercapacitor and slowly released during periods of lower power generation.
The DC link voltage has to change according to the fluctuating power to charge and discharge the supercapacitor bank during a wave. The DC link voltage is controlled by the current through the DC/DC converter, where the reference current is computed in a programmable logic control (PLC) and transmitted to the converter. The control system is divided into two parts. The first part measures the generated power and calculates the reference DC link voltage, yielding a nonlinear control system. The subsequent voltage control loop ensures that the DC link voltage follows this reference.
As a safety measure, a braking chopper is integrated to dissipate excess energy. This prevents the voltage from rising above a specific limit. The chopper works independently and is, therefore, regarded as a disturbance to the control system. In addition, the chopper does not have to intervene if the control system works correctly.

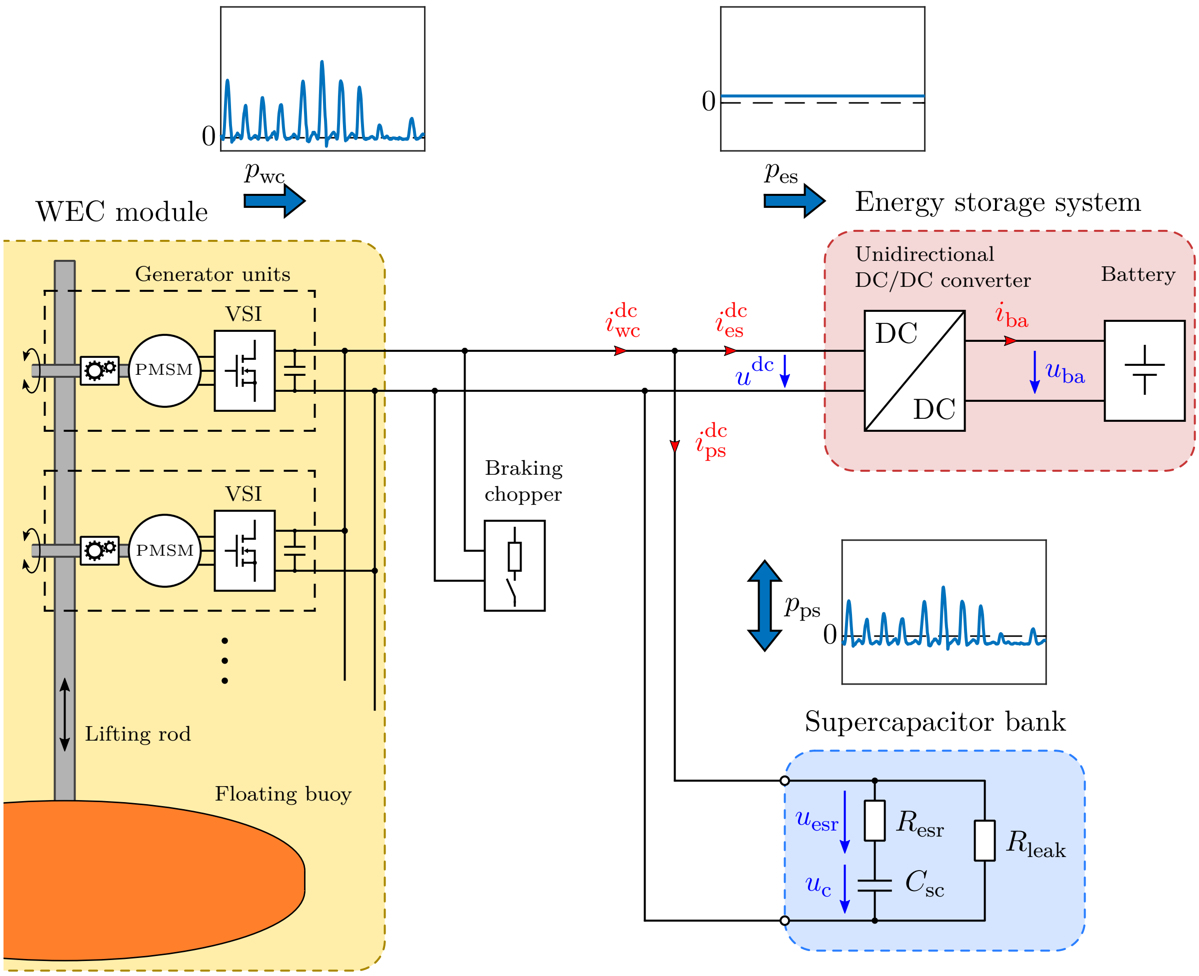

Figure 3.24: The electrical circuit of the wave energy converter and illustration of the power flow, where p_{wc} is the fluctuating power from the WEC, p_{ps} is the power flowing in and out of the supercapacitors, and p_{es} is the smoothed power flow into the battery.

Fig. 3.24 shows the WEC's electrical system schematic as realised at the test site. The WEC's floating buoy swims on the water, moving up and down with each wave. The lifting rod is attached to the buoy and moves with it. The vertical movement is converted into a rotary

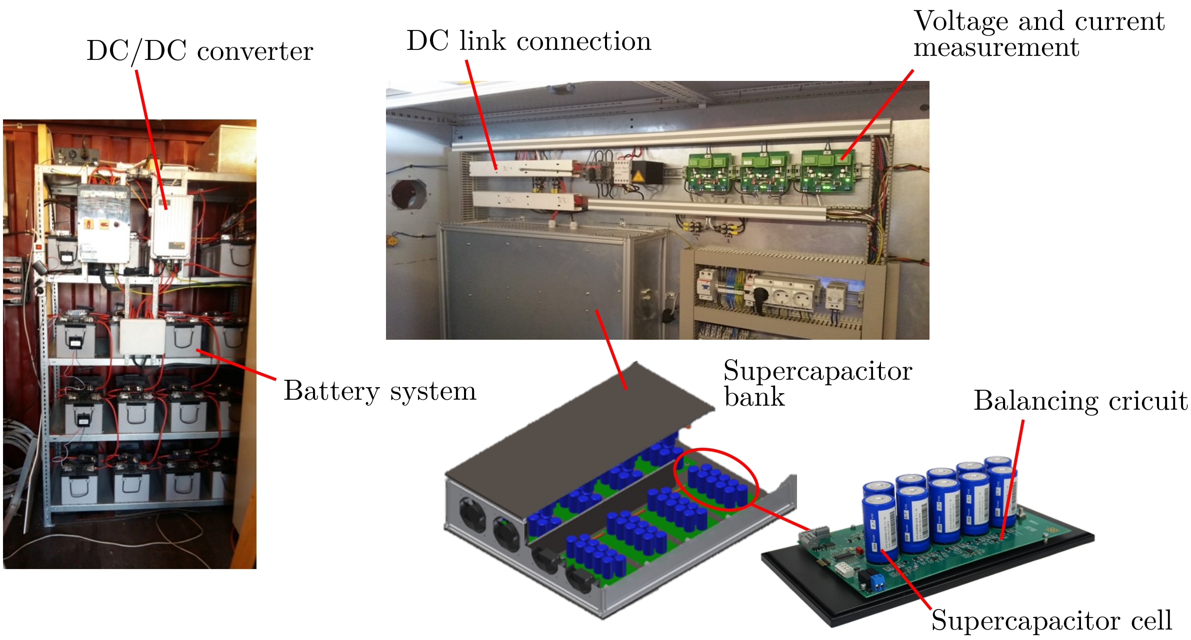

Figure 3.25: Photo and computer-aided design (CAD) illustration of the supercapacitor bank, the battery system and the control cabinet with the voltage and current measurement.

movement via the rollers of several generator units, which are pressed onto the rod with springs. A generator unit that is an earlier version than the one described in Sec. 2.4 has been used. The main differences are that a gearbox is still used here, the rated power is only about 3 kW, and the maximum DC link voltage is limited to an absolute maximum of 400 V. For additional safety, the voltage is limited to $u_{\text{max}}^{\text{dc}} = 380$ V. The VSI requires a minimum voltage for the current control, which mainly depends on the rotational speed of the permanent magnet synchronous machine (PMSM). Therefore, the voltage should not fall below $u_{\text{min}}^{\text{dc}} = 300$ V.

The PMSM is current-controlled by the VSI, which allows the torque of the generator rollers to be set. In this way, the mechanical power can be converted into electrical power by decelerating the movement of the rod. All DC outputs of the generator units are connected in parallel to the DC link.

As supercapacitor cells have a relatively low nominal voltage, several cells are connected in series to form a supercapacitor bank. The cells used have a nominal voltage $u_{\text{sc,nom},i}$ of 2.7 V and a capacitance of $C_{\text{sc},i} = 350$ F [245]. With a maximally permissible DC link voltage of 400 V, at least 149 cells are required in series. The developed supercapacitor bank consists of $N_{\text{sc}} = 160$ cells connected in series, divided into 16 modules with ten cells each.

The cell voltages are balanced by connecting a balancing circuit in parallel to each cell. It consists of a resistor and a bipolar transistor connected in series. An analogue circuit compares the voltage of two adjacent cells and uses the transistor to control the current through the resistor. The supercapacitor bank and the other components are shown in Fig. 3.25.

Due to the series connection of the cells, the equivalent series resistances $R_{\text{esr},i}$ of each cell add up, resulting in the total resistance

$$R_{\text{esr}} = \sum_{i=1}^{N_{\text{sc}}} R_{\text{esr},i} \,. \tag{3.89}$$

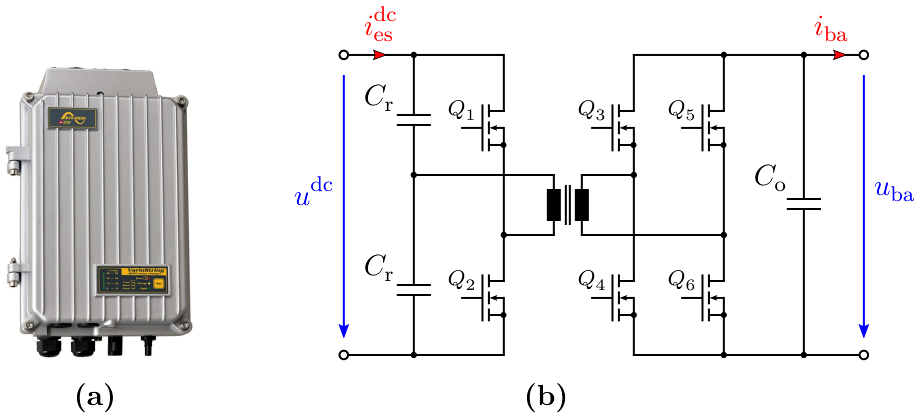

Figure 3.26: Photo of the DC/DC converter VarioString VS-70 (a) and the LLC half-bridge topology (b).

Here, this results in an ESR of 512 mΩ. The overall capacitance C_{sc} is given by

$$C_{sc} = \frac{1}{\sum_{i=1}^{N_{sc}} \frac{1}{C_{sc,i}}} . \tag{3.90}$$

Assuming that each cell has the same capacitance, the calculation can be simplified to

$$C_{sc} = \frac{C_{sc,i}}{N_{sc}} , \tag{3.91}$$

which results in 2.19 F. The VSI of the generator units have a DC link capacitor to stabilise the voltage at their terminals. However, these are electrolytic capacitors with 1410 μF, which are very small compared to the capacity of the supercapacitor bank and can therefore be neglected. The other parameters are calculated similarly, leading to the electrical parameters of the supercapacitor bank, listed in Table 3.1.

Due to the specified limits of the DC link voltage u^{dc}, the energy stored in the supercapacitors cannot be fully utilised. The maximum available energy in steady-state conditions that can be used for power smoothing is, according to (3.87), about 16.5 Wh. That is around 38 % of the energy contained in the bank.

There are several methods for estimating the required storage capacitance [240, 259, 260]. For a rough estimate, it is assumed that the WEC generates the maximum power over 2 s, which is the typical duration of a power pulse. The prototype has eight generator units installed, each with a rated output of 3 kW. This results in an energy of around 12 Wh, which the installed supercapacitor bank must provide.

Fig. 3.26(a) shows the unidirectional DC/DC converter manufactured by Studer Innotec, which is used to charge 48-V-batteries from the DC link. The DC/DC converter is designed to be installed in a photovoltaic application. However, its specifications listed in Table 3.1 are ideally suited for the application considered here. A very high efficiency is achieved by a resonant LLC half-bridge topology, shown in Fig. 3.26(b). This topology allows zero voltage switching (ZVS), leading to low switching losses [261].

The DC/DC converter can be configured to operate in a current-control mode, which enables the current i_{es}^{dc} to be controlled. The reference current $i_{es,ref}^{dc}$ is transmitted via a serial RS-232 communication bus from a PLC in which the control of the DC link voltage is implemented. The

Table 3.1: Eletrical parameters of the used components.

Unit	Name	Parameter	Value
Supercapacitor Cell	Rated Capacitance	$C_{\mathrm{sc},i}$	350 F
	Equivalent Series Resistor	$R_{\mathrm{esr},i}$	3.2 mΩ
	Rated Voltage	$u_{\mathrm{sc,nom},i}$	2.7 V
	Absolute Maximum Current	$i_{\mathrm{sc,max},i}$	170 A
	Maximum Leakage Current	$i_{\mathrm{leak},i}$	0.30 mA
Supercapacitor bank	Number supercapacitor cells	N_{sc}	160
	Rated Capacitance	C_{sc}	2.19 F
	Equivalent Series Resistor	R_{esr}	512 mΩ
	Rated Voltage	$u_{\mathrm{sc,nom}}$	432 V
	Absolute Maximum Current	$i_{\mathrm{sc,max}}$	170 A
	Maximum power	$p_{\mathrm{sc,max}}$	73.4 kW
DC/DC converter	Nominal Power	$p_{\mathrm{es,nom}}$	4.2 kW
	Maximum Input Voltage	$u^{\mathrm{dc}}_{\mathrm{es,max}}$	600 V
	Maximum Input Current	$i^{\mathrm{dc}}_{\mathrm{es,max}}$	13 A
	Nominal Battery Voltages	$u_{\mathrm{ba,nom}}$	48 V
	Maximum Battery Current	$i_{\mathrm{ba,max}}$	70 A
	Maximum Efficiency	η	> 98 %

PLC can measure the currents and voltages in the system, the wave height, and the position of the floating buoy.

Control of the DC link

The control of the DC link must fulfil two objectives. Firstly, the battery current i_{ba} should be as constant as possible to increase the battery's lifetime. Secondly, the DC link voltage should remain within the limits $u^{\mathrm{dc}}_{\mathrm{min}}$ and $u^{\mathrm{dc}}_{\mathrm{max}}$ and maintain the nominal voltage $u^{\mathrm{dc}}_{\mathrm{nom}}$ on average. In this case, the nominal voltage $u^{\mathrm{dc}}_{\mathrm{nom}} = 350$ V is chosen. As a result, the energy stored from the nominal voltage to the upper voltage limit is approximately the same as from the nominal voltage to the lower voltage limit.
The stored energy in the capacitor bank is, according to (3.85), proportional to the square of the capacitance voltage u_{c}. This means that if energy is to be stored in the supercapacitor bank, the DC link voltage u^{dc} must increase. If energy is to be released, the voltage must decrease. Hence, the DC link voltage must fluctuate accordingly for power smoothing to work with a supercapacitor connected directly to the DC link.
The DC link voltage results from the current $i^{\mathrm{dc}}_{\mathrm{ps}}$ through the capacitor bank and is given by

$$u^{\mathrm{dc}} = u_{\mathrm{esr}} + u_{\mathrm{c}} = R_{\mathrm{esr}}\, i^{\mathrm{dc}}_{\mathrm{ps}} + \frac{1}{C_{\mathrm{sc}}} \int i^{\mathrm{dc}}_{\mathrm{ps}}\, \mathrm{d}t + u_{\mathrm{c},0}\,, \tag{3.92}$$

where the voltage $u_{\mathrm{c},0}$ is the initial voltage over the capacitance C_{sc} at $t=0$ s.
The DC link voltage u^{dc} can be controlled with the current

$$i^{\mathrm{dc}}_{\mathrm{es}} = i^{\mathrm{dc}}_{\mathrm{wc}} - i^{\mathrm{dc}}_{\mathrm{ps}} \tag{3.93}$$

flowing into the energy storage system through the DC/DC converter. The current $i_{\mathrm{wc}}^{\mathrm{dc}}$ from the WEC is interpreted as a disturbance. The dynamics of the DC/DC converter are approximated by a first-order transfer function with the time constant τ_{es}. Laboratory experiments have shown that this assumption describes the behaviour sufficiently well. This yields the transfer function of the DC link voltage with

$$\frac{u^{\mathrm{dc}}(s)}{i_{\mathrm{es,ref}}^{\mathrm{dc}}(s)} = -\frac{1 + s\,R_{\mathrm{esr}}\,C_{\mathrm{sc}}}{s\,C_{\mathrm{sc}}\,(1 + s\,\tau_{\mathrm{es}})}\,. \tag{3.94}$$

The system exhibits integral behaviour, so a proportional (P) controller is sufficient for reference tracking. However, a stationary control deviation can still occur since the disturbing current $i_{\mathrm{wc}}^{\mathrm{dc}}$ acts on the system. This can be compensated for by a controller with additional integral control action [84, Sec. 7]. This results in a proportional-integral (PI) controller with transfer function

$$\frac{i_{\mathrm{es,ref}}^{\mathrm{dc}}(s)}{u_{\mathrm{ref}}^{\mathrm{dc}}(s) - u^{\mathrm{dc}}(s)} = V_{\mathrm{r}}\frac{1 + s\,\tau_{\mathrm{r}}}{s\,\tau_{\mathrm{r}}}\,. \tag{3.95}$$

Due to the double integrator, the controller is tuned according to the symmetrical optimum (SO) to achieve a maximum phase margin of 37° [80, Sec. 1.3.2], which yields

$$V_{\mathrm{r}} = -\frac{C_{\mathrm{sc}}}{2\,\tau_{\mathrm{es}}} \quad \text{and} \quad \tau_{\mathrm{r}} = 4\,\tau_{\mathrm{es}}\,. \tag{3.96}$$

The control of the DC link voltage u^{dc} also enables the energy in the supercapacitor bank to be controlled in accordance with (3.88). To keep the battery current i_{ba} constant, the power p_{es} through the DC/DC converter must also be constant due to the approximately constant battery voltage u_{ba}. Therefore, the power p_{es} should be the average of the generated power p_{wc} minus the losses. By filtering the generated power p_{wc} with a low-pass filter with a correspondingly low cutoff frequency, the average generated power $\overline{p}_{\mathrm{wc}}$ is obtained (see Appendix A.6). The desired power $p_{\mathrm{c,ref}}$ of the capacitance C_{sc} can be calculated as

$$p_{\mathrm{c,ref}} = p_{\mathrm{wc}} - \overline{p}_{\mathrm{wc}} - p_{\mathrm{esr}}\,, \tag{3.97}$$

where

$$p_{\mathrm{esr}} = R_{\mathrm{esr}}\,\left(i_{\mathrm{ps}}^{\mathrm{dc}}\right)^2 \tag{3.98}$$

is the power dissipated in the equivalent series resistor R_{esr}. With the nonlinear differential equation

$$\frac{\mathrm{d}}{\mathrm{d}t}u_{\mathrm{c,ref}} = \frac{1}{C_{\mathrm{sc}}}\,\frac{p_{\mathrm{c,ref}}}{u_{\mathrm{c,ref}}}\,, \tag{3.99}$$

the reference voltage $u_{\mathrm{c,ref}}$ over the capacitance C_{sc} can be calculated. Since the voltage $u_{\mathrm{c,ref}}$ must not become zero, a saturation function is added after the integration to keep the reference voltage within the permissible range from $u_{\mathrm{min}}^{\mathrm{dc}}$ to $u_{\mathrm{max}}^{\mathrm{dc}}$. The saturation function f_{sat} is defined by

$$f_{\mathrm{sat}}(x_{\mathrm{min}},\,x,\,x_{\mathrm{max}}) := \begin{cases} x_{\mathrm{min}}, & x \leq x_{\mathrm{min}} \\ x, & x_{\mathrm{min}} < x < x_{\mathrm{max}} \\ x_{\mathrm{max}}, & x \geq x_{\mathrm{max}}\,. \end{cases} \tag{3.100}$$

A feedforward control is required to control the voltage u_{c}, achieved by adding the voltage u_{esr} to the reference voltage $u_{\mathrm{c,ref}}$, yielding the reference DC link voltage

$$u_{\mathrm{ref}}^{\mathrm{dc}} = u_{\mathrm{c,ref}} + u_{\mathrm{esr}} = u_{\mathrm{c,ref}} + R_{\mathrm{esr}}\,i_{\mathrm{ps}}^{\mathrm{dc}}\,. \tag{3.101}$$

This feedforward control with the voltage u_{esr} over the ESR of the supercapacitors enables the capacitance voltage u_{c} to be controlled and, thus, the stored energy ΔE_{sc} in the supercapacitor bank to be controlled directly.

A restoring current i_{res} is introduced, which should cause the DC link voltage to fluctuate around its nominal voltage $u_{\mathrm{nom}}^{\mathrm{dc}}$ on average. Otherwise, the voltage would drift. If energy is to be stored in the supercapacitors ($p_{\mathrm{wc}} > p_{\mathrm{es}}$) and the DC link voltage is already above the nominal voltage ($u_{\mathrm{c,ref}} > u_{\mathrm{nom}}^{\mathrm{dc}}$), then the DC/DC converter should increase the power p_{es}. If energy is required ($p_{\mathrm{wc}} < p_{\mathrm{es}}$) and the DC link voltage is below the nominal voltage ($u_{\mathrm{c,ref}} < u_{\mathrm{nom}}^{\mathrm{dc}}$), then p_{es} should decrease. Therefore, the restoring current is defined as

$$i_{\mathrm{res}} := \begin{cases} -V_{\mathrm{res}}\left(u_{\mathrm{c,ref}} - u_{\mathrm{nom}}^{\mathrm{dc}}\right), & \\ \qquad\qquad \text{if} \quad p_{\mathrm{wc}} > p_{\mathrm{es}} \ \wedge \ u_{\mathrm{c,ref}} > u_{\mathrm{nom}}^{\mathrm{dc}} \\ \qquad\qquad \text{or} \quad p_{\mathrm{wc}} < p_{\mathrm{es}} \ \wedge \ u_{\mathrm{c,ref}} < u_{\mathrm{nom}}^{\mathrm{dc}} \\ 0\,, \qquad \text{otherwise.} \end{cases} \tag{3.102}$$

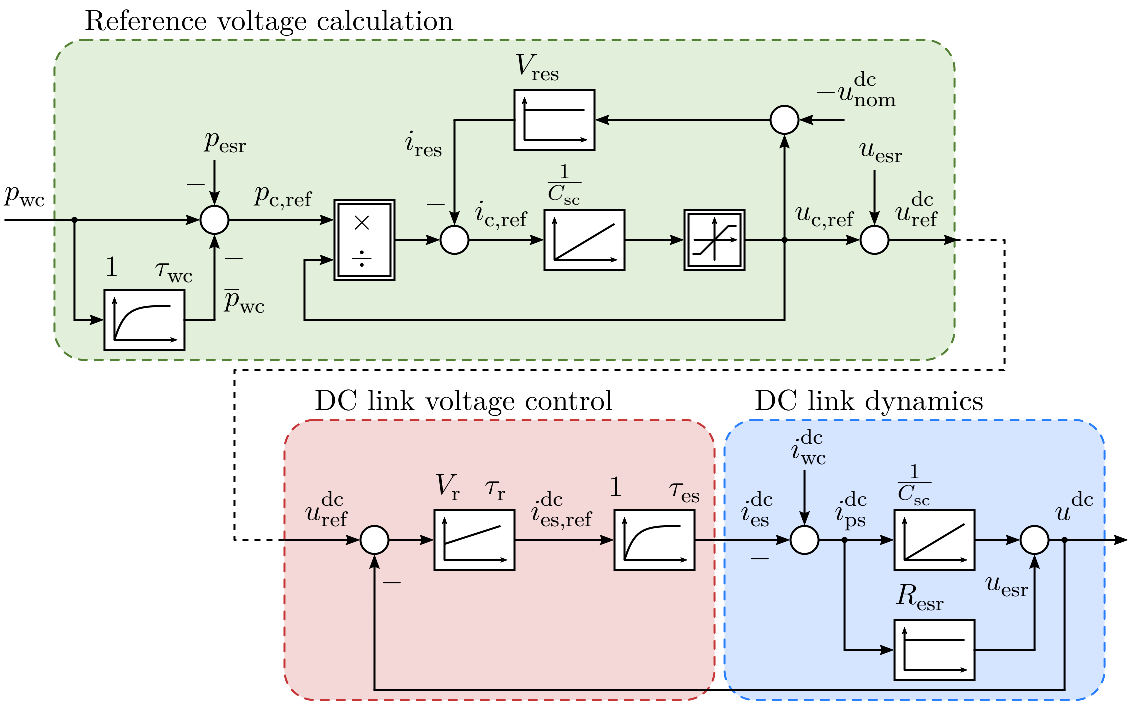

Figure 3.27: Block diagram of the voltage control loop for power smoothing.

Fig. 3.27 shows the block diagram of the proposed control system. The restoring current is added to the reference current $i_{\mathrm{ps,ref}}^{\mathrm{dc}}$ before the integration. This leads to both an integrating and a filtering behaviour of this restoring term. The crossover frequency of its transfer function

$$\frac{u_{\mathrm{c,ref}}(s)}{u_{\mathrm{c,ref}}(s) - u_{\mathrm{nom}}^{\mathrm{dc}}(s)} = -\frac{V_{\mathrm{res}}}{s\,C_{\mathrm{sc}}} \tag{3.103}$$

is given by

$$f_{\mathrm{res}} = \frac{V_{\mathrm{res}}}{2\pi\,C_{\mathrm{sc}}}\,. \tag{3.104}$$

The crossover frequency is set to one-tenth of the lowest frequency of the waves that can occur, which is approximately 0.15 Hz.
With the introduced saturation of the voltage $u_{\mathrm{c,ref}}$ according to 3.100, the reference voltage is limited to the desired operating range. This ensures that the DC link voltage does not exceed the limits, even if more energy has to be stored due to very high power peaks. The fast voltage control loop guarantees that this excessive energy is fed directly into the batteries. Although this increases the stress on the batteries, it can be tolerated as this only occurs in exceptional cases. The alternative would be to dissipate it via the braking chopper, but this should be avoided as it would lead to a loss of efficiency.

Stability Analysis

A stability analysis is carried out in the state-space to prove the nonlinear control system's stability. Due to the different structure, the controller design differs substantially from the one presented in Sec. 3.2. Therefore, the system dynamics are very different, so a separate analysis is required. The nonlinear dynamics of the system are given by

$$\left.\begin{aligned}
\frac{\mathrm{d}}{\mathrm{d}t}u_{\mathrm{c}} &= \frac{1}{C_{\mathrm{sc}}}\left(i_{\mathrm{wc}}^{\mathrm{dc}} - i_{\mathrm{es}}^{\mathrm{dc}}\right) \\
\frac{\mathrm{d}}{\mathrm{d}t}i_{\mathrm{es}}^{\mathrm{dc}} &= \frac{1}{\tau_{\mathrm{ps}}}\left[V_{\mathrm{r}}\left(\underbrace{f_{\mathrm{sat}}\left(u_{\mathrm{min}}^{\mathrm{dc}},\, u_{\mathrm{c,ref}},\, u_{\mathrm{max}}^{\mathrm{dc}}\right) + R_{\mathrm{esr}}\, i_{\mathrm{c}}}_{=u_{\mathrm{ref}}^{\mathrm{dc}}} - \underbrace{\left(u_{\mathrm{c}} + R_{\mathrm{esr}}\, i_{\mathrm{c}}\right)}_{=u^{\mathrm{dc}}}\right) + \xi_{\mathrm{es,ref}}^{\mathrm{dc}} - i_{\mathrm{es}}^{\mathrm{dc}}\right] \\
\frac{\mathrm{d}}{\mathrm{d}t}\xi_{\mathrm{es,ref}}^{\mathrm{dc}} &= \frac{V_{\mathrm{r}}}{\tau_{\mathrm{r}}}\left(\underbrace{f_{\mathrm{sat}}\left(u_{\mathrm{min}}^{\mathrm{dc}},\, u_{\mathrm{c,ref}},\, u_{\mathrm{max}}^{\mathrm{dc}}\right) + R_{\mathrm{esr}}\, i_{\mathrm{c}}}_{=u_{\mathrm{ref}}^{\mathrm{dc}}} - \underbrace{\left(u_{\mathrm{c}} + R_{\mathrm{esr}}\, i_{\mathrm{c}}\right)}_{=u^{\mathrm{dc}}}\right) \\
\frac{\mathrm{d}}{\mathrm{d}t}u_{\mathrm{c,ref}} &= \frac{1}{C_{\mathrm{sc}}}\left(\frac{p_{\mathrm{wc}} - \overline{p}_{\mathrm{wc}} - p_{\mathrm{esr}}}{u_{\mathrm{c,ref}}} \underbrace{- V_{\mathrm{res}}\left(u_{\mathrm{c,ref}} - u_{\mathrm{nom}}^{\mathrm{dc}}\right)}_{=:i_{\mathrm{res}}}\right) \\
\frac{\mathrm{d}}{\mathrm{d}t}\overline{p}_{\mathrm{wc}} &= \frac{1}{\tau_{\mathrm{wc}}}\left(p_{\mathrm{wc}} - \overline{p}_{\mathrm{wc}}\right) ,
\end{aligned}\right\} \tag{3.105}$$

where the state $\xi_{\mathrm{es,ref}}^{\mathrm{dc}}$ is introduced for the integral action of the PI-controller.
A linearised small-signal state-space representation must be determined to analyse the stability of the system. The saturation function f_{sat} is nonlinear, but since the operation point of the DC link voltage lies between the limits $u_{\mathrm{min}}^{\mathrm{dc}}$ and $u_{\mathrm{max}}^{\mathrm{dc}}$, the saturation can be neglected for the small-signal representation, yielding

$$\left.\begin{aligned}
\frac{\mathrm{d}}{\mathrm{d}t}i_{\mathrm{es}}^{\mathrm{dc}} &= \frac{1}{\tau_{\mathrm{ps}}}\Big(V_{\mathrm{r}}\left(u_{\mathrm{c,ref}} - u_{\mathrm{c}}\right) + \xi_{\mathrm{es,ref}}^{\mathrm{dc}} - i_{\mathrm{es}}^{\mathrm{dc}}\Big) \\
\frac{\mathrm{d}}{\mathrm{d}t}\xi_{\mathrm{es,ref}}^{\mathrm{dc}} &= \frac{V_{\mathrm{r}}}{\tau_{\mathrm{r}}}\left(u_{\mathrm{c,ref}} - u_{\mathrm{c}}\right) .
\end{aligned}\right\} \tag{3.106}$$

Notice that u_{esr} and R_{esr} do not appear in (3.106) as the feedforward control compensates for them. Only the dissipated power p_{esr} remains in the dynamics of $u_{\mathrm{c,ref}}$ in (3.105). It is dissipated at the equivalent series resistor R_{esr} and cannot be utilised.

Furthermore, in (3.105), the powers are replaced by multiplying their corresponding current and voltage. It is assumed that the averaged DC link voltage $\overline{u}^{\mathrm{dc}}$ and the operation point $u^{\mathrm{dc}\star}$ are constant and correspond to its nominal value $u^{\mathrm{dc}}_{\mathrm{nom}}$. This assumption is reasonable, as the DC link voltage u^{dc} changes only slightly compared to the current $i^{\mathrm{dc}}_{\mathrm{wc}}$ from the WEC, as can be seen from the results shown below. The nonlinear dynamics of the reference voltage $u_{\mathrm{c,ref}}$ and the averaged input current $\overline{i}_{\mathrm{wc}}$ are thus given by

$$\left.\begin{aligned}\frac{\mathrm{d}}{\mathrm{d}t}u_{\mathrm{c,ref}} &= \frac{1}{C_{\mathrm{sc}}}\left(\frac{u^{\mathrm{dc}}_{\mathrm{nom}}(i^{\mathrm{dc}}_{\mathrm{wc}}-\overline{i}_{\mathrm{wc}})-R_{\mathrm{esr}}(i^{\mathrm{dc}}_{\mathrm{wc}}-i^{\mathrm{dc}}_{\mathrm{es}})^2}{u_{\mathrm{c,ref}}}-V_{\mathrm{res}}\left(u_{\mathrm{c,ref}}-u^{\mathrm{dc}}_{\mathrm{nom}}\right)\right)\\ \frac{\mathrm{d}}{\mathrm{d}t}\overline{i}_{\mathrm{wc}} &= \frac{1}{\tau_{\mathrm{wc}}}\left(i^{\mathrm{dc}}_{\mathrm{wc}}-\overline{i}_{\mathrm{wc}}\right).\end{aligned}\right\} \tag{3.107}$$

According to (3.59), linearisation around the operating point $\boldsymbol{x}^\star := (u^\star_{\mathrm{c}}, i^{\mathrm{dc}\star}_{\mathrm{es}}, \xi^{\mathrm{dc}\star}_{\mathrm{es,ref}}, u^\star_{\mathrm{c,ref}}, \overline{i}^\star_{\mathrm{wc}})^\top$ results in the small-signal state-space representation of the DC link control system as

$$\begin{aligned}\frac{\mathrm{d}}{\mathrm{d}t}\underbrace{\begin{pmatrix}\Delta u_{\mathrm{c}}\\ \Delta i^{\mathrm{dc}}_{\mathrm{es}}\\ \Delta\xi^{\mathrm{dc}}_{\mathrm{es,ref}}\\ \Delta u_{\mathrm{c,ref}}\\ \Delta\overline{i}_{\mathrm{wc}}\end{pmatrix}}_{=:\Delta\boldsymbol{x}} &= \underbrace{\begin{bmatrix}0 & -\frac{1}{C_{\mathrm{sc}}} & 0 & 0 & 0\\ -\frac{V_{\mathrm{r}}}{\tau_{\mathrm{ps}}} & -\frac{1}{\tau_{\mathrm{ps}}} & \frac{1}{\tau_{\mathrm{ps}}} & \frac{V_{\mathrm{r}}}{\tau_{\mathrm{ps}}} & 0\\ -\frac{V_{\mathrm{r}}}{\tau_{\mathrm{r}}} & 0 & 0 & \frac{V_{\mathrm{r}}}{\tau_{\mathrm{r}}} & 0\\ 0 & \frac{2\,R_{\mathrm{esr}}\,(\overline{i}^\star_{\mathrm{wc}}-i^{\mathrm{dc}\star}_{\mathrm{es}})}{C_{\mathrm{sc}}\,u^\star_{\mathrm{c,ref}}} & 0 & \alpha_{44} & -\frac{u^{\mathrm{dc}}_{\mathrm{nom}}}{C_{\mathrm{sc}}\,u^\star_{\mathrm{c,ref}}}\\ 0 & 0 & 0 & 0 & -\frac{1}{\tau_{\mathrm{wc}}}\end{bmatrix}}_{=:\boldsymbol{A}}\begin{pmatrix}\Delta u_{\mathrm{c}}\\ \Delta i^{\mathrm{dc}}_{\mathrm{es}}\\ \Delta\xi^{\mathrm{dc}}_{\mathrm{es,ref}}\\ \Delta u_{\mathrm{c,ref}}\\ \Delta\overline{i}_{\mathrm{wc}}\end{pmatrix}\\ &\quad+\underbrace{\begin{pmatrix}\frac{1}{C_{\mathrm{sc}}}\\ 0\\ 0\\ \frac{u^{\mathrm{dc}}_{\mathrm{nom}}-2\,R_{\mathrm{esr}}\,(\overline{i}^\star_{\mathrm{wc}}-i^{\mathrm{dc}\star}_{\mathrm{es}})}{C_{\mathrm{sc}}\,u^\star_{\mathrm{c,ref}}}\\ \frac{1}{\tau_{\mathrm{wc}}}\end{pmatrix}}_{=:\boldsymbol{B}}\Delta i^{\mathrm{dc}}_{\mathrm{wc}}\end{aligned} \tag{3.108}$$

with the output vector

$$\underbrace{\begin{pmatrix}\Delta i^{\mathrm{dc}}_{\mathrm{es}}\\ \Delta u^{\mathrm{dc}}\end{pmatrix}}_{=:\Delta\boldsymbol{y}} = \underbrace{\begin{bmatrix}0 & 1 & 0 & 0 & 0\\ 1 & -R_{\mathrm{esr}} & 0 & 0 & 0\end{bmatrix}}_{=:\boldsymbol{C}}\begin{pmatrix}\Delta u_{\mathrm{c}}\\ \Delta i^{\mathrm{dc}}_{\mathrm{es}}\\ \Delta\xi^{\mathrm{dc}}_{\mathrm{es,ref}}\\ \Delta u_{\mathrm{c,ref}}\\ \Delta\overline{i}_{\mathrm{wc}}\end{pmatrix} + \begin{pmatrix}0\\ R_{\mathrm{esr}}\end{pmatrix}\Delta i^{\mathrm{dc}}_{\mathrm{wc}}\,, \tag{3.109}$$

and the coefficient

$$\alpha_{44} = -\frac{1}{C_{\mathrm{sc}}}\left(\frac{u^{\mathrm{dc}}_{\mathrm{nom}}\,(\overline{i}^\star_{\mathrm{wc}}-\overline{i}_{\mathrm{wc}})-R_{\mathrm{esr}}\left(\overline{i}^\star_{\mathrm{wc}}-i^{\mathrm{dc}\star}_{\mathrm{es}}\right)^2}{(u^\star_{\mathrm{c,ref}})^2}+V_{\mathrm{res}}\right). \tag{3.110}$$

A linear time-invariant (LTI) system is exponentially stable if and only if its characteristic polynomial $\chi_{\boldsymbol{A}}(s)$ is a Hurwitz polynomial, which is given here as [84, Sec. 5.4.2]

$$\chi_{\boldsymbol{A}}(s) = \det(s\boldsymbol{I} - \boldsymbol{A}) = \frac{1}{\tau_{\mathrm{wc}}}\,(1 + s\,\tau_{\mathrm{wc}})\,\Big(a_0 + s\,a_1 + s^2\,a_2 + s^3\,a_3 + s^4\,a_4\Big)\,, \tag{3.111}$$

with

$$\left.\begin{aligned} a_0 &= \frac{V_{\mathrm{r}}\,\alpha_{44}}{C_{\mathrm{sc}}\,\tau_{\mathrm{r}}\,\tau_{\mathrm{ps}}} \\ a_1 &= \frac{-V_{\mathrm{r}}}{C_{\mathrm{sc}}\,\tau_{\mathrm{ps}}}\left(\frac{1}{\tau_{\mathrm{r}}} - \alpha_{44} + \frac{2\,R_{\mathrm{esr}}\,(\overline{i}^{\star}_{\mathrm{wc}} - i^{\mathrm{dc}\star}_{\mathrm{es}})}{\tau_{\mathrm{r}}\,u_{\mathrm{c,ref}}}\right) \\ a_2 &= \frac{-V_{\mathrm{r}}}{C_{\mathrm{sc}}\,\tau_{\mathrm{ps}}} - \frac{\alpha_{44}}{\tau_{\mathrm{ps}}} + \frac{-V_{\mathrm{r}}}{\tau_{\mathrm{ps}}}\,\frac{2\,R_{\mathrm{esr}}\,(\overline{i}^{\star}_{\mathrm{wc}} - i^{\mathrm{dc}\star}_{\mathrm{es}})}{C_{\mathrm{sc}}\,u_{\mathrm{c,ref}}} \\ a_3 &= \frac{1}{\tau_{\mathrm{ps}}} - \alpha_{44} \\ a_4 &= 1\,. \end{aligned}\right\} \tag{3.112}$$

The term $\frac{1}{\tau_{\mathrm{wc}}}\,(1 + s\,\tau_{\mathrm{wc}})$ can be factored out. It is stable for all $\tau_{\mathrm{wc}} > 0$ and, therefore, does not need to be considered for the stability analysis, which reduces the order of the polynomial to four. According to the Hurwitz criterion, the system is stable if [84, Sec. 5.4.2]

(i) all coefficients a_i are positive (i.e. $a_i > 0$ for $i \in \{1, 2, \ldots\}$) and

(ii) all leading principal minors D_i of the Hurzwitz matrix are positive.

Due to the redundancy of the Hurwitz criterion and according to the Liénard-Chipart criterion, for a fourth-order polynomial, it is sufficient to test only the leading principal minors

$$\left.\begin{aligned} &D_1 = a_1 \qquad \text{and} \\ &D_3 = a_1\,a_2\,a_3 - a_1^2\,a_4 - a_0\,a_3^2 \end{aligned}\right\} \tag{3.113}$$

for positivity in addition to the coefficients a_i [221, Sec. 3.4.5].
Determinate D_3 also leads to a fourth-order polynomial in arguments $\overline{i}^{\star}_{\mathrm{wc}}$, $i^{\mathrm{dc}\star}_{\mathrm{es}}$ and $u^{\star}_{\mathrm{c,ref}}$ due to the squaring of α_{44}, which is why a numerical approach is chosen to prove the positivity of different operating points. The physical limitations are considered and used accordingly to account for the worst case. Fig. 3.28 shows the coefficients a_0, a_1, a_2, a_3 and determinant D_3 over the current $\overline{i}^{\star}_{\mathrm{wc}}$ and for two different reference voltages $u^{\star}_{\mathrm{c,ref}} = u^{\mathrm{dc}}_{\mathrm{min}}$ and $u^{\star}_{\mathrm{c,ref}} = u^{\mathrm{dc}}_{\mathrm{max}}$. Further analyses show that the worst case for stability is when the reference voltage $u^{\star}_{\mathrm{c,ref}}$ is set to the minimum DC link voltage $u^{\mathrm{dc}}_{\mathrm{min}}$, the current $i^{\mathrm{dc}\star}_{\mathrm{es}}$ flowing into the DC/DC converter is set to $i^{\mathrm{dc}}_{\mathrm{es,max}}$, and the current $\overline{i}^{\star}_{\mathrm{wc}}$ is set to zero. The blue curves in Fig. 3.28 show this case.
Each value is positive at least in the range $-40\ \mathrm{A} < \overline{i}^{\star}_{\mathrm{wc}} < 700\ \mathrm{A}$. It is physically impossible for these limits to be exceeded because the generator units cannot produce a current greater than 700 A and only consume a minimum power in standby mode. Hence, the analysed system is exponentially stable.

Measurement Results

The measurement results of the DC link control were recorded under typical sea conditions. The measurement results are compared to the simulation results to validate the model. The

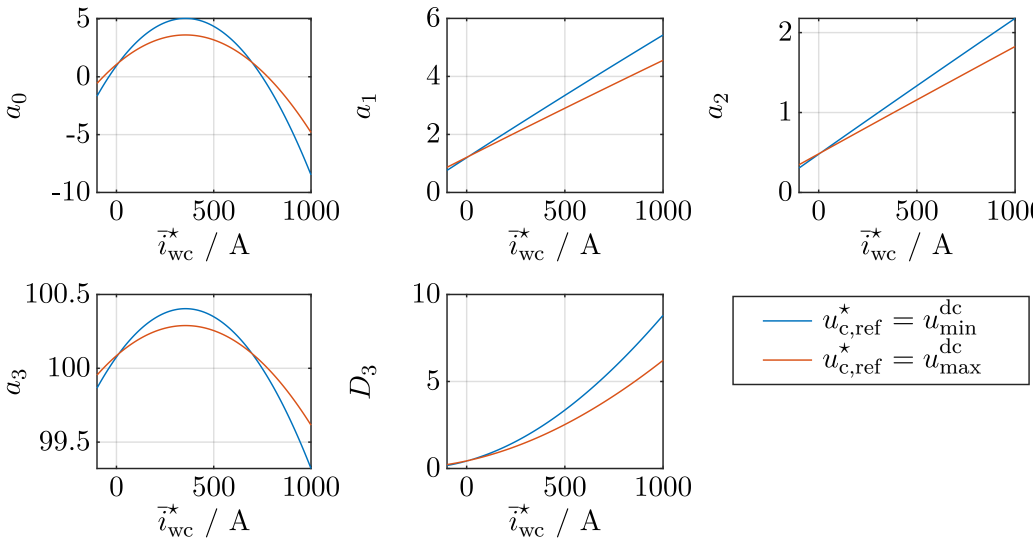

Figure 3.28: Numerical stability analysis of the coefficients a_0, a_1, a_2, a_3 and determinant D_3 over the input operational current $\vec{i}^{\star}_{\mathrm{wc}}$ for two different reference voltages $u^{\star}_{\mathrm{c,ref}} = u^{\mathrm{dc}}_{\mathrm{min}}$ [—] and $u^{\star}_{\mathrm{c,ref}} = u^{\mathrm{dc}}_{\mathrm{max}}$ [—].

generated current $i^{\mathrm{dc}}_{\mathrm{wc}}$ and the power p_{wc} of the generator units are used as input data for the simulation.

Fig. 3.29 shows the results, with the input data in blue [—], the measured results in red [—], and the simulation results in yellow [—]. The first subplot shows the relative rod position h_{wc} to illustrate the movement of the point absorber. The next subplot shows the measured WEC current $i^{\mathrm{dc}}_{\mathrm{wc}}$ and the current $i^{\mathrm{dc}}_{\mathrm{es}}$ that flows into the DC/DC converter. The third subplot shows the fluctuating DC link voltage u^{dc}. The power p_{wc} of the generator units and the resulting smoothed power p_{es} are shown at the bottom.

At the time of the measurement, the wave height was around 1 m. The current peaks in $i^{\mathrm{dc}}_{\mathrm{wc}}$ of the generator units occur when the rod is moving upwards. This is where the most power is generated, as seen in the last subplot. In general, the shapes of the currents and the corresponding powers are very similar. This is due to the high capacitance, which leads to a minimal change in the DC link voltage u^{dc} and, therefore, does not significantly influence the power. Thus, the power is mainly determined by the current. The measured smoothed power p_{es} fluctuates slightly more than the simulated power. This is mainly due to parameter uncertainties and noise.

The DC link voltage u^{dc} can be reproduced very well by the simulation. The average voltage is approximately the targeted 350 V, achieved by the restoring current i_{res}, as defined in (3.102). Voltage peaks can also be observed in the DC link voltage, corresponding to the generated power peaks. Each wave causes a high current flow into the supercapacitor bank, which leads to a corresponding voltage at the ESR of the capacitors that causes these voltage peaks. Therefore, its modelling is essential to calculate the reference voltage correctly.

Disregarding these voltage peaks, it can be seen that there are grouped time intervals where more energy is generated than in others. This results from the tendency of larger waves to group, which is called wave groupiness [13, Sec. 3.3.4], [262]. This can also be recognised in the lifting rod movement. Thus, power smoothing must not only smooth the power between two waves but also over these sets of waves for a longer period.

As seen in the last subplot, the resulting power p_{es} into the energy storage system is well

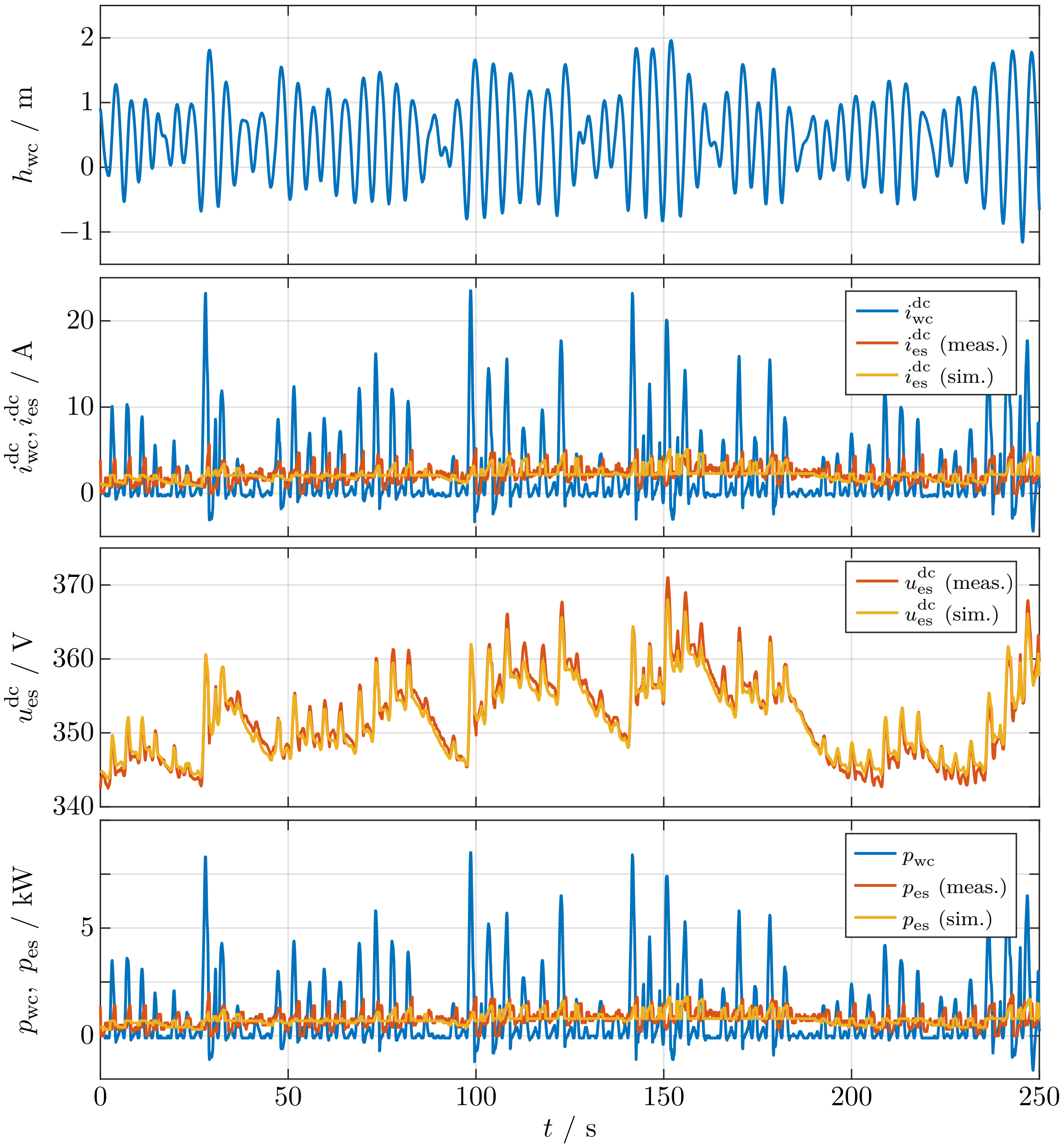

Figure 3.29: Comparison of the measured [—] and simulated [—] quantities of the DC link control, with the rod position h at the top, followed by the current $i_{\mathrm{wc}}^{\mathrm{dc}}$ and the smoothed current $i_{\mathrm{es}}^{\mathrm{dc}}$, the DC link voltage u^{dc} and the power of the generator units p_{wc} and the smoothed power p_{es}. The currents $i_{\mathrm{wc}}^{\mathrm{dc}}$ and the power of the generator units p_{wc} are used as inputs for the simulation [—].

smoothed, even over several wave groups. This confirms that the system parameters and the designed controller are correctly chosen and working well. This guarantees a longer battery lifetime. Furthermore, the simulation can reproduce the measured quantities well, validating the model.

3.3.3 Power Smoothing with a Controllable Short-Term Energy Storage Unit

As shown in the previous section, power smoothing is essential for effectively utilising wave energy. The disadvantage of the previous implementation is that the supercapacitors are connected directly to the DC link and, therefore, could not be utilised optimally. A more efficient approach is to connect the supercapacitors via the bidirectional DC/DC converter presented in Sec. 2.3. Specification (S4) stipulates that it should be possible for any ESS to be connected to the DC/DC converter. This makes the supercapacitor voltage u_{sc} independent of the DC link voltage, and its capacitance can be better utilised. Moreover, this approach can achieve better power smoothing as the power flow can be controlled directly.
The developed control strategy is presented using simulations. The measurement results above are consistent with the simulation results, which validates the model. Consequently, it can be assumed that the control system developed here will also work in practice.
Fig. 3.30 shows the supercapacitor module, which is in the same aluminium housing as the other power electronic devices so that it can be directly connected to the DC/DC converter. This creates a compact, waterproof and robust storage unit that can also be used in a harsh marine environment (Specification (S1)). It is also possible to connect several supercapacitor modules in series to the DC/DC converter to increase the power and energy capacity. On the right side of the figure is an example of a string with two supercapacitor modules.

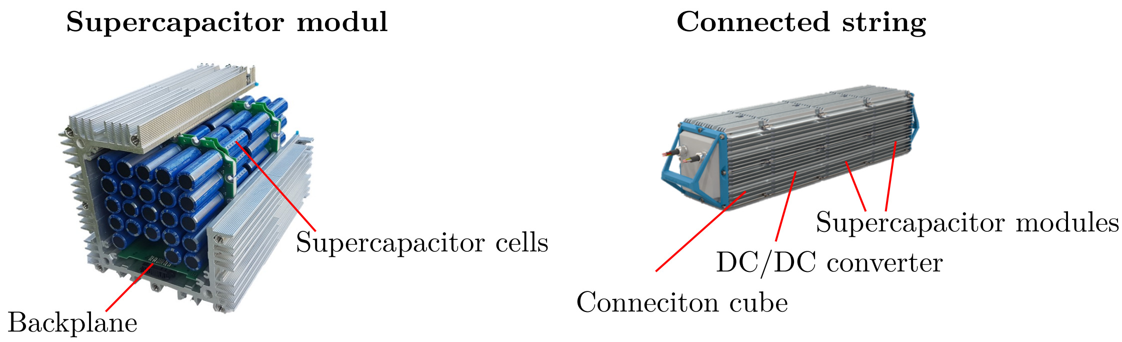

Figure 3.30: Photo of the supercapacitor module and the connected string with the DC/DC converter.

Power smoothing for wave energy converters with supercapacitors and DC/DC converters is also discussed in the literature. In [241–243], the supercapacitors are connected to the DC link via a bidirectional DC/DC converter. However, only one DC/DC converter with a supercapacitor bank is used in all cases. This means that standard voltage control of the DC/DC converter is sufficient to achieve power smoothing. Due to the modularity required here (Specification (S7)), connecting several DC/DC converters parallel to the common DC link must be possible.
The challenge of parallel-connected storage units in combination with distributed energy generation is often discussed for DC microgrid [169, 184]. Batteries are typically used there to ensure the microgrid's self-sufficiency. The microgrid should be controlled so that the stored energy is balanced between the distributed storage units to avoid a deep discharge or overcharging of one energy storage unit while maintaining the DC link voltage within the specified range. For this purpose, droop control with virtual resistance is used, as already presented in Sec. 3.1.2.

Droop control with virtual resistance mimics the behaviour of a real voltage source with an internal resistance by reducing the controlled output voltage proportionally to the current. Here, the DC/DC converter controls the DC link voltage $u_{\mathrm{ps}}^{\mathrm{dc}}$. Its output current $i_{\mathrm{ps}}^{\mathrm{dc}}$ on the DC link side is fed back via the virtual droop resistor R_{d} and subtracted from the reference voltage $u_{\mathrm{ps,ref}}^{\mathrm{dc}}$. By adjusting the droop resistance R_{d}, a compromise can be made between current sharing among the DC/DC converters and voltage tracking. For $R_{\mathrm{d}} = 0\ \Omega$, it results in classical voltage control without droop control, achieving good voltage tracking. Increasing the resistance R_{d} improves the current sharing between the DC/DC converters and deteriorates the voltage tracking.

In [184], fuzzy logic is used for a microgrid to adjust the virtual resistance to balance the stored energy and reduce the voltage deviation in the DC link. The fuzzy logic decides on the switch between different control strategies depending on the DC link voltage. A certain stationary voltage deviation always remains, as this contains information and is necessary for the decision-making process. This is implemented as a decentralised solution without the need for communication.

In [169], a good energy balance is achieved by adapting the virtual resistance through a central control system via communication. A double-layer hierarchical control strategy was proposed to manage the SoC of multiple batteries within the system. However, due to the centralised control, there is a single point of failure, and voltage control is not necessarily guaranteed.

For this case, balancing the stored energy among the supercapacitor modules is also desirable. When the supercapacitor units must be discharged, the storage unit with the most stored energy should deliver the most power. The same applies to charging, where the unit with the least energy should absorb the most. When the energy is balanced, it allows the available capacitance to be ideally utilised. It also ensures that the same power is available for all DC/DC converters. The power of the DC/DC converter is limited by the inductance current i_{l}, respectively, the current i_{sc} after the LC filter which flows into the supercapacitor unit. This means that the available power of the DC/DC converter depends mainly on the supercapacitor voltage u_{sc}, i.e. the SoE. If the SoE is always kept at a medium level, this also ensures that the DC/DC converters can absorb and deliver sufficient power.

The primary source of information should be the DC link voltage, which eliminates the necessity of a communication connection. Thus, a decentralised control approach can be pursued, and the system's modularity can be retained (Specification (S7)). Another complication is that a highly dynamic behaviour is required for power smoothing. To fulfil these requirements, a control strategy is designed that uses both droop methods, droop control with virtual resistance and droop control with characteristic droop curve, introduced in Sec. 3.1.2 and Sec. 3.1, respectively. The analysed system from Sec. 3.2 is extended by the supercapacitor units. These are connected directly to the WEC modules to position them as close as possible to the generation units. Thus, the already smoothed power is transmitted via the transmission line so that the power does not have to oscillate back and forth between the generation units and the grid inverter, minimising losses. Due to the very short connection between the generating units of the WEC and the supercapacitor units, the impedance between the modules is neglected. Fig. 3.31 shows the electrical circuit where the power smoothing units are included.

The droop control implemented for the grid inverters remains the same as discussed in Sec. 3.2, as does the derating function f_{ec} in (3.10), which reduces the power output of the generating units in case of overvoltage. If in this configuration, i.e. without the supercapacitor units, the generated power would fluctuate as shown in the previous section, the power p_{g} fed into the grid would fluctuate accordingly, given that the number of inverters corresponds to the power of the generating units. With power smoothing, the number of inverters can be reduced. Then, the installed inverter power must correspond to the maximum average generated power. With WECs, the difference between average and peak power is extremely significant, allowing massive

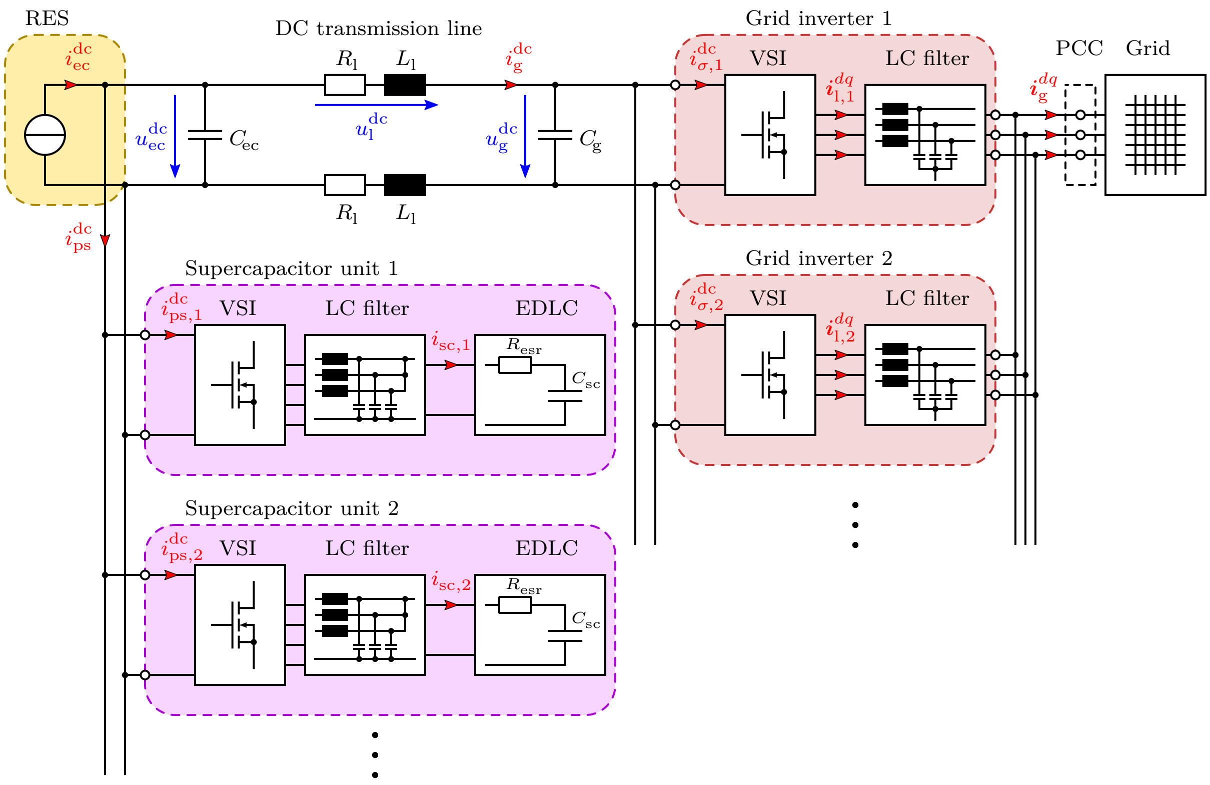

Figure 3.31: The electrical circuit of the power smoothing system.

material and cost savings. As the above results show, a factor of five or even more is expected. Assuming the power p_{g} flowing into the grid corresponds to the average generated power. Any fluctuation in the generated power causes then the DC link voltage to change. The rate of change in the voltage depends on the DC link capacitances C_{ec} and C_{g}. As those are very small, the voltage changes quickly. Therefore, to smooth the fluctuating power of the WEC, the DC/DC converters must control the voltage. Assuming the DC/DC converters could ideally control the DC link voltage, the fluctuating power of the WEC could be ideally smoothed out, and the average power generated flows to the inverters. Apart from the power losses, on average, no current flows into the supercapacitor units. But if, for example, the average generated power increases, the DC/DC converters compensate for this power difference accordingly due to the voltage control. This causes the SoE to rise steadily. To get the SoE back to the nominal value, the power of the grid inverters must be increased. As the inverter power increases linearly with the voltage according to the droop curve, the DC/DC converters can increase the voltage in the DC link via their reference voltage $u_{\mathrm{ps,ref}}^{\mathrm{dc}}$, thus increasing the power of the inverters. Hence, no communication system is required between the DC/DC converters and the grid inverters. The information can be transmitted solely via the DC link voltage.

Because the DC/DC converters must maintain a specific DC link voltage to control the grid inverter power, voltage control without control deviation is necessary. For this reason, the droop control with a characteristic droop curve cannot be implemented in the DC/DC converter, as it is basically a P-controller where a control deviation remains with this method. Therefore, a PI controller is implemented to control the DC link voltage.

However, ideal voltage control is impossible as several DC/DC converters must be connected in parallel. Fig. 3.32 shows the behaviour of two parallel-connected DC/DC converters without droop control, meaning $R_{\mathrm{d}} = 0\ \Omega$. The left-hand column shows the absolute ideal case. In the right-hand column, a tiny voltage measurement error was inserted for a DC/DC converter using an offset of 0.5 V. The subplots in the first row show the generated power p_{ec} [—], the total power p_{ps} [—] that flows into the DC/DC converters, and the power p_{g} [—] that flows into the grid inverter. The subplots in the second row show the DC link voltages $u^{\mathrm{dc}}_{\mathrm{ec}}$ [—] and $u^{\mathrm{dc}}_{\mathrm{g}}$ [—] on the RES side and the grid inverter side, respectively, and the reference voltage $u^{\mathrm{dc}}_{\mathrm{ps,ref}}$ [- - -] of the DC/DC converter. The subplots in the third row show the supercapacitor current $i_{\mathrm{sc},1/2}$ of both supercapacitor units, and the last subplots show the corresponding $\mathrm{SoE}_{1/2}$.

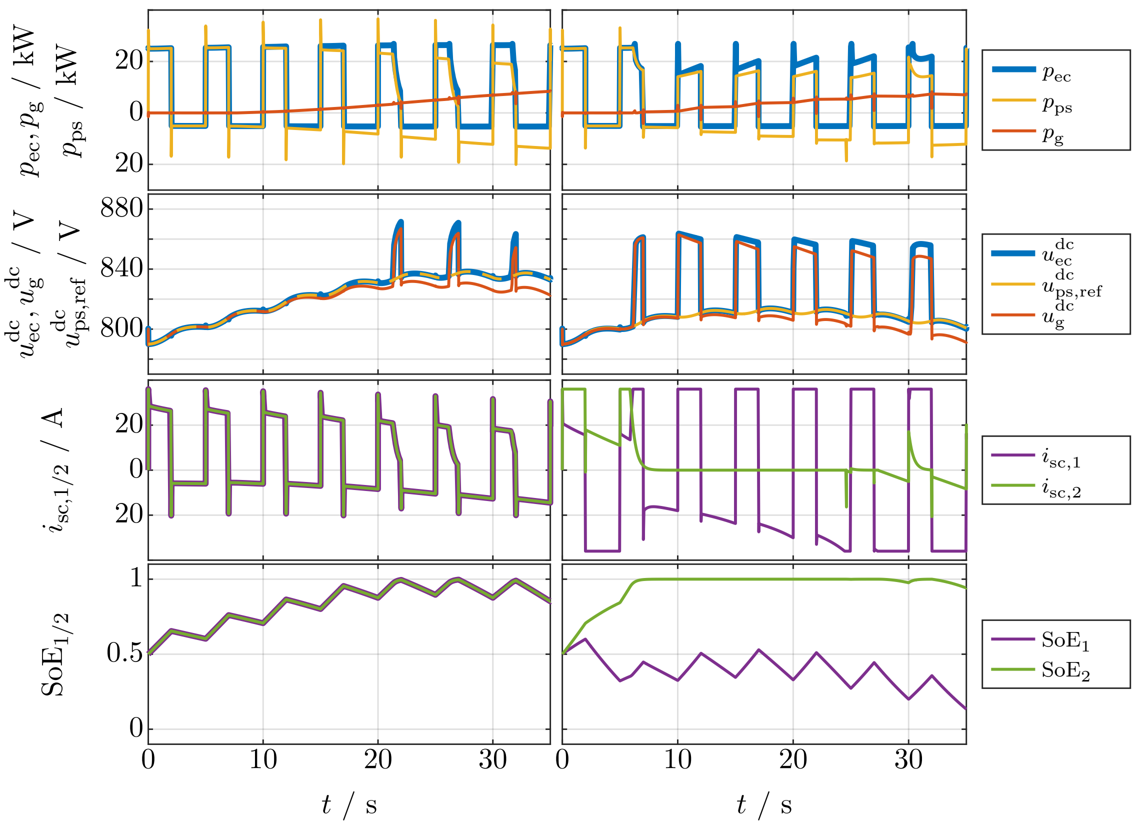

Figure 3.32: Comparison of voltage control with two parallel-connected DC/DC converters without droop control ($R_{\mathrm{d}} = 0\ \Omega$), with the ideal case shown in the left column and the case with measurement error shown in the right column. In the first two subplots, the quantities of the RES side are indicated with a blue line [—], the grid side with a red line [—], and those from the power smoothing units with a yellow line [—]. The two lower subplots refer to the two supercapacitors, with the quantities of the first unit in violet [—] and the second in green [—].

For the simulation, the generated power p_{ec} of the WEC is approximated with a square wave signal. The period is set to 5 s, corresponding to a typical sea state. It was further assumed that the WEC delivers its full power for 2 s. This is significantly more than is generated in reality but represents a more challenging case for the power smoothing system. For the rest of the period, it is assumed that the WEC consumes 20 % of the nominal power. This considers that reactive control is used for optimal control of the WEC (see Sec. 1.2.3).

In the ideal case in the left column, both DC/DC converters behave precisely the same. In the first 20 s, they ideally compensate for the fluctuation of the generated power p_{ec} and keep the DC link voltage at its reference value $u^{\mathrm{dc}}_{\mathrm{ps,ref}}$. As the inverter power increases with a delay due to the implemented low-pass filter of the droop controller, the SoE of both supercapacitor units increase. At around 21 s, the supercapacitors are fully charged so that the currents $i_{\mathrm{sc},1/2}$ must be reduced accordingly. This causes the DC link voltage to rise as the generated power is not drawn from either the DC/DC converters or the grid inverters. The voltage rises abruptly so that the generator units reduce their power following the derating function f_{ec}. This ensures that the voltage does not continue to rise and possibly destroy components.

However, the ideal case cannot be assumed. A tiny difference in the measured voltage already makes the control strategy no longer work. An actual line impedance or a slight measurement inaccuracy can cause that voltage difference. A measurement inaccuracy of the second DC/DC converter was simulated here by adding an offset of 0.5 V to the actual DC link voltage. As a result, the second DC/DC converter [—] initially draws more current from the DC link ($i_{\mathrm{sc}} > 0$ A) than the first [—]. Thereby, the voltage controller limits the current to the maximum current $i_{\mathrm{sc,max}}$. When the generated power p_{ec} becomes negative, the current directions of the two DC/DC converters are even opposite. This means a current flows from the second supercapacitor into the first, and energy oscillates from cycle to cycle. Consequently, SoE_1 and SoE_2 diverge. By the third pulse, the second supercapacitor is fully charged and can no longer draw current, which results in the first one having to take over voltage control on its own. However, as its power alone is insufficient to absorb the totally generated power, the generator units must derate their power for overvoltage protection.

The oscillating energy and premature derating lead to a massive loss of efficiency. What is worse, however, is that $\mathrm{SoE}_{1/2}$ drift apart and thus ultimately puts a power smoothing unit out of action. This shows that droop control is essential for power smoothing units connected in parallel.

Fig. 3.33 shows the simulation results with constant droop resistance $R_{\mathrm{d},1/2} = 1\ \Omega$. As before, an offset was simulated in the DC link voltage measurement for the second DC/DC converter. Additionally, SoE_1 is set to 50 %, and SoE_2 is set to 75 % to account for different initial conditions.

Due to the droop resistance R_{d}, the voltage can no longer be ideally controlled. A static control deviation remains, which depends on the current $i_{\mathrm{ps}}^{\mathrm{dc}}$ and droop resistance R_{d}. Consequently, every pulse of the generated power p_{ec} is also reflected in the DC link voltages $u_{\mathrm{ec}}^{\mathrm{dc}}$ and $u_{\mathrm{g}}^{\mathrm{dc}}$. As the grid inverters determine their power p_{g} via the DC link voltage $u_{\mathrm{g}}^{\mathrm{dc}}$ using the droop curve, the remaining fluctuations must be smoothed using the implemented low-pass filter with time constant τ_{d} (see Fig. 3.7).

However, despite the simulated measurement inaccuracy, the current sharing among the two DC/DC converters has improved significantly. The currents always have the same direction so that there is no more oscillating energy between the two supercapacitors. Since the droop resistance here is constant and identical for both DC/DC converters, the currents $i_{\mathrm{sc},1/2}$ are approximately equal. That causes the second supercapacitor to become fully charged earlier, and the DC/DC converter has to reduce the current accordingly. As a result, the DC link voltage rises, and the first DC/DC converter tries to compensate for this and increases its current until it reaches its capacity limit. It seems SoE_1 and SoE_2 equalise, but this is only due to the boundary. They drift apart as soon as the grid inverters feed more current into the grid, and the supercapacitors are discharged again.

To balance the stored energy among the supercapacitor modules, adjusting the droop resistance R_{d} as a function of SoE is necessary. Fig. 3.34 shows the block diagram of the implemented control system for power smoothing with adaptive droop resistance. The virtual droop resistance $R_{\mathrm{d},i}$ for the power smoothing unit i is calculated with

$$R_{\mathrm{d},i} \coloneqq f_{\mathrm{sat}}\left(R_{\mathrm{d,min}},\, R_{\mathrm{d,nom}} + \mathrm{sign}\left(i_{\mathrm{ps},i}^{\mathrm{dc}}\right) R_{\mathrm{soe}}\left(\mathrm{SoE}_i - \overline{\mathrm{SoE}}\right),\, R_{\mathrm{d,max}}\right) \tag{3.114}$$

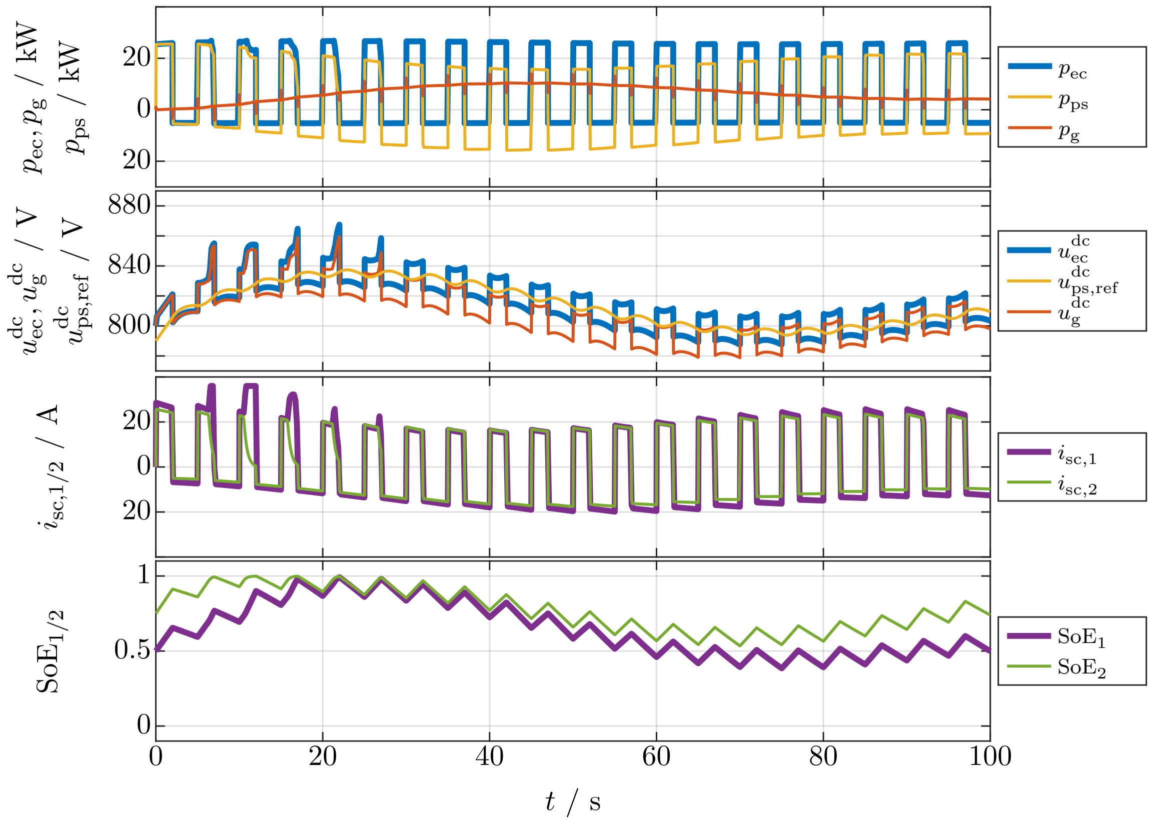

Figure 3.33: Simulation results with constant droop resistance $R_{d,1/2} = 1\ \Omega$. In the first two subplots, the quantities of the RES side are indicated with a blue line [—], the grid side with a red line [—], and those from the power smoothing units with a yellow line [—]. The two lower subplots refer to the two supercapacitors, with the quantities of the first unit in violet [—] and the second in green [—].

where the sign function and the saturation function f_{sat} according to (3.100) are used. The saturation ensures that the droop resistance remains within the minimum and maximum resistances $R_{d,min}$ and $R_{d,max}$ and does not become negative.
This relationship ensures that the supercapacitor unit with the lowest SoE draws the most power from the DC link when required and delivers the least power when discharging is needed. If the SoE_i corresponds to the overall average value given by

$$\overline{\mathrm{SoE}} = \frac{1}{N_{ps}} \sum_{i=1}^{N_{ps}} \mathrm{SoE}_i\,, \tag{3.115}$$

where N_{ps} is the number of power smoothing units, the droop resistance $R_{d,i}$ corresponds to its nominal value $R_{d,nom}$. For example, if SoE_i is below the average $\overline{\mathrm{SoE}}$ ($\mathrm{SoE}_i - \overline{\mathrm{SoE}} < 0$), this unit should reduce the droop resistance when charging, i.e. when $i^{dc}_{ps,i} > 0$ A, to draw more current than the others. The resistance should be increased accordingly when discharging is required.
The average state of energy $\overline{\mathrm{SoE}}$ is also used in the red box of Fig. 3.34 to control the reference DC link voltage $u^{dc}_{ps,ref}$ and, thus, the power p_g of the grid inverters. If $\overline{\mathrm{SoE}}$ exceeds the reference value $\mathrm{SoE}_{ref} = 0.5$, the DC link voltage should be increased to increase the grid inverters' power. A PI controller is also used for this purpose. The controller parameters were determined empirically based on the Ziegler-Nichols method (see [95, Sec. 9.4]) and improved through trial

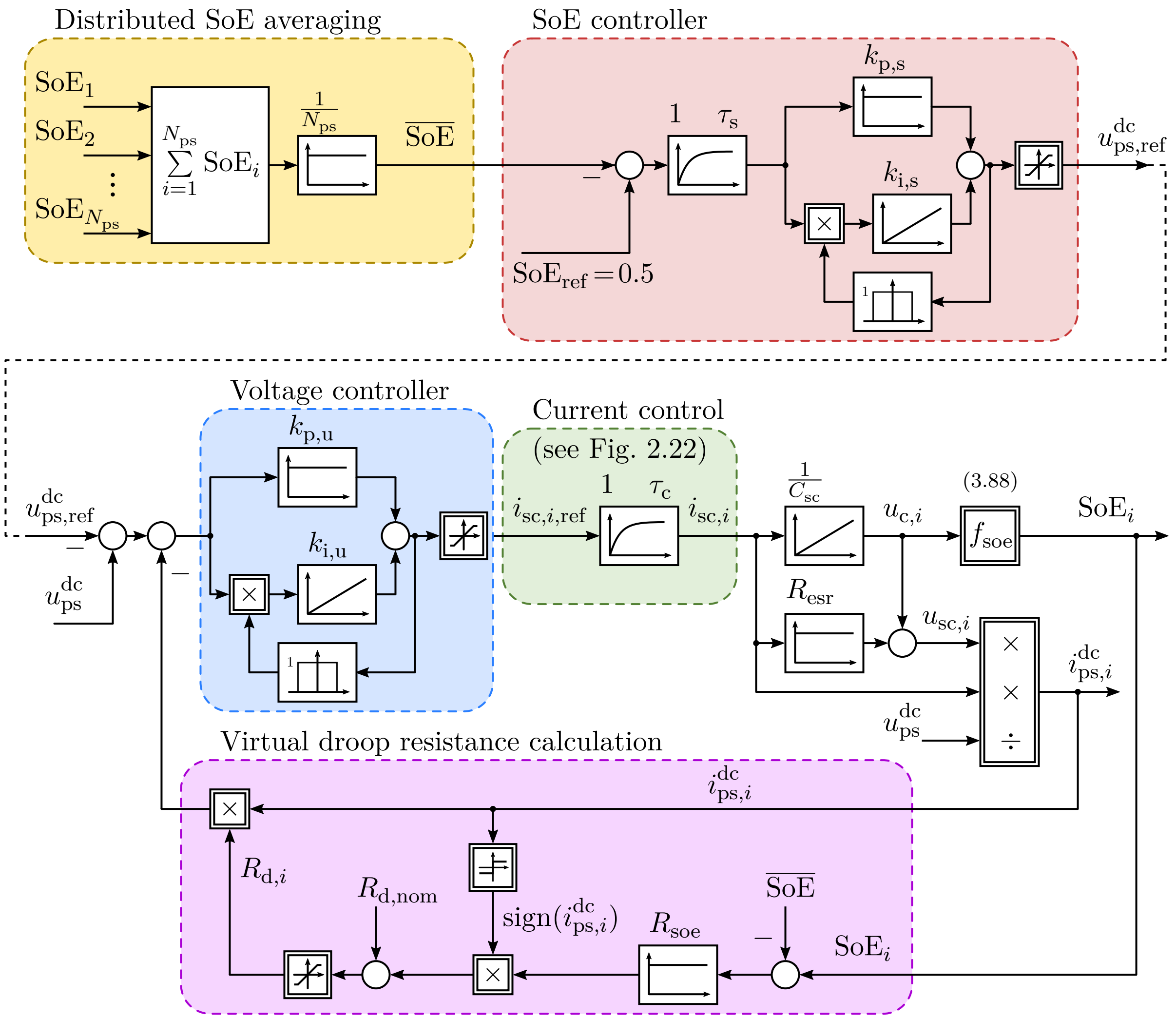

Figure 3.34: Block diagram of the droop control with virtual resistance R_{d} for the DC/DC converter with connected supercapacitor module and the SoE controller, which generates the reference voltage $u^{\mathrm{dc}}_{\mathrm{ps,ref}}$.

and error. An additional low-pass filter with a time constant τ_{s} was implemented to dampen the natural fluctuation of $\overline{\mathrm{SoE}}$. Like all other parts in Fig. 3.34, the SoE controller can be implemented decentrally on each DC/DC converter. It is only required that each DC/DC converter is aware of $\overline{\mathrm{SoE}}$.

The average state of energy $\overline{\mathrm{SoE}}$ is an important quantity in this system. Therefore, it must be available for every power smoothing unit. In this context, the need for a communication system becomes apparent, which is at the expense of the flexibility and reliability of the system. However, it only needs to be known to the DC/DC converters, not the grid inverters. The information, therefore, does not have to be transmitted over a long distance alongside the transmission line, which would be much more prone to errors. Moreover, the loss of information is not critical for the system. If the communication link fails, the worst-case scenario is described in Fig. 3.33. The DC/DC converters can detect the loss of communication and react accordingly, for example, by assuming an average state of energy $\overline{\mathrm{SoE}}$ of 0.5. This causes all SoE_i to converge to the assumed value. However, this means that voltage control and, thus, reference power control of the grid inverters no longer optimally work. It can, therefore, result in the generating units having to derate their power, which leads to energy losses and a reduction in overall efficiency. However, this should only be the case temporarily until the problem has been resolved.

Communication with the devices must generally be available for data analyses, software updates, and system monitoring. This can also be used to optimise the control system. A communication system can be tolerated if the messages do not have to be transmitted quickly and in real-time and if a failure does not become system-critical, as is the case here.

Nevertheless, so-called consensus algorithms [263] can be implemented to increase the system's robustness. Consensus algorithms aim to agree on a certain value within a group of agents by exchanging information via a communication system. It can be shown that there needs to be only one communication link to the respective neighbours of an agent to achieve a global consensus [263]. This means it is tolerable for a communication link between two agents to fail if at least one link remains. This prevents the entire system from reaching a standstill due to a single fault. Consensus algorithms for determining the average value of distributed states are presented in [264] and [265].

Fig. 3.35 shows the simulation results with adaptive droop resistance R_d and SoE control. The parameters used are listed in Tab. 3.2. The subplots are arranged as before, including an additional subplot at the bottom showing the two droop resistances $R_{\mathrm{d},1}$ and $R_{\mathrm{d},2}$. To illustrate the functional capability of the adaptive droop control, the initial values of SoE_1 [—] and SoE_2 [—] are set to 100 % and 0 %, respectively.

During the first four pulses of generated power p_ec, the second power smoothing unit [—] draws the maximum possible power during the charging process ($p_\mathrm{ec} > p_\mathrm{g}$) to rapidly increase the SoE_2. As the second power smoothing unit initially has an SoE_2 of 0 %, its power is minimal, which means that the generated power p_ec exceeds the available power of the DC/DC converters. Hence, the generating units must derate their power due to the resulting overvoltage. When discharging ($p_\mathrm{ec} < p_\mathrm{g}$), the second unit delivers no power, and the current $i_{\mathrm{sc},2}$ remains nearly zero so that the SoE_2 remains constant. The discharging power is provided entirely by the first power smoothing unit [—].

From the second pulse onwards, the first power smoothing unit can absorb power again, as the SoE_2 has dropped after the first discharge. However, due to the large divergence between SoE_1 and SoE_2, the charging current $i_{\mathrm{sc},1}$ is limited through the droop resistance $R_{\mathrm{d},1}$. During these first four pulses, the droop resistances alternate between the maximum and minimum resistance $R_{\mathrm{d,max}}$ and $R_{\mathrm{d,min}}$ due to the introduced dependence on the sign of the current $i_{\mathrm{ps},i}^{\mathrm{dc}}$. This results in the more fully charged supercapacitor being prioritised when discharging and the less charged supercapacitor being prioritised when charging, leading to the convergence of both states of energy after around 20 s. After that, both droop resistances $R_{\mathrm{d},1/2}$ remain at the nominal resistance $R_{\mathrm{d,nom}}$, ensuring ideal current sharing and identical behaviour of the power smoothing units.

The final simulation results of the proposed power smoothing control are shown in Fig. 3.36, where five parallel-connected power smoothing units are implemented. The scenario is selected as before, but the generated power p_ec is increased and the number N_g of grid inverters is set to five to match with the five power smoothing units. It is a coincidence that the number of inverters and power smoothing units are the same. Generally, the installed power of the grid inverters must match the generated average power. The power of the power smoothing units must match the generated peak power minus the generated average power.

The initial values of SoE_i are set to 0 %, 25 %, 50 %, 75 %, and 100 %, respectively, to illustrate their convergence as before. The behaviour is similar to the previous simulation, with two power smoothing units. The supercapacitors whose SoE is above average are prioritised when discharging, and the less charged supercapacitors are prioritised when charging.

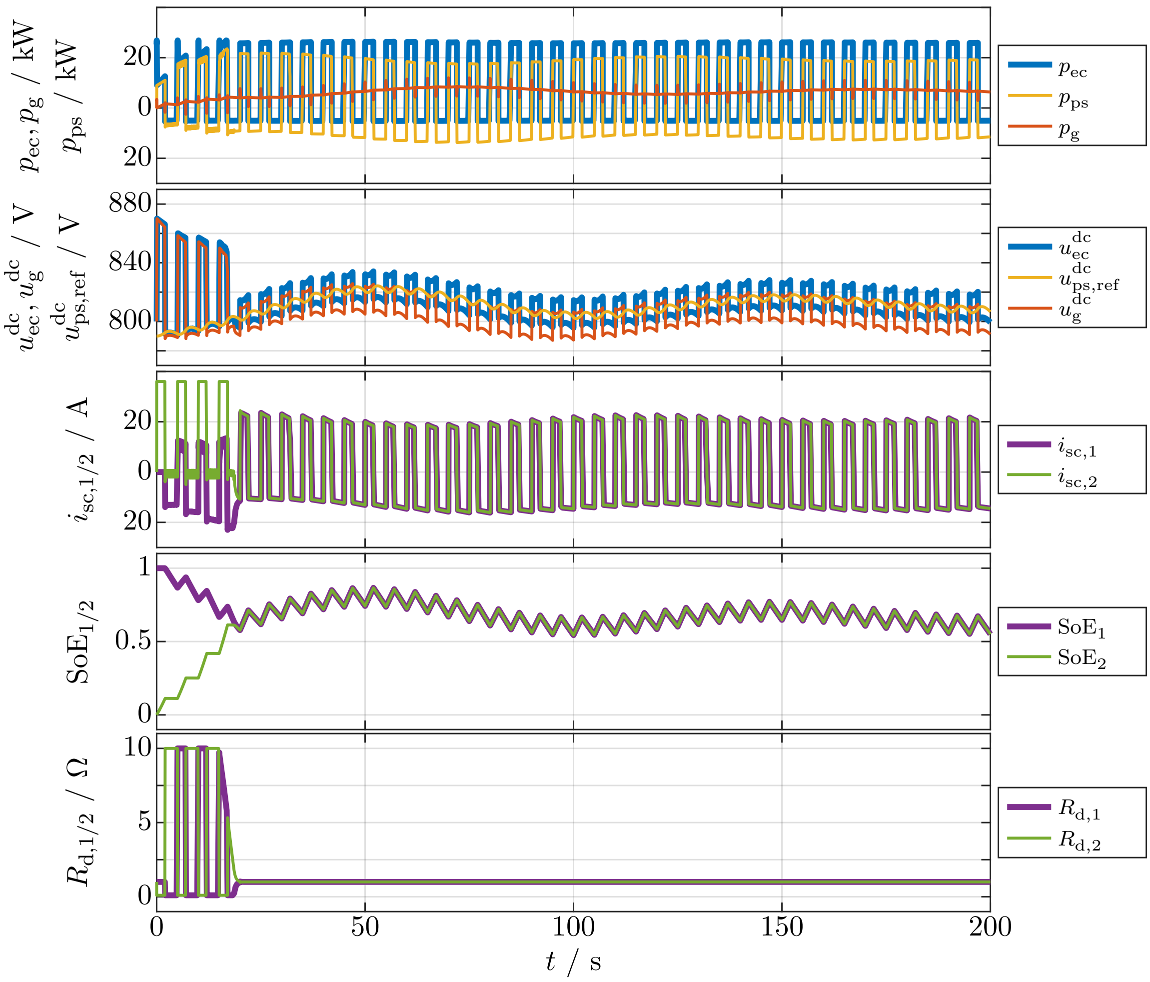

Figure 3.35: Simulation results with adaptive droop resistance R_d and SoE control. In the first two subplots, the quantities of the RES side are indicated with a blue line [—], the grid side with a red line [—], and those from the power smoothing units with a yellow line [—]. The three lower subplots refer to the two supercapacitors, with the quantities of the first unit in violet [—] and the second in green [—].

This results in the more fully charged supercapacitor being prioritised when discharging and the less charged supercapacitor being prioritised when charging. The further they deviate from the average, the more they are prioritised accordingly. This leads again to a convergence of all states of energy SoE_i at around 20 s. After that, all droop resistances $R_{d,i}$ retain the nominal resistance $R_{d,nom}$, and the behaviour of the power smoothing units are again identical.
Due to the large amount of data, only the first 50 s of the transient response are shown. Nevertheless, this is also the more interesting part, as the states of energy SoE_i converge here. After this, all five power smoothing units behave identically again, and the transient process continues similarly to that shown in Fig. 3.35.
This result shows that the proposed control algorithm works excellently with several power smoothing units and grid inverters connected in parallel. Thus, the modularity and flexibility of the overall system are guaranteed.

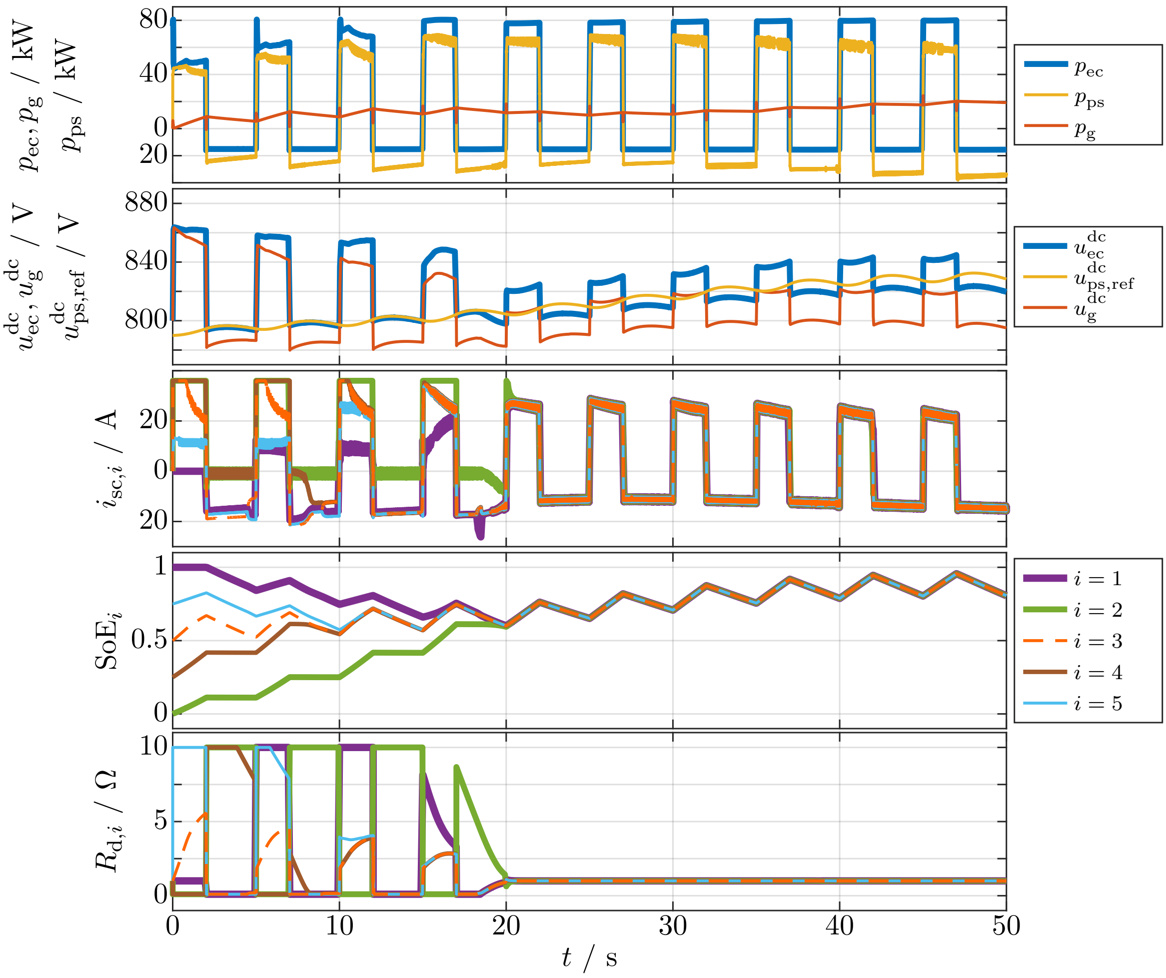

Figure 3.36: Simulation results of the proposed power smoothing control with five power smoothing units. In the first two subplots, the quantities of the RES side are indicated with a blue line [—], the grid side with a red line [—], and those from the power smoothing units with a yellow line [—]. The three lower subplots refer to the five supercapacitors units with index $i \in \{1, 2, \ldots, 5\}$.

Table 3.2: Control parameters of the power smoothing system associated with the simulation results shown in Fig. 3.35.

Unit	Name	Parameter	Value
Grid inverter	Number of grid inverter	N_{g}	2
	RMS grid voltage	U_{g}	230 V
	Nominal induction current	$i^{d}_{\mathrm{l,nom}}$	10.3 A
	Supply voltage 1	$u^{\mathrm{dc}}_{\mathrm{s,1}}$	770 V
	Supply voltage 2	$u^{\mathrm{dc}}_{\mathrm{s,2}}$	780 V
	Feed-in voltage 1	$u^{\mathrm{dc}}_{\mathrm{f,1}}$	800 V
	Feed-in voltage 2	$u^{\mathrm{dc}}_{\mathrm{f,2}}$	810 V
	Droop gain	K_{d}	$(10\ \mathrm{V})^{-1}$
	Low-pass filter time constant	τ_{d}	159.2 s
Renewable energy sources	Number of generating units	N_{ec}	8
	Derating voltage 1	$u^{\mathrm{dc}}_{\mathrm{c,1}}$	850 V
	Derating voltage 2	$u^{\mathrm{dc}}_{\mathrm{c,2}}$	880 V
DC link	Grid-side capacitance	C_{g}	1.62 mF
	RES-side capacitance	C_{ec}	8.1 mF
	Transmission line length	l_{l}	1000 m
	Transmission line resistance	R_{l}	0.51 Ω
	Specific transmission line inductance	L'_{l}	$1\ \frac{\mu\mathrm{H}}{\mathrm{m}}$
Power smoothing unit	Number of power smoothing units	N_{ps}	2
	Supercapacitor capacitance	C_{sc}	1.25 F
	Supercapacitor ESR	R_{esr}	1.32 Ω
	Maximum supercapacitor voltage	$u_{\mathrm{sc,max}}$	528 V
	Minimum supercapacitor voltage	$u_{\mathrm{sc,min}}$	200 V
	Usable supercapacitor energy	$\Delta E_{\mathrm{es,nom}}$	41.5 Wh
SoE controller	Proportional gain	$k_{\mathrm{p,s}}$	100 V
	Integral gain	$k_{\mathrm{i,s}}$	$0.2\ \frac{\mathrm{V}}{\mathrm{s}}$
	Low-pass filter time constant	τ_{s}	1.59 s
Voltage controller	Proportional gain	$k_{\mathrm{p,u}}$	$28.4\ \frac{\mathrm{A}}{\mathrm{V}}$
	Integral gain	$k_{\mathrm{i,u}}$	$0.57\ \frac{\mathrm{A}}{\mathrm{Vs}}$
	Maximum supercapacitor current	$i_{\mathrm{sc,max}}$	36 A
	Current control time constant	τ_{c}	0.14 ms
Droop resistance	Nominal droop resistance	$R_{\mathrm{d,nom}}$	1 Ω
	Minimum droop resistance	$R_{\mathrm{d,min}}$	0.1 Ω
	Maximum droop resistance	$R_{\mathrm{d,max}}$	10 Ω
	SoE droop resistance gain	R_{soe}	70 Ω

Chapter 4

Conclusion and Outlook

This thesis presented a complete power electronics system consisting of three power electronic devices, including all control strategies necessary for the grid connection of renewable energy sources, particularly a novel wave energy converter (WEC). The challenge was to create a stable system with these devices that could smooth the naturally fluctuating power of the WEC while maintaining a high degree of efficiency, modularity, and flexibility to achieve economies of scale more quickly.

A dynamic state-space model was introduced for all three power electronic devices, namely the DC/DC converter, the motor drive and the grid inverter. Based on these models, controllers were designed and implemented on a microcontroller and tested on industrial and commercially available hardware. The motor drive with the specially developed electrical machine constitutes the main component of the bidirectional direct drive power take-off (PTO) system of the WEC. The PTO system must be as efficient as possible. Any efficiency reduction in the PTO system disproportionately affects the overall efficiency of the WEC. To achieve maximum efficiency, a generic experimental identification method has been developed to determine the optimal current vectors leading to minimum losses and maximum efficiency, including iron and inverter losses.

The grid inverter is the interface to the public grid and must fulfil correspondingly high requirements, such as grid codes or electromagnetic compatibility (EMC). Another requirement was that the inverter had to match the high modularity of the overall system. It should, therefore, be possible to increase the installed power as required. A new topology has been developed to fulfil these requirements, allowing several grid inverters to be connected fully in parallel. This means they can be simultaneously connected on both the AC and DC sides. This unique feature offers exceptional modularity, redundancy, expandability and reliability for the overall system. The topology was explained in detail, and a corresponding model in the state-space representation was introduced. A PI state feedback controller was designed and tested to optimise the control and efficiency of the grid inverters.

The parallel connection of the grid inverters requires a control strategy that distributes the current evenly across all inverters and prevents circulating currents. A droop control was developed to ensure that these requirements are met. The general functioning of the control system was explained, and a stability analysis was carried out to confirm a stable operation. A parameter analysis was also conducted to determine optimisation potential and system limits.

Due to the natural movement of the waves, the WEC generates fluctuating power, which must first be smoothed before it can be fed into the grid. For this reason, a supercapacitor unit was integrated into the system. The supercapacitor unit was initially integrated passively into the DC link for the experimental test with the full-sized prototype of a WEC module. This allowed the system to be tested under typical sea conditions and the model to be validated.

Based on this, a power smoothing control was developed, in which the supercapacitors are connected to the DC link via the bidirectional DC/DC converter. This approach can achieve better power smoothing as the power flow can be controlled directly. A new droop control was proposed that enables optimum power smoothing, simultaneously ensuring energy balancing and avoiding energy oscillations among the distributed short-term storage units.

Future work should aim at validating and testing the proposed control strategies for power smoothing first at an experimental setup and then on an actual prototype of a WEC. Reactive control of the WEC should also be implemented on the generator units to maximise efficiency. This poses the challenge of working for natural irregular waves that are difficult to predict. Despite the extensive literature, there is still a need for research and optimisation regarding its implementation for an industrial system.

The experiments should provide a more detailed assessment of the actual requirements of the power smoothing system to further improve it and optimise its efficiency. For instance, the reference value of the supercapacitor's SoE can be set to higher values, which reduces the supercapacitor current and minimises losses. However, this is only possible if the currently prevailing sea state is considered, as sufficient capacity must still be reserved for power peaks. Furthermore, the SoE should also be varied to compensate for power fluctuations with more extended periods, such as those caused by wave groupiness, as discussed in Sec. 3.3.2. Information on the actual sea state must also be included here. The WEC control and the power smoothing system are thus further interlinked, which leads to interesting control engineering challenges.

Since developing this power electronics system, semiconductor devices have been further improved. New SiC-MOSFETs that have even higher voltage strength are now available. This allows a higher DC link voltage to be applied. The low voltage directive covers devices with a DC voltage of up to 1500 V [266], which can be fully utilised with the newer SiC-MOSFETs. This would make some aspects more complicated, such as the construction of the electrical machine and the design of the circuit boards. Still, it would have many more advantages that outweigh the disadvantages. Transmission line losses would be drastically reduced, allowing much greater distances to be bridged. The generating units, i.e. the electric machine and PV strings, could provide more voltage, increasing power and efficiency. The grid inverters could also be connected to AC grids with a higher RMS voltage, e.g. 800 V grids, which would also significantly increase their power. An increased DC link voltage could also help to counteract the problem of low inertia in the public grid, as described in Sec. 3.1.1. For this purpose, it would be advantageous to couple the droop controllers on the AC and DC sides (see Appendix A.7).

Bibliography

[1] S. Krüner and C. M. Hackl, "Experimental Identification of the Optimal Current Vectors for a Permanent-Magnet Synchronous Machine in Wave Energy Converters," *Energies*, vol. 12, no. 5, 2019.

[2] S. Krüner, Z. Song, and C. M. Hackl, "3D-Modulation and PI State-Feedback Control of Voltage Source Inverters with Split DC-Link," in *2021 IEEE 30th International Symposium on Industrial Electronics (ISIE)*, pp. 1–7, 2021.

[3] S. Krüner and C. M. Hackl, "Nonlinear Modelling and Control of a Power Smoothing System for a Novel Wave Energy Converter Prototype," *Sustainability*, vol. 14, no. 21, 2022.

[4] Z. Song, S. Krüner, and C. M. Hackl, "Modeling and Proportional-Integral State Feedback Control of Fully Parallel Grid-Connected Inverters," *IEEE Open Journal of the Industrial Electronics Society*, vol. 6, pp. 618–636, 2025.

[5] United Nations, "Transforming our world: the 2030 Agenda for Sustainable Development," 2015. Available online: https://sdgs.un.org/2030agenda. Accessed: 2022-11-06.

[6] United Nations, "The Ocean Conference - Factsheet," June 2017. Available online: https://www.un.org/sustainabledevelopment/wp-content/uploads/2017/05/Ocean-fact-sheet-package.pdf. Accessed: 2022-08-31.

[7] IRENA, "Innovation outlook: Ocean energy technologies," tech. rep., International Renewable Energy Agency, Abu Dhabi, 2020.

[8] G. Mørk, S. Barstow, A. Kabuth, and M. Teresa Pontes, "Assessing the Global Wave Energy Potential," in *29th International Conference on Ocean, Offshore Mechanics and Arctic Engineering*, vol. 3, June 2010.

[9] Q. Gao, B. Ding, N. Ertugrul, and Y. Li, "Impacts of mechanical energy storage on power generation in wave energy converters for future integration with offshore wind turbine," *Ocean Engineering*, vol. 261, p. 112136, 2022.

[10] United Nations, "Sustainable Development Goals." Available online: https://www.un.org-/sustainabledevelopment/. Accessed: 2022-11-06.

[11] U. Blum, E. Rosenthal, and B. Diekmann, *Energie – Grundlagen für Ingenieure und Naturwissenschaftler*. Springer Fachmedien Wiesbaden, 2020.

[12] A. F. de O. Falcão, "Wave energy utilization: A review of the technologies," *Renewable and Sustainable Energy Reviews*, vol. 14, no. 3, pp. 899–918, 2010.

[13] A. Pecher and J. Kofoed, *Handbook of Ocean Wave Energy*. Springer, Cham, 2017.

[14] M. Karimirad, *Offshore Energy Structures - For Wind Power, Wave Energy and Hybrid Marine Platforms.* Springer Cham Heidelberg New York Dordrecht London, 2014.

[15] B. G. Reguero, I. J. Losada, and F. J. Méndez, "A global wave power resource and its seasonal, interannual and long-term variability," *Applied Energy*, vol. 148, pp. 366–380, 2015.

[16] *A Global Wave Energy Resource Assessment*, vol. All Days of *International Ocean and Polar Engineering Conference*, July 2008. ISOPE-I-08-370.

[17] L. Rusu and F. Onea, "The performance of some state-of-the-art wave energy converters in locations with the worldwide highest wave power," *Renewable and Sustainable Energy Reviews*, vol. 75, pp. 1348–1362, 2017.

[18] K. Gunn and C. Stock-Williams, "Quantifying the global wave power resource," *Renewable Energy*, vol. 44, pp. 296–304, 2012.

[19] H. Ritchie, P. Rosado, and M. Roser, "Energy," *Our World in Data*, 2023. Available online: https://ourworldindata.org/energy. Accessed: 2024-11-05.

[20] J.-B. Eggers, M. Behnisch, J. Eisenlohr, H. Poglitsch, W.-F. Phung, M. Muenzinger, C. Ferrara, and T. Kuhn, "PV-Ausbauerfordernisse versus Gebäudepotenzial: Ergebnis einer gebäudescharfen Analyse für ganz Deutschland," in *35. PV-Symposium*, Sept. 2020.

[21] S. Astariz and G. Iglesias, "Output power smoothing and reduced downtime period by combined wind and wave energy farms," *Energy*, vol. 97, pp. 69–81, 2016.

[22] M. Veigas and G. Iglesias, "A Hybrid Wave-Wind Offshore Farm for an Island," *International Journal of Green Energy*, vol. 12, no. 6, pp. 570–576, 2015.

[23] I. Fairley, M. Lewis, B. Robertson, M. Hemer, I. Masters, J. Horrillo-Caraballo, H. Karunarathna, and D. E. Reeve, "A classification system for global wave energy resources based on multivariate clustering," *Applied Energy*, vol. 262, p. 114515, 2020.

[24] S. H. Salter, "Wave power," *Nature*, vol. 249, pp. 720–724, Jun 1974.

[25] A. F. Falcão and J. C. Henriques, "Oscillating-water-column wave energy converters and air turbines: A review," *Renewable Energy*, vol. 85, pp. 1391–1424, 2016.

[26] K. Budar and J. Falnes, "A resonant point absorber of ocean-wave power," *Nature*, vol. 256, pp. 478–479, Aug 1975.

[27] C. Hackl, C. Dirscherl, and K. Schechner, "Modellierung und Regelung von Windkraftanlagen (see https://arxiv.org/abs/1703.08661 for the English translation)," in *Elektrische Antriebe – Regelung von Antriebssystemen* (D. Schröder, ed.), ch. 10.3, pp. 1504–1585, Springer-Verlag, 2021.

[28] D. V. Evans, "A theory for wave-power absorption by oscillating bodies," *Journal of Fluid Mechanics*, vol. 77, no. 1, p. 1–25, 1976.

[29] C. C. Mei, "Hydrodynamic principles of wave power extraction," *Philosophical Transactions of the Royal Society A: Mathematical, Physical and Engineering Sciences*, vol. 370, no. 1959, pp. 208–234, 2012.

[30] A. Babarit, "A database of capture width ratio of wave energy converters," *Renewable Energy*, vol. 80, pp. 610–628, 2015.

[31] M. Schmela, "SolarPower Europe: Global Market Outlook for Solar Power 2024-2028," tech. rep., SolarPower Europe, 2024.

[32] F. Z. Joyce Lee, "Global Wind Report 2024," tech. rep., GWEC - Global Wind Energy Council, Apr. 2024.

[33] IRENA, "Renewable Capacity Statistics 2022," tech. rep., International Renewable Energy Agency, Apr. 2022.

[34] Catapult, "Tidal Stream and Wave Energy Cost Reduction and Industrial Benefit," tech. rep., Catapult - Offshore Renewable Energy, May 2018.

[35] IEA, "Net Zero by 2050 - A Roadmap for the Global Energy Sector," tech. rep., International Energy Agency, 2021.

[36] IEA-OES, "Annual Report: An Overview of Ocean Energy Activities in 2021," tech. rep., IEA - Ocean Energy Systems, 2022.

[37] M. Schmela, "SolarPower Europe: Global Market Outlook for Solar Power 2022-2026," tech. rep., SolarPower Europe, 2022.

[38] IRENA, "Renewable Power Generation Costs in 2021," tech. rep., International Renewable Energy Agency, Abu Dhabi, 2022.

[39] IRENA, "Renewable Power Generation Costs in 2017," tech. rep., International Renewable Energy Agency, Abu Dhabi, 2018.

[40] D. Magagna, *Ocean Energy - Technology Development Report 2020.* Publications Office of the European Union, 2020. EUR 30509 EN.

[41] P. Sinn, *Vergleich einer neuartigen Wellenkraftwerkstechnologie mit existierenden Stromversorgungsmöglichkeiten an einem dezentralen Modellstandort.* Dissertation, Technische Universität München, München, 2016.

[42] R. Ahamed, K. McKee, and I. Howard, "Advancements of wave energy converters based on power take off (PTO) systems: A review," *Ocean Engineering*, vol. 204, p. 107248, 2020.

[43] J. Falnes, *Ocean Waves and Oscillating Systems: Linear Interactions Including Wave-Energy Extraction.* Cambridge University Press, 2002.

[44] E. Anderlini, D. I. M. Forehand, E. Bannon, and M. Abusara, "Reactive control of a wave energy converter using artificial neural networks," *International Journal of Marine Energy*, vol. 19, pp. 207 – 220, 2017.

[45] W. E. Cummins, "The Impulse Response Function and Ship Motions," in *Symposium on Ship Theory*, Citeseer, 1962.

[46] "WAMIT," 2021. Available online: https://www.wamit.com/. Accessed: 2023-01-03.

[47] "NEMOH," 2022. Available online: https://lheea.ec-nantes.fr/valorisation/logiciels-et-brevets/nemoh-presentation/. Accessed: 2023-01-03.

[48] W. Sheng, "Wave energy conversion and hydrodynamics modelling technologies: A review," *Renewable and Sustainable Energy Reviews*, vol. 109, pp. 482–498, 2019.

[49] A. Babarit and A. H. Clément, "Optimal Latching Control of a Wave Energy Device in Regular and Irregular Waves," *Applied Ocean Research*, vol. 28, pp. 77–91, Apr. 2006.

[50] D. I. M. Forehand, A. E. Kiprakis, A. J. Nambiar, and A. R. Wallace, "A Fully Coupled Wave-to-Wire Model of an Array of Wave Energy Converters," *IEEE Transactions on Sustainable Energy*, vol. 7, pp. 118–128, Jan 2016.

[51] P. Ricci, J. Lopez, M. Santos, J. L. Villate, P. Ruiz Minguela, F. Salcedo, and A. F. O. Falcão, "Control Strategies for a simple Point-Absorber Connected to a Hydraulic Power Take-off," in *8th European Wave and Tidal Energy Conference*, Jan. 2009.

[52] J. V. Ringwood, G. Bacelli, and F. Fusco, "Energy-Maximizing Control of Wave-Energy Converters: The Development of Control System Technology to Optimize Their Operation," *IEEE Control Systems Magazine*, vol. 34, pp. 30–55, Oct 2014.

[53] J. Hals, J. Falnes, and T. Moan, "A Comparison of Selected Strategies for Adaptive Control of Wave Energy Converters," *Journal of Offshore Mechanics and Arctic Engineering*, vol. 133, Mar. 2011. 031101.

[54] E. Ozkop and I. H. Altas, "Control, power and electrical components in wave energy conversion systems: A review of the technologies," *Renewable and Sustainable Energy Reviews*, vol. 67, pp. 106–115, 2017.

[55] A. Babarit, G. Duclos, and A. H. Clément, "Comparison of latching control strategies for a heaving wave energy device in random sea," *Applied Ocean Research*, vol. 26, no. 5, pp. 227–238, 2004.

[56] T. K. A. Brekken, "On Model Predictive Control for a point absorber Wave Energy Converter," in *2011 IEEE Trondheim PowerTech*, pp. 1–8, June 2011.

[57] J. Cretel, A. W. Lewis, G. Lightbody, and G. P. Thomas, "An Application of Model Predictive Control to a Wave Energy Point Absorber," *IFAC Proceedings Volumes*, vol. 43, no. 1, pp. 267–272, 2010. 1st IFAC Conference on Control Methodologies and Technology for Energy Efficiency.

[58] J. Falnes and J. Hals, "Heaving buoys, point absorbers and arrays," *Philosophical Transactions of the Royal Society A: Mathematical, Physical and Engineering Sciences*, vol. 370, no. 1959, pp. 246–277, 2012.

[59] A. Babarit and A. H. Clément, "Application of the Optimal Command Method to the Control of the SEAREV Wave Energy Converter: A study on the Influence of Time Constants on the Efficiency of the Latching Control," in *2009 European Control Conference (ECC)*, pp. 3737–3742, Aug 2009.

[60] R. Genest, F. Bonnefoy, A. H. Clément, and A. Babarit, "Effect of non-ideal power take-off on the energy absorption of a reactively controlled one degree of freedom wave energy converter," *Applied Ocean Research*, vol. 48, pp. 236–243, 2014.

[61] *Optimum Reactive Control and Control by Latching of a Wave-Absorbing Semisubmerged Heaving Sphere*, vol. 21st International Conference on Offshore Mechanics and Arctic Engineering, Volume 4 of *International Conference on Offshore Mechanics and Arctic Engineering*, June 2002.

[62] S. Jahdi, O. Alatise, R. Bonyadi, P. Alexakis, C. A. Fisher, J. A. O. Gonzalez, L. Ran, and P. Mawby, "An Analysis of the Switching Performance and Robustness of Power MOSFETs Body Diodes: A Technology Evaluation," *IEEE Transactions on Power Electronics*, vol. 30, pp. 2383–2394, May 2015.

[63] R. W. Erickson and D. Maksimović, *Fundamentals of Power Electronics.* Springer Nature Switzerland AG, third edition ed., 2020.

[64] R. Teodorescu, M. Liserre, and P. Rodríguez, *Grid Converters for Photovoltaic and Wind Power Systems.* John Wiley & Sons, Ltd, 2011.

[65] J. Wang, J. Li, X. Zhou, T. Zhao, A. Q. Huang, R. Callanan, F. Husna, and A. Agarwal, "10 kV SiC MOSFET Based Boost Converter," in *2008 IEEE Industry Applications Society Annual Meeting*, pp. 1–6, Oct 2008.

[66] A. Q. Huang, Q. Zhu, L. Wang, and L. Zhang, "15 kV SiC MOSFET: An enabling technology for medium voltage solid state transformers," *CPSS Transactions on Power Electronics and Applications*, vol. 2, no. 2, pp. 118–130, 2017.

[67] P. Landsmann, *Sensorless Control of Synchronous Machines by Linear Approximation of Oversampled Current.* PhD thesis, Fakultät für Elektrotechnik und Informationstechnik, Technischen Universität München, 2014.

[68] J. Richter, *Modellbildung, Parameteridentifikation und Regelung hoch ausgenutzter Synchronmaschinen.* PhD thesis, Karlsruher Institut für Technologie (KIT), 2016.

[69] S. Yang, D. Xiang, A. Bryant, P. Mawby, L. Ran, and P. Tavner, "Condition Monitoring for Device Reliability in Power Electronic Converters: A Review," *IEEE Transactions on Power Electronics*, vol. 25, pp. 2734–2752, Nov 2010.

[70] Rubycon, *Radial Lead Aluminum Electrolytic Capacitors.* Datasheet. Available online: https://www.rubycon.co.jp/wp-content/uploads/catalog-aluminum/BXW.pdf. Accessed: 2023-11-01.

[71] Nichicon, *Aluminum Electrolytic Capacitors.* Datasheet. Available online: https://www.nichicon.co.jp/english/series_items/catalog_pdf/e-ucp.pdf. Accessed: 2023-11-01.

[72] NICHICON CORPORATION, *General Descriptions of Aluminum Electrolytic Capacitors*, 2022. Available online: https://www.nichicon.co.jp/english/products/pdf/aluminum.pdf. Accessed: 2023-11-01.

[73] A. Albertsen, "Electrolytic Capacitor Lifetime Estimation," *Bodos Power Magazine*, pp. 52–54, Apr. 2010.

[74] S. G. Parler, "Deriving Life Multipliers for Electrolytic Capacitors," in *IEEE Power Electronics Society Newsletter*, vol. Vol. 16, pp. pp. 11–12, Feb. 2004.

[75] TDK Electronics AG, *Aluminum Electrolytic Capacitors – General technical information*, Aug. 2022. Available online: https://www.tdk-electronics.tdk.com/download/185386/6ad5ed9e1ff4f727c328cb92da2adf2b/pdf-generaltechnicalinformation.pdf. Accessed: 2023-11-01.

[76] DIN EN IEC 61000-3-2: 2019-11, "Elektromagnetische Verträglichkeit (EMV) – Teil 3-2: Grenzwerte – Grenzwerte für Oberschwingungsströme," Standard, VDE Verband der Elektrotechnik Elektronik Informationstechnik e.V., 2019.

[77] DIN EN IEC 61000-6-3: 2022-06, "Elektromagnetische Verträglichkeit (EMV) – Teil 6-3: Fachgrundnormen – Störaussendung von Geräten in Wohnbereichen," Standard, VDE Verband der Elektrotechnik Elektronik Informationstechnik e.V., 2022.

[78] J. Lunze, *Regelungstechnik 2 – Mehrgrößensysteme, Digitale Regelung.* Springer Vieweg Berlin, Heidelberg, 10 ed., 2020.

[79] C. R. Paul, *Introduction to Electromagnetic Compatibility.* John Wiley & Sons, Inc., Hoboken, New Jersey., second edition ed., 2006.

[80] D. Schröder and J. Böcker, eds., *Elektrische Antriebe – Regelung von Antriebssystemen.* Springer Berlin Heidelberg, 2020.

[81] D. Schröder and R. Marquardt, *Leistungselektronische Schaltungen: Funktion, Auslegung und Anwendung.* Springer-Verlag GmbH, 2019. OCLC: 1089721583.

[82] A. Mora, J. Juliet, A. Santander, and P. Lezana, "Dead-Time and Semiconductor Voltage Drop Compensation for Cascaded H-Bridge Converters," *IEEE Transactions on Industrial Electronics*, vol. 63, pp. 7833–7842, Dec 2016.

[83] S. Bernet, *Selbstgeführte Stromrichter am Gleichspannungszwischenkreis: Funktion, Modulation und Regelung.* Springer-Verlag, 2012.

[84] C. M. Hackl, *Non-identifier based adaptive control in mechatronics: Theory and Application.* No. 466 in Lecture Notes in Control and Information Sciences, Berlin: Springer International Publishing, May 2017.

[85] E. Clarke, *Circuit analysis of AC power systems*, vol. 1. John Wiley & Sons Inc., 1950.

[86] K. Zhou and D. Wang, "Relationship Between Space-Vector Modulation and Three-Phase Carrier-Based PWM: A Comprehensive Analysis," *IEEE Transactions on Industrial Electronics*, vol. 49, pp. 186–196, Feb 2002.

[87] Z. Yu, "Space-Vector PWM With TMS320C24x/F24x Using Hardware and Software Determined Switching Patterns," tech. rep., Texas Instruments, 1999.

[88] F. Gustafsson, "Determining the Initial States in Forward-Backward Filtering," *IEEE Transactions on Signal Processing*, vol. 44, no. 4, pp. 988–992, 1996.

[89] Texas Instruments, *AMC1302 Precision, ±50-mV Input, Reinforced Isolated Amplifier*, 2021. Datasheet. Available online: https://www.ti.com/product/AMC1302. Accessed: 2023-11-01.

[90] C. P. Basso, *Switch-Mode Power Supplies - SPICE Simulations and Practical Designs.* McGraw-Hill Education, second ed., 2014.

[91] R. D. Middlebrook and S. Cuk, "A general unified approach to modelling switching-converter power stages," in *1976 IEEE Power Electronics Specialists Conference*, pp. 18–34, June 1976.

[92] M. G. Villalva, J. R. Gazoli, and E. R. Filho, "Comprehensive approach to modeling and simulation of photovoltaic arrays," *IEEE Transactions on Power Electronics*, vol. 24, pp. 1198–1208, May 2009.

[93] H. Lutz and W. Wendt, *Taschenbuch der Regelungstechnik mit MATLAB und Simulink*. Edition Harri Deutsch, Verlag Europa-Lehrmittel | Nourney, Vollmer GmbH & Co. KG, 2014.

[94] O. Föllinger, *Regelungstechnik | Einführung in die Methoden und ihre Anwendung*. VDE Verlag GmbH, 2016.

[95] J. Lunze, *Regelungstechnik 1 – Systemtheoretische Grundlagen, Analyse und Entwurf einschleifiger Regelungen*. Springer Vieweg Berlin, Heidelberg, 12 ed., 2020.

[96] Y. Peng, D. Vrancic, and R. Hanus, "Anti-windup, Bumpless, and Conditioned Transfer Techniques for PID Controllers," *IEEE Control Systems Magazine*, vol. 16, no. 4, pp. 48–57, 1996.

[97] A. Püschel, W. Winzig, and M. Theel, "Entwicklung der Globalstrahlung 1983 - 2020 in Deutschland," tech. rep., Deutscher Wetterdienst, 2022.

[98] H. Wirth, "Aktuelle Fakten zur Photovoltaik in Deutschland," tech. rep., Fraunhofer-Institut für Solare Energiesysteme ISE, Aug. 2022. Version from 12.8.2022.

[99] S. Philipps, "Photovoltaics Report," tech. rep., Fraunhofer-Institut für Solare Energiesysteme ISE, 2023.

[100] A. Einstein, "Über einen die Erzeugung und Verwandlung des Lichtes betreffenden heuristischen Gesichtspunkt," *Annalen der Physik*, vol. 322, no. 6, pp. 132–148, 1905.

[101] "The Nobel Prize in Physics 1921," 1921. Available online: https://www.nobelprize.org/prizes/physics/1921/summary/. Accessed: 2022-06-19.

[102] A. Wagner, *Photovoltaik Engineering: Handbuch für Planung, Entwicklung und Anwendung*, vol. 5 of *VDI-Buch*. Springer-Verlag GmbH, Dec. 2019.

[103] N. Femia, G. Petrone, G. Spagnuolo, and M. Vitelli, "Optimization of perturb and observe maximum power point tracking method," *IEEE Transactions on Power Electronics*, vol. 20, pp. 963–973, July 2005.

[104] K. Hussein, I. Muta, T. Hoshino, and M. Osakada, "Maximum photovoltaic power tracking: an algorithm for rapidly changing atmospheric conditions," *IEE Proceedings - Generation, Transmission and Distribution*, vol. 142, pp. 59–64(5), January 1995.

[105] W. Xiao, N. Ozog, and W. G. Dunford, "Topology study of photovoltaic interface for maximum power point tracking," *IEEE Transactions on Industrial Electronics*, vol. 54, pp. 1696–1704, June 2007.

[106] W. Xiao, W. G. Dunford, P. R. Palmer, and A. Capel, "Regulation of photovoltaic voltage," *IEEE Transactions on Industrial Electronics*, vol. 54, pp. 1365–1374, June 2007.

[107] L. Nousiainen, J. Puukko, A. Mäki, T. Messo, J. Huusari, J. Jokipii, J. Viinamäki, D. T. Lobera, S. Valkealahti, and T. Suntio, "Photovoltaic generator as an input source for power electronic converters," *IEEE Transactions on Power Electronics*, vol. 28, pp. 3028–3038, June 2013.

[108] J. Richter, A. Dollinger, and M. Doppelbauer, "Iron loss and parameter measurement of permanent magnet synchronous machines," in *2014 International Conference on Electrical Machines (ICEM)*, pp. 1635–1641, Sept 2014.

[109] L. Xu and J. Yao, "A Compensated Vector Control Scheme of a Synchronous Reluctance Motor Including Saturation and Iron Losses," *IEEE Transactions on Industry Applications*, vol. 28, pp. 1330–1338, Nov 1992.

[110] C. M. Hackl, J. Kullick, and N. Monzen, "Generic loss minimization for nonlinear synchronous machines by analytical computation of optimal reference currents considering copper and iron losses," in *2021 IEEE International Conference on Industrial Technology (ICIT)*, Institute of Electrical and Electronics Engineers (IEEE), Jan. 2021. (accepted for publication; Special Session "Electric drives for electrical mobility and green energy ").

[111] H. Eldeeb, C. M. Hackl, L. Horlbeck, and J. Kullick, "A unified theory for optimal feedforward torque control of anisotropic synchronous machines," *International Journal of Control*, vol. 91, no. 10, pp. 2273–2302, 2018.

[112] C. Hackl, M. Kamper, J. Kullick, and J. Mitchell, "Current control of reluctance synchronous machines with online adjustment of the controller parameters," in *2016 IEEE 25th International Symposium on Industrial Electronics (ISIE)*, pp. 153–160, June 2016.

[113] S.-W. Su, H. Börngen, C. M. Hackl, and R. Kennel, "Nonlinear Current Control of Reluctance Synchronous Machines With Analytical Flux Linkage Prototype Functions," *IEEE Open Journal of the Industrial Electronics Society*, vol. 3, pp. 582–593, 2022.

[114] G. Rang, J. Lim, K. Nam, H.-B. Ihm, and H.-G. Kim, "A MTPA control scheme for an IPM synchronous motor considering magnet flux variation caused by temperature," in *Nineteenth Annual IEEE Applied Power Electronics Conference and Exposition, 2004. APEC '04.*, vol. 3, pp. 1617–1621 Vol.3, Feb 2004.

[115] E. Armando, R. I. Bojoi, P. Guglielmi, G. Pellegrino, and M. Pastorelli, "Experimental Identification of the Magnetic Model of Synchronous Machines," *IEEE Transactions on Industry Applications*, vol. 49, pp. 2116–2125, Sept 2013.

[116] S. L. Kellner, M. Seilmeier, and B. Piepenbreier, "Impact of iron losses on parameter identification of permanent magnet synchronous machines," in *2011 1st International Electric Drives Production Conference*, pp. 11–16, Sept 2011.

[117] J. Kullick and C. M. Hackl, "Nonlinear modeling, identification and optimal feedforward torque control of induction machines using steady-state machine maps," *IEEE Transactions on Industrial Electronics*, pp. 1–1, 2022.

[118] ZVEI & Konsortium DC-INDUSTRIE2, "Systemkonzept DC-INDUSTRIE2," tech. rep., ZVEI e. V., 2022.

[119] S. Dasgupta, S. K. Sahoo, and S. K. Panda, "Single-Phase Inverter Control Techniques for Interfacing Renewable Energy Sources With Microgrid—Part I: Parallel-Connected Inverter Topology With Active and Reactive Power Flow Control Along With Grid Current Shaping," *IEEE Transactions on Power Electronics*, vol. 26, pp. 717–731, March 2011.

[120] X. Meng, Z. Liu, H. Zheng, and J. Liu, "A Universal Controller Under Different Operating States for Parallel Inverters With Seamless Transfer Capability," *IEEE Transactions on Power Electronics*, vol. 35, pp. 9794–9812, Sep. 2020.

[121] B. Wei, J. M. Guerrero, J. C. Vásquez, and X. Guo, “A Circulating-Current Suppression Method for Parallel-Connected Voltage-Source Inverters With Common DC and AC Buses,” *IEEE Transactions on Industry Applications*, vol. 53, pp. 3758–3769, July 2017.

[122] P. P. Das, S. Chattopadhayay, and M. Palmal, “A d–q Voltage Droop Control Method With Dynamically Phase-Shifted Phase-Locked Loop for Inverter Paralleling Without Any Communication Between Individual Inverters,” *IEEE Transactions on Industrial Electronics*, vol. 64, pp. 4591–4600, June 2017.

[123] H. Abu-Rub, J. Holtz, J. Rodriguez, and G. Baoming, “Medium-Voltage Multilevel Converters—State of the Art, Challenges, and Requirements in Industrial Applications,” *IEEE Transactions on Industrial Electronics*, vol. 57, pp. 2581–2596, Aug 2010.

[124] F. Rojas, R. Kennel, R. Cardenas, R. Repenning, J. C. Clare, and M. Diaz, “A New Space-Vector-Modulation Algorithm for a Three-Level Four-Leg NPC Inverter,” *IEEE Transactions on Energy Conversion*, vol. 32, pp. 23–35, March 2017.

[125] J. Zaragoza, J. Pou, S. Ceballos, E. Robles, C. Jaen, and M. Corbalan, “Voltage-Balance Compensator for a Carrier-Based Modulation in the Neutral-Point-Clamped Converter,” *IEEE Transactions on Industrial Electronics*, vol. 56, no. 2, pp. 305–314, 2009.

[126] C. Wang and Y. Li, “Analysis and Calculation of Zero-Sequence Voltage Considering Neutral-Point Potential Balancing in Three-Level NPC Converters,” *IEEE Transactions on Industrial Electronics*, vol. 57, no. 7, pp. 2262–2271, 2010.

[127] A. Nabae, I. Takahashi, and H. Akagi, “A New Neutral-Point-Clamped PWM Inverter,” *IEEE Transactions on Industry Applications*, vol. IA-17, pp. 518–523, Sep. 1981.

[128] O. Kalmbach, C. Dirscherl, and C. M. Hackl, “Discrete-Time DC-Link Voltage and Current Control of a Grid-Connected Inverter with LCL-Filter and Very Small DC-Link Capacitance,” *Energies*, vol. 13, p. 5613, Jan. 2020.

[129] S. L. Lorenzen, A. B. Nielsen, and L. Bede, “Control of A Grid Connected Converter During Weak Grid Conditions,” in *2016 IEEE 7th International Symposium on Power Electronics for Distributed Generation Systems (PEDG)*, pp. 1–6, 2016.

[130] S. Grunau and F. W. Fuchs, “Effect of Wind-Energy Power Injection into Weak Grids,” *European Wind Energy Conference and Exhibition 2012, EWEC 2012*, vol. 2, pp. 1150–1156, Jan. 2012.

[131] M. Liserre, F. Blaabjerg, and S. Hansen, “Design and control of an LCL-filter-based three-phase active rectifier,” *IEEE Transactions on Industry Applications*, vol. 41, no. 5, pp. 1281–1291, 2005.

[132] M. Liserre, A. Dell’Aquila, and F. Blaabjerg, “Genetic algorithm based design of the active damping for a LCL-filter three-phase active rectifier,” in *Eighteenth Annual IEEE Applied Power Electronics Conference and Exposition, 2003. APEC ’03.*, vol. 1, pp. 234–240 vol.1, 2003.

[133] R. Meyer and A. Mertens, “Design and Optimization of LCL Filters for Grid-Connected Converters,” in *2012 15th International Power Electronics and Motion Control Conference (EPE/PEMC)*, pp. LS7a.1–1–LS7a.1–6, 2012.

[134] R. Luhtala, T. Messo, T. Roinila, H. Alenius, E. de Jong, A. Burstein, and A. Fabian, "Identification of Three-Phase Grid Impedance in the Presence of Parallel Converters," *Energies*, vol. 12, no. 14, 2019.

[135] L. Jessen and F. W. Fuchs, "Modeling of Inverter Output Impedance for Stability Analysis in Combination with Measured Grid Impedances," in *2015 IEEE 6th International Symposium on Power Electronics for Distributed Generation Systems (PEDG)*, pp. 1–7, 2015.

[136] R. Luhtala, T. Roinila, and T. Messo, "Implementation of Real-Time Impedance-Based Stability Assessment of Grid-Connected Systems Using MIMO-Identification Techniques," *IEEE Transactions on Industry Applications*, vol. 54, no. 5, pp. 5054–5063, 2018.

[137] T. Messo, R. Luhtala, A. Aapro, and T. Roinila, "Accurate Impedance Model of a Grid-Connected Inverter for Small-Signal Stability Assessment in High-Impedance Grids," *IEEJ Journal of Industry Applications*, vol. 8, no. 3, pp. 488–496, 2019.

[138] N. Hoffmann and F. W. Fuchs, "Online Grid Impedance Estimation for the Control of Grid Connected Converters in Inductive-Resistive Distributed Power-Networks Using Extended Kalman-Filter," in *2012 IEEE Energy Conversion Congress and Exposition (ECCE)*, pp. 922–929, 2012.

[139] A. Knop and F. W. Fuchs, "High Frequency Grid Impedance Analysis by Current Injection," in *2009 35th Annual Conference of IEEE Industrial Electronics*, pp. 536–541, 2009.

[140] M. Sigle, W. Liu, and K. D. Karlsruhe, "On the Impedance of the Low-Voltage Distribution Grid At Frequencies Up to 500 kHz," in *2012 IEEE International Symposium on Power Line Communications and Its Applications*, pp. 30–34, 2012.

[141] S. Cobreces, E. Bueno, F. J. Rodriguez, F. Huerta, and P. Rodriguez, "Influence analysis of the effects of an inductive-resistive weak grid over L and LCL filter current hysteresis controllers," in *2007 European Conference on Power Electronics and Applications*, pp. 1–10, Sep. 2007.

[142] D. Yang, X. Ruan, and H. Wu, "Impedance Shaping of the Grid-Connected Inverter with LCL Filter to Improve Its Adaptability to the Weak Grid Condition," *IEEE Transactions on Power Electronics*, vol. 29, pp. 5795–5805, Nov 2014.

[143] N. Mohammed, M. Ciobotaru, and G. Town, "Online Parametric Estimation of Grid Impedance Under Unbalanced Grid Conditions," *Energies*, vol. 12, no. 24, 2019.

[144] M. Liserre, R. Teodorescu, and F. Blaabjerg, "Stability of Photovoltaic and Wind Turbine Grid-Connected Inverters for a Large Set of Grid Impedance Values," *IEEE Transactions on Power Electronics*, vol. 21, no. 1, pp. 263–272, 2006.

[145] N. P. W. Strachan and D. Jovcic, "Stability of a Variable-Speed Permanent Magnet Wind Generator With Weak AC Grids," *IEEE Transactions on Power Delivery*, vol. 25, no. 4, pp. 2779–2788, 2010.

[146] Y. Jiao and F. C. Lee, "LCL Filter Design and Inductor Current Ripple Analysis for a Three-Level NPC Grid Interface Converter," *IEEE Transactions on Power Electronics*, vol. 30, no. 9, pp. 4659–4668, 2015.

[147] J. Dannehl, M. Liserre, and F. W. Fuchs, "Filter-Based Active Damping of Voltage Source Converters With LCL Filter," *IEEE Transactions on Industrial Electronics*, vol. 58, no. 8, pp. 3623–3633, 2011.

[148] L. Ott, *Modellbasierte Stabilitätsuntersuchungen in Niederspannungs-DC-Verteilnetzen.* PhD thesis, Friedrich-Alexander Universität Erlangen-Nürnberg, 2019.

[149] R. Araneo, S. Lammens, M. Grossi, and S. Bertone, "EMC Issues in High-Power Grid-Connected Photovoltaic Plants," *IEEE Transactions on Electromagnetic Compatibility*, vol. 51, pp. 639–648, Aug 2009.

[150] Y. Sun, Y. Liu, M. Su, H. Han, X. Li, and X. Li, "Topology and Control of a Split-Capacitor Four-Wire Current Source Inverter With Leakage Current Suppression Capability," *IEEE Transactions on Power Electronics*, vol. 33, no. 12, pp. 10803–10814, 2018.

[151] Z. Lin, X. Ruan, L. Jia, W. Zhao, H. Liu, and P. Rao, "Optimized Design of the Neutral Inductor and Filter Inductors in Three-Phase Four-Wire Inverter With Split DC-Link Capacitors," *IEEE Transactions on Power Electronics*, vol. 34, no. 1, pp. 247–262, 2019.

[152] M. Dai, M. N. Marwali, J. Jung, and A. Keyhani, "A Three-Phase Four-Wire Inverter Control Technique for a Single Distributed Generation Unit in Island Mode," *IEEE Transactions on Power Electronics*, vol. 23, no. 1, pp. 322–331, 2008.

[153] T. Hornik and Q. Zhong, "Parallel PI Voltage - H∞ Current Controller for the Neutral Point of a Three-Phase Inverter," *IEEE Transactions on Industrial Electronics*, vol. 60, no. 4, pp. 1335–1343, 2013.

[154] Q.-C. Zhong, J. Liang, G. Weiss, C. M. Feng, and T. C. Green, "H^∞ Control of the Neutral Point in Four-Wire Three-Phase DC–AC Converters," *IEEE Transactions on Industrial Electronics*, vol. 53, no. 5, pp. 1594–1602, 2006.

[155] R. Zhang, D. Boroyevich, V. H. Prasad, H. . Mao, F. C. Lee, and S. Dubovsky, "A Three-Phase Inverter with A Neutral Leg with Space Vector Modulation," in *Proceedings of APEC 97 - Applied Power Electronics Conference*, vol. 2, pp. 857–863 vol.2, Feb 1997.

[156] L. Hadjidemetriou, E. Kyriakides, and F. Blaabjerg, "A New Hybrid PLL for Interconnecting Renewable Energy Systems to the Grid," *IEEE Transactions on Industry Applications*, vol. 49, pp. 2709–2719, Nov 2013.

[157] C. M. Hackl and M. Landerer, "A Unified Method for Generic Signal Parameter Estimation of Arbitrarily Distorted Single-Phase Grids With DC-Offset," *IEEE Open Journal of the Industrial Electronics Society*, vol. 1, pp. 235–246, 2020.

[158] G. Ludyk, *Theoretische Regelungstechnik 2.* Springer-Verlag, 1995.

[159] C. Dirscherl, J. Fessler, C. M. Hackl, and H. Ipach, "State-feedback controller and observer design for grid-connected voltage source power converters with LCL-filter," in *Proceedings of the 2015 IEEE International Conference on Control Applications (CCA 2015)*, (Sydney, Australia), pp. 215–222, Institute of Electrical and Electronics Engineers (IEEE), Sep 2015.

[160] G. Franklin, J. D. Powell, and M. L. Workman, *Digital Control of Dynamic Systems.* Ellis-Kagle Press, third edition ed., Nov. 1998.

[161] A. E. Bryson and Y.-C. Ho, *Applied Optimal Control: Optimization, Estimation and Control.* Routledge, may 1975.

[162] J. P. Hespanha, *Linear Systems Theory: Second Edition*. Princeton University Press, 2018.

[163] VDE – Verband der Elektrotechnik Elektronik Informationstechnik e.V., "Generators connected to the low-voltage distribution network - Technical requirements for the connection to and parallel operation with low-voltage distribution networks," *VDE-AR-N 4105 Anwendungsregel:2018-11*, 2018.

[164] Matlab, "dlqr," 2023. Available online: https://ch.mathworks.com/help/control/-ref/dlqr.html. Accessed: 2023-03-31.

[165] V. Mahendru, K. Hirose, T. Kaipia, W. de Kesel, G. Luber, R. Pelta, M. Jain, J. Peronnet, D. Goswami, and R. Sharma, "LVDC: electricity for the 21st century," tech. rep., International Electrotechnical Commission, Sept. 2017.

[166] a. W. P. o. Z. e. Open Direct Current Alliance, "ODCA," 2024. Available online: https://odca.zvei.org/. Accessed: 2024-09-01.

[167] J. M. Guerrero, J. C. Vasquez, J. Matas, L. G. de Vicuna, and M. Castilla, "Hierarchical Control of Droop-Controlled AC and DC Microgrids – A General Approach Toward Standardization," *IEEE Transactions on Industrial Electronics*, vol. 58, pp. 158–172, Jan 2011.

[168] D. Saha, N. Bazmohammadi, J. C. Vasquez, and J. M. Guerrero, "Multiple Microgrids: A Review of Architectures and Operation and Control Strategies," *Energies*, vol. 16, no. 2, 2023.

[169] T. Dragičević, J. M. Guerrero, J. C. Vasquez, and D. Škrlec, "Supervisory Control of an Adaptive-Droop Regulated DC Microgrid With Battery Management Capability," *IEEE Transactions on Power Electronics*, vol. 29, pp. 695–706, Feb 2014.

[170] H. Kakigano, Y. Miura, and T. Ise, "Distribution Voltage Control for DC Microgrids Using Fuzzy Control and Gain-Scheduling Technique," *IEEE Transactions on Power Electronics*, vol. 28, pp. 2246–2258, May 2013.

[171] V. Nasirian, A. Davoudi, F. L. Lewis, and J. M. Guerrero, "Distributed Adaptive Droop Control for DC Distribution Systems," *IEEE Transactions on Energy Conversion*, vol. 29, pp. 944–956, Dec 2014.

[172] R. Ryndzionek and L. Sienkiewicz, "Evolution of the HVDC Link Connecting Offshore Wind Farms to Onshore Power Systems," *Energies*, vol. 13, no. 8, 2020.

[173] P. Bresesti, W. L. Kling, R. L. Hendriks, and R. Vailati, "HVDC Connection of Offshore Wind Farms to the Transmission System," *IEEE Transactions on Energy Conversion*, vol. 22, pp. 37–43, March 2007.

[174] M. Barnes, D. Van Hertem, S. P. Teeuwsen, and M. Callavik, "HVDC Systems in Smart Grids," *Proceedings of the IEEE*, vol. 105, pp. 2082–2098, Nov 2017.

[175] J. M. Guerrero, J. Matas, L. Garcia de Vicuna, M. Castilla, and J. Miret, "Decentralized Control for Parallel Operation of Distributed Generation Inverters Using Resistive Output Impedance," *IEEE Transactions on Industrial Electronics*, vol. 54, pp. 994–1004, April 2007.

[176] E. Espina, J. Llanos, C. Burgos-Mellado, R. Cárdenas-Dobson, M. Martínez-Gómez, and D. Sáez, “Distributed Control Strategies for Microgrids: An Overview,” *IEEE Access*, vol. 8, pp. 193412–193448, 2020.

[177] M. Noritake, K. Hirose, M. Yamasaki, T. Oosawa, and H. Mikami, “Evaluation Results of Power Supply to ICT Equipment using HVDC Distribution System,” in *Intelec 2010*, pp. 1–8, June 2010.

[178] A. Pratt, P. Kumar, and T. V. Aldridge, “Evaluation of 400V DC Distribution in Telco and Data Centers to Improve Energy Efficiency,” in *INTELEC 07 - 29th International Telecommunications Energy Conference*, pp. 32–39, Sep. 2007.

[179] L. Ott, Y. Han, B. Wunder, J. Kaiser, F. Fersterra, M. Schulz, and M. März, “An Advanced Voltage Droop Control Concept for Grid-Tied and Autonomous DC Microgrids,” in *2015 IEEE International Telecommunications Energy Conference (INTELEC)*, pp. 1–6, Oct 2015.

[180] BDEW – Bundesverband der Energie- und Wasserwirtschaft e.V., “50,2-Hertz-Problem: Allgemeine Informationen,” July 2012. Available online: https://www.bdew.de/energie/systemstabilitaetsverordnung/502hertzproblem/. Accessed: 2024-09-23.

[181] Bundesministerium für Justiz, “Verordnung zur Gewährleistung der technischen Sicherheit und Systemstabilität des Elektrizitätsversorgungsnetzes (Systemstabilitätsverordnung - SysStabV),” July 2012. Available online: https://www.gesetze-im-internet.de/sysstabv/BJNR163510012.html. Accessed: 2024-09-23.

[182] VDE – Verband der Elektrotechnik Elektronik Informationstechnik e.V., “Verhalten bei Über-/Unterfrequenz,” Sept. 2011. Available online: https://www.vde.com/de/fnn/arbeitsgebiete/sicherer-betrieb-dez/ueber-und-unterfrequenz. Accessed: 2023-06-24.

[183] J. M. Guerrero, L. G. de Vicuna, J. Matas, M. Castilla, and J. Miret, “A Wireless Controller to Enhance Dynamic Performance of Parallel Inverters in Distributed Generation Systems,” *IEEE Transactions on Power Electronics*, vol. 19, pp. 1205–1213, Sep. 2004.

[184] N. L. Diaz, T. Dragicevic, J. C. Vasquez, and J. M. Guerrero, “Intelligent Distributed Generation and Storage Units for DC Microgrids – A New Concept on Cooperative Control Without Communications Beyond Droop Control,” *IEEE Transactions on Smart Grid*, vol. 5, pp. 2476–2485, 2014.

[185] Z. Shuai, S. Mo, J. Wang, Z. J. Shen, W. Tian, and Y. Feng, “Droop control method for load share and voltage regulation in high-voltage microgrids,” *Journal of Modern Power Systems and Clean Energy*, vol. 4, pp. 76–86, January 2016.

[186] M. Savaghebi, A. Jalilian, J. C. Vasquez, and J. M. Guerrero, “Secondary Control Scheme for Voltage Unbalance Compensation in an Islanded Droop-Controlled Microgrid,” *IEEE Transactions on Smart Grid*, vol. 3, pp. 797–807, June 2012.

[187] J. J. Grainger and W. D. Stevenson, *Power System Analysis*. McGraw-Hill, 1994.

[188] F. Milano, F. Dörfler, G. Hug, D. J. Hill, and G. Verbič, “Foundations and Challenges of Low-Inertia Systems,” in *2018 Power Systems Computation Conference (PSCC)*, pp. 1–25, June 2018.

[189] P. Tielens and D. Van Hertem, “The relevance of inertia in power systems,” *Renewable and Sustainable Energy Reviews*, vol. 55, pp. 999–1009, 2016.

[190] B. K. Poolla, D. Groß, and F. Dörfler, “Placement and Implementation of Grid-Forming and Grid-Following Virtual Inertia and Fast Frequency Response,” *IEEE Transactions on Power Systems*, vol. 34, pp. 3035–3046, July 2019.

[191] C. Arghir, T. Jouini, and F. Dörfler, “Grid-forming Control for Power Converters based on Matching of Synchronous Machines,” *Automatica*, vol. 95, pp. 273–282, 2018.

[192] C. Dirscherl, *Modeling and control of wind turbine systems with doubly-fed induction machines.* Dissertation, Technische Universität München, München, 2022.

[193] S. Muller, M. Deicke, and R. W. De Doncker, “Doubly fed induction generator systems for wind turbines,” *IEEE Industry Applications Magazine*, vol. 8, pp. 26–33, May 2002.

[194] European Commission and Joint Research Centre, T. Telsnig, A. Georgakaki, S. Letout, A. Kuokkanen, A. Mountraki, E. Ince, D. Shtjefni, G. Joanny Ordonez, O. Eulaerts, and M. Grabowska, *Clean Energy Technology Observatory, Wind energy in the European Union : status report on technology development, trends, value chains and markets : 2022.* Publications Office of the European Union, 2022.

[195] W. Cao, Y. Xie, and Z. Tan, “Wind Turbine Generator Technologies,” in *Advances in Wind Power* (R. Carriveau, ed.), ch. 7, Rijeka: IntechOpen, 2012.

[196] J. Morren, S. W. H. de Haan, W. L. Kling, and J. A. Ferreira, “Wind Turbines Emulating Inertia and Supporting Primary Frequency Control,” *IEEE Transactions on Power Systems*, vol. 21, pp. 433–434, Feb 2006.

[197] VDE – Verband der Elektrotechnik Elektronik Informationstechnik e.V., “Technical requirements for the connection and operation of customer installations to the medium voltage network,” *VDE-AR-N 4110 Anwendungsregel:2018-11*, 2018.

[198] H. Berndt, M. Hermann, H. D. Kreye, R. Reinisch, U. Scherer, and J. Vanzetta, “TransmissionCode 2007 – Netz- und Systemregeln der deutschen Übertragungsnetzbetreiber,” *Verband der Netzbetreiber – VDN – e.V. beim VDEW*, Aug. 2007.

[199] J. Rocabert, A. Luna, F. Blaabjerg, and P. Rodríguez, “Control of Power Converters in AC Microgrids,” *IEEE Transactions on Power Electronics*, vol. 27, pp. 4734–4749, Nov 2012.

[200] M. Chen, D. Zhou, A. Tayyebi, E. Prieto-Araujo, F. Dörfler, and F. Blaabjerg, “On Power Control of Grid-Forming Converters: Modeling, Controllability, and Full-State Feedback Design,” *IEEE Transactions on Sustainable Energy*, pp. 1–12, 2023.

[201] N. Mohammed and M. Ciobotaru, “Adaptive Power Control Strategy for Smart Droop-Based Grid-Connected Inverters,” *IEEE Transactions on Smart Grid*, vol. 13, pp. 2075–2085, May 2022.

[202] X. Meng, J. Liu, and Z. Liu, “A Generalized Droop Control for Grid-Supporting Inverter Based on Comparison Between Traditional Droop Control and Virtual Synchronous Generator Control,” *IEEE Transactions on Power Electronics*, vol. 34, pp. 5416–5438, June 2019.

[203] G. Delille, B. Francois, and G. Malarange, “Dynamic Frequency Control Support by Energy Storage to Reduce the Impact of Wind and Solar Generation on Isolated Power System’s Inertia,” *IEEE Transactions on Sustainable Energy*, vol. 3, pp. 931–939, Oct 2012.

[204] S. Golestan, M. Monfared, F. D. Freijedo, and J. M. Guerrero, “Performance Improvement of a Prefiltered Synchronous-Reference-Frame PLL by Using a PID-Type Loop Filter,” *IEEE Transactions on Industrial Electronics*, vol. 61, pp. 3469–3479, July 2014.

[205] Q.-C. Zhong and G. Weiss, “Synchronverters: Inverters That Mimic Synchronous Generators,” *IEEE Transactions on Industrial Electronics*, vol. 58, no. 4, pp. 1259–1267, 2011.

[206] Q.-C. Zhong, P.-L. Nguyen, Z. Ma, and W. Sheng, “Self-Synchronized Synchronverters: Inverters Without a Dedicated Synchronization Unit,” *IEEE Transactions on Power Electronics*, vol. 29, pp. 617–630, Feb 2014.

[207] J. Liu, Y. Miura, H. Bevrani, and T. Ise, “A Unified Modeling Method of Virtual Synchronous Generator for Multi-Operation-Mode Analyses,” *IEEE Journal of Emerging and Selected Topics in Power Electronics*, vol. 9, pp. 2394–2409, April 2021.

[208] S. D’Arco and J. A. Suul, “Equivalence of Virtual Synchronous Machines and Frequency-Droops for Converter-Based MicroGrids,” *IEEE Transactions on Smart Grid*, vol. 5, pp. 394–395, Jan 2014.

[209] L. Huang, H. Xin, Z. Wang, K. Wu, H. Wang, J. Hu, and C. Lu, “A Virtual Synchronous Control for Voltage-Source Converters Utilizing Dynamics of DC-Link Capacitor to Realize Self-Synchronization,” *IEEE Journal of Emerging and Selected Topics in Power Electronics*, vol. 5, pp. 1565–1577, Dec 2017.

[210] A. Tayyebi, A. Anta, and F. Dörfler, “Grid-Forming Hybrid Angle Control and Almost Global Stability of the DC-AC Power Converter,” *IEEE Transactions on Automatic Control*, pp. 1–16, 2022.

[211] X. Quan, A. Q. Huang, and H. Yu, “A Novel Order Reduced Synchronous Power Control for Grid-Forming Inverters,” *IEEE Transactions on Industrial Electronics*, vol. 67, pp. 10989–10995, Dec 2020.

[212] L. Zhang, L. Harnefors, and H.-P. Nee, “Power-Synchronization Control of Grid-Connected Voltage-Source Converters,” *IEEE Transactions on Power Systems*, vol. 25, pp. 809–820, May 2010.

[213] DIN EN 60038 (VDE 0175-1): 2012-04, “CENELEC – Normspannungen,” Standard, VDE Verband der Elektrotechnik Elektronik Informationstechnik e.V., 2012.

[214] K. Schechner, F. Bauer, and C. M. Hackl, “Nonlinear DC-link PI control for airborne wind energy systems during pumping mode,” in *Airborne Wind Energy: Advances in Technology Development and Research* (R. Schmehl, ed.), Springer Singapore, 2019.

[215] L. Ott, Y. Han, O. Stephani, J. Kaiser, B. Wunder, M. März, and K. Rykov, “Modelling and Measuring Complex Impedances of Power Electronic Converters for Stability Assessment of Low-Voltage DC-Grids,” in *2015 IEEE First International Conference on DC Microgrids (ICDCM)*, pp. 51–56, June 2015.

[216] M. Dzieia, H. Hübscher, D. Jagla, J. Klaue, H.-J. Petersen, and H. Wickert, *Elektronik Tabellen – Betriebs- und Automatisierungstechnik*. Westermann Berufliche Bildung, 2022.

[217] Littlefuse, "Fuseology – Design Guide," tech. rep., Littelfuse, Inc., 2022. Available online: https://m.littelfuse.com/~/media/electronics/product_catalogs/littelfuse_fuseology_selection_guide.pdf.pd. Accessed: 2023-12-17.

[218] K. Küpfmüller and G. Kohn, *Theoretische Elektrotechnik und Elektronik*. Springer Berlin Heidelberg, 1993.

[219] H. Wang, T. Saha, and R. Zane, "Impedance-Based Stability Analysis and Design Considerations for DC Current Distribution with Long Transmission Cable," in *2017 IEEE 18th Workshop on Control and Modeling for Power Electronics (COMPEL)*, pp. 1–8, July 2017.

[220] DIN VDE 0100-520, "Errichten von Niederspannungsanlagen – Auswahl und Errichtung elektrischer Betriebsmittel – Teil 520: Kabel- und Leitungsanlagen," Standard, VDE Verband der Elektrotechnik Elektronik Informationstechnik e.V., 2023.

[221] G. Ludyk, *Theoretische Regelungstechnik 1*. Springer-Verlag, 1995.

[222] Matlab, "rlocus," 2023. Available online: https://ch.mathworks.com/help/control/ref/dynamicsystem.rlocus.html. Accessed: 2023-05-20.

[223] M. Santos, F. Salcedo, D. B. Haim, J. L. Mendia, P. Ricci, J. Villate, J. Khan, D. Leon, S. Arabi, A. Moshref, G. Bhuyan, A. Blavette, D. O'Sullivan, and R. Alcorn, "INTEGRATING WAVE AND TIDAL CURRENT POWER: Case Studies Through Modelling and Simulation," Research Report Document No: T0331, International Energy Agency Implementing Agreement on Ocean Energy Systems, Mar 2011.

[224] A. Blavette, D. L. O'Sullivan, A. W. Lewis, and M. G. Egan, "Impact of a wave farm on its local grid: Voltage limits, flicker level and power fluctuations," in *2012 Oceans - Yeosu*, pp. 1–9, May 2012.

[225] D. B. Murray, M. G. Egan, J. G. Hayes, and D. L. O'Sullivan, "Applications of Supercapacitor Energy Storage for a Wave Energy Converter System," in *8th European Wave and Tidal Energy Conference*, 2009.

[226] M. Rahm, O. Svensson, C. Bostrom, R. Waters, and M. Leijon, "Experimental results from the operation of aggregated wave energy converters," *IET Renewable Power Generation*, vol. 6, pp. 149–160, May 2012.

[227] J. Sjolte, G. Tjensvoll, and M. Molinas, "Power Collection from Wave Energy Farms," *Applied Sciences*, vol. 3, no. 2, pp. 420–436, 2013.

[228] H. Bailey, B. Robertson, J. Ortiz, and B. Buckham, "Stochastic Methods to Predict WEC Array Power for Grid Integration," in *11th European Wave and Tidal Energy Conference*, 2015.

[229] *Study of the Smoothing Effect On the Power Production In an Array of SEAREV Wave Energy Converters*, vol. All Days of *International Ocean and Polar Engineering Conference*, July 2008.

[230] S.-A. Amamra and J. Marco, "Vehicle-to-Grid Aggregator to Support Power Grid and Reduce Electric Vehicle Charging Cost," *IEEE Access*, vol. 7, pp. 178528–178538, 2019.

[231] A. F. de O Falcão, "Control of an oscillating-water-column wave power plant for maximum energy production," *Applied Ocean Research*, vol. 24, no. 2, pp. 73 – 82, 2002.

[232] T. Yoshida, M. Sanada, S. Morimoto, and Y. Inoue, "Study of Flywheel Energy Storage System for Power Leveling of Wave Power Generation System," in *2012 15th International Conference on Electrical Machines and Systems (ICEMS)*, pp. 1–5, Oct 2012.

[233] Z. Zhou, M. Benbouzid, J. F. Charpentier, F. Scuiller, and T. Tang, "A review of energy storage technologies for marine current energy systems," *Renewable and Sustainable Energy Reviews*, vol. 18, pp. 390 – 400, 2013.

[234] O. K. D. Peter Kurzweil, *Elektrochemische Speicher – Superkondensatoren, Batterien, Elektrolyse-Wasserstoff, Rechtliche Rahmenbedingungen.* Springer Vieweg Wiesbaden, 2018.

[235] D. Linzen, S. Buller, E. Karden, and R. W. De Doncker, "Analysis and Evaluation of Charge-Balancing Circuits on Performance, Reliability, and Lifetime of Supercapacitor Systems," *IEEE Transactions on Industry Applications*, vol. 41, pp. 1135–1141, Sep. 2005.

[236] Y. Diab, P. Venet, and G. Rojat, "Comparison of the Different Circuits Used for Balancing the Voltage of Supercapacitors: Studying Performance and Lifetime of Supercapacitors," in *ESSCAP'06*, (Lausanne, Switzerland), p. on CD, Nov 2006.

[237] M. E. Glavin, P. K. W. Chan, S. Armstrong, and W. G. Hurley, "A stand-alone photovoltaic supercapacitor battery hybrid energy storage system," in *2008 13th International Power Electronics and Motion Control Conference*, pp. 1688–1695, Sep. 2008.

[238] C. Abbey and G. Joos, "Supercapacitor Energy Storage for Wind Energy Applications," *IEEE Transactions on Industry Applications*, vol. 43, pp. 769–776, May 2007.

[239] W. Li, G. Joos, and C. Abbey, "A Parallel Bidirectional DC/DC Converter Topology for Energy Storage Systems in Wind Applications," in *2007 IEEE Industry Applications Annual Meeting*, pp. 179–185, Sep. 2007.

[240] J. Aubry, P. Bydlowski, B. Multon, H. BEN AHMED, and B. Borgarino, "Energy Storage System Sizing for Smoothing Power Generation of Direct Wave Energy Converters," in *ICOE 2010*, (Bilbao, Spain), pp. ISBN 978–84–693–5467–4, October 2010.

[241] P. Moreno-Torres, M. Blanco, G. Navarro, and M. Lafoz, "Power Smoothing System for Wave Energy Converters by means of a Supercapacitor-Based Energy Storage System," in *17th European Conference on Power Electronics and Applications (EPE'15 ECCE-Europe)*, pp. 1–9, Sept 2015.

[242] Z. Nie, X. Xiao, P. Hiralal, X. Huang, R. McMahon, M. Zhang, and W. Yuan, "Designing and Testing Composite Energy Storage Systems for Regulating the Outputs of Linear Wave Energy Converters," *Energies*, vol. 10, no. 1, 2017.

[243] G. Rajapakse, S. Jayasinghe, A. Fleming, and M. Negnevitsky, "Grid Integration and Power Smoothing of an Oscillating Water Column Wave Energy Converter," *Energies*, vol. 11, no. 7, 2018.

[244] I. S. Michael Sterner, *Energiespeicher – Bedarf, Technologien, Integration.* Springer Vieweg Berlin, Heidelberg, 2017.

[245] Maxwell Technologies, *BC Series Ultracapacitors - BCAP0350.* Datasheet. Available online: https://maxwell.com/products/ultracapacitors/cells/. Accessed: 2023-11-01.

[246] A. Burke, “Ultracapacitors: why, how, and where is the technology,” *Journal of Power Sources*, vol. 91, no. 1, pp. 37 – 50, 2000.

[247] R. A. D. Lijun Gao and S. Liu, “Power Enhancement of an Actively Controlled Battery/Ultracapacitor Hybrid,” *IEEE Transactions on Power Electronics*, vol. 20, pp. 236–243, Jan 2005.

[248] H. Helmholtz, “Ueber einige Gesetze der Vertheilung elektrischer Ströme in körperlichen Leitern mit Anwendung auf die thierisch-elektrischen Versuche,” *Annalen der Physik*, vol. 165, no. 6, pp. 211–233, 1853.

[249] H. Bernstein, *Bauelemente der Elektronik.* Berlin, München, Boston: De Gruyter Oldenbourg, 2015.

[250] P. A. Tipler and G. Mosca, *Physik.* Springer Spektrum Berlin, Heidelberg, 2019.

[251] Eaton, “Supercapacitor selection guide,” tech. rep., Electronics Division, 2022. Available online: https://www.eaton.com/content/dam/eaton/products/electronic-components/resources/technical/eaton-supercapacitor-quick-selection-guide.pdf. Accessed: 2024-10-07.

[252] L. Zubieta and R. Bonert, “Characterization of double-layer capacitors for power electronics applications,” *IEEE Transactions on Industry Applications*, vol. 36, pp. 199–205, Jan 2000.

[253] L. Shi and M. L. Crow, “Comparison of Ultracapacitor Electric Circuit Models,” in *2008 IEEE Power and Energy Society General Meeting - Conversion and Delivery of Electrical Energy in the 21st Century*, pp. 1–6, July 2008.

[254] S. Fletcher, I. Kirkpatrick, R. Dring, R. Puttock, R. Thring, and S. Howroyd, “The modelling of carbon-based supercapacitors: Distributions of time constants and Pascal Equivalent Circuits,” *Journal of Power Sources*, vol. 345, pp. 247 – 253, 2017.

[255] M. Nikkhoo, E. Farjah, and T. Ghanbari, “A simple method for parameters identification of three branches model of supercapacitors,” in *2016 24th Iranian Conference on Electrical Engineering (ICEE)*, pp. 1586–1590, May 2016.

[256] P. Kurzweil, *Angewandte Elektrochemie – Grundlagen, Messtechnik, Elektroanalytik, Energiewandlung, technische Verfahren.* Springer Vieweg Wiesbaden, 2020.

[257] A. Kuperman, M. Mellincovsky, C. Lerman, I. Aharon, N. Reichbach, G. Geula, and R. Nakash, “Supercapacitor Sizing Based on Desired Power and Energy Performance,” *IEEE Transactions on Power Electronics*, vol. 29, pp. 5399–5405, Oct 2014.

[258] L. Ma, C. Hu, and F. Cheng, “State of Charge and State of Energy Estimation for Lithium-Ion Batteries Based on a Long Short-Term Memory Neural Network,” *Journal of Energy Storage*, vol. 37, p. 102440, 2021.

[259] N. Daratha, H. Polinder, and M. de Sousa Prado, “A first-order energy storage requirements estimation for an Archimedes Wave Swing Park,” in *2008 IEEE International Conference on Sustainable Energy Technologies*, pp. 1161–1165, Nov 2008.

[260] E. Wu and A. M. Knight, “Considerations for sizing energy storage technologies in wave energy systems,” in *2017 20th International Conference on Electrical Machines and Systems (ICEMS)*, pp. 1–6, Aug 2017.

[261] F. D. Domenico, A. Steiner, and J. Catly, “Design of a 600 W HB LLC Converter using 600 V CoolMOS^{TM} P6,” tech. rep., Infineon Technologies AG, 2015.

[262] J. H. List, “Wave groupiness variations in the nearshore,” *Coastal Engineering*, vol. 15, no. 5, pp. 475–496, 1991.

[263] R. Olfati-Saber, J. A. Fax, and R. M. Murray, “Consensus and Cooperation in Networked Multi-Agent Systems,” *Proceedings of the IEEE*, vol. 95, pp. 215–233, Jan 2007.

[264] L. Meng, T. Dragicevic, J. M. Guerrero, and J. C. Vasquez, “Dynamic Consensus Algorithm Based Distributed Global Efficiency Optimization of a Droop Controlled DC Microgrid,” in *2014 IEEE International Energy Conference (ENERGYCON)*, pp. 1276–1283, May 2014.

[265] V. Nasirian, S. Moayedi, A. Davoudi, and F. L. Lewis, “Distributed Cooperative Control of DC Microgrids,” *IEEE Transactions on Power Electronics*, vol. 30, pp. 2288–2303, April 2015.

[266] European Parliament, “DIRECTIVE 2014/35/EU OF THE EUROPEAN PARLIAMENT AND OF THE COUNCIL of 26 February 2014 on the harmonisation of the laws of the Member States relating to the making available on the market of electrical equipment designed for use within certain voltage limits,” *Official Journal of the European Union*, 2014. Available online: https://eur-lex.europa.eu/legal-content/EN/TXT/?uri=CELEX:32014L0035. Accessed: 2024-05-24.

[267] L. Papula, *Mathematik für Ingenieure und Naturwissenschaftler - Band 2*. Springer Fachmedien Wiesbaden, 2015.

[268] W. R. Evans, “Graphical Analysis of Control Systems,” *Transactions of the American Institute of Electrical Engineers*, vol. 67, pp. 547–551, Jan 1948.

List of Figures

1.1 The Global Goals or Sustainable Development Goals from the 2030 Agenda adopted by the United Nations in 2015, taken from [10]. 2
1.2 Classification of the global coastlines into six groups of wave energy potential, from low (class 1) to high energy (class 6), with corresponding mean H_s-T_w joint occurrence matrices. The figure is taken from [23] and slightly adapted. 5
1.3 Illustrations of the functioning principle of WECs for the three main categories. . 6
1.4 Globally installed capacity of PV [—] [31], onshore wind [—] [32], offshore wind [—] [32, 33] and wave [—] [7, 34–36] and the expected outlook in dashed lines. 7
1.5 Current LCOE and estimated LCOE reduction over the installed capacity (Figure is taken from [7]). 8
1.6 Globally weighted average LCOE of PV [—] [38], onshore wind [—] [38, 39] and offshore wind [—] [38]. 9
1.7 Rendering of the hybrid platform, equipped with wave energy converter, wind turbines and PV modules on the left and a picture of the prototype on the right. 10
1.8 Illustration of the functioning principle of the floating WEC. 10
1.9 Picture of the point absorber prototype in Crete on the left and a detailed picture of the PTO system on the right. 11
1.10 Overview of the modular power electronics system with all possible components and references to the corresponding section in this thesis. 15

2.1 Photo of the basic power electronics components and the modular housing. . . . 20
2.2 Block diagram of the three devices with the different variations of the star-point connection. 21
2.3 Electrical circuit of the basic power electronics with the split DC link capacitors and the six SiC-MOSFETs. 22
2.4 One half-bridge of the VSI with (a) the two MOSFETs, (b) the equivalent circuit of the MOSFETs and (c) the simplification of the half-bridge. 23
2.5 Exemplary current $i^\mathrm{dc}_\mathrm{c,h}$ through the capacitor of the grid inverter with a constant input DC current $i^\mathrm{dc} = 5$ A during ten switching periods T_sw. 24
2.6 Illustration of the (a) TO-247 package of the MOSFET, (b) creation of the parasitic capacitance, and (c) the simplified single-phase circuit with the differential- and common-mode interference. 27
2.7 Circuit of the examined three-phase two-level inverter topology with the six switching elements. 28
2.8 Example of a PWM for one half-bridge, where the switching state σ in the lower subplot is generated by comparison of the scaled reference voltage [—] with the carrier sawtooth signal [—]. 29

2.9 Voltage hexagon spanned by the six active voltage vectors in the (α,β)-plane, the reference voltages $\boldsymbol{u}^{abc}_{\mathrm{f,ref}}$ [—] in the sector $k_{\mathrm{s}} = 2$ composed by the adjacent switching vectors [—] and the voltage limits for PWM [- - -] and SVM [- - -]. 33
2.10 Block diagram of the space vector pulse width modulation (SVPWM). 34
2.11 Comparison of the filtered results of PWM in the upper subplot and SVM in the second subplot with the sum of all three voltages [—] and the same reference voltages [- - -], which results in the same line-to-line voltages $\boldsymbol{u}^{a\text{-}b\text{-}c}$, shown in the lower subplot. 35
2.12 Three-dimensional voltage space represented in an orthogonal projection onto the (α,β)-, (α,γ)- and (γ,β)-plane with the reference voltage vector $\boldsymbol{u}^{abc}_{\mathrm{ref}}$ [—] in the sector $k_{\mathrm{s}} = 2$ composed by the adjacent switching vectors [—]. 36
2.13 The electrical circuit of the current measurement with the reinforced isolated amplifier AMC1302. 38
2.14 Frequency response of the gain V_{amc} of the amplifier AMC1302 [89] with the discussed frequencies written on top corresponding to the dashed lines. 38
2.15 The top subplot shows the PWM carrier signal c_{pwm} [—] with a constant compare value c_{ref} [—] and the lower subplot shows an exemplary current i_{l} [—] and the amplifiers scaled output [—] as well as the typical trigger point [- - -] and the multiple sample points [×]. 39
2.16 Photo of the DC/DC converter without the housing. 40
2.17 The electrical circuit of the three-phase bidirectional synchronous buck converter. 40
2.18 The electrical circuit of one phase of the bidirectional synchronous buck converter with the illustration of the voltage measurement and a connected load resistance R_{sec}. 41
2.19 Frequency responses of the controller $G_{\mathrm{r,u}}(s)$ [—] and the transfer function $G_{\mathrm{dd,u}}(s)$ from (2.49) with $R_{\mathrm{sec}} = 10\ \Omega$ [—], $R_{\mathrm{sec}} = 50\ \Omega$ [—] and $R_{\mathrm{sec}} \to \infty\ \Omega$ [—]. The discussed frequencies are written on top corresponding to the dashed lines. 44
2.20 Frequency responses of the resulting open-loop $F_{\mathrm{o,u}}(s)$, with no load resistance R_{sec} [—]. The influence of the delay on the phase is shown by the dashed line [- - -]. The discussed frequencies are written on top corresponding to the dashed lines. . 45
2.21 Frequency responses of the controller $G_{\mathrm{r,u}}(s)$ [—] and the transfer function $G_{\mathrm{dd,i}}(s)$ from (2.49) with $R_{\mathrm{sec}} = 10\ \Omega$ [—], $R_{\mathrm{sec}} = 50\ \Omega$ [—] and $R_{\mathrm{sec}} \to \infty\ \Omega$ [—]. The discussed frequencies are written on top corresponding to the dashed lines. 47
2.22 Block diagram of the implemented discrete current controller for one phase. . . . 48
2.23 Measured result of the step response with $\tau_{\mathrm{avg}} = \frac{3}{2}\,T_{\mathrm{s}}$ [—] and $\tau_{\mathrm{avg}} = 2\,T_{\mathrm{s}}$ [—]. . 49
2.24 Frequency responses of the resulting open-loop transfer function $F_{\mathrm{o,i}}(s)$, with $R_{\mathrm{sec}} = 10\ \Omega$ [—], $R_{\mathrm{sec}} = 50\ \Omega$ [—] and $R_{\mathrm{sec}} \to \infty\ \Omega$ [—]. The influence of the delay on the phase is shown by the dashed line. The discussed frequencies are written on top corresponding to the dashed lines. 50
2.25 Equivalent circuit of a PV array. 50
2.26 Exemplary current-voltage (I-V) in the upper and power-voltage (P-V) characteristics in the lower subplot of a PV array, each with full [—] and half [- - -] radiation and the respective MPPs [♦]. The resistive load characteristics of the proposed controller is shown by the yellow line [—]. The MPP voltage u_{mpp} and the open circuit voltage $u_{\mathrm{pv,oc}}$ are written on top corresponding to the dashed lines [- - -]. 51
2.27 PV Test array with twelve modules on the roof of the office. 53
2.28 Transient response of the P&O algorithm with constant [—] and variable [—] step size after the DC/DC converter is started. 54

2.29 Photo of the motor drive, the electrical machine, and the generator unit. 55
2.30 Illustration of the cross-section of a PMSM. 55
2.31 Electrical equivalent circuit of the PMSM. 57
2.32 Signal flow diagram of the electrical machine. 58
2.33 Block diagram of the current control loop for the electrical machine. 59
2.34 Step responses of the current controller designed according to MO [—], SO [—] and where the controller is experimentally tuned [—]. 60
2.35 Illustration of the operation areas with the transient line [·····], the current limit [- - -] and the voltage limit [—] for two different speeds with $\omega_{\mathrm{p},1} < \omega_{\mathrm{p},2}$. 61
2.36 Illustration of the MTPC hyperbola [—], torque contour lines [—] and the current limit [- - -] with a linearised flux linkage. 62
2.37 Photo of the test bench with the machine under test on the left side and the drive machine on the right, which consists of two electrical machines, each with a motor drive. 63
2.38 Measured flux linkage maps of ψ_{s}^{d} in the upper subplots and ψ_{s}^{q} in the lower subplots, where the top view with the black contour lines is shown on the left and the corresponding 3D plot is shown on the right. 64
2.39 Block diagram of the cascaded torque control loop for the direct measurement of the current vector with maximum efficiency. 65
2.40 (a) Measured torque contour lines [—] and resulting trajectories for the two MTPC methods with linearised [—] and nonlinear [—] flux linkages and the measured trajectories with the maximum efficiency for different shaft speeds of 100 rpm [—], 200 rpm [—] and 300 rpm [—] in the (d,q)-plane. (b) Efficiency [—] for a shaft speed of 300 rpm and a constant torque of -15 Nm and the two points of MTPC for linear approximated [×] and nonlinear [×] flux linkages and the point of maximum efficiency [♦]. 67
2.41 The electrical circuit of the grid inverter. 69
2.42 LCL filter of one phase with parasitic resistances. 71
2.43 Frequency responses of the LCL filter with $L_{\mathrm{g}} = 4$ mH [—], $L_{\mathrm{g}} = 200$ μH [—] and $L_{\mathrm{g}} = 10$ μH [—]. The discussed frequencies are written on top corresponding to the dashed lines, whereby f_{rl} and f_{res} are only marked for the blue line. The dashed red lines [- - -] are marking the range limits within the resonance frequency f_{res} should lie. 72
2.44 Simulation result of the voltage $u_{\mathrm{nm,f}}$ and the correlation with the switching states $\boldsymbol{\sigma}^{abc}$ for a single grid inverter with floating star-point. 75
2.45 Simulation results of two parallel connected inverters with floating star-point with the currents $\boldsymbol{i}_{\mathrm{l},1/2}^{abc}$ in the first subplot and the circulating γ-current in the second subplot. 76
2.46 Comparison of the current ripples between a grid inverter with star-point connection [—] and with floating star-point [—]. 77
2.47 Block diagram of the continuous PI state feedback controller (PI-SFC). 82
2.48 Block diagram of the control loop with PI state feedback controller (PI-SFC) and observer. 84
2.49 Block diagram of the experimental setup. 86
2.50 Measurement results of the PI controller [—] and the PI-SFC [—] under normal grid conditions with a grid inductance of 500 μH. 88
2.51 Illustration of the emulated scenarios of the grid voltages $\boldsymbol{u}_{\mathrm{g}}^{abc}$ in the first subplot, and the corresponding grid voltages $\boldsymbol{u}_{\mathrm{g}}^{dq\gamma}$ in the second subplot. 89

2.52 Measurement results of the PI controller [—] and the PI-SFC [—] under FRT conditions with a grid inductance of 500 μH. 90
2.53 Measurement results of the PI controller [—] and the PI-SFC [—] with FRT condition and a grid inductance of 1000 μH. 91
2.54 Measurement results of the PI controller [—] and the PI-SFC [—] with harmonic distortion and FRT condition and a grid inductance of 2000 μH. 92
2.55 The electrical circuit of multiple parallel-connected grid inverters. 94

3.1 Electrical circuit of the developed DC grid for the integration of renewable energy sources, particularly wave energy. 97
3.2 An exemplary characteristic droop curve for adjusting the active power in the event of over- or underfrequency according to the current standard VDE-AR-N 4105 [163, Sec. 5.7.4.3]. 98
3.3 Equivalent circuit of two voltage controlled units using droop control with virtual resistances $R_{d,1}$ and $R_{d,2}$. 104
3.4 Block diagram of the droop controller with cascaded current and voltage control loops. 104
3.5 Implemented droop control curves for the RES in the first subplot and for the grid inverters in the second subplot. 106
3.6 Block diagram of the droop controller for derating the reference current of renewable energy sources. 107
3.7 Block diagram of the droop controller with characteristic droop curve for the grid inverters. 108
3.8 Electrical circuit of a single grid inverter with a qualitative power flow diagram on top. 111
3.9 Illustration of the combination of the generating units for wave energy converters (WEC), wind turbines (WT) and photovoltaics (PV) into one current source. 116
3.10 Model simplification for short transmission lines. 117
3.11 Electrical circuit with the simplified transmission line model. 118
3.12 Block diagram of the DC link dynamics of the resulting DC link dynamics of the energy conversion (EC) system. 119
3.13 Root locus plot with varying droop gain K_d for the operating points (a) $i_l^{d\star} = i_{l,nom}^d$, (b) $i_l^{d\star} = 0$ A, and (c) $i_l^{d\star} = -i_{l,nom}^d$. 125
3.14 Zoomed area around the centre of the root locus plot with varying droop gain K_d for the operating points (a) $i_l^{d\star} = i_{l,nom}^d$, (b) $i_l^{d\star} = 0$ A, and (c) $i_l^{d\star} = -i_{l,nom}^d$. The poles for $K_d = (10\text{ V})^{-1}$ are marked with a blue asterisk [$\ast$]. 126
3.15 Root locus plot with varying droop time constant τ_d and with $K_d = (10\text{ V})^{-1}$ for the operating points (a) $i_l^{d\star} = i_{l,nom}^d$, (b) $i_l^{d\star} = 0$ A, and (c) $i_l^{d\star} = -i_{l,nom}^d$. 128
3.16 Root locus plot with varying DC link capacitance C_{dc} and with $K_d = (10\text{ V})^{-1}$ for the operating points (a) $i_l^{d\star} = i_{l,nom}^d$, (b) $i_l^{d\star} = 0$ A, and (c) $i_l^{d\star} = -i_{l,nom}^d$. The poles for the implemented DC link capacitance with $C_{dc} = 810$ μF are marked with a blue asterisk [$\ast$]. 129
3.17 Step responses with a DC link capacitance of $C_{dc} = 810$ μF [—] and $C_{dc} = 200$ μF [—], where the input signal is the current i_{ec}^{dc} [—] of the RES. 130
3.18 Root locus plot with varying droop gain K_d with $i_l^{d\star} = i_{l,nom}^d$ for the transmission line length (a) $l_l = 1$ m, (b) $l_l = 100$ m, and (c) $l_l = 1000$ m. The poles for $K_d = (10\text{ V})^{-1}$ are marked with a blue asterisk [$\ast$]. 131

3.19 Root locus plot with varying transmission line length l_l with $i_l^{d\star} = i_{l,\mathrm{nom}}^{d}$ and $K_\mathrm{d} = (10\ \mathrm{V})^{-1}$ for (a) $R_{l,0} = 0\ \mathrm{m}\Omega$ and (b) $R_{l,0} = 10\ \mathrm{m}\Omega$. The lengths $l_l = 1$ m, $l_l = 100$ m, and $l_l = 1000$ m are marked with a blue [$\ast$], red [$\ast$], and yellow [$\ast$] asterisk, respectively. 131
3.20 Step response with $R_{l,0} = 0\ \mathrm{m}\Omega$ [—] and $R_{l,0} = 10\ \mathrm{m}\Omega$ [—]. 132
3.21 Ragone diagram of the specific energy and power of batteries and capacitors [234, Sec. 2.1.2]. 134
3.22 Schematic structure of an electrochemical double-layer capacitor and the equivalent circuit beneath. 135
3.23 (a) RC model and (b) three-branch model for highly dynamic applications of supercapacitors. 136
3.24 The electrical circuit of the wave energy converter and illustration of the power flow, where p_wc is the fluctuating power from the WEC, p_ps is the power flowing in and out of the supercapacitors, and p_es is the smoothed power flow into the battery. 138
3.25 Photo and computer-aided design (CAD) illustration of the supercapacitor bank, the battery system and the control cabinet with the voltage and current measurement. 139
3.26 Photo of the DC/DC converter VarioString VS-70 (a) and the LLC half-bridge topology (b). 140
3.27 Block diagram of the voltage control loop for power smoothing. 143
3.28 Numerical stability analysis of the coefficients a_0, a_1, a_2, a_3 and determinant D_3 over the input operational current $\bar{i}_\mathrm{wc}^\star$ for two different reference voltages $u_\mathrm{c,ref}^\star = u_\mathrm{min}^\mathrm{dc}$ [—] and $u_\mathrm{c,ref}^\star = u_\mathrm{max}^\mathrm{dc}$ [—]. 147
3.29 Comparison of the measured [—] and simulated [—] quantities of the DC link control, with the rod position h at the top, followed by the current $i_\mathrm{wc}^\mathrm{dc}$ and the smoothed current $i_\mathrm{es}^\mathrm{dc}$, the DC link voltage u^dc and the power of the generator units p_wc and the smoothed power p_es. The currents $i_\mathrm{wc}^\mathrm{dc}$ and the power of the generator units p_wc are used as inputs for the simulation [—]. 148
3.30 Photo of the supercapacitor module and the connected string with the DC/DC converter. 149
3.31 The electrical circuit of the power smoothing system. 151
3.32 Comparison of voltage control with two parallel-connected DC/DC converters without droop control ($R_\mathrm{d} = 0\ \Omega$), with the ideal case shown in the left column and the case with measurement error shown in the right column. In the first two subplots, the quantities of the RES side are indicated with a blue line [—], the grid side with a red line [—], and those from the power smoothing units with a yellow line [—]. The two lower subplots refer to the two supercapacitors, with the quantities of the first unit in violet [—] and the second in green [—]. 152
3.33 Simulation results with constant droop resistance $R_{\mathrm{d},1/2} = 1\ \Omega$. In the first two subplots, the quantities of the RES side are indicated with a blue line [—], the grid side with a red line [—], and those from the power smoothing units with a yellow line [—]. The two lower subplots refer to the two supercapacitors, with the quantities of the first unit in violet [—] and the second in green [—]. 154
3.34 Block diagram of the droop control with virtual resistance R_d for the DC/DC converter with connected supercapacitor module and the SoE controller, which generates the reference voltage $u_\mathrm{ps,ref}^\mathrm{dc}$. 155

3.35 Simulation results with adaptive droop resistance R_d and SoE control. In the first two subplots, the quantities of the RES side are indicated with a blue line [—], the grid side with a red line [—], and those from the power smoothing units with a yellow line [—]. The three lower subplots refer to the two supercapacitors, with the quantities of the first unit in violet [—] and the second in green [—]. . 157
3.36 Simulation results of the proposed power smoothing control with five power smoothing units. In the first two subplots, the quantities of the RES side are indicated with a blue line [—], the grid side with a red line [—], and those from the power smoothing units with a yellow line [—]. The three lower subplots refer to the five supercapacitors units with index $i \in \{1, 2, \dots, 5\}$. 158

A.1 Block diagram of a closed-loop system. 194
A.2 Signal flow diagram of a first-order low-pass filter in two different representations. 196

Appendix A

Formulary and Calculations

This chapter lists some formulae and presents some detailed calculations that are necessary within the scope of this thesis.

A.1 Clarke Transformation

The (a,b,c)-reference frame and the rotating (α,β,γ)-reference frame, can be transformed into each other by means of the Clarke transformation matrices [84, Sec. 14.2.4], [85]

$$\boldsymbol{T}_{\mathrm{c}} := \kappa \begin{bmatrix} 1 & -\frac{1}{2} & -\frac{1}{2} \\ 0 & \frac{\sqrt{3}}{2} & -\frac{\sqrt{3}}{2} \\ \frac{1}{\sqrt{2}} & \frac{1}{\sqrt{2}} & \frac{1}{\sqrt{2}} \end{bmatrix} \quad \text{and} \quad \boldsymbol{T}_{\mathrm{c}}^{-1} := \frac{1}{\kappa} \begin{bmatrix} \frac{2}{3} & 0 & \frac{\sqrt{2}}{3} \\ -\frac{1}{3} & \frac{1}{\sqrt{3}} & \frac{\sqrt{2}}{3} \\ -\frac{1}{3} & -\frac{1}{\sqrt{3}} & \frac{\sqrt{2}}{3} \end{bmatrix}, \tag{A.1}$$

whereby the relationship

$$\boldsymbol{x}^{\alpha\beta\gamma} = \boldsymbol{T}_{\mathrm{c}}\, \boldsymbol{x}^{abc} \quad \text{and} \quad \boldsymbol{x}^{abc} = \boldsymbol{T}_{\mathrm{c}}^{-1}\, \boldsymbol{x}^{\alpha\beta\gamma} \tag{A.2}$$

applies. Thereby, κ is the scaling factor. In this thesis, an amplitude-correct transformation with $\kappa = \frac{2}{3}$ is consequently chosen, which yields

$$\boldsymbol{T}_{\mathrm{c}} = \begin{bmatrix} \frac{2}{3} & -\frac{1}{3} & -\frac{1}{3} \\ 0 & \frac{1}{\sqrt{3}} & -\frac{1}{\sqrt{3}} \\ \frac{\sqrt{2}}{3} & \frac{\sqrt{2}}{3} & \frac{\sqrt{2}}{3} \end{bmatrix} \quad \text{and} \quad \boldsymbol{T}_{\mathrm{c}}^{-1} = \begin{bmatrix} 1 & 0 & \frac{1}{\sqrt{2}} \\ -\frac{1}{2} & \frac{\sqrt{3}}{2} & \frac{1}{\sqrt{2}} \\ -\frac{1}{2} & -\frac{\sqrt{3}}{2} & \frac{1}{\sqrt{2}} \end{bmatrix}. \tag{A.3}$$

Only for symmetrical systems with

$$x^a + x^b + x^c = 0\,, \tag{A.4}$$

the amplitude-correct transformation yields

$$\begin{aligned} x^{\alpha} &= \kappa \left(x^{a} - \frac{1}{2}\,x^{b} - \frac{1}{2}\,x^{c} \right) \\ &\overset{(\mathrm{A.4})}{=} \kappa \left(x^{a} - \frac{1}{2}\,x^{b} - \frac{1}{2}\left(-x^{a} - x^{b}\right) \right) \\ &= \kappa\,\frac{3}{2}\,x^{a} \\ &\overset{(\kappa=\frac{2}{3})}{=} x^{a}\,. \end{aligned} \tag{A.5}$$

Note that the geometrical length of the vector is given by

$$\left\| \boldsymbol{x}^{\alpha\beta\gamma} \right\| = \kappa \sqrt{\frac{3}{2}}\, \left\| \boldsymbol{x}^{abc} \right\| \overset{(\kappa=\frac{2}{3})}{=} \sqrt{\frac{2}{3}}\, \left\| \boldsymbol{x}^{abc} \right\|\,. \tag{A.6}$$

The electrical power is given by

$$\begin{aligned} p_{\mathrm{el}} &= \left(\boldsymbol{u}^{abc} \right)^{\top}\, \boldsymbol{i}^{abc} \\ &= \left(\boldsymbol{T}_{\mathrm{c}}^{-1}\, \boldsymbol{u}^{\alpha\beta\gamma} \right)^{\top} \left(\boldsymbol{T}_{\mathrm{c}}^{-1}\, \boldsymbol{i}^{\alpha\beta\gamma} \right) \\ &= \left(\boldsymbol{u}^{\alpha\beta\gamma} \right)^{\top} \left(\boldsymbol{T}_{\mathrm{c}}^{-1} \right)^{\top} \boldsymbol{T}_{\mathrm{c}}^{-1}\, \boldsymbol{i}^{\alpha\beta\gamma} \\ &= \frac{2}{3\kappa^{2}} \left(\boldsymbol{u}^{\alpha\beta\gamma} \right)^{\top}\, \boldsymbol{i}^{\alpha\beta\gamma} \\ &\overset{(\kappa=\frac{2}{3})}{=} \frac{3}{2} \left(\boldsymbol{u}^{\alpha\beta\gamma} \right)^{\top}\, \boldsymbol{i}^{\alpha\beta\gamma}\,. \end{aligned} \tag{A.7}$$

A coefficient $\kappa = \sqrt{\frac{2}{3}}$ gives a power-correct transformation for generic systems, with

$$\| \boldsymbol{x}^{abc} \| = \| \boldsymbol{x}^{\alpha\beta\gamma} \| \quad \text{and} \quad p_{\mathrm{el}} = (\boldsymbol{u}^{abc})^{\top} \boldsymbol{i}^{abc} = (\boldsymbol{u}^{\alpha\beta})^{\top} \boldsymbol{i}^{\alpha\beta}\,. \tag{A.8}$$

A.2 Park Transformation

The fixed (α,β,γ)-reference frame and the rotating (d,q,γ)-reference frame, can be transformed into each other by means of the Park transformation matrices [84, Sec. 14.3.2]

$$\boldsymbol{T}_{\mathrm{p}}(\phi_{\mathrm{p}}) = \begin{bmatrix} \cos(\phi_{\mathrm{p}}) & -\sin(\phi_{\mathrm{p}}) & 0 \\ \sin(\phi_{\mathrm{p}}) & \cos(\phi_{\mathrm{p}}) & 0 \\ 0 & 0 & 1 \end{bmatrix} \quad \text{and} \quad \boldsymbol{T}_{\mathrm{p}}^{-1}(\phi_{\mathrm{p}}) = \begin{bmatrix} \cos(\phi_{\mathrm{p}}) & \sin(\phi_{\mathrm{p}}) & 0 \\ -\sin(\phi_{\mathrm{p}}) & \cos(\phi_{\mathrm{p}}) & 0 \\ 0 & 0 & 1 \end{bmatrix}, \tag{A.9}$$

whereby the relationship

$$\boldsymbol{x}^{\alpha\beta\gamma} = \boldsymbol{T}_{\mathrm{p}}\, \boldsymbol{x}^{dq\gamma} \quad \text{and} \quad \boldsymbol{x}^{dq\gamma} = \boldsymbol{T}_{\mathrm{p}}^{-1}\, \boldsymbol{x}^{\alpha\beta\gamma} \tag{A.10}$$

applies. The transformation angle ϕ_{p} is usually the angle between the α- and d-axis and time variant with

$$\frac{\mathrm{d}}{\mathrm{d}t}\phi_{\mathrm{p}} = \omega_{\mathrm{p}}\,. \tag{A.11}$$

The time derivative of the transformation matrices results in

$$\frac{\mathrm{d}}{\mathrm{d}t}\boldsymbol{T}_\mathrm{p} = \omega_\mathrm{p}\,\boldsymbol{J}_0\,\boldsymbol{T}_\mathrm{p} \quad \text{and} \quad \frac{\mathrm{d}}{\mathrm{d}t}\boldsymbol{T}_\mathrm{p}^{-1} = -\omega_\mathrm{p}\,\boldsymbol{J}_0\,\boldsymbol{T}_\mathrm{p}^{-1}\,, \tag{A.12}$$

whereby the matrix $\boldsymbol{J}_0$ is given as

$$\boldsymbol{J}_0 \coloneqq \begin{bmatrix} 0 & -1 & 0 \\ 1 & 0 & 0 \\ 0 & 0 & 0 \end{bmatrix}\,. \tag{A.13}$$

Furthermore, the identities

$$\boldsymbol{T}_\mathrm{p}(\phi_1+\phi_2) = \boldsymbol{T}_\mathrm{p}(\phi_1)\,\boldsymbol{T}_\mathrm{p}(\phi_2)\,, \tag{A.14}$$

$$\boldsymbol{T}_\mathrm{p}^{-1}(\phi_\mathrm{p}) = \boldsymbol{T}_\mathrm{p}^{\top}(\phi_\mathrm{p}) = \boldsymbol{T}_\mathrm{p}(-\phi_\mathrm{p})\,, \tag{A.15}$$

and

$$\boldsymbol{J}_0\,\boldsymbol{T}_\mathrm{p} = \boldsymbol{T}_\mathrm{p}\,\boldsymbol{J}_0 \tag{A.16}$$

hold. The electrical power in the (α,β,γ)-reference frame and the rotating (d,q,γ)-reference frame remain equal with

$$p_\mathrm{el} \overset{(\kappa=\frac{2}{3})}{=} \frac{3}{2}\left(\boldsymbol{u}^{\alpha\beta\gamma}\right)^{\top}\boldsymbol{i}^{\alpha\beta\gamma} = \frac{3}{2}\left(\boldsymbol{u}^{dq\gamma}\right)^{\top}\boldsymbol{i}^{dq\gamma}\,, \tag{A.17}$$

regardless of the scaling factor κ of the Clarke transformation.

The simplified Park transformation can be used for systems without a γ-component, e.g., for star-connected electrical machines. Thereby, only the upper left (2×2)-submatrices of $\boldsymbol{T}_\mathrm{p}$, $\boldsymbol{T}_\mathrm{p}^{-1}$ and $\boldsymbol{J}_0$ for the (α,β)-reference frame and (d,q)-reference frame are applied, which yields

$$\boldsymbol{T}_\mathrm{p}^{\star}(\phi_\mathrm{p}) = \begin{bmatrix} \cos(\phi_\mathrm{p}) & -\sin(\phi_\mathrm{p}) \\ \sin(\phi_\mathrm{p}) & \cos(\phi_\mathrm{p}) \end{bmatrix}\,, \qquad \left(\boldsymbol{T}_\mathrm{p}^{\star}\right)^{-1}(\phi_\mathrm{p}) = \begin{bmatrix} \cos(\phi_\mathrm{p}) & \sin(\phi_\mathrm{p}) \\ -\sin(\phi_\mathrm{p}) & \cos(\phi_\mathrm{p}) \end{bmatrix}\,, \tag{A.18}$$

and

$$\boldsymbol{J} \coloneqq \boldsymbol{T}_\mathrm{p}^{\star}\left(\frac{\pi}{2}\right) = \begin{bmatrix} 0 & -1 \\ 1 & 0 \end{bmatrix}\,. \tag{A.19}$$

A.3 Transformation of the Grid Inverter Dynamics

The dynamics of the grid inverter in the (a,b,c)-reference frame are defined in (2.117). The transformation into the rotating (d,q,γ)-reference frame is shown using the example of the inductance current $\boldsymbol{i}_\mathrm{l}^{abc}$, which is given by

$$\frac{\mathrm{d}}{\mathrm{d}t}\boldsymbol{i}_\mathrm{l}^{abc} = \frac{1}{L_\mathrm{f}}\left[\boldsymbol{u}_\mathrm{f}^{abc} - (R_\mathrm{f}+R_\mathrm{c})\,\boldsymbol{i}_\mathrm{l}^{abc} + R_\mathrm{c}\,\boldsymbol{i}_\mathrm{g}^{abc} - \boldsymbol{u}_\mathrm{cf}^{abc}\right]\,. \tag{A.20}$$

Applying the Clarke transformation (see Appendix A.1) leads to

$$\frac{\mathrm{d}}{\mathrm{d}t}\left(\boldsymbol{T}_\mathrm{c}^{-1}\boldsymbol{i}_\mathrm{l}^{\alpha\beta\gamma}\right) = \frac{1}{L_\mathrm{f}}\left[\boldsymbol{T}_\mathrm{c}^{-1}\,\boldsymbol{u}_\mathrm{f}^{\alpha\beta\gamma} - (R_\mathrm{f}+R_\mathrm{c})\,\boldsymbol{T}_\mathrm{c}^{-1}\,\boldsymbol{i}_\mathrm{l}^{\alpha\beta\gamma} + R_\mathrm{c}\,\boldsymbol{T}_\mathrm{c}^{-1}\,\boldsymbol{i}_\mathrm{g}^{\alpha\beta\gamma} - \boldsymbol{T}_\mathrm{c}^{-1}\,\boldsymbol{u}_\mathrm{cf}^{\alpha\beta\gamma}\right]\,. \tag{A.21}$$

Multiplying the equation with the matrix $\boldsymbol{T}_\mathrm{c}$ from left leads to

$$\begin{aligned}\boldsymbol{T}_\mathrm{c}\frac{\mathrm{d}}{\mathrm{d}t}\Big(\boldsymbol{T}_\mathrm{c}^{-1}\boldsymbol{i}_\mathrm{l}^{\alpha\beta\gamma}\Big) = \frac{\mathrm{d}}{\mathrm{d}t}\boldsymbol{i}_\mathrm{l}^{\alpha\beta\gamma} &= \boldsymbol{T}_\mathrm{c}\frac{1}{L_\mathrm{f}}\Big[\boldsymbol{T}_\mathrm{c}^{-1}\boldsymbol{u}_\mathrm{f}^{\alpha\beta\gamma} - (R_\mathrm{f}+R_\mathrm{c})\,\boldsymbol{T}_\mathrm{c}^{-1}\boldsymbol{i}_\mathrm{l}^{\alpha\beta\gamma} + R_\mathrm{c}\,\boldsymbol{T}_\mathrm{c}^{-1}\boldsymbol{i}_\mathrm{g}^{\alpha\beta\gamma} - \boldsymbol{T}_\mathrm{c}^{-1}\boldsymbol{u}_\mathrm{cf}^{\alpha\beta\gamma}\Big] \\ &= \frac{1}{L_\mathrm{f}}\Big[\boldsymbol{u}_\mathrm{f}^{\alpha\beta\gamma} - (R_\mathrm{f}+R_\mathrm{c})\,\boldsymbol{i}_\mathrm{l}^{\alpha\beta\gamma} + R_\mathrm{c}\,\boldsymbol{i}_\mathrm{g}^{\alpha\beta\gamma} - \boldsymbol{u}_\mathrm{cf}^{\alpha\beta\gamma}\Big]\,.\end{aligned} \tag{A.22}$$

The next step is to apply the Park transformation to the time derivative of the inductance current $\boldsymbol{i}_\mathrm{l}^{\alpha\beta\gamma}$, which yields

$$\begin{aligned}\frac{\mathrm{d}}{\mathrm{d}t}\boldsymbol{i}_\mathrm{l}^{\alpha\beta\gamma} &= \frac{\mathrm{d}}{\mathrm{d}t}\Big(\boldsymbol{T}_\mathrm{p}\,\boldsymbol{i}_\mathrm{l}^{dq\gamma}\Big) \\ &= \left(\frac{\mathrm{d}}{\mathrm{d}t}\boldsymbol{T}_\mathrm{p}\right)\boldsymbol{i}_\mathrm{l}^{dq\gamma} + \boldsymbol{T}_\mathrm{p}\left(\frac{\mathrm{d}}{\mathrm{d}t}\boldsymbol{i}_\mathrm{l}^{dq\gamma}\right) \\ &= \omega_\mathrm{g}\,\boldsymbol{J}_0\,\boldsymbol{T}_\mathrm{p}\,\boldsymbol{i}_\mathrm{l}^{dq\gamma} + \boldsymbol{T}_\mathrm{p}\left(\frac{\mathrm{d}}{\mathrm{d}t}\boldsymbol{i}_\mathrm{l}^{dq\gamma}\right) \\ &= \boldsymbol{T}_\mathrm{p}\left(\omega_\mathrm{g}\,\boldsymbol{J}_0\,\boldsymbol{i}_\mathrm{l}^{dq\gamma} + \frac{\mathrm{d}}{\mathrm{d}t}\boldsymbol{i}_\mathrm{l}^{dq\gamma}\right)\end{aligned} \tag{A.23}$$

Thereby, the product rule for derivatives was applied. The derivation of the Park transformation causes the typical cross-couplings in the (d,q,γ)-reference frame. Inserting this result in the previous equation and multiplying it with the inverse Park transformation matrix $\boldsymbol{T}_\mathrm{p}^{-1}$ from left leads to

$$\begin{aligned}\frac{\mathrm{d}}{\mathrm{d}t}\boldsymbol{i}_\mathrm{l}^{dq\gamma} &= \boldsymbol{T}_\mathrm{p}^{-1}\frac{1}{L_\mathrm{f}}\Big[\boldsymbol{u}_\mathrm{f}^{\alpha\beta\gamma} - (R_\mathrm{f}+R_\mathrm{c})\,\boldsymbol{i}_\mathrm{l}^{\alpha\beta\gamma} + R_\mathrm{c}\,\boldsymbol{i}_\mathrm{g}^{\alpha\beta\gamma} - \boldsymbol{u}_\mathrm{cf}^{\alpha\beta\gamma}\Big] - \omega_\mathrm{g}\,\boldsymbol{J}_0\,\boldsymbol{i}_\mathrm{l}^{dq\gamma} \\ &= \boldsymbol{T}_\mathrm{p}^{-1}\frac{1}{L_\mathrm{f}}\Big[\boldsymbol{T}_\mathrm{p}\boldsymbol{u}_\mathrm{f}^{dq\gamma} - (R_\mathrm{f}+R_\mathrm{c})\,\boldsymbol{T}_\mathrm{p}\boldsymbol{i}_\mathrm{l}^{dq\gamma} + R_\mathrm{c}\,\boldsymbol{T}_\mathrm{p}\boldsymbol{i}_\mathrm{g}^{dq\gamma} - \boldsymbol{T}_\mathrm{p}\boldsymbol{u}_\mathrm{cf}^{dq\gamma}\Big] - \omega_\mathrm{g}\,L_\mathrm{f}\,\boldsymbol{J}_0\,\boldsymbol{i}_\mathrm{l}^{dq\gamma} \\ &= \frac{1}{L_\mathrm{f}}\Big[\boldsymbol{u}_\mathrm{f}^{dq\gamma} - \big(R_\mathrm{f}+R_\mathrm{c} + \omega_\mathrm{g}\,L_\mathrm{f}\,\boldsymbol{J}_0\big)\,\boldsymbol{i}_\mathrm{l}^{dq\gamma} + R_\mathrm{c}\,\boldsymbol{i}_\mathrm{g}^{dq\gamma} - \boldsymbol{u}_\mathrm{cf}^{dq\gamma}\Big]\end{aligned} \tag{A.24}$$

Likewise, the other differential equations for $\boldsymbol{u}_\mathrm{cf}^{abc}$ and $\boldsymbol{i}_\mathrm{g}^{abc}$ are transformed, yielding the dynamics in the (d,q,γ)-reference frame in (2.118).

A.4 Calculation of the Transfer Function from the State Space

Given is the generic system

$$\left.\begin{aligned}\frac{\mathrm{d}}{\mathrm{d}t}\boldsymbol{x} &= \boldsymbol{A}\,\boldsymbol{x} + \boldsymbol{B}\,\boldsymbol{u} + \boldsymbol{E}\,\boldsymbol{d} \\ \boldsymbol{y} &= \boldsymbol{C}\,\boldsymbol{x} + \boldsymbol{D}\,\boldsymbol{u}\,,\end{aligned}\right\} \tag{A.25}$$

with

$$
\begin{aligned}
\text{state vector} \quad & \boldsymbol{x} \in \mathbb{R}^{n} \ , \\
\text{input vector} \quad & \boldsymbol{u} \in \mathbb{R}^{m} \ , \\
\text{disturbance vector} \quad & \boldsymbol{d} \in \mathbb{R}^{p} \ , \\
\text{output vector} \quad & \boldsymbol{y} \in \mathbb{R}^{r} \ , \\
\text{system matrix} \quad & \boldsymbol{A} \in \mathbb{R}^{n\times n} \ , \\
\text{input matrix} \quad & \boldsymbol{B} \in \mathbb{R}^{n\times m} \ , \\
\text{disturbance matrix} \quad & \boldsymbol{E} \in \mathbb{R}^{n\times p} \ , \\
\text{output matrix} \quad & \boldsymbol{C} \in \mathbb{R}^{r\times n} \ , \text{ and} \\
\text{feedthrough matrix} \quad & \boldsymbol{D} \in \mathbb{R}^{r\times m} \ .
\end{aligned}
$$

Applying the Laplace transformation to the state vector gives [93, Sec 3.5.4]

$$
\frac{\mathrm{d}}{\mathrm{d}t}\boldsymbol{x} \quad \circ\!\!-\!\!\!-\!\!\bullet \quad s\,\boldsymbol{x}(s) - \boldsymbol{x}(0)\,. \tag{A.26}
$$

With $\boldsymbol{x}(0) = \boldsymbol{0}$, the equation of states in the frequency domain results in [93, Sec 12.2.3]

$$
\left.
\begin{aligned}
s\,\boldsymbol{x}(s) &= \boldsymbol{A}\,\boldsymbol{x}(s) + \boldsymbol{B}\,\boldsymbol{u}(s) + \boldsymbol{E}\,\boldsymbol{d}(s) \\
\boldsymbol{y}(s) &= \boldsymbol{C}\,\boldsymbol{x}(s) + \boldsymbol{D}\,\boldsymbol{u}(s)\,.
\end{aligned}
\right\} \tag{A.27}
$$

Solving the first equation for $\boldsymbol{x}$, yields

$$
\boldsymbol{x}(s) = \left(s\,\boldsymbol{I} - \boldsymbol{A}\right)^{-1}\left(\boldsymbol{B}\,\boldsymbol{u}(s) + \boldsymbol{E}\,\boldsymbol{d}(s)\right)\,. \tag{A.28}
$$

The inverse of the matrix $(s\,\boldsymbol{I} - \boldsymbol{A})$ is the adjugate matrix $\mathrm{adj}(s\,\boldsymbol{I} - \boldsymbol{A})$ divided by its determinant $\det(s\,\boldsymbol{I} - \boldsymbol{A})$. The adjugate matrix of a square matrix $\boldsymbol{X} \in R^{n\times n}$ is the transposed cofactor matrix $\boldsymbol{C}_{\mathrm{x}}^{\top}$, which is given by [267, Sec. 4.2]

$$
\begin{aligned}
\mathrm{adj}(\boldsymbol{X}) = \boldsymbol{C}_{\mathrm{x}}^{\top} &= \begin{bmatrix}
+m_{11} & -m_{12} & \dots & (-1)^{n-1}\,m_{1n} \\
-m_{21} & +m_{22} & \dots & (-1)^{n}\,m_{2n} \\
\vdots & \vdots & \ddots & \vdots \\
(-1)^{n-1}\,m_{n1} & (-1)^{n}\,m_{n2} & \dots & (-1)^{n-1}\,m_{nn}
\end{bmatrix}^{\top} \\
&= \begin{bmatrix}
+m_{11} & -m_{21} & \dots & (-1)^{n-1}\,m_{n1} \\
-m_{12} & +m_{22} & \dots & (-1)^{n}\,m_{n2} \\
\vdots & \vdots & \ddots & \vdots \\
(-1)^{n-1}\,m_{1n} & (-1)^{n}\,m_{2n} & \dots & (-1)^{n-1}\,m_{nn}
\end{bmatrix}.
\end{aligned} \tag{A.29}
$$

There, m_{ij} is the determinant of the $(n-1)\times(n-1)$ submatrix of $\boldsymbol{X}$, with row i and the column j removed. Note the transposition of the cofactor matrix, which can easily be missed.

Inserting this into the Laplace transformation of the output equation, results in

$$
\left.
\begin{aligned}
\boldsymbol{y}(s) &= \left[\boldsymbol{C}\left(s\,\boldsymbol{I} - \boldsymbol{A}\right)^{-1}\boldsymbol{B} + \boldsymbol{D}\right]\boldsymbol{u}(s) + \boldsymbol{C}\left(s\,\boldsymbol{I} - \boldsymbol{A}\right)^{-1}\boldsymbol{E}\,\boldsymbol{d}(s) \\
&= \underbrace{\frac{\boldsymbol{C}\,\mathrm{adj}(s\,\boldsymbol{I} - \boldsymbol{A})\boldsymbol{B} + \det(s\,\boldsymbol{I} - \boldsymbol{A})\boldsymbol{D}}{\det(s\,\boldsymbol{I} - \boldsymbol{A})}}_{:=\boldsymbol{G}_{\mathrm{u}}(s)}\boldsymbol{u}(s) + \underbrace{\frac{\boldsymbol{C}\,\mathrm{adj}(s\,\boldsymbol{I} - \boldsymbol{A})\boldsymbol{E}}{\det(s\,\boldsymbol{I} - \boldsymbol{A})}}_{:=\boldsymbol{G}_{\mathrm{d}}(s)}\boldsymbol{d}(s)\,,
\end{aligned}
\right\} \tag{A.30}
$$

where $\boldsymbol{G}_{\mathrm{u}}(s)$ are the transfer functions from the input vector $\boldsymbol{u}(s)$ to output vector $\boldsymbol{y}(s)$, and $\boldsymbol{G}_{\mathrm{d}}(s)$ are the transfer functions from the disturbance vector $\boldsymbol{d}(s)$ to output vector $\boldsymbol{y}(s)$.
The denominator polynomial of both transfer functions is defined by the determinant of $(s\,\boldsymbol{I}-\boldsymbol{A})$. This means that the characteristic polynomial $\chi_{\boldsymbol{A}}(s)$ can also be given as

$$\chi_{\boldsymbol{A}}(s) = \det\left(s\,\boldsymbol{I} - \boldsymbol{A}\right). \tag{A.31}$$

Thereby, the zeros of the polynomial are the poles of the system, which can be used to analyse the stability of the system. If all poles are in the left s-half plane, the system is stable. If the calculation of the zeros of $\chi_{\boldsymbol{A}}(s)$ is too complex, the polynomial can also be examined with the help of the Hurwitz criteria. A linear time-invariant (LTI) system is exponentially stable if and only if its characteristic polynomial $\chi_{\boldsymbol{A}}(s)$ is a Hurwitz polynomial (see [84, Sec. 5.4.2] and [221, Sec. 3.4.5]).

A.5 Root Locus

The root locus method was invented by Walter R. Evans in 1948 [268]. It is a graphical method to examine the locations of the poles or roots of a closed-loop transfer function for different controller gains k. In addition to stability, this also allows the dynamic behaviour of a system to be assessed.

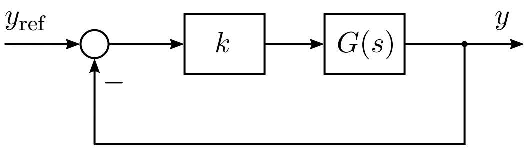

Figure A.1: Block diagram of a closed-loop system.

Fig. A.1 shows the block diagram of a closed-loop system. The open-loop transfer function $F_{\mathrm{o}}(s)$ is the combination of the controller k and the plant $G(s)$ with

$$F_{\mathrm{o}}(s) = k\,G(s) = k\,\frac{N(s)}{D(s)}\,, \tag{A.32}$$

where $N(s)$ is the numerator and $D(s)$ is the denominator of $G(s)$. In the classical root locus method, only the influence of the variation in the proportional part of the controller is considered. Thus, only a P controller with gain k is considered. The dynamic parts of a controller can be included in $G(s)$. The transfer function $F_{\mathrm{cl}}(s)$ of the closed-loop system can be given by

$$F_{\mathrm{cl}}(s) = \frac{y(s)}{y_{\mathrm{ref}}(s)} = \frac{F_{\mathrm{o}}(s)}{1+F_{\mathrm{o}}(s)} = \frac{1}{1+F_{\mathrm{o}}(s)^{-1}} = \frac{k\,N(s)}{D(s)+k\,N(s)}\,. \tag{A.33}$$

With the characteristic equation

$$\chi_{\mathrm{cl}}(s) = 1 + F_{\mathrm{o}}(s) = D(s) + k\,N(s) = 0 \tag{A.34}$$

of the closed-loop transfer function $F_{\mathrm{cl}}(s)$, its poles (roots) can be calculated. The root locus plot is obtained by drawing the poles for each k in the complex s-plane. Thereby, the curves start at the poles of the open-loop transfer function $F_{\mathrm{o}}(s)$ for $k = 0$ and end in its zeros for

$k \to \infty$. In the figures, the open-loop poles are marked with a cross [**×**] and the zeros with a circle [**O**] (i.e., **×**→**O**). Since for causal systems the number of poles must be greater than or equal to the number of zeros, the curves that do not end in a zero go to infinity for $k \to \infty$.

Simulation software such as MATLAB provides functions to plot the root locus for a given transfer function. However, sometimes it is more interesting to analyse the system behaviour when varying a parameter other than the controller gain. For example, a system with the transfer function

$$H(s) = \frac{b_0 + b_1\,s + b_2\,s^2}{1 + \tau\,s + a_2\,s^2 + a_3\,s^3} \tag{A.35}$$

should be examined for the variation of τ. Since the MATLAB function *rlocus* assumes an open-loop transfer function $F_\mathrm{o}(s)$ and returns the pole locations of the closed-loop system with varying controller gains k [222], a standard transfer function like $H(s)$ cannot be analysed directly with this function.

Considering the characteristic equation of the transfer function $H(s)$ with

$$1 + \tau\,s + a_2\,s^2 + a_3\,s^3 = 0\,, \tag{A.36}$$

it can be reformulated in the known form of (A.34), which gives

$$\left.\begin{aligned} 1 + a_2\,s^2 + a_3\,s^3 + \tau\,s &= 0 \\ \frac{1 + a_2\,s^2 + a_3\,s^3}{1 + a_2\,s^2 + a_3\,s^3} + \tau\,\frac{s}{1 + a_2\,s^2 + a_3\,s^3} &= 0 \\ 1 + \tau\,\underbrace{\frac{s}{1 + a_2\,s^2 + a_3\,s^3}}_{:=H'(s)} &= 0\,. \end{aligned}\right\} \tag{A.37}$$

Rearranging the characteristic equation leads to the known form for closed-loop system and the new transfer function $H'(s)$. The zeros of the characteristic equation are not affected by this conversion, which is why the function *rlocus* with the argument $H'(s)$ can be used to investigate the influence of τ on the original transfer function $H(s)$ [93, Sec. 6.4.4].

It should be noted that a standard transfer function was considered here, not a control loop. If the influence of a parameter on a control loop needs to be analysed, the closed-loop transfer function $F_\mathrm{cl}(s)$ needs to be calculated and used for this method.

Often it is the case that more coefficients depend on a specific physical parameter. In this case, the root locus can be created numerically by varying the parameter and calculating the poles of the transfer function.

A.6 First-Order Low-Pass Filter

A low-pass filter is often required in power electronics, which is why its implementation is briefly presented here. The transfer function of a first-order low-pass filter (PT1 element) is given by

$$\frac{y(s)}{u(s)} = \frac{K}{1 + s\,\tau}\,, \tag{A.38}$$

where K is the filter gain, and τ is the filter time constant. Note that τ is used, and not T, as T could be confused with an inverse frequency $\frac{1}{f}$. Here,

$$T = \frac{1}{f} \qquad \text{and} \qquad \tau = \frac{1}{\omega} \tag{A.39}$$

are generally used. The cutoff frequency f_c of the filter at which the magnitude has dropped by 3 dB is given by

$$f_\mathrm{c} = \frac{\omega_\mathrm{c}}{2\pi} = \frac{1}{2\pi\,\tau}\,. \tag{A.40}$$

The step response $y_\sigma(t)$ of the low-pass filter is an e-function of the form

$$y_\sigma(t) = K\left(1 - e^{-\frac{t}{\tau}}\right)\,. \tag{A.41}$$

After the time τ, the output y has reached about 63.2 % of the final value. After 5τ, the output is about 99.3 % of the final value, and the filter is considered steady.

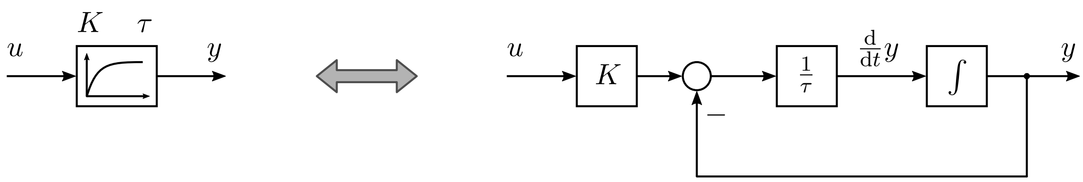

Figure A.2: Signal flow diagram of a first-order low-pass filter in two different representations.

Fig. A.2 shows the signal flow diagram of a first-order low-pass filter in two different representations. The left representation is the combined representation with a single block, and on the right is the equivalent representation with an integrator. It can be derived by applying the Laplace transformation to (A.38), which yields

$$y(s)\,(1 + s\,\tau) = K\,u(s) \qquad \bullet\!\!-\!\!\!-\!\!\circ \qquad y + \tau\,\frac{\mathrm{d}}{\mathrm{d}t}y = K\,u\,. \tag{A.42}$$

This gives the differential equation of the first-order low-pass filter with

$$\frac{\mathrm{d}}{\mathrm{d}t}y = \dot{y} = \frac{1}{\tau}\left(K\,u - y\right)\,. \tag{A.43}$$

It can be implemented by means of the rectangular rule, which yields

$$\left.\begin{aligned} \dot{y}[k] &= \frac{1}{\tau}\left(K\,u[k] - y[k-1]\right) \\ y[k] &= y[k-1] + T_\mathrm{s}\,\dot{y}[k]\,, \end{aligned}\right\} \tag{A.44}$$

where $k \in \mathbb{N}$ denotes the discrete-time index and T_s is the sampling time. With this two-line implementation, an approximation to the time derivative $\dot{y}$ of the output y is available. If this is not necessary, the filter can also be implemented in one line, resulting in

$$y[k] = y[k-1] + \frac{T_\mathrm{s}}{\tau}\,(K\,u[k] - y[k-1]) \ . \tag{A.45}$$

It is important to note that the cutoff frequency f_c must not be set too close to the sampling frequency

$$f_\mathrm{s} = \frac{1}{T_\mathrm{s}} \,. \tag{A.46}$$

Otherwise, quantisation errors occur, and the step response shows overshoots. This is actually not possible with a first-order transfer function and should therefore be avoided to prevent undesired behaviour. A tenfold distance with

$$f_\mathrm{c} \leq \frac{1}{10} f_\mathrm{s} \tag{A.47}$$

should be maintained. If this is not possible, an infinite impulse response (IIR) structure with another discretisation method such as Tustin's method must be used.

A popular alternative is the moving average filter because it is more tangible and easier to understand. The moving average filter is given by

$$y[k] = \frac{1}{N}\sum_{i=0}^{N-1} u[k-i] = \frac{1}{N}\,(u[k] + u[k-1] + \ldots + u[k-N+1]) \ , \tag{A.48}$$

where N is the number of elements over which the average is taken. This also means that N elements have to be stored.

It can be shown that the moving average is almost identical to a first-order filter. Making the reasonable assumption that the oldest input value $u[k-N]$ is approximately the last average value $y[k-1]$, meaning $u[k-N] \approx y[k-1]$. Therefore, adding $u[k-N] - y[k-1] \approx 0$ to (A.48) does not change the equation and it results in

$$\begin{aligned} y[k] &= \frac{1}{N}\sum_{i=0}^{N-1} u[k-i] + \frac{1}{N}\underbrace{(u[k-N] - y[k-1])}_{\approx 0} \\ &= \frac{1}{N}u[k] + \underbrace{\frac{1}{N}\,(u[k-1] + u[k-2] + \ldots + u[k-N+1] + u[k-N])}_{=\,y[k-1]} - \frac{1}{N}y[k-1] \\ &= y[k-1] + \frac{1}{N}\,(u[k] - y[k-1]) \ . \end{aligned} \tag{A.49}$$

This is identical to the implementation of the first-order low-pass filter in (A.45), with

$$N = \frac{\tau}{T_\mathrm{s}} \,. \tag{A.50}$$

If saving the N elements is only a means to an end, the more straightforward implementation of the low-pass filter can save memory and computing time.

To further reduce the quantisation error, it is advantageous to slightly rearrange the equation to

$$y[k] = \frac{1}{N}\,(N\,y[k-1] + u[k] - y[k-1]) \ . \tag{A.51}$$

If the filter is to be implemented on a microcontroller without a floating point arithmetic and only integers must be used, it is beneficial to choose the filter time as a power of two with

$$N = \frac{\tau}{T_\mathrm{s}} = 2^{n_\mathrm{sh}}\,, \tag{A.52}$$

where $n_\mathrm{sh} \in \mathbb{N}$. This allows the filter to be implemented using the bit-shift operations $<<$ and $>>$ with

$$x * 2^{n_\mathrm{sh}} \;=\; x << n_\mathrm{sh} \qquad \text{and} \qquad x \,/\, 2^{n_\mathrm{sh}} \;=\; x >> n_\mathrm{sh}\,, \tag{A.53}$$

which makes the computation very efficient. It results in

$$y[k] = ((y[k-1] << n_\mathrm{sh}) + u[k] - y[k-1]) >> n_\mathrm{sh}\,. \tag{A.54}$$

A.7 Coupling of AC and DC Droop Control Methods

As discussed in Sec. 3.1.1, increasing the DC link voltage would also have advantages in counteracting the emerging problem of low inertia in the public power grid. Various methods, such as the droop control, are proposed in the literature to solve this problem. The proposed droop control for the DC grid, which combines the two existing methods of the characteristic droop curve and the virtual droop resistance, could be extended to the AC grid with additional grid support character.

The droop gain K_d can be adjusted depending on the rate of change of the grid frequency $\dot{\omega}_\mathrm{g}$, with

$$\omega_\mathrm{g} = 2\pi\, f_\mathrm{g}\,. \tag{A.55}$$

For example, the relation

$$\frac{\mathrm{d}}{\mathrm{d}t} K_\mathrm{d} = -\frac{1}{\tau_\mathrm{f}} \left(k_\mathrm{f}\, \dot{\omega}_\mathrm{g} - K_\mathrm{d}\right) \tag{A.56}$$

can be introduced, where an additional low-pass filter with time constant τ_f is added. The gain k_f defines how much the droop gain K_d changes.

When the grid frequency f_g drops, insufficient generated power is available, and the current must be increased to support the grid. According to the relation, the droop gain K_d and, thus, the current on the grid side increases, when the grid frequency f_g drops ($\dot{\omega}_\mathrm{g} < 0$). Accordingly, the current is reduced when the grid frequency rises. The immediately required, or excessive energy can be taken from, or stored into the DC link capacitors. Subsequently, the power smoothing units can be utilised over a more extended period.